Naval Research Laboratory

Washington, DC 20375-5320

NRL/MR/6721--97-7912

Advanced Radiation Theory Support Annual Report 1996, Final Report

Radiation Hydrodynamics Branch
Plasma Physics Division

March 10, 1997

REPORT DOCUMENTATION PAGE

Form Approved
OMB No. 0704-0188

1. AGENCY USE ONLY (*Leave Blank*)	2. REPORT DATE	3. REPORT TYPE AND DATES COVERED
	March 10, 1997	Final Report

4. TITLE AND SUBTITLE

Advanced Radiation Theory Support Annual Report 1996, Final Report

5. FUNDING NUMBERS

6. AUTHOR(S)

Radiation Hydrodynamics Branch

7. PERFORMING ORGANIZATION NAME(S) AND ADDRESS(ES)

Naval Research Laboratory
Washington, DC 20375-5320

8. PERFORMING ORGANIZATION REPORT NUMBER

NRL/MR/6721--97-7912

9. SPONSORING/MONITORING AGENCY NAME(S) AND ADDRESS(ES)

Defense Special Weapons Agency
6801 Telegraph Road
Alexandria, VA 22310

10. SPONSORING/MONITORING AGENCY REPORT NUMBER

11. SUPPLEMENTARY NOTES

This research was sponsored by the Defense Special Weapons Agency under Job Order Titles, "Advanced Radiation Theory Support," MIPR No. 96-2008, "Operational Simulator Support, No. 96-2070, and "Decade Load PRS Design," No. 96-2167.

12a. DISTRIBUTION/AVAILABILITY STATEMENT

Approved for public release; distribution unlimited.

12b. DISTRIBUTION CODE

13. ABSTRACT (*Maximum 200 words*)

This report describes the work of the Radiation Hydrodynamics Branch during FY96 in support of the DSWA PRS program. Critical issues covered are: (1) Modeling ACE 4 experiments, (2) Spectroscopic PRS diagnosis, (3) Atomic model development, (4) Long time implosions, power flow, and stability on Decade Quad, (5) Analysis of time resolved Z-pinch data, and (6) Fast commutation of high current in double wire array Z-pinch loads.

14. SUBJECT TERMS

Z-pinch physics
ACE 4
Diagnostic line ratios
Plasma radiation source
Long time implosions
Rayleigh-Taylor instability
Radiation MHD
Decade Quad

15. NUMBER OF PAGES

173

16. PRICE CODE

17. SECURITY CLASSIFICATION OF REPORT	18. SECURITY CLASSIFICATION OF THIS PAGE	19. SECURITY CLASSIFICATION OF ABSTRACT	20. LIMITATION OF ABSTRACT
UNCLASSIFIED	UNCLASSIFIED	UNCLASSIFIED	UL

CONTENTS

Synopsis

This NRL Memorandum Report is Code 6720's final report to the Defense Special Weapons Agency (DSWA) for FY 1996. The report describes in detail our short and long-range theory support aimed at improving DSWA's Plasma Radiation Source (PRS) capability for Nuclear Weapons Effects simulation. During FY 96, the K shell radiation yield of DSWA's ACE 4 generator increased an order of magnitude, and the experiments that produced this improvement were closely supported by modeling in Code 6720. Work proceeded on several medium and longer term objectives. Planning and design of the Decade Quad device, with particular emphasis on power flow, load design and attendant stability, was a major effort in the latter half of the fiscal year. Longer term research proceeded on the atomic data which will be needed to interpret experiments and design advanced loads for higher current machines such as Decade Quad. Analysis of time resolved data from the Saturn generator at Sandia National Laboratories yielded valuable insights into the role of gradients, pulsewidth, and precursor plasmas in influencing radiative output.

EXECUTIVE SUMMARY

This report describes the theory support of DSWA's Plasma Radiation Source (PRS) program carried out by NRL's Radiation Hydrodynamics Branch (Code 6720) in FY 1996. Included is work called for in MIPRs 96-2008, Advanced Radiation Theory Support, 96-2070, Operational Simulator Theory Support, and 96-2167, Decade Load PRS Design.

The technical goals of the PRS program are centered in two areas: improved yields and better simulation fidelity. X-ray doses sufficient in both intensity and spectral distribution are needed for meaningful effects testing. Because it is a research task to realize these goals cost-effectively with pulsed power generators, a theory support program that consists of both short and long range elements is essential. The short range elements of the program employ the theroretical capabilities that have been developed over the years (funded by DNA/DSWA and other sources) to provide support and guidance for maintaining and upgrading currently operational machines. Longer range elements of the program address the need for improved theoretical capabilities to address problems in future machine and load designs and questions such as: what are the tradeoffs in load and generator design that can be used to improve the coupling between the generator and load, what are the best loads for optimizing x-ray energy production within a specified x-ray band, and what are the physical processes responsible for improving radiation performance and how can they be manipulated and controlled? Through its support of this theory effort, DSWA has replaced cut-and-try methods with quantitative understanding of what goes on in power flow, in electrical energy coupling to a load, and in load dynamics so that it is now possible to design around problems as they arise and eliminate speculation from the program that otherwise leads to the notion of "show stoppers". *In the theory program suported by DSWA over the last few years, considerable progress has been made toward determining how machines and PRS loads should be designed to achieve DSWA's goals.* The successes in Sandia's PBFA-Z program this year are in part the product of that progress resulting from DSWA's consistent support of theory and analysis.

During FY 96, the short range aspects of the theory support program also played an important role in quantifying and supporting the progress that was made in improving ACE 4's performance. While ACE 4 is the most powerful of the inductive store generators built to date, it is also somewhat inefficient at generating x rays. At the beginning of the FY, the best Ar K-shell yield (near 3 keV

photon energy) obtained on ACE 4 had been a disappointing 1 kJ. At the end of the year, the Ar yield as well as that of Ne (1 keV photons) had increased an order of magnitude. These yields are finally in agreement with the yields that were predicted to be achievable with ACE 4's present design. This same theoretical evaluation of ACE 4 proposed that a direct drive mode of operation would be more efficient in the long run provided the large inductance of ACE 4 could be reduced. Thus, a team structure comprising Maxwell Labs, NRL, and DSWA, explored three different approaches this year to enhancing the performance of ACE 4. These approaches are: (1) a traditional opening switch approach to sharpen the risetime of the current, (2) a direct drive approach using no switch elements in which there is essentially no power conditioning and therefore too much inductance, and (3) a form of plasma switch known as the tandem puff configuration in which an injected flashboard plasma commutes the current directly onto the load. The tandem puff emerged as the most effective way to operate ACE 4 in its present configuration. It was able to demonstrate the greatly increased yields cited above. Code 6720's day-to-day support of these efforts was documented in more than 100 pages of monthly progress reports submitted throughout the year, and is summarized with the perspective of an entire year in Sec. 1.

Two types of analysis are routinely performed in Code 6720. In one type, the baseline performance of a given machine/load combination can be predicted and/or better designs and performance trends suggested prior to an experiment. In this way, problems with the experiment or with the analysis can be identified, quantified, and corrected. In the second type, a retrodictive analysis is used to infer the parameters (temperature and density structures, etc.) of the PRS plasma from data collected during an experiment. Both analyses are necessary and mutually support one another in advancing the PRS art. Both require extensive atomic data bases for the radiating PRS elements, some of which have been built up over the years of DNA/DSWA support. In Sec. II a large database of calculations of K-shell line ratio and power contours for radiating pinches of Ne, Ar, Al and Ti is presented along with an extensive discussion of their assumptions, methods, and conditions for validity. This chapter should serve as a very useful tool for the community in analyzing Z pinch data. In Sec II, we also present retrodictive analyses of the key ACE 4 shots showing that the Ar K-shell yield increase for ACE 4 was produced by doubling both the density and the fraction of puffed gas that participated in the radiating pinch. One of the best neon shots exhibited an impressive 82% mass participation, comparing favorably with the best results from

non-inductive store, waterline machines.

An excellent example of the continuing need for high quality atomic data is provided by the quest for improved simulation fidelity. Better fidelity means (in part) the production of higher fluences of photons of energy near 5 keV. One of the most promising options for making these photons is the efficient stripping to and excitation of the titanium K shell. To get to the K shell the plasma must first overcome L-shell radiation losses to traverse the L shell, and, in the case of Ti, this has been a significant challenge on existing machines. To assess the required temperatures, densities, and ionization times to accomplish this goal necessitates comprehensive atomic data for the L shell stages. Such an atomic model will inevitably lead to spectroscopic diagnostics which can then be applied to interpret ongoing experiments. The beginning atomic model development for L-shell Ti is discussed in Sec. III.

Another promising path to enhanced simulation fidelity is to place the test object closer to the Plasma Radiation Source, thereby gaining higher fluences via the $1/r^2$ effect. This approach has long been constrained by the deleterious effects of debris impact on the sample. We have explored a novel solution to this problem - the use of LiH as both a return current structure and debris shield. This design has been investigated in detail and reported to DSWA in NRL Memorandum Report 6720-96-7868, dated September 4, 1996. The tradeoffs in Ar K-shell transmissivity, debris impact velocity, and source-sample distance, would allow a 16-fold increase in available fluence in Ar puff scenarios, as one example.

Toward the middle of FY 96, our work on Decade Quad (DQ) accelerated. We were part of the team that prepared a criteria document that was delivered to DSWA in July. Current conservative designs for DQ anticipate a short circuit current of 7-8 MA reached in a risetime of 300-350 ns. The main criterion for initial acceptability of DQ is the achievement of 20 kJ Ar K-shell radiation yield. Higher ultimate radiation goals are desired and achievable - it should eventually be possible to double the Ar yield to 40 kJ. To ensure that these goals would be accomplished, NRL Code 6720 was selected to coordinate the load physics research and development for DQ, and this effort began just prior to the end of FY 96. The work proceeded along two main lines, beginning with the determination of a baseline load(s) of low risk designed to produce the 20 kJ. A 2.5 cm radius annulus of Ar with mass load 150-200 μg/cm, or alternatively, a filled cylinder of 3.6 cm radius of the same mass load were chosen as the baseline cases to get to the 20 kJ goal. Concurrently, work

proceeded on advanced loads which would be capable of at least doubling this yield. We have also been involved in power flow modeling for DQ - the conservative design referred to above has not been frozen as of the end of FY 96. Short circuit currents of 10 MA are feasible, which would greatly reduce the risk and enhance the versatility of DQ as a PRS machine. We urge DSWA to carefullly consider enhanced current options, which have also been proposed by Pulse Sciences Inc. and are essential for long implosion time machines. Code 6720's work on the DQ load physics and full transmission line power flow modeling during FY 96 is presented in Secs. IV and V, respectively.

The Rayleigh-Taylor (RT) instability occurs in the Z pinch environment because a magnetic field, with essentially no mass or inertia, accelerates a fluid, namely the pinch plasma, of finite mass. X-ray yields could potentially be unacceptably reduced when this instability grows too rapidly since some substantial fraction of radial kinetic energy could possibly be transformed to axial kinetic energy, and the compression will be reduced or disrupted. There is as yet no firm basis for quantifying such a yield reduction. It is clear that in extreme cases, such as breakup of the full imploding plasma shell, the yield will be compromised. The first direct drive neon shots on ACE 4, for example, produced only a few kJ of K shell radiation when complete disruption occurred. How much and under what conditions, if at all significantly, will the yield will be compromised when "moderate" disruption occurs is one of the most important topics requiring future investigation.

Sec. VI presents an investigation which shows that certain tailored density profiles can suppress the RT instability in imploding pinches. Often referred to as structured loads, they make it possible to extend the outer radius to better utilize long duration pulses such as those of Decade and ACE 4. The effective gravity, hence the growth rate of the instability, is reduced when the shock wave encounters layers of increasing plasma density. In this section, the load stability studies are also applied to the ACE 4 tandem puff configuration.

Present Z pinches that radiate well appear to consist of a hot core surrounded by a cooler shell. Evidence for this continued to accumulate during FY 96, from so many machines and so clear-cut that many in the community consider the case proven. This evidence now consists of: (1) Time resolved data from Mg coated Al wire experiments on both Double EAGLE and PHOENIX that show the Mg boiling off the Al wires, drawn into the axis, and radiating earlier and with a higher temperature than the Al which forms a cooler shell of the assembled pinch. (2) Ti coated Al

wire data from Saturn showing similar phenomena for those two elements. (3) Spatially resolved spectroscopy from Al wire shots on Saturn which directly demonstrates the decrease in temperature from the axis outward. (4) The need for temperature gradients to explain the predominance of L over K shell radiation in even the most successful K shell experiments. (5) ACE 4 pinhole image data from mixed Ar:Ne shots showing the cooler Ne K shell emitting region extending over at least double the radius of the hot Ar K shell source. (6) The decreasing size of pinches as viewed with filtered pinhole imaging at increasingly higher x-ray energies.

The cooler shell plasma represents a reservoir of energy which is essentially wasted in experiments in which the goal is to maximize the K shell yield. If we could learn how to control these gradients with tailored load or pulse power designs the K shell yields could be doubled or better without having to increase current. Perhaps the best and most comprehensive data ever taken of Z pinch plasmas is that from recent 90 wire Al experiments on Saturn at Sandia National Laboratories. Excellent space, time, and spectral resolution was obtained. Sec. VII presents a detailed analysis of that data and discussion of its implications. Note that reasonably good Al K-shell yields of 50-55 kJ were achieved with only about 20% mass participation, a dramatic demonstration of the fact that greatly enhanced K-shell yields are, in principle, achievable with existing simulators. Any chance of realizing this yield enhancement requires an in-depth understanding of the structure of the pinch, how that structure comes about, and how changes in load design affect it. Sec. VII discusses how an optimum interaction between experiment and theory can be set up to produce the kind of interaction that is needed to accomplish such a goal. The analysis points to the important role that precursor plasma plays in contolling the pinch's peak densities and x-ray powers.

For many years, work has proceeded on various configurations of plasma switches to sharpen the current risetime at the load. These switches have had success at current levels of 1 MA or so, but have encountered severe difficulty at several MA. The recent ACE 4 tandem puff work is one of the first good results at such higher current levels. It utilizes a concept that might more fruitfully be applied to wire loads. Thus, Sec. VIII presents a novel and promising form of plasma power conditioning: commutation of current in nested concentric wire arrays in which the current in the outer array is switched to the inner array. The advantage of wire arrays over gas puffs is that the plasma initial conditions can be more carefully controlled. Advantages of this proposed design for pinch stability are also discussed in this section.

I. MODELING OF ACE 4 EXPERIMENTS

A. ACE 4 - Direct Drive Experiments

The work that was done this past year in support of direct drive experiments represents the early stage of development of direct drive technology, which could play a significant role in influencing DECADE load and machine design. In this section the potential of ACE 4 for producing neon and argon K-shell emission is analyzed theoretically and then these results are compared with those obtained experimentally.

The ACE 4 direct drive circuit model is shown in Fig. 1. The quarter cycle time of this circuit is nearly 2 μs, which implies that implosion times need to be long in order to insure reasonable energy coupling to the load. Two common techniques for achieving long implosion times are (1) implode from large radius and (2) implode larger mass.

Imploding from large radius involves an assessment of the effects of load stability on the ability of the load to radiate K-shell photons. This is currently an active area of research, as there is no consensus in the DSWA/DOE community as to how stability directly effects the ability of a plasma to radiate K-shell photons. One way to establish this relationship theoretically is to perform 2-D/3-D, non-LTE, full radiation transport, radiation hydrodynamics calculations. However, this full capability does not exist in the community. Our 2-D models use a CRE model for modeling the equation of state and ionization dynamics but the plasmas are assumed to be transparent or else a local probability of escape model is used to model radiation transport. Other models used by the community, e.g., at Sandia Laboratories, use three temperature radiative diffusion models which are only valid for LTE conditions. These models may be valid for low temperature tungsten loads but they do not accurately characterize a high temperature, non-LTE plasma.

Increasing the load mass as a technique for lengthening the implosion time can be done to the extent that the energy-per-ion at stagnation remains large enough that the plasma can effectively emit K-shell photons. Over the years there have been numerous scaling laws developed to predict the tradeoffs between the available machine energy, the mass, and the ability of the load to radiate in the K shell. In this work the scaling relations shown in Fig. 2 are used. These relations are an extension of the scaling work done in Refs. 1-3. The extension is made based on the 1-D effort that went into studying the scaling of K-shell emission in the low η regime. These predictions should be valid to within a factor of two for experiments with $\eta \geq 1.5$, that are reasonably 1-D, and for which thermalization of kinetic energy during the stagnation of the plasma on axis is the primary mechanism for producing K-shell photons. These relations can underestimate the emission of K-shell photons obtained experimentally from low Z materials such as neon or aluminum because other heating mechanisms such as resistive heating and plasma recompression are sufficient to maintain these plasmas in the K-shell ionization stage. The temperature at which K-shell occupation is strong scales as $Z^{2.9}$. On the other hand, a very rapid thermalization of kinetic energy (such as what takes place in a 1-D implosion) is needed to overcome radiative cooling and allow high Z materials to reach the temperatures needed for K-shell emission.

Fig. 3 displays the potential of ACE 4 for producing neon and argon K-shell emission as predicted by a 0-D snowplow analysis that uses the scaling relations of Fig. 2. These results are based on the assumptions of 1/7 compression and that 5 cm is the maximum

Manuscript approved January 3, 1997

initial outer radius of a uniform fill load that one can implode and still produce neon K-shell yields that are in reasonable accord with 1-D results. Given this potential, it is unlikely that ACE 4 in the circuit configuration of Fig. 1 will ever be a prolific radiator of argon K-shell emission. Given the radiative limitations of this configuration, from a theoretical point of view the most important aspect of the direct drive experiments was to assess our ability to model these large radius experiments rather than optimize K-shell emission.

A schematic diagram of the diode region of the direct drive experiments is shown in Fig. 4. Note, this is a different configuration then was utilized in the tandem puff experiments. There a mask with a prescribed diameter hole is placed directly over the anode plane in order to define the implosion radius and shield the flash-board region of the diode from external plasma. In the direct drive experiments a baffle configuration was designed by Maxwell and NRL code 6770 to perform the same function as the mask but allow a larger field of view for the diagnostics.

The first set of "direct drive" experiments were completed in May. These experiments are viewed as a first step in developing direct drive technology. In this regard, a discussion of some of the highlights and problems encountered in this initial set of experiments are summarized below.

At the time of our visit to Maxwell Laboratories it was discovered that the peak neon K-shell yields achieved were in agreement with the maximum calculated yields. However, the measured implosion times (Fig. 5) were much longer, several hundred ns, than the calculated implosion times (see Fig. 3). This comparison between experimental and calculated implosion times is based on the assumptions that the mass of the load and its distribution are known (S-Cubed's [Hylton Murphy's] mass calculations were used) and that the ACE 4 circuit parameters are known. There are, therefore, several approaches that can be taken towards resolving this disagreement depending on which of the two assumptions one challenges.

One approach is to assume that the circuit parameters are known, then the difference between calculated and measured implosion time is related to the determination of the kinematic mass, which is obtained from modeling the circuit and knowing the implosion time. This mass turns out to be greater than the calculated mass in Fig. 5, which was calculated assuming knowledge of the puff gas valve and baffle gas kinetics. If the puff gas mass distribution is unknown, the kinematic mass calculation needs to make assumptions about it. At first, therefore, a shell implosion from 5 cm is assumed. If a uniform fill distribution had been modeled, which was originally thought to be the experimental distribution, then the kinematic masses would be even larger than those displayed in Fig. 6.

Another approach is to assume that the circuit model is inaccurate, then, by assuming that 90% of the generator current pushes on the load and adding an additional 5 nh to the circuit we could reproduce the generator current and voltage trace as a function of implosion time. Based on these assumptions, the predicted yields and mass loads are shown as a function of implosion time for a 5 cm shell implosion (Fig. 7) and a 5 cm uniform

fill implosion (Fig. 8). The experimental yields are also shown in these figures. The best match between experimental and calculated yields suggest that the load configuration may be more indicative of a shell implosion rather than a uniform fill as originally thought. Mass loads predicted by this model are also much larger than Murphy's calculated masses. This is not meant in any way to discredit his calculations. There are many other mechanisms other than larger mass loads that could lead to longer implosion times, e.g., if the baffles are leaking gas out to large radius. Note, the speculation that the circuit model was totally inadequate for modeling the load current was initially supported by the generator and load current data shown in Fig. 9. However, even after changing nozzles, changing the way the anode mesh is strung, preionizing the gas, and using the same mask technique as used in the February tandem puff experiments, the load current monitor still read appreciably lower than the generator monitor (only about a 10% reduction is expected). Based on the scattered values for load current as a function of implosion time (Fig. 9), there is a strong suspicion that the load current monitor is faulty.

There was an attempt to begin an investigation into tailored density profiles by putting a small amount of additional mass at large radius. However, because of the gas baffle configuration this was very difficult to implement. The extra mass was introduced mainly at the outer radius of the initial gas, which is not far enough out to substantially increase the implosion time (drive current) and K-shell yield. The results did show an increase in implosion time but there was no noticeable increase in neon K-shell yield. These experiments need to be repeated when the mass load, load configuration, and load current are better defined. Fig. 10 displays 0-D snowplow K-shell yield predictions for the 5 cm uniform fill load that has in addition a low density fill gas between 5 and 12 cm. A comparison between Fig. 10 and Fig. 3 illustrates the theoretical potential for using this technique to enhance K-shell yield.

In summary these direct drive experiments produced as much neon K-shell emission as predicted. However, the baffle configuration and load current monitor readings made it impossible to correlate quantitatively our models with experiment because of lack of knowledge of the experimental load mass and configuration. Given this uncertainty, the next set of direct drive experiments which were performed in September (but not yet fully analyzed) were designed to eliminate some uncertainties in the mass, mass distribution, and current transfer to the load. This was accomplished by eliminating the baffle configuration and using Sandia's standard 6 cm diameter uniform fill nozzle.

References

1) K. G. Whitney, J. W. Thornhill, J. P. Apruzese, and J. Davis, J. Appl. Phys. 67, 1725 (1990).

2) J. W. Thornhill, K.G. Whitney, C. Deeney, and P. D. LePell, Phys. Plasmas 1, 321 (1994).

3) J.W. Thornhill, K. G. Whitney, J. Davis, and J. P. Apruzese, J. Appl. Phys. 80, 710 (1996).

ACE 4 Direct Drive Circuit Model

NRL

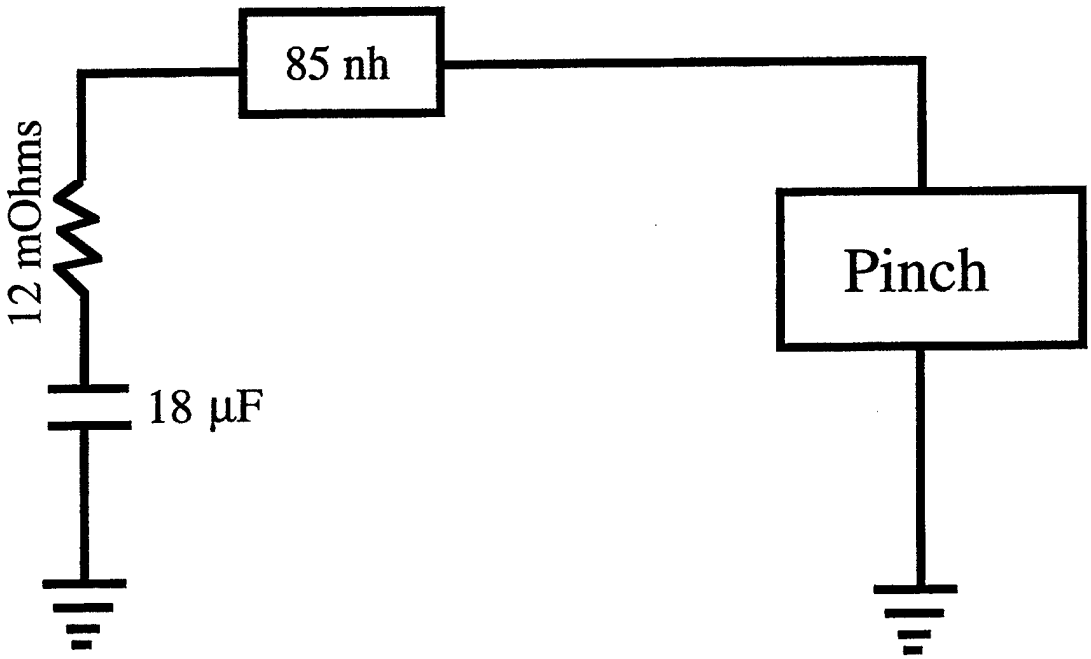

Fig. 1

Z Scaling of K-shell Emission

$$\eta = \frac{\text{Kinetic energy (j/cm)} \bullet 1.1 \bullet 10^{-5}}{\text{Mass (g/cm)} \bullet Z^{2.41}}$$

Z is the atomic number

$$\alpha = \frac{2.58 \bullet 10^{-12} \bullet Z^{5.96}}{\exp(-20.6/Z^{.9})} \bullet \text{maximum } (1.0, \eta^2/(\eta+12))$$

β = minimum of

0.3 • Kinetic energy (j/cm)

or

$$\frac{0.3 \bullet \text{Kinetic energy (j/cm)} \bullet \text{Mass(g/cm)}}{\alpha}$$

K-Yield (j/cm) = β for $\eta > 1.5$

K-Yield (j/cm) = $\beta \bullet (\eta - 0.5)$ for $1.0 < \eta < 1.5$

K-Yield (j/cm) = $\beta/2 \bullet (1 - ((1-\eta)/0.25)^{.5})$ for $0.75 < \eta < 1.0$

K-Yield (j/cm) = 0.0 for $\eta < 0.75$

Note, there is no accounting for innershell absorption effects in this scaling, important for Mass(Z) > 700 μg/cm • $(Z/13)^3$. Also this scaling is based on CRE calculations, i.e. there is no account for the time dependence of the ionization process.

Fig. 2

Direct Drive

5 cm radius uniform fill load

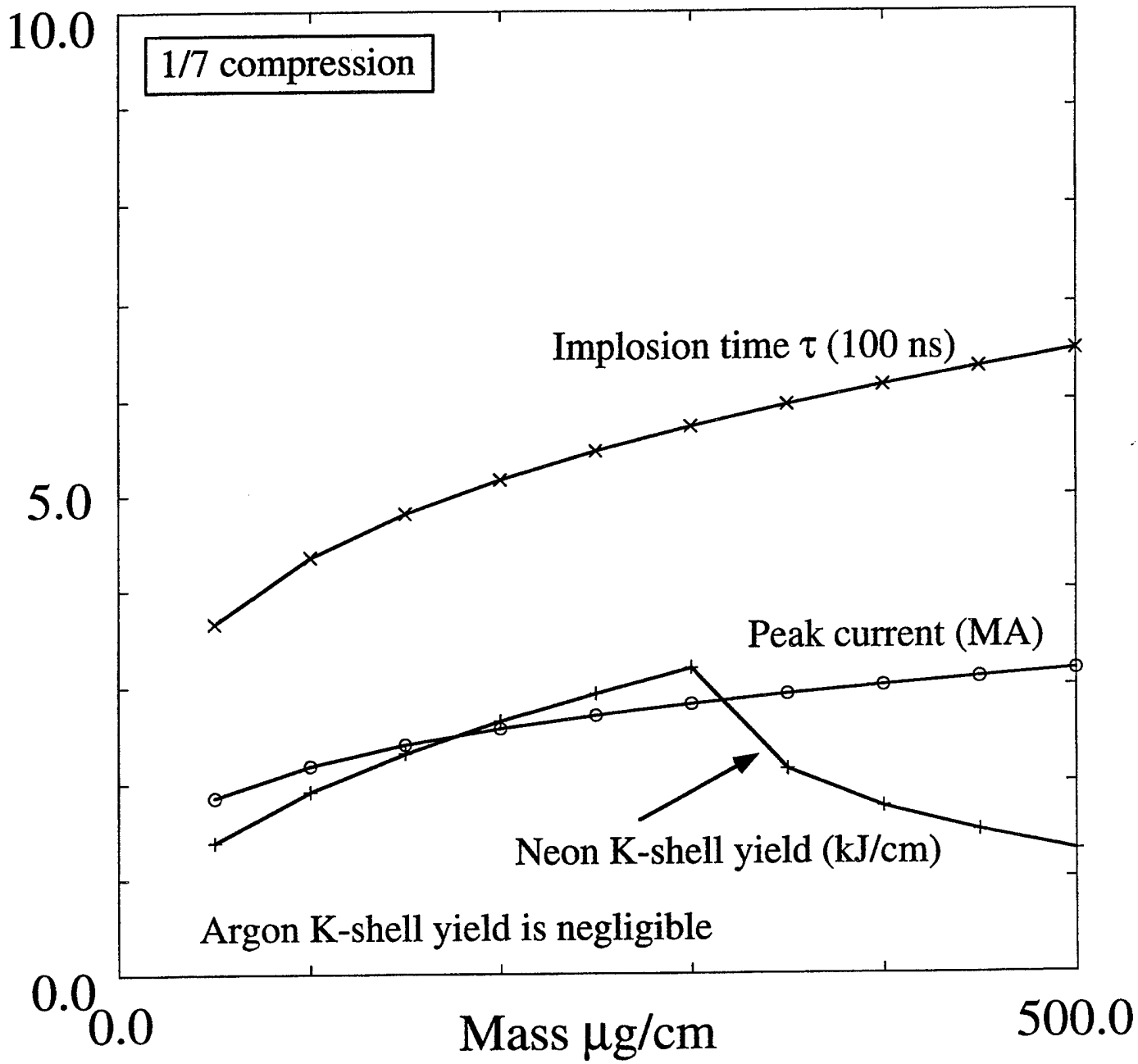

Fig. 3

ACE 4 DIRECT DRIVE Configuration

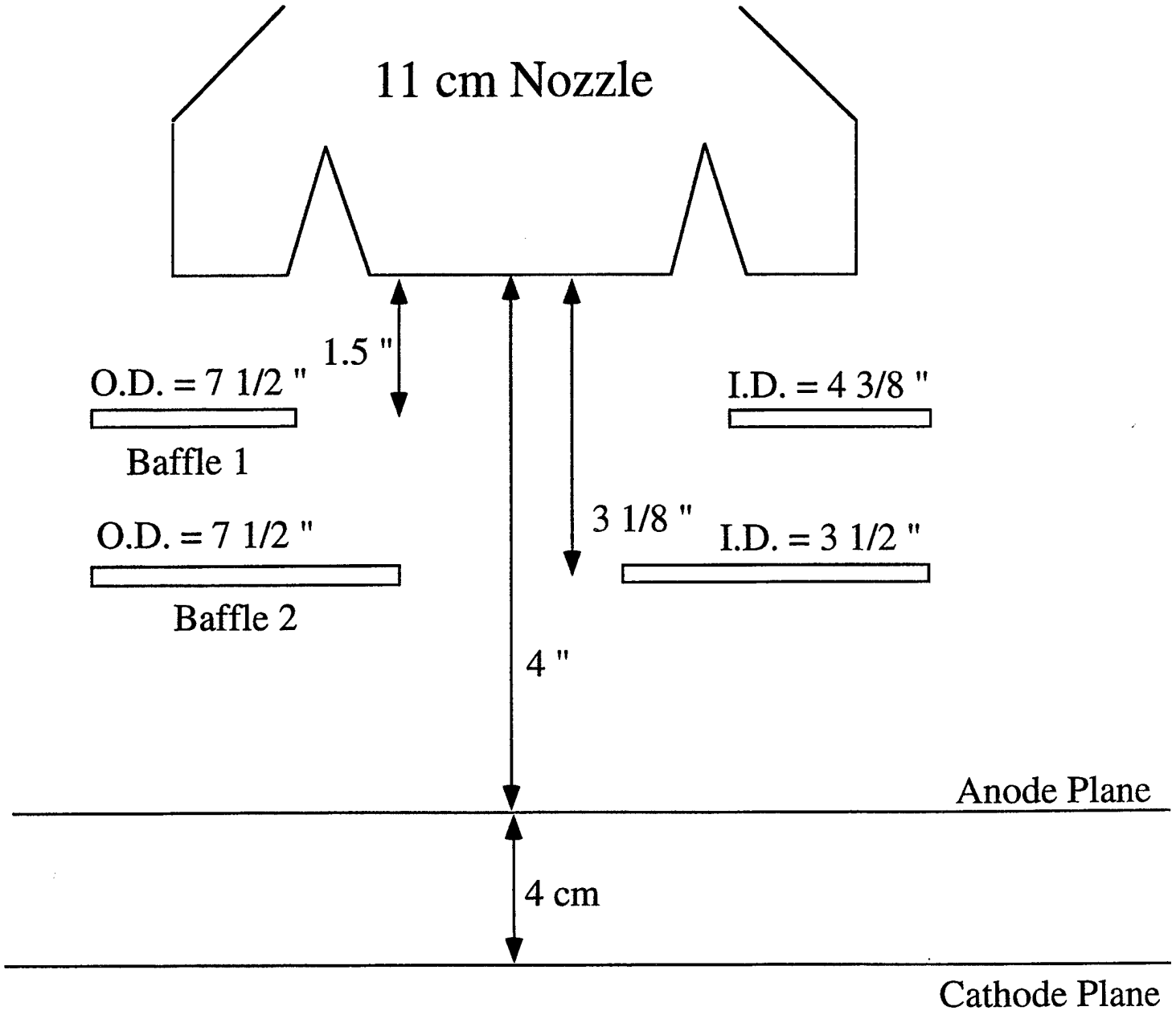

Fig. 4

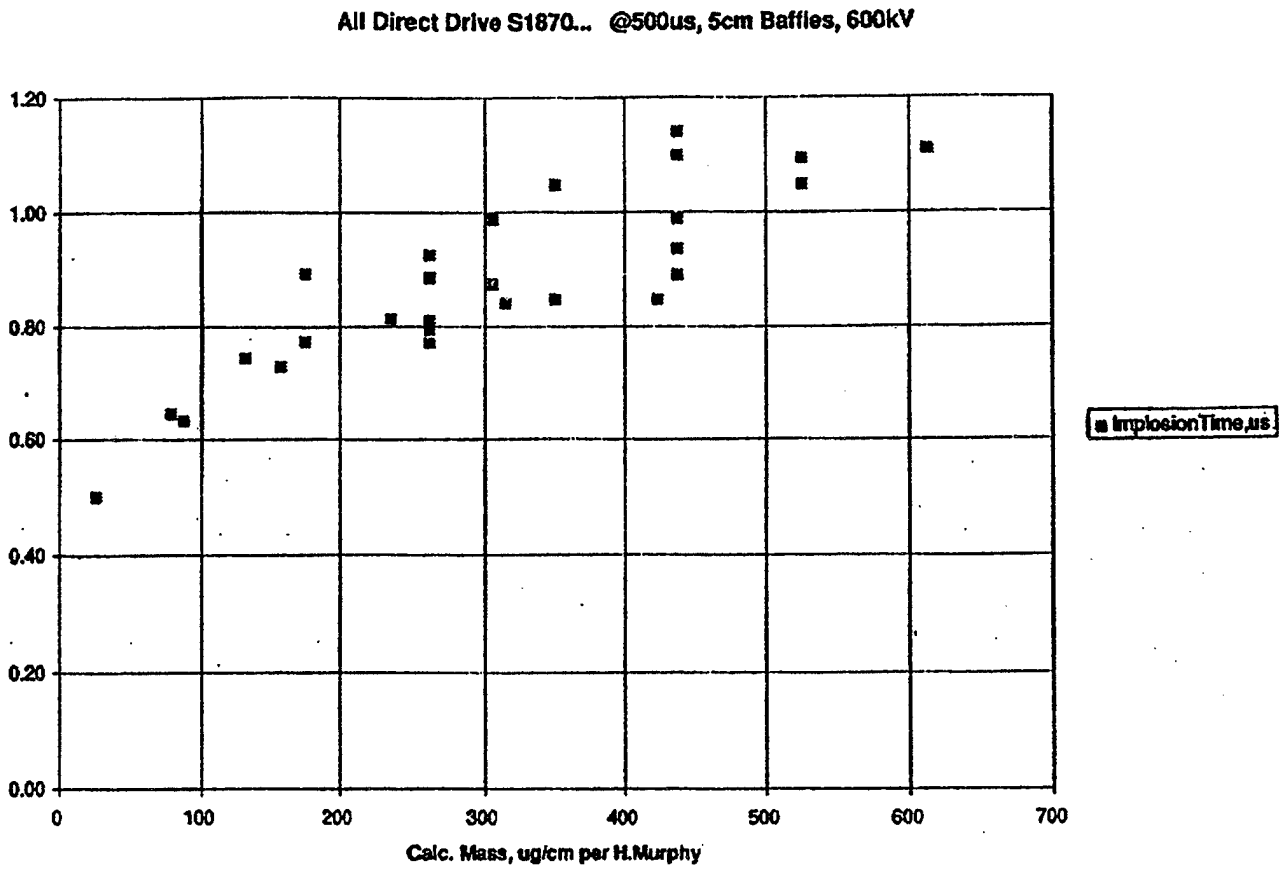
All Direct Drive S1870... @500us, 5cm Baffles, 600kV
1.20
1.00
0.80
0.60
0.40
0.20
0.00
0
100
200
300
400
500
600
700
Calc. Mass, ug/cm per H.Murphy
ImplosionTime,us

Fig. 5

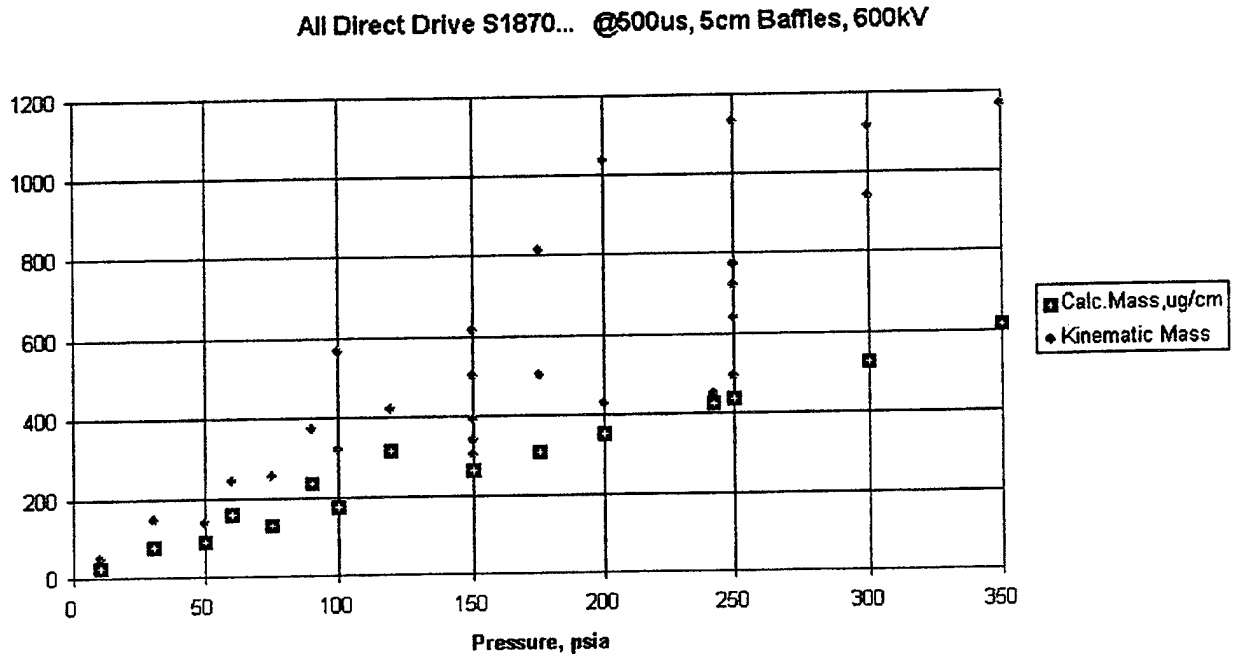
All Direct Drive S1870... @500us, 5cm Baffles, 600kV
1200
1000
800
600
400
200
0
0
50
100
150
200
250
300
350
Pressure, psia
Calc.Mass,ug/cm
Kinematic Mass

Fig. 6

Ace 4 Direct Drive

NRL 6720

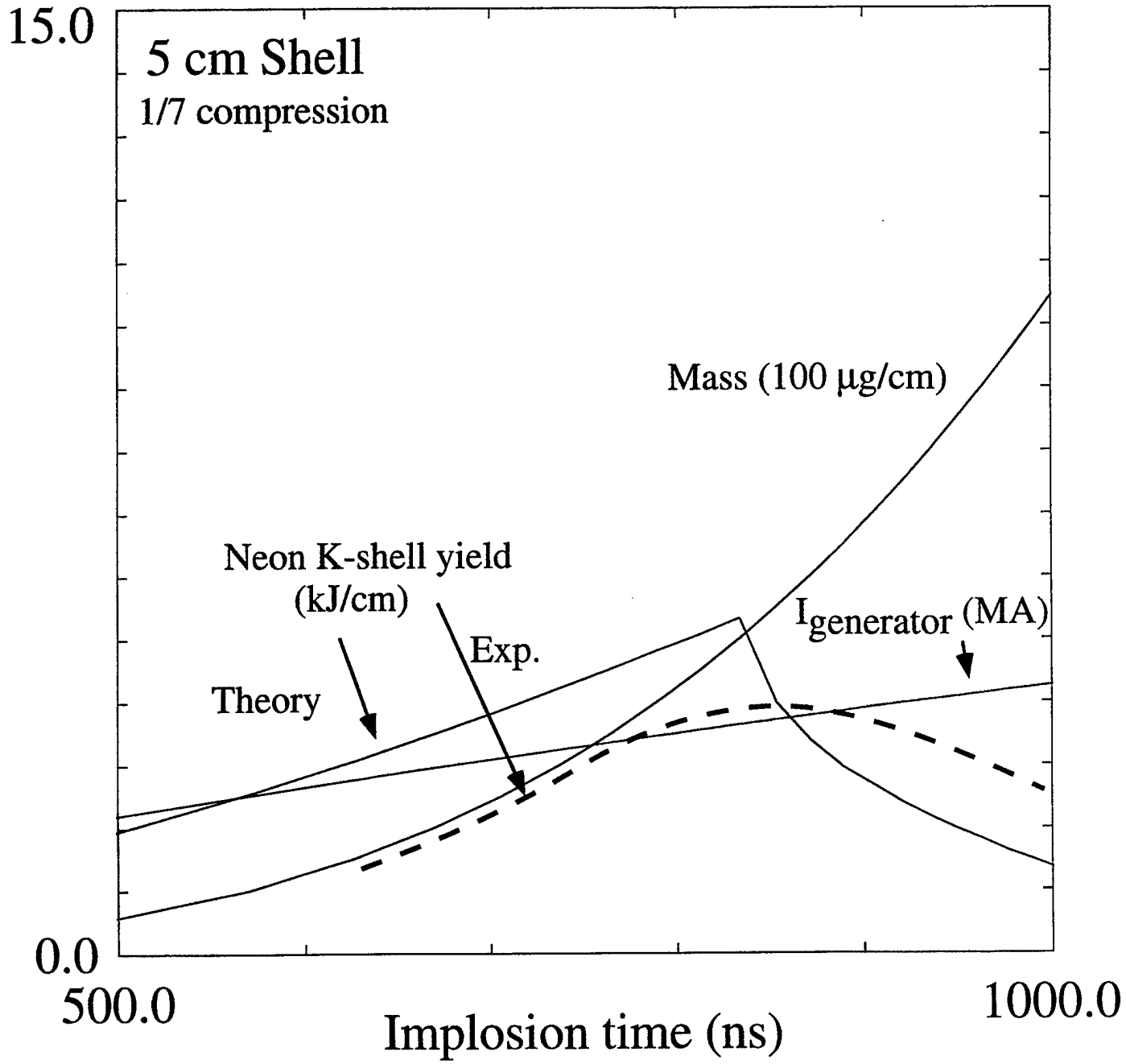

Fig. 7

Ace 4 Direct Drive

NRL 6720

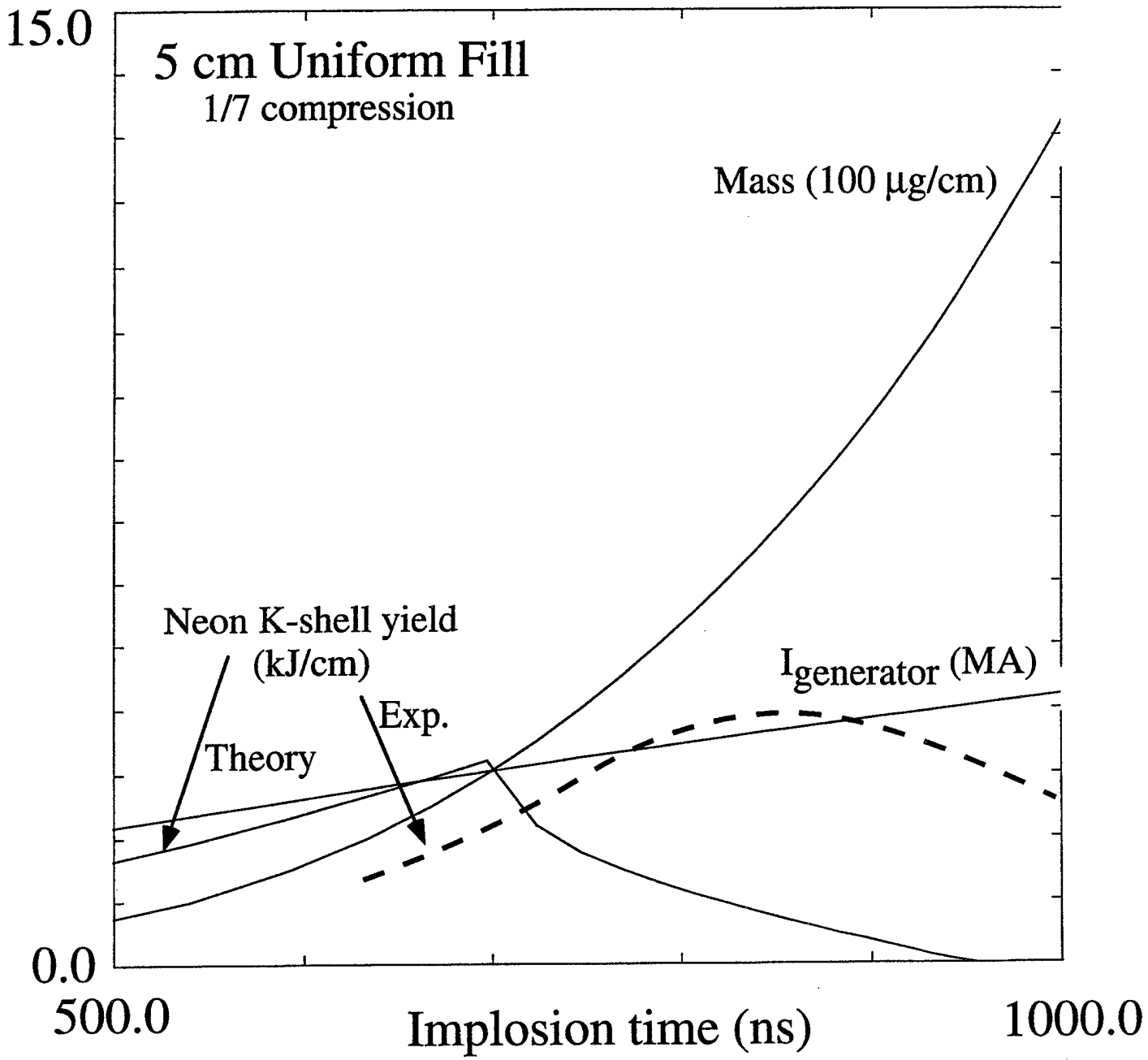

Fig. 8

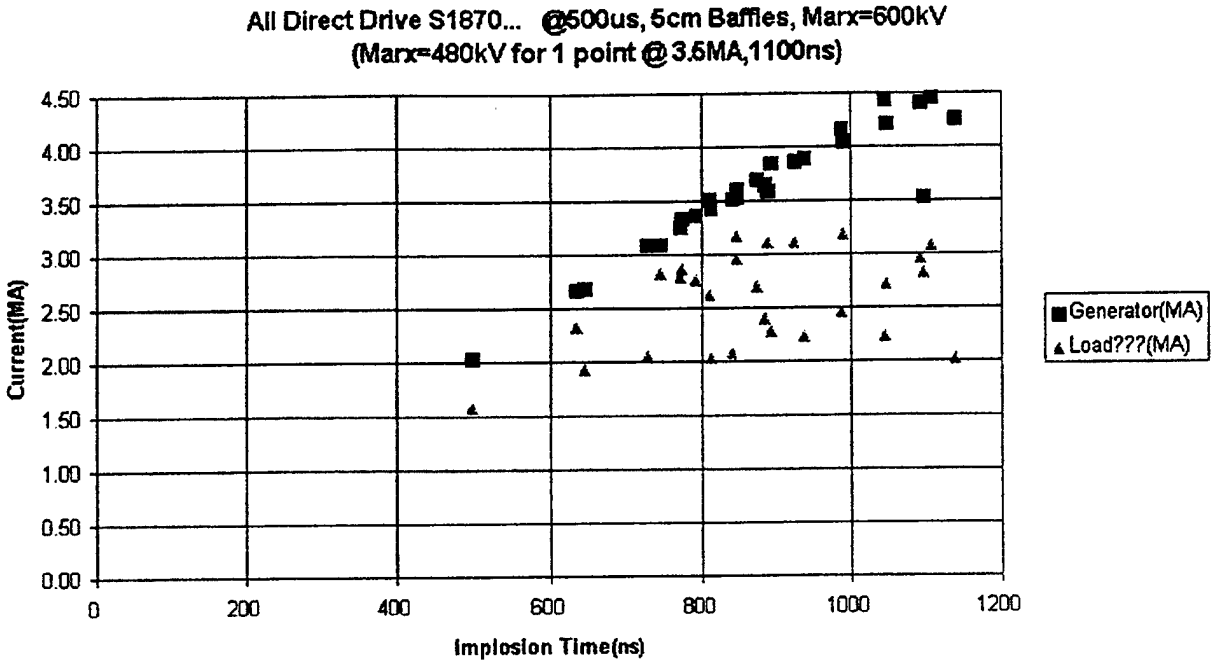
All Direct Drive S1870... @500us, 5cm Baffles, Marx=600kV
(Marx=480kV for 1 point @ 3.5MA,1100ns)
Current(MA)
4.50
4.00
3.50
3.00
2.50
2.00
1.50
1.00
0.50
0.00
0
200
400
600
800
1000
1200
Implosion Time(ns)
Generator(MA)
Load???(MA)

Fig. 9

Direct Drive

5 cm radius uniform fill plasma

Low density outer fill plasma
from 5 cm to 12 cm

15 % of plasma mass is
in low density outer fill

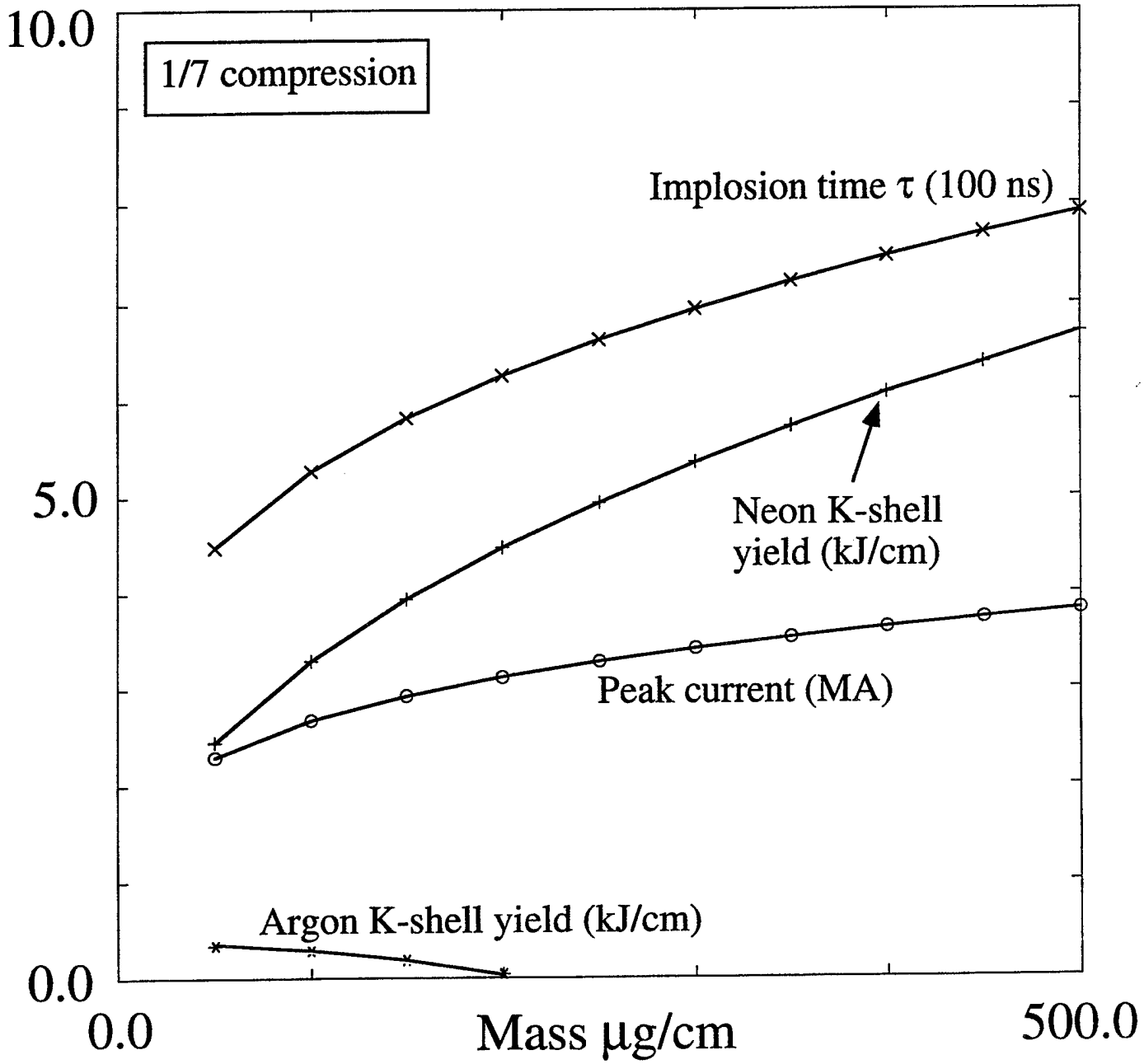

Fig. 10

B. ACE 4 Tandem Puff Experiments (Jan-Feb 1996)

A theoretical assessment of the PRS load performance of the tandem puff experiments that were completed in February 1996 was presented at the March 28-29 ACE 4 meeting. Some of the highlights of this work are summarized below.

Figure 1 displays experimental and 0-D snowplow results for the 13 cm radius, 480 kV capacitor charge experiments. The experimental neon K-shell yields are plotted in accord with their experimental implosion time (implosion time was fiduciated to when the B-dot probe located near the top of the cathode was activated). The mass that is read below each experimental yield point corresponds to a "kinematic mass", which is the mass that is self-consistent with the implosion time and the circuit model employed, see Fig. 2. Ted Cochran's 2-D analysis had shown that these 13 cm radius loads are very unstable so it was not a surprise that the experimental yields were factors of 2-3 below 0-D snowplos estimates. In addition, the kinematic mass was not even close to the mass obtained by integrating the measured density profiles (see Fig. 3;measurements were made by NRL code 6770) which again suggest non-1D and less than ideal behavior. Note, 0-D snowplow yield results presented in this section are based on the 1-D scaling relations discussed in the Direct Drive Section.

Figure 4 shows experimental and 0-D snowplow argon and neon K-shell yields for the 7 cm radius loads at 480 kV charge. These loads are only marginally 2-D stable (assuming a uniform fill distribution from 7 cm radius). Marginally stable means that the mass per unit length in a spike region of the stagnated plasma is less than a factor of 10 greater than that in a bubble region. Given that these loads are not 1-D theoretically, it was surprising to get as good agreement between a 0-D snowplow analysis and experiment as was attained. This helped us to encourage Phil Coleman to perform experiments at higher charge voltage. The yield results of these 600 kV experiments are shown in Fig. 4. While there was some increase in argon K-shell yield over the 480 kV yields, the increase was not as large as we had hoped based on our 0-D snowplow and 1-D analysis. Even the trends were not in the same direction, e.g., we expected the yield to increase as the mass was increased from 100 μg/cm to 200 μg/cm and it did not. A preliminary assessment for this load is that not all of the current that is modeled is getting to the load and/or instability effects are limiting performance. Since there were only three experiments performed at the 600 kV setting (discounting wire on axis shots), more experiments are needed to obtain a better assessment.

Figure 6 shows experimental and 0-D results for the 1.75 cm radius nozzle experiments performed at 600 kV charge. The experimental yields per unit length for this configuration are nearly the same as for the 7 cm radius implosions. Simple analysis shows that the mass may have been to low to optimize yield. Again, because there were only two shots taken, more experiments with this configuration are needed for better assessment.

A comparison between Fig. 7 and Fig. 8 illustrates the potential for the tandem puff configuration if some of the front end inductance is reduced, e.g., if the 125 nh shown in Figure 2 is reduced to 85 nh.

In general, we were very encouraged by the results of the February tandem puff experiments. However, load and machine performance could have been better assessed if loads for which we have some theoretical and experimental experience had been used. This can be fulfilled either by using nozzles (preferably tilted) of 2.25 - 1.5 cm radius, or going to smaller than 7 cm diameter uniform fill implosions. Even a 5 cm radius mask should produce a significantly more 1-D implosion than the 7 cm radius mask. Some of these suggestions were implemented in the August tandem puff experiments.

Tandem Puff Theory

13 cm radius 480 kV charge

0 - D Snow-plow Model

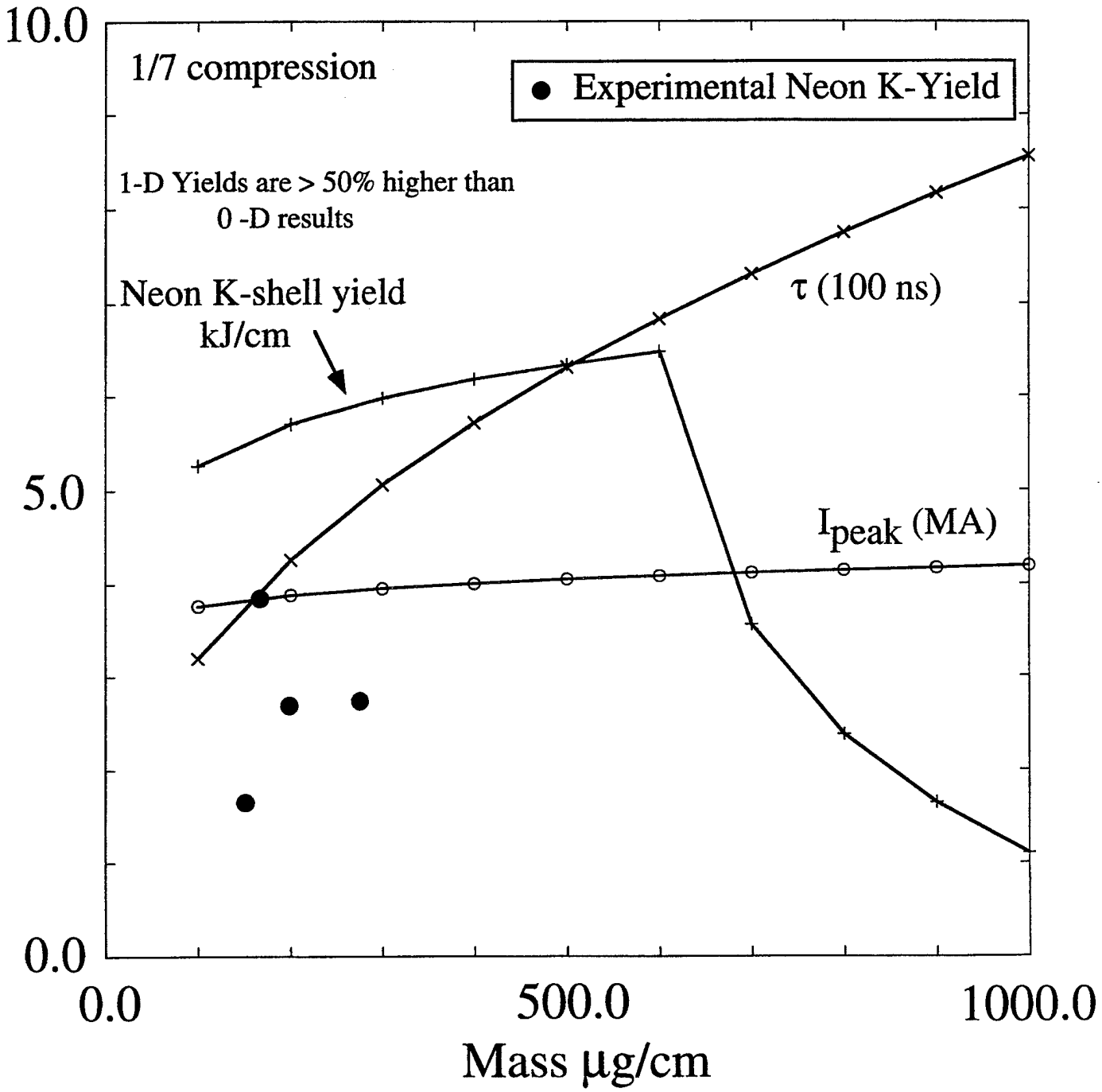

Fig. 1

ACE 4 Tandem Puff Circuit Model

NRL

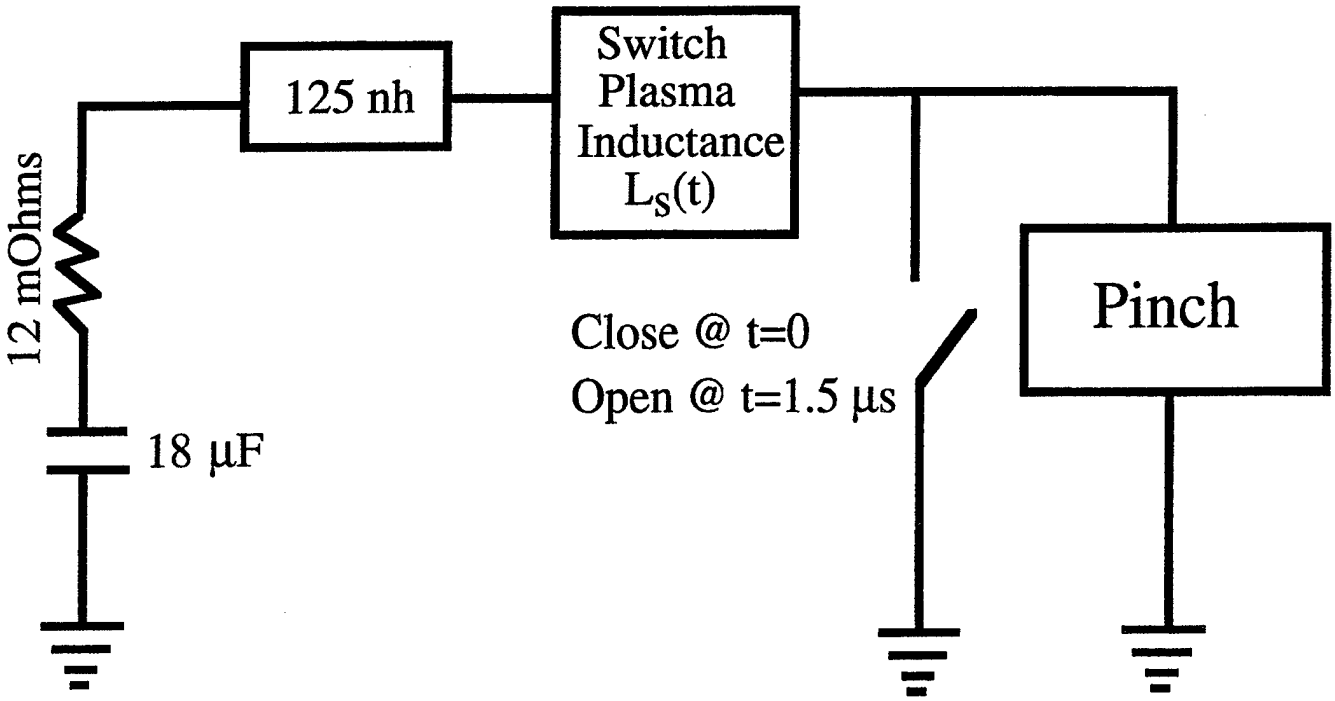

$L_S(t) = 27$ nh x $t/1.5$ μs for $t < 1.5$ μs

$L_S(t) = 27$ nh for $t > 1.5$ μs

The switch is modeled as a time dependent resistance with the following characteristics:

$R_S(t) = 0.0$ Ohms for $t < 1.5$ μs

$R_S(t) = 1.0$ Ohms x $(t-1.5$ μs$)/0.2$ μs for $t > 1.5$ μs

Fig. 2

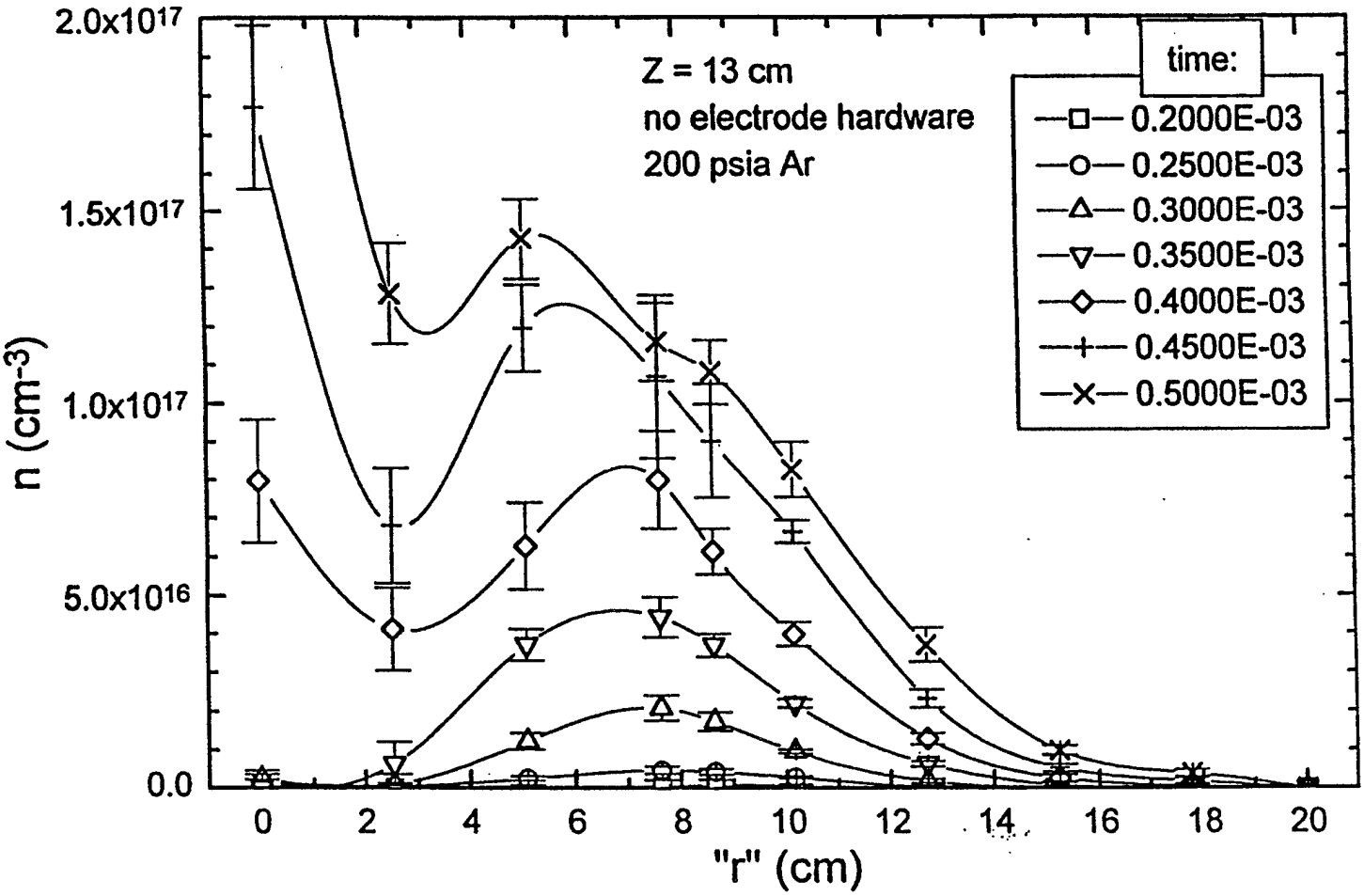

Fig. 3 Argon number density as a function of delay time and radial position away from the axis of the pinch. Measurements were taken (by NRL Code 6770) 13 cm away axially from the nozzle exit. An 11 cm radius nozzle was used.

Tandem Puff Theory

480 kV charge
0-D Snowplow Model
7 cm initial radius
Uniform fill
1/7 compression

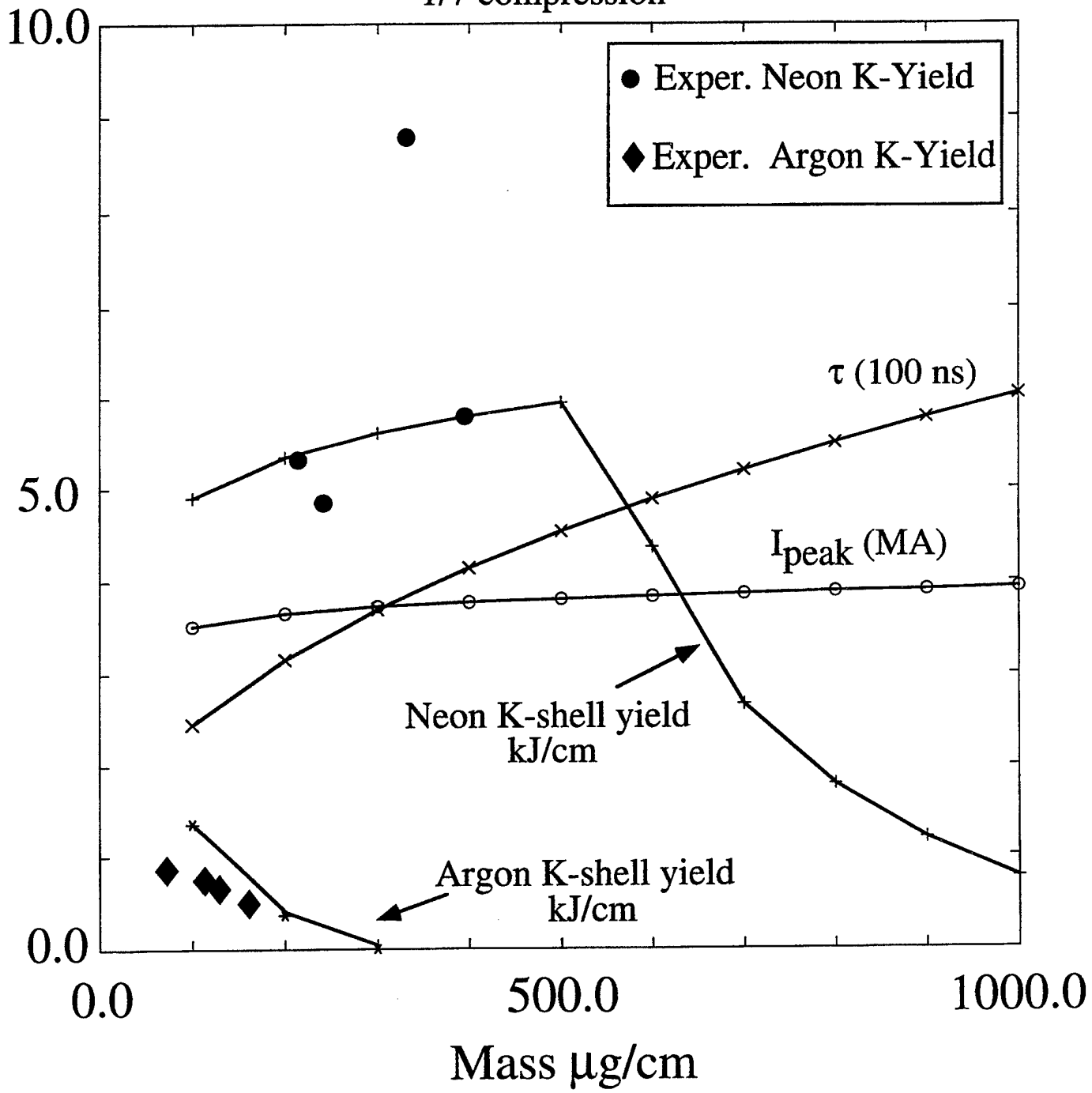

Fig. 4

Tandem Puff Theory

600 kV charge
7 cm initial radius
Uniform fill
0 - D Snow-plow Model

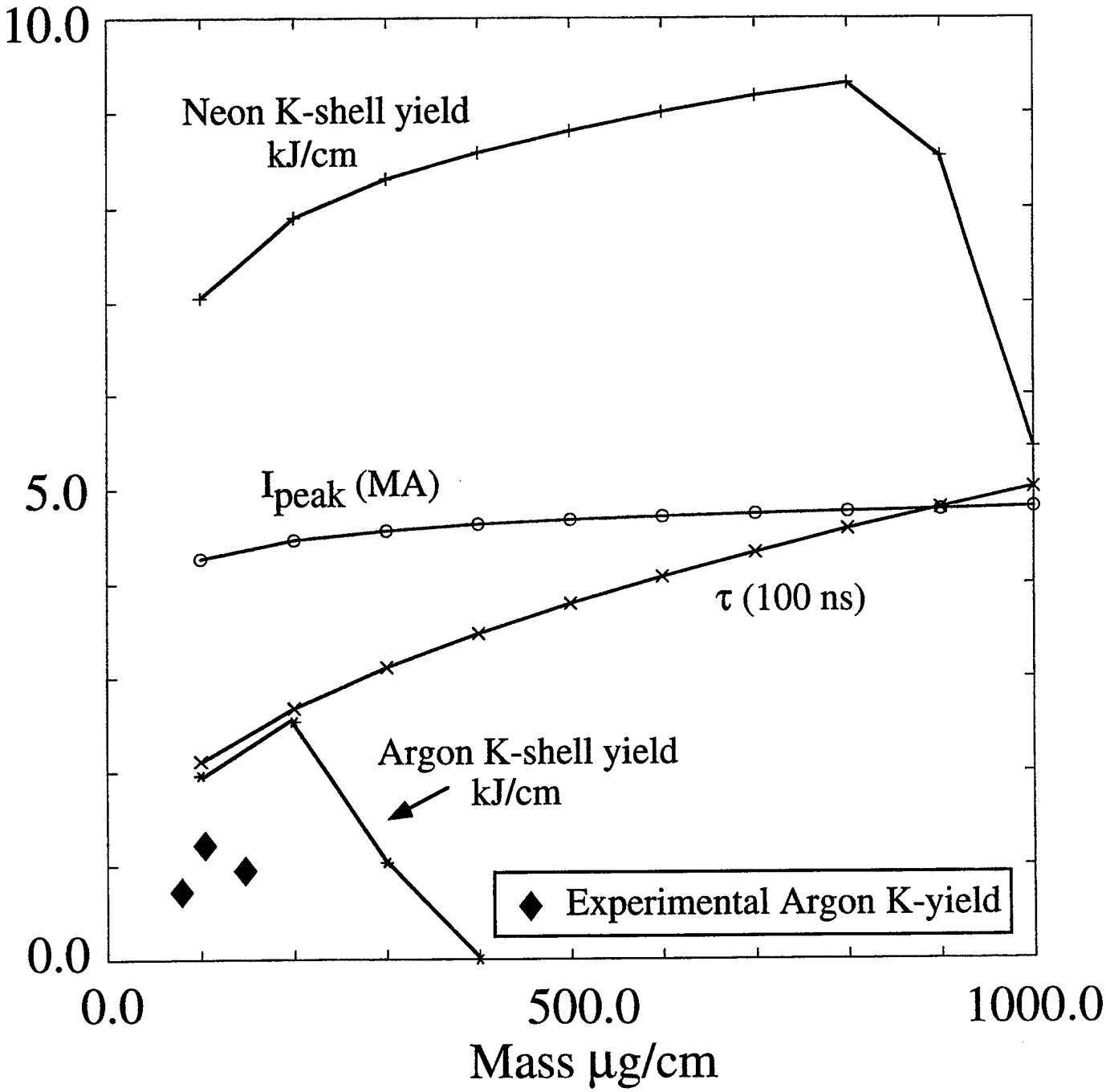

Fig. 5

Tandem Puff Theory

1.75 cm radius Nozzle
600 kV charge
0 - D Slug Model
4 cm length pinch

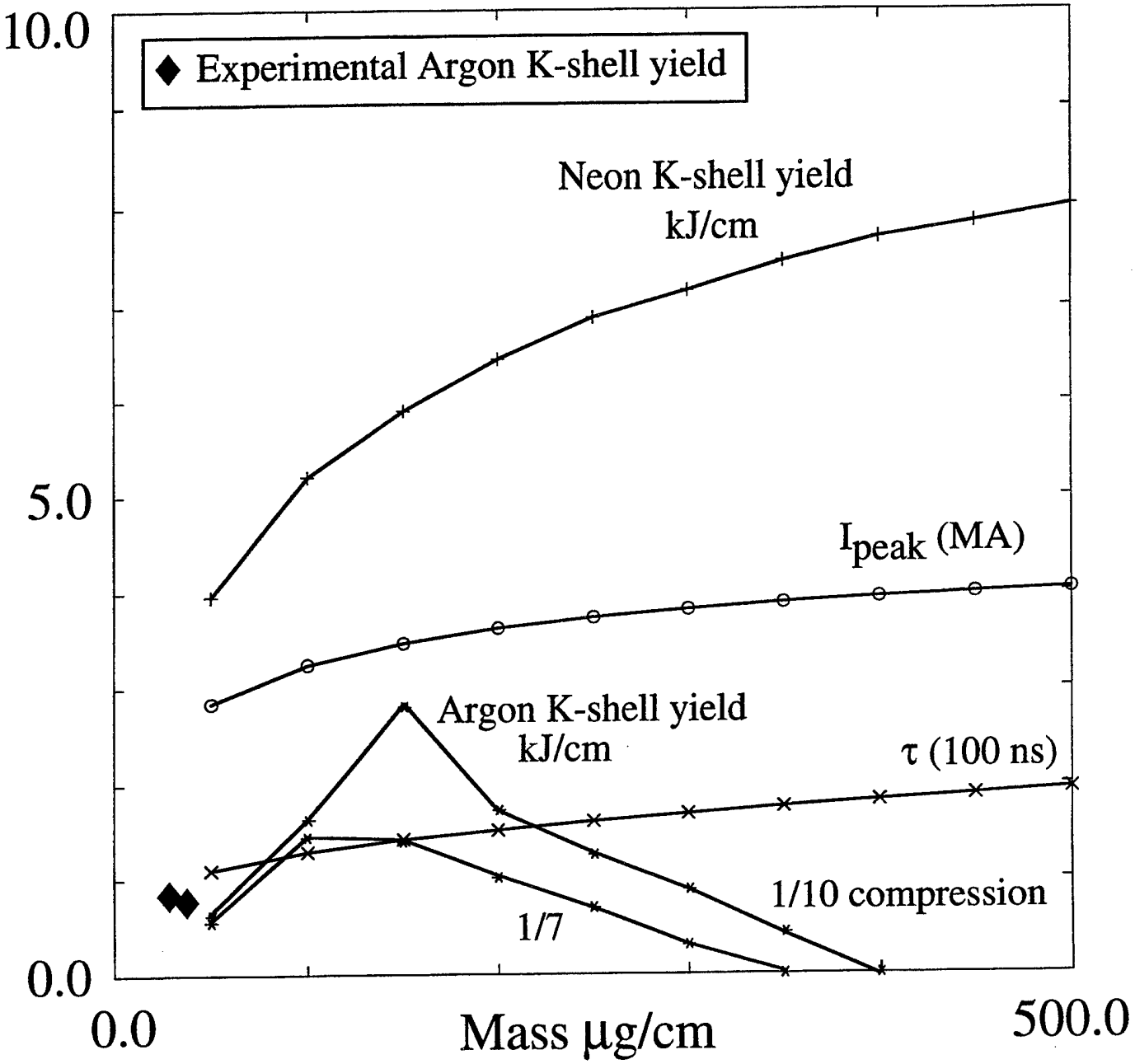

Fig. 6

Tandem Puff Theory

1.75 cm radius Nozzle
640 kV charge
0 - D Slug Model
4 cm length pinch

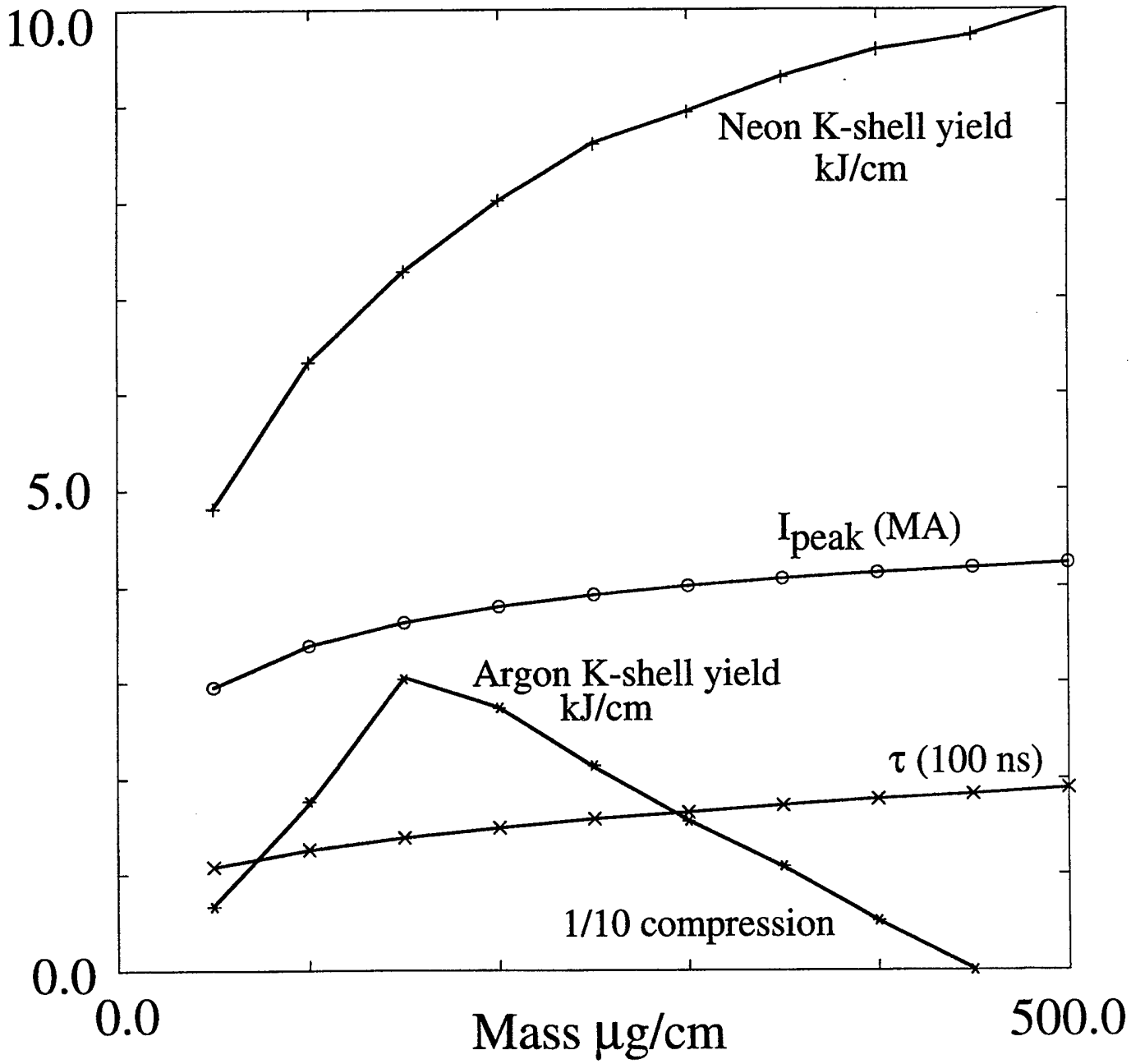

Fig. 7

Tandem Puff Theory

1.75 cm radius Nozzle

640 kV charge 4 cm length pinch

0 - D Slug Model

85 nH front end inductance

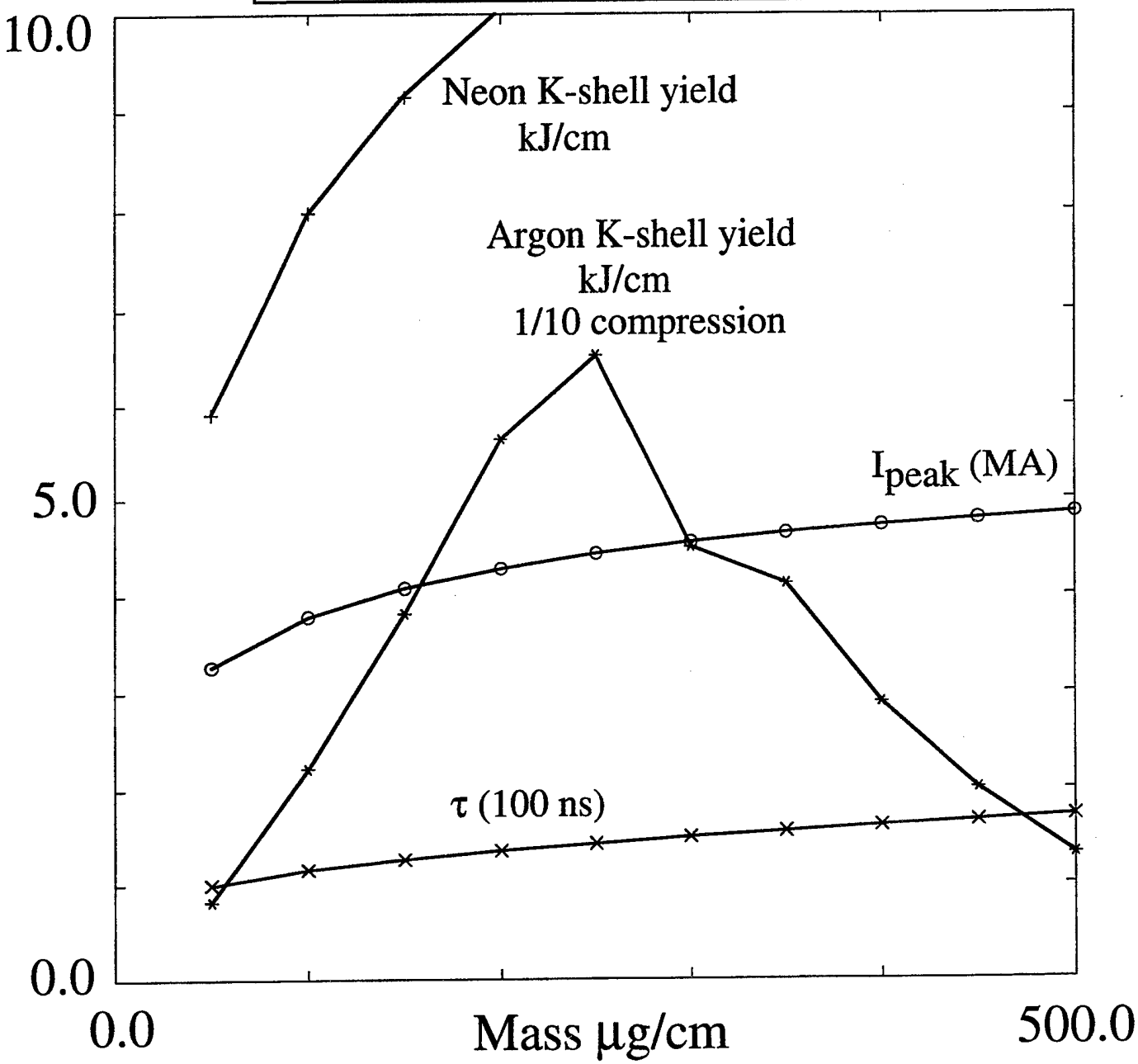

Fig. 8

C. ACE 4 Tandem Puff Experiments (August 1996)

In August it was decided to restore ACE 4 to the 9 cm radius switch/Tandem puff configuration that was used in January and February and try to replicate and improve upon those earlier results. The August Tandem puff experiments are analyzed in terms of the first of the two areas of concern mentioned in the preliminary Jan - Feb assessment above: 1) a more accurate determination of the load current and 2) a more quantitative analysis of the effects of instabilities on the ability of the plasma to radiate K-shell photons.

Table 1 contains a preliminary summary of the experimental results for the 600 kV capacitor charge shots. The implosion times for shot 1977 and shot 1993 are taken from the time the linear rise of the load current crosses the time axis to the time of peak K-shell emission, see Figs. 1 and 2. The remainder of the implosion times listed in Table 1 are taken from the the absolute time of the start of K-shell emission fiduciated to shot 1977 for the 7 cm mask experiments and fiduciated to shot 1993 for the 5 cm and smaller mask experiments.

From our January experience with the Tandem puff we had a strong suspicion that the current getting to to load was not the same as was being modeled. On the other hand, based on experiences with Direct Drive load current monitor measurements there was also a strong suspicion that the load current monitor readings were suspect. Given these uncertainties it is thought that while plasma shielding effects may cause the current measured by the load monitor to be off in magnitude relative to the real load current, its form is a reasonable representation of the the shape of the load current as a function of time. Therefore, calculations were performed using prescribed current profiles having the form of the load current monitor readings for shot 1977 (see Fig. 1) but with multiplying factors of 1.0, 1.15 and 1.3. The factor of 1.3 brings the load current almost up to the upstream current monitor reading at 1.5 μs, which should be the upper limit for the magnitude of the load current at that time. Using the prescribed current profiles as well as knowledge of the gas distribution of the 14 cm diameter masked loads (measured by NRL Code 6770), see Fig. 3, it is possible to find a set of mass loads, currents and implosion times that is consistent with 0-D snowplow calculations and experiment.

If the mass is integrated from 0-10 cm for a delay time of 431 μs, see Figs. 3 and 4, then the mass of the neon load of shot 1977 is approximately 250 μg/cm. By comparing this mass and the experimental implosion time of 600 ns with the snowplow results shown in Fig. 5, the best match between experiment and calculations is obtained when the current profile used in the calculations is the same as that of the load current monitor for shot 1977. The snowplow calculations predict that a 320 μg/cm load will implode in 600 ns at this lowest current setting. If the same process is repeated for shot 1992, the integrated argon mass of 170 μg/cm and experimental implosion time of 485 ns match up best with the factor of 1.15 and 1.3 multipliers on the load monitor current profile, see Fig. 6. Note, the above analyses presume that there is little variation along the diode axis in the mass-per-unit-length and the mass distributions as shown in Figs. 3 and 4. The information displayed in these figures is obtained from measurements at an axial position of 1 cm away from the anode mesh.

The calculated K-shell yields that correspond with the mass loads shown in Fig. 5 at the lowest current monitor multiplier are shown in Fig. 7 for neon loads with mass distributions similar to shot 1977 and in Fig. 8 for argon loads with mass distributions similar to shot 1992 and current multipliers of 1.15 and 1.3. The calculated peak load currents are also displayed in this figure. The 7.5 kJ/cm neon yield predicted by Fig. 7 for a 250 μg/cm neon load is much less than the 18 kJ/cm yield obtained experimentally. However, only thermalization of kinetic energy is considered as a mechanism for producing K-shell photons in the snowplow model scaling calculations while these photons can also be produced by ohmic heating or late time re-compressions in the experimental plasma. Given the 100 ns experimental K-shell pulse width and the fact that it is much easier to produce K-shell photons from a low Z-element by these other mechanisms, it is unlikely that all of the experimental neon K-shell emission is due to kinetic energy thermalization during the first compression of the plasma on axis. The K-shell yield obtained by integrating under the FWHM of the first K-shell pulse is a better indicator of the experimental K-shell emission produced only by thermalization of kinetic energy. It is this yield that should be compared with 0-D snowplow and 1-D scaling predictions. In this regard the 7.5 kJ/cm model prediction and the 9 kJ/cm (see Fig. 1) experimental yield are in good agreement. The 2.5-4.5 kJ/cm of calculated argon K-shell emission is substantially larger than the experimental yield of 1.4 kJ/cm from shot 1992. One expects that neon K-shell yield should not be as dramatically reduced by instabilities as argon K-shell yield since it is much easier to ionize neon into the K-shell

Next the 5 cm radius mask experiments were examined to check on the assessment of load current made from the 7 cm radius mask experiments. The analysis is more speculative for the 5 cm experiments because the mass distribution of these loads has not been measured as yet (it would be nice to have this information in the future). Given this uncertainty, truncated versions (at 5 cm) of the mass distributions shown in Fig. 3 were used. While it is doubtful that these are the experimental distributions, it is assumed that they contain nearly the same mass as the experimental plasmas. This mass is 148 μg/cm for argon shot 1993 and it is 222 μg/cm for shot 1994. The implosion times for these loads are 270 ns and 290 ns, respectively. These times and mass loads are then compared with 0-D snowplow results for the three current profiles. In this case, the current profile enhanced by a factor of 1.3 over the current measured by the load monitor provides the best agreement between calculations and experiment, see Fig. 9. The predicted peak current for shot 1993 is 3.4 MA as shown in Fig. 10 along with a comparison between experimental and calculated argon K-shell yields. In general, a 5 cm load is strongly influenced by instabilities, which according to preliminary studies tend to reduce K-shell emission below 1-D/0-D K-shell scaling predictions. Therefore, the fact that the experimental K-shell yield is as large as the calculated yield strongly supports the conclusion that the peak load current was at least 3.4 MA for shot 1993. Fig. 10 shows a precipitous fall off in experimental K-shell yield with mass. More shots are needed to assess whether this fall off is a statistical trend or an aberration.

The same procedure that was used for the 5 cm radius mask experiments is applied to the 3 cm mask experiments. In this case the integrated mass out to 3 cm as taken from Fig. 3 is 165 μg/cm for the 75 psi gas pressure shots 1995 and 2000. It is 132 μg/cm for the 60

psi shots 1997 and 1998 and it is 220 μg/cm for the 100 psi shot 1996. The 0-D snowplow results for mass and implosion time for the three current multipliers are shown in Fig. 10 and the predicted K-shell yields are shown in Fig. 11. In terms of matching implosion times and mass loads the multipliers of 1.15 and 1.3 on the load monitor current provide the best match between experiment and calculations. However, the calculated K-shell emission for the 1.15 current profile are smaller than a factor of 1/5 the experimental yields, with the exception of shot 1998. The K-shell yield comparison between experiment and calculations indicates that a load monitor current multiplier of at least a factor of 1.3 is needed in order to increase the calculated yields to where they begin to agree with experimental yields. The larger current could be due to a faster current rise than is being modeled or it may be due to the presence of mass at larger radii than 3.0 cm. The presence of mass at larger radius would also bring the calculated implosion times for the 1.3 multiplier case more in agreement with the experimental implosion times.

An important lesson that has been learned throughout the ACE 4 experiments is that it is very difficult to assess load and machine performance if the load mass and mass distribution are not well characterized. Indeed, a good deal of the preceding analysis is speculative for this very reason. Ideally, one would like to have a load that has a perfectly annular or uniform fill density profile along the entire axis of the pinch for several reasons: 1) higher compression, powers and perhaps yield are achieved when asymmetries and instabilities are minimized (note, in Saturn aluminum experiments differences in wire number produced a factor of five difference in K-shell yield), 2) the implosion time would be a good indicator of the currents that are pushing on the load, and 3) such a load is required in order to quantify experimentally the effects of the Rayleigh-Taylor instability on the ability of a large initial radius plasma to radiate K-shell photons.

Ace 4 Tandem Puff Experiments

(Preliminary Results)

Shot#	Z	Delay time (μs)	Press (psi)	Mask Dia. (cm)	K-shell Yield (kJ/cm)	Est. τ (ns)	Abs. time Xray start (ns)
1977	Ne	431	80	14	18.5	600	1474
1992	Ar	613	10	14	1.4	485	1359
1993	Ar	613	20	10	2.6	275	1169
1994	Ar	613	30	10	1.2	295	1189
1995	Ar	613	75	6	2.5	239	1133
1996	Ar	613	100	6	1.0	274	1168
1997	Ar	613	60	6	2.2	236	1130
1998	Ar	613	60	6	0.5	198	1092
2000	Ar	613	75	6	1.5	268	1162

Table 1

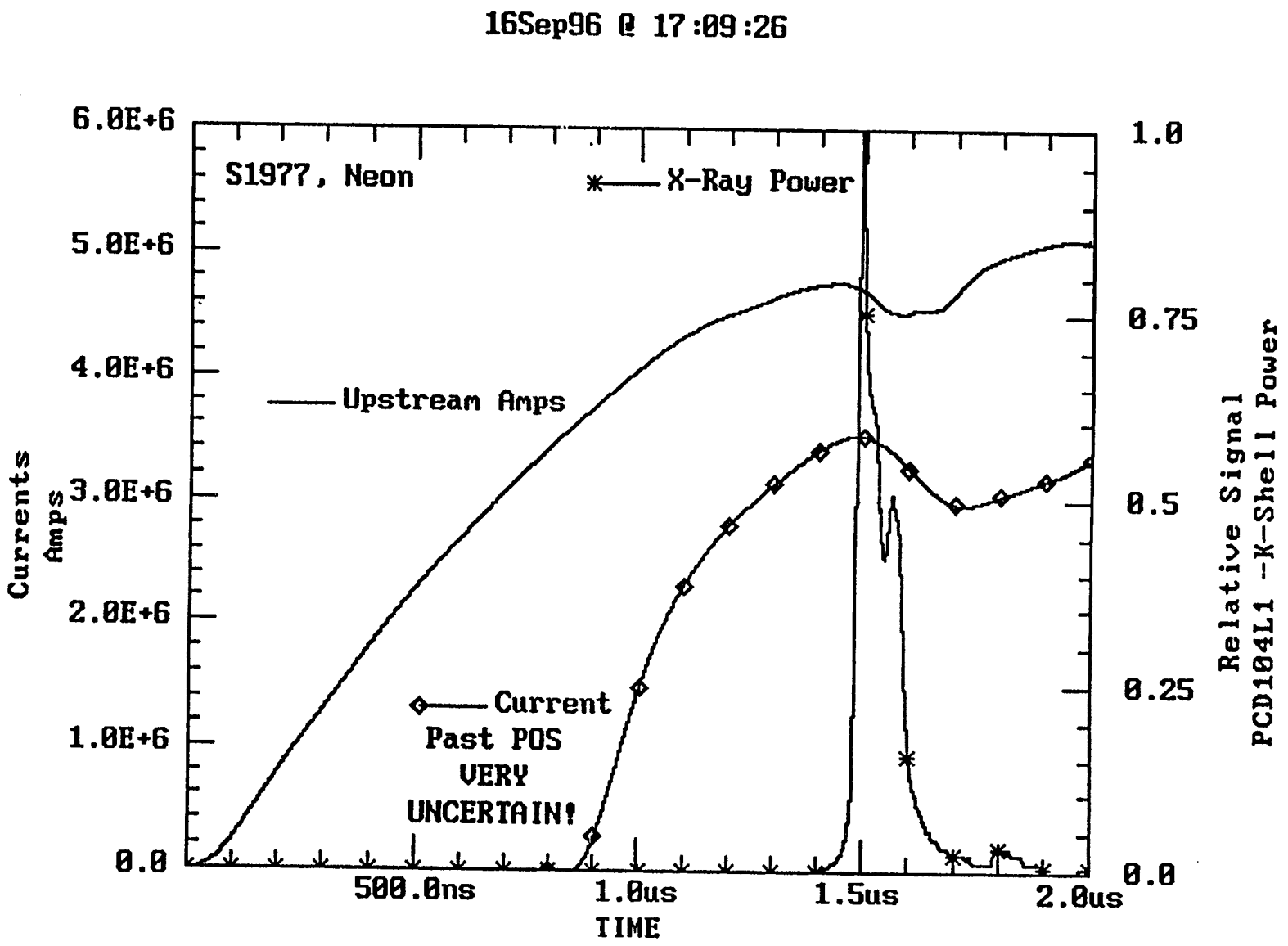

Fig. 1 Measured upstream and load currents for neon shot 1977, which used a 7 cm radius mask, a delay time of 431 μs and a pressure of 80 psi.

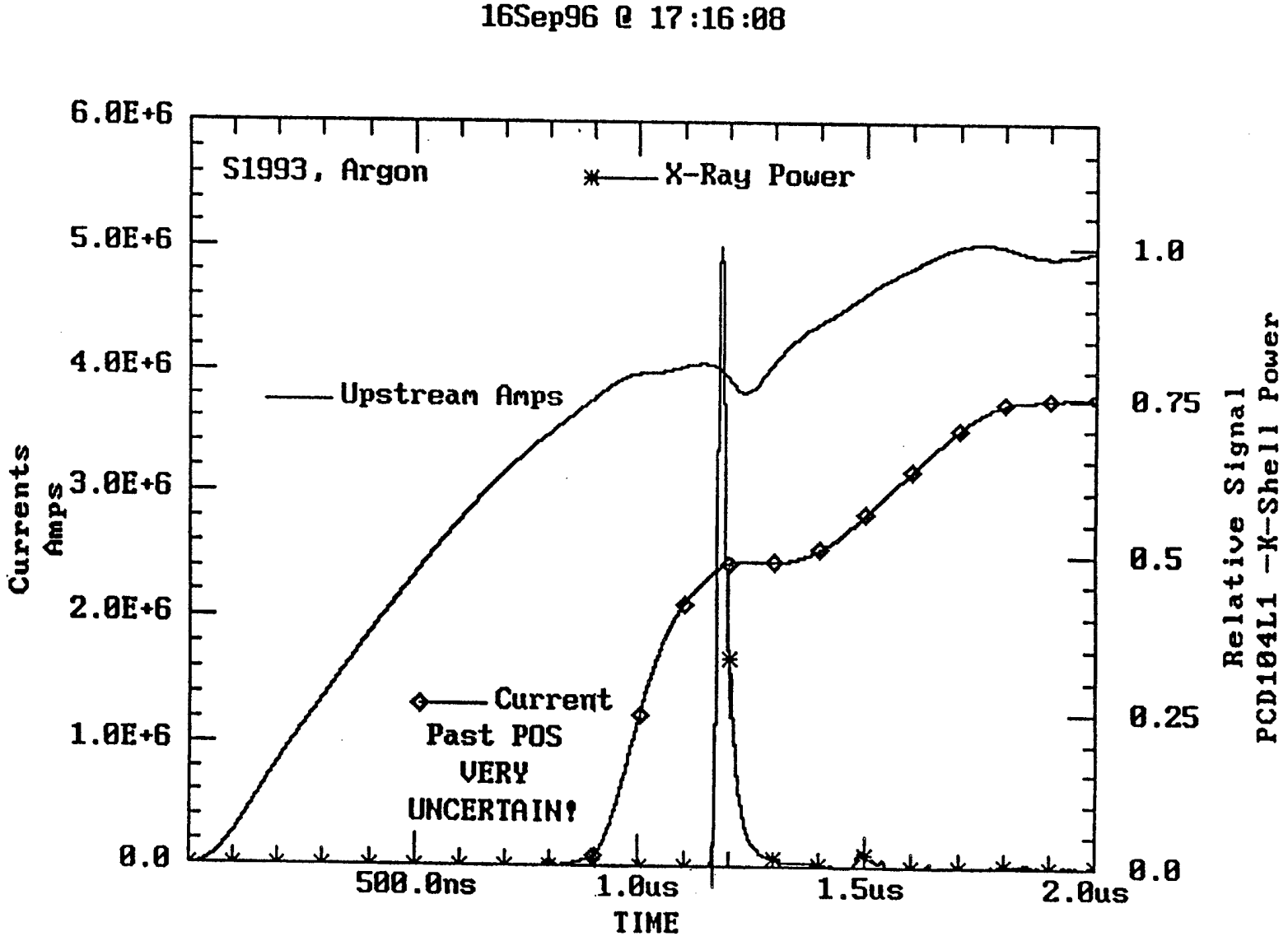

Fig. 2 Measured upstream and load currents for argon shot 1993, which used a 5 cm radius mask, a delay time of 613 μs and a pressure of 20 psi.

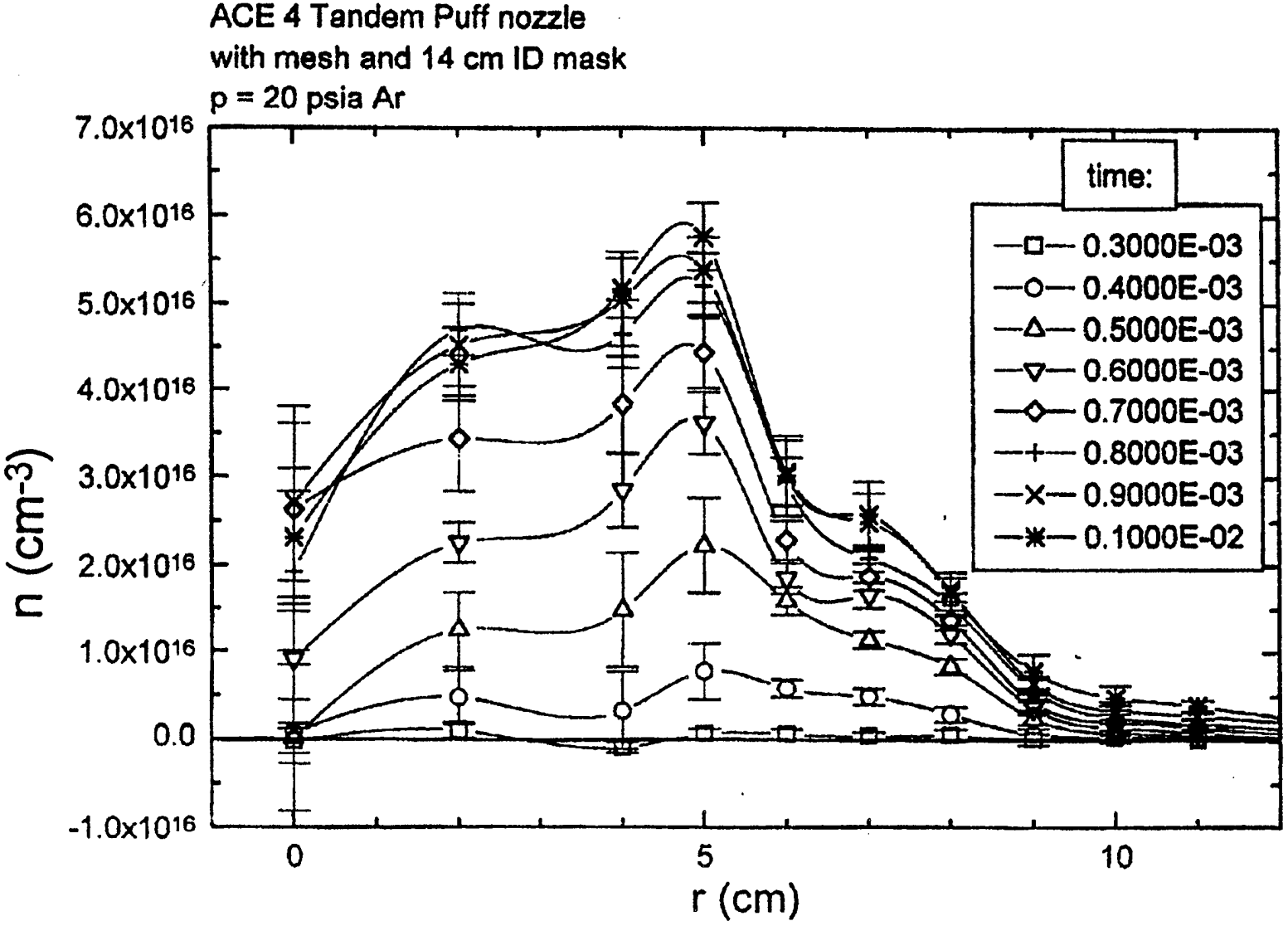

Fig. 3 Argon number density as a function of delay time and radial position away from the axis of the pinch. Measurements were taken (by NRL Code 6770) 13 cm away axially from the nozzle exit. An 11 cm radius nozzle was used and a 5 cm radius mask was over the anode mesh.

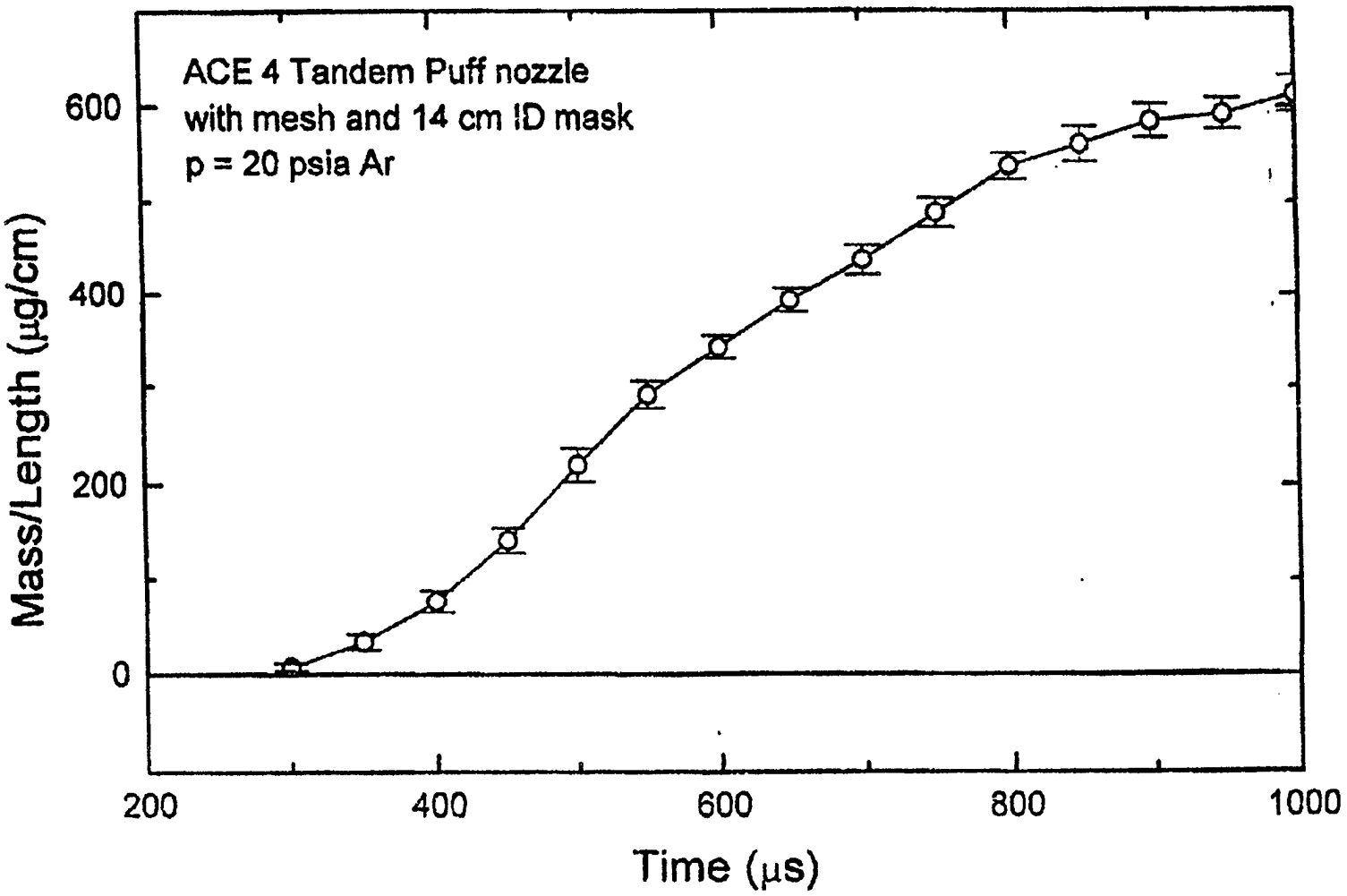

Fig. 4 Radially integrated mass-per-unit-length as a function of delay time for the argon mass distributions shown in Fig. 3.

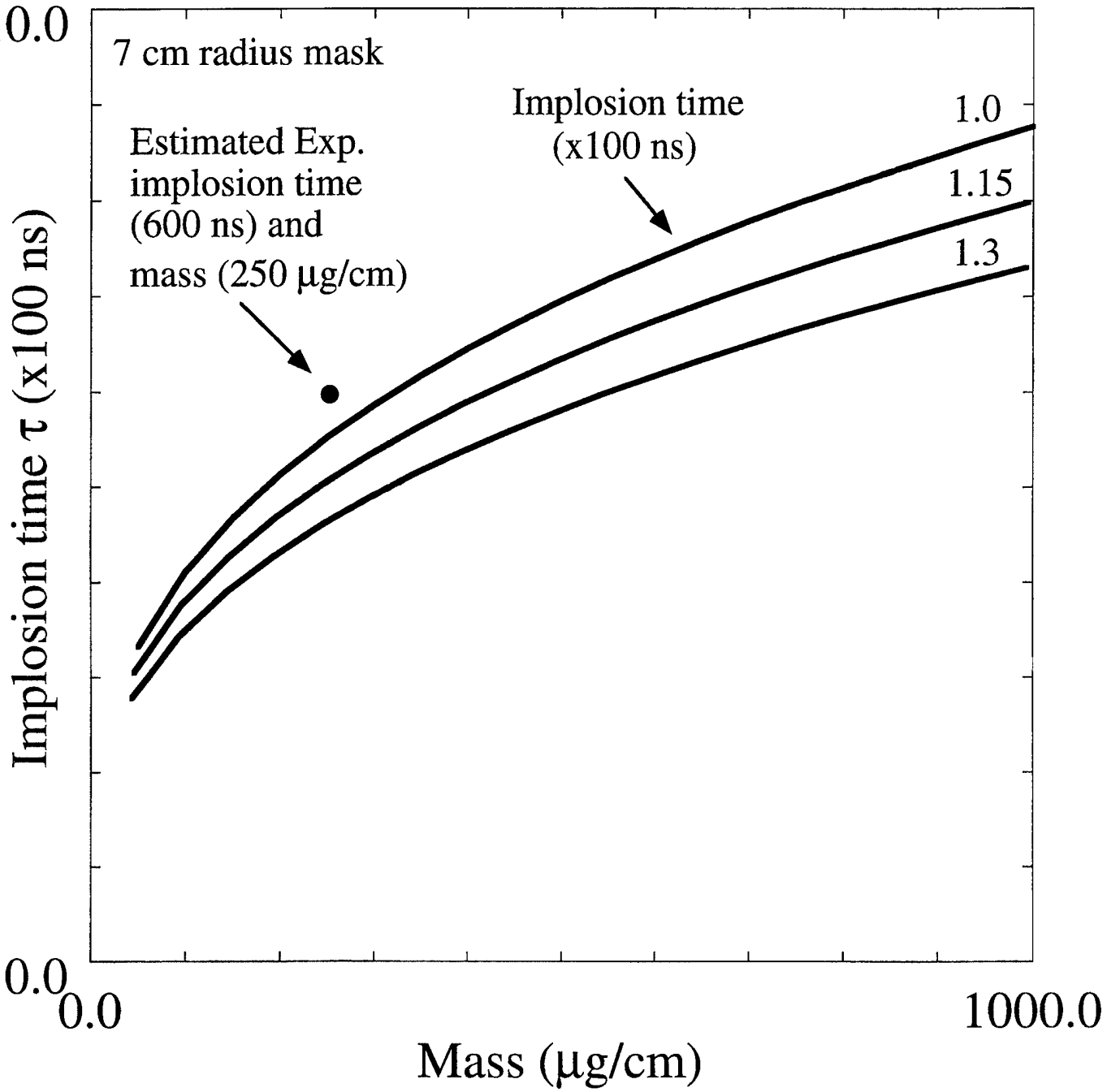

Fig. 5 Calculated implosion time as a function of mass load for current multipliers of 1.0,1.15, and 1.3 on the load current monitor reading of neon shot 1977. The initial radius and mass distribution are similar to shot 1977.

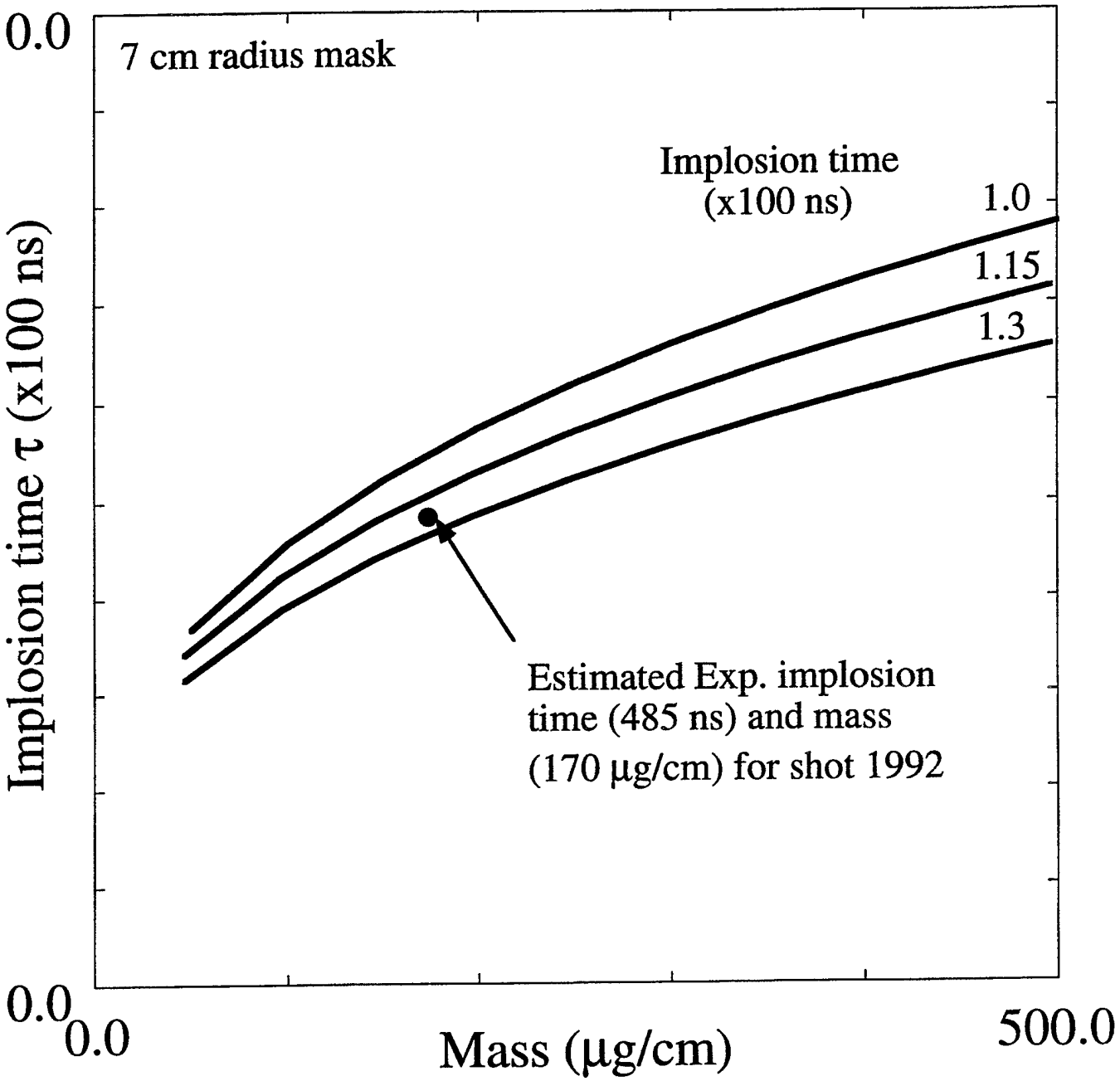

Fig. 6 Calculated implosion time as a function of mass load for current multipliers of 1.0, 1.15, and 1.3 on the load current monitor reading of shot 1977. The inital radius and mass distribution are similar to shot 1992.

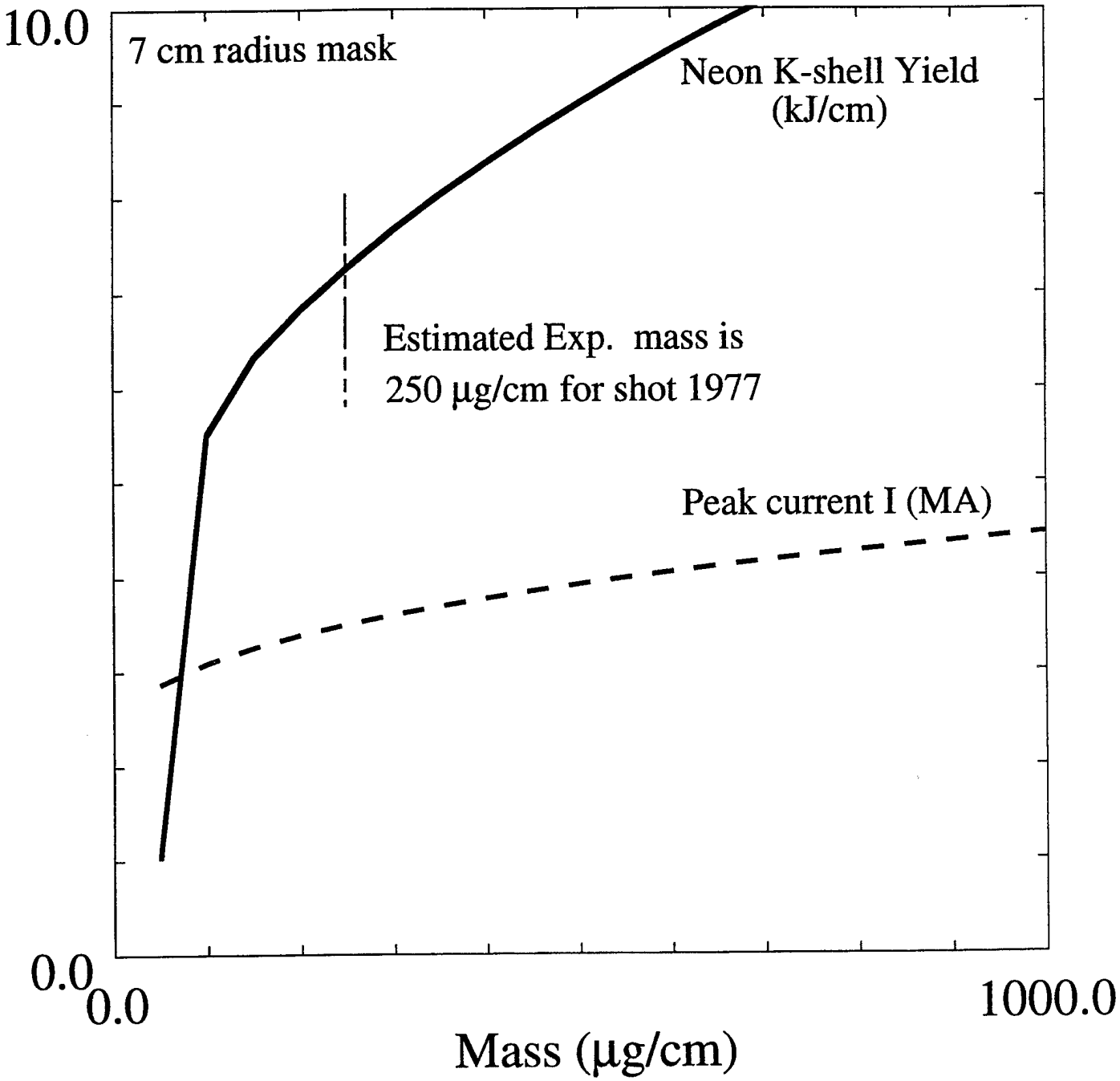

Fig. 7 Snow plow model predictions for peak current and neon K-shell yield as a function of mass load. Loads have a mass density profile similar to shot 1977 and a load current given by the current monitory reading for shot 1977.

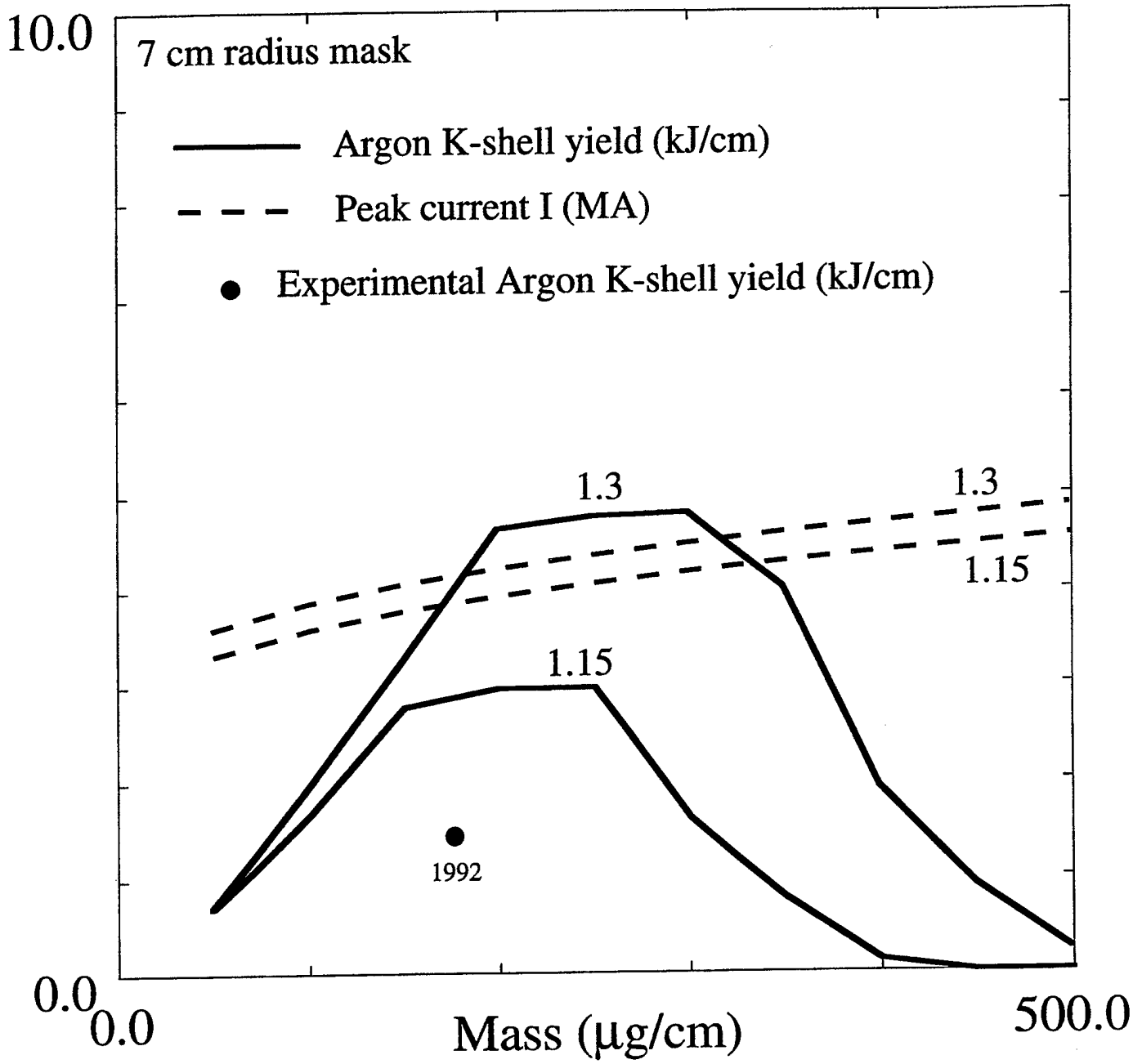

Fig. 8 Snow plow model predictions for peak current and argon K-shell yield as a function of mass load and multipliers of 1.15 and 1.3 on the load current monitor reading of shot 1977. The initial radius and mass distribution are similar to shot 1992.

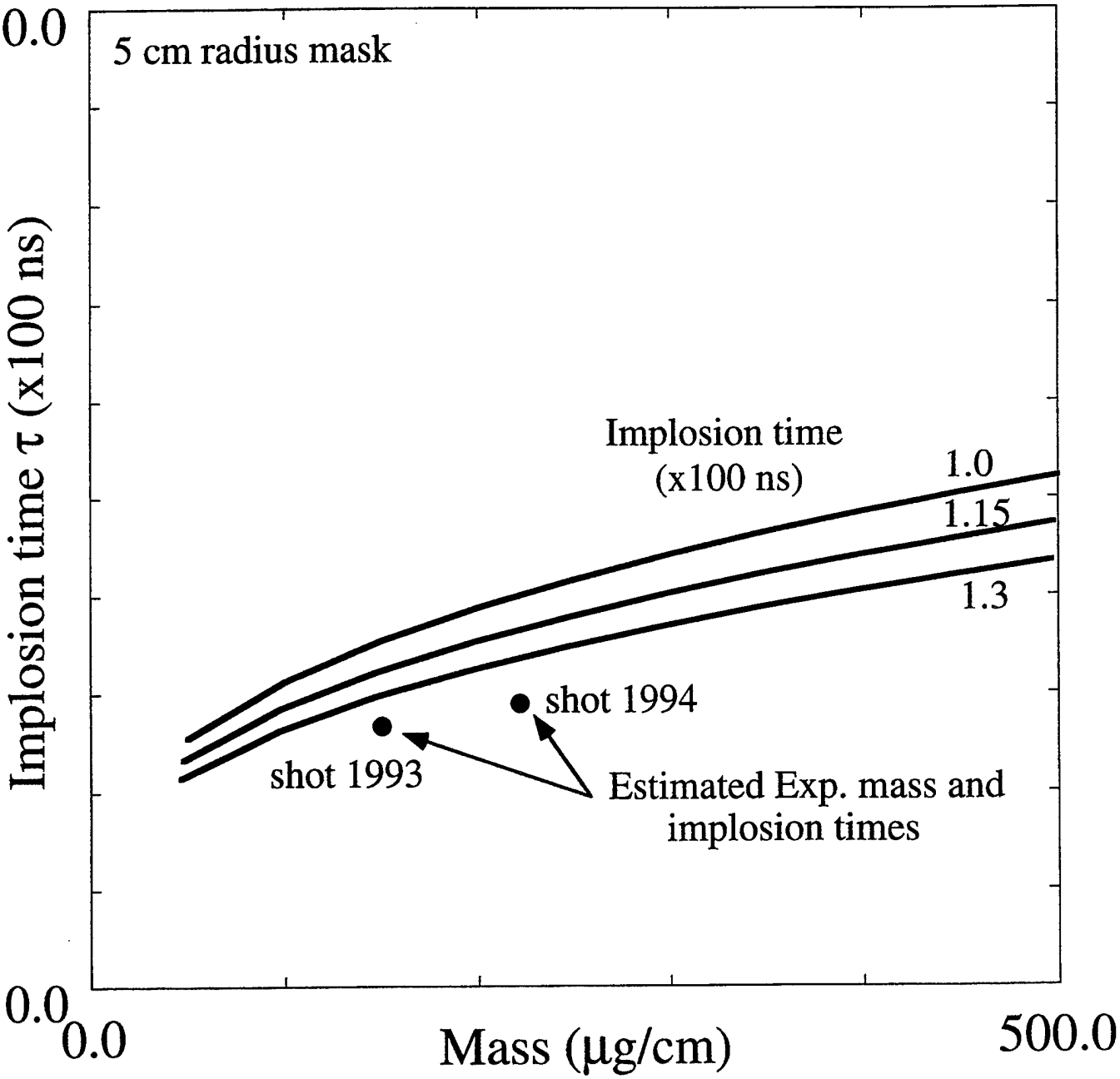

Fig. 9 Calculated implosion time as a function of mass load for current multipliers of 1.0, 1.15, and 1.3 on the load current monitor reading of shot 1977. The initial radius and mass distributions are similar to shots 1993 and 1994.

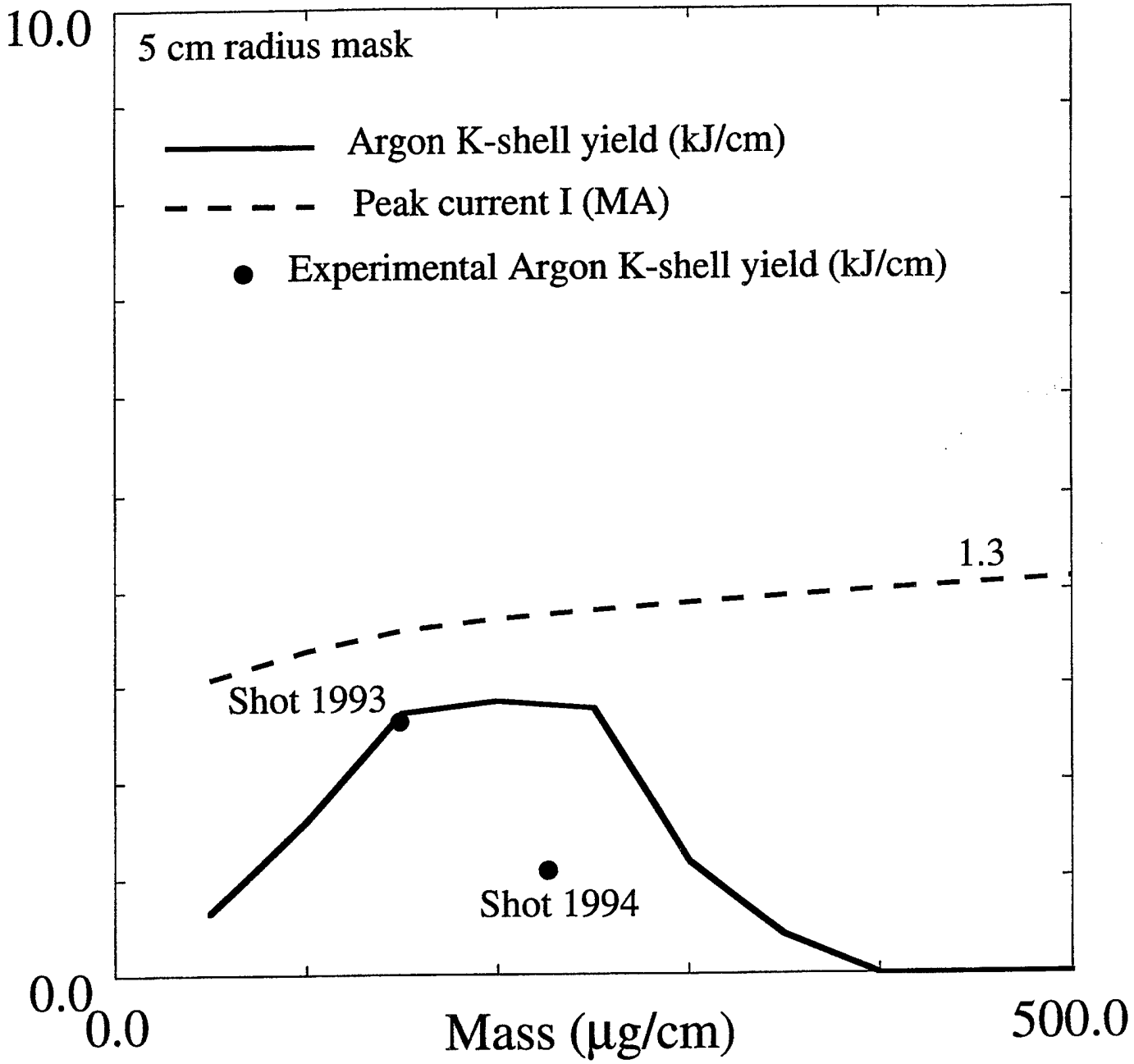

Fig. 10 Snow plow model predictions for peak current and argon K-shell yield as a function of mass load and a multiplier of 1.3 on the load current monitor reading of shot 1977. The initial radius and mass distribution are similar to shots 1993 and 1994.

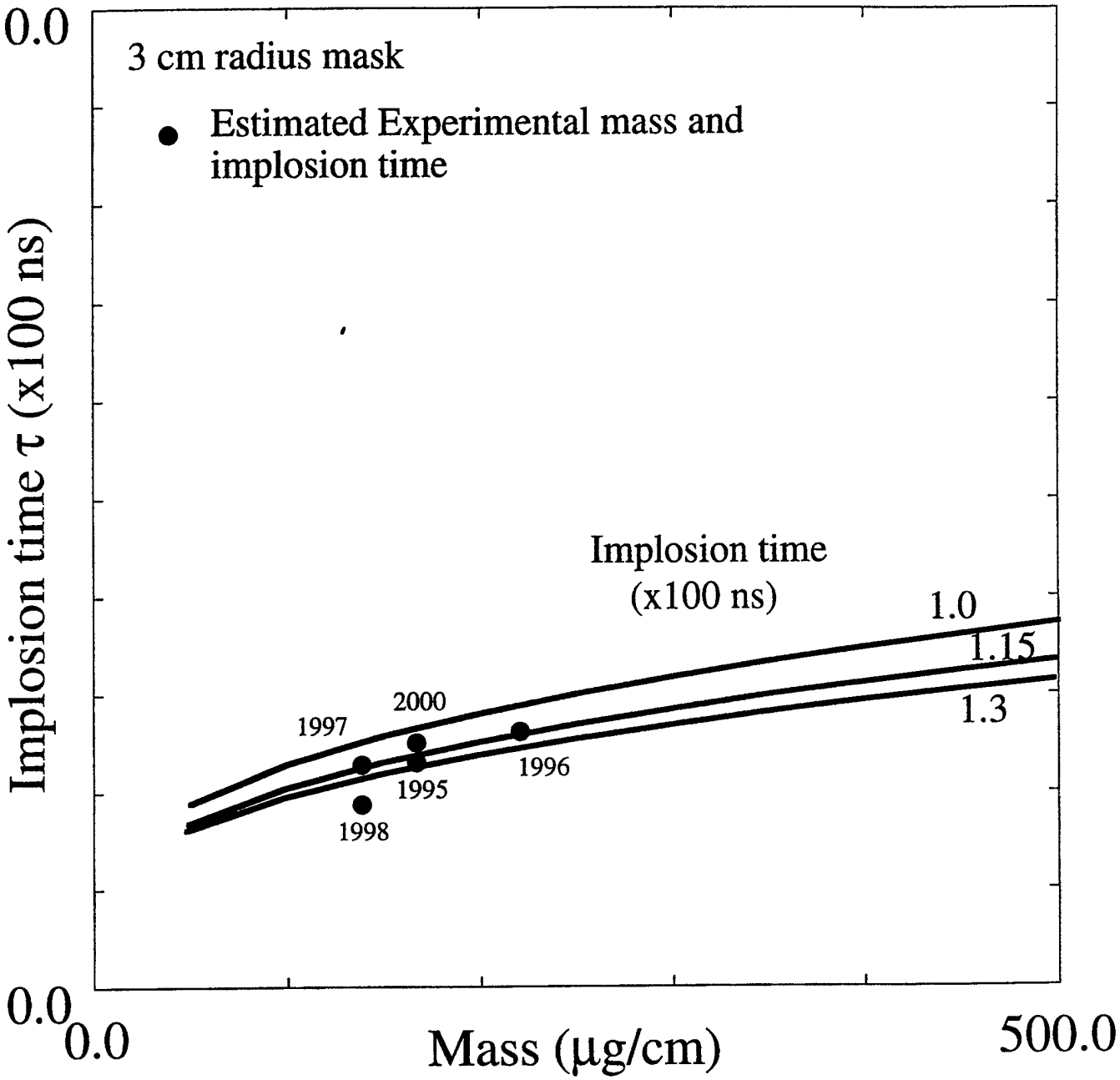

Fig. 11 Calculated implosion time as a function of mass load for current multipliers of 1.0, 1.15, and 1.3 on the load current monitor reading of neon shot 1977. The initial radius and mass distribution are similar to shots 1995, 1996,1997,1998 and 2000.

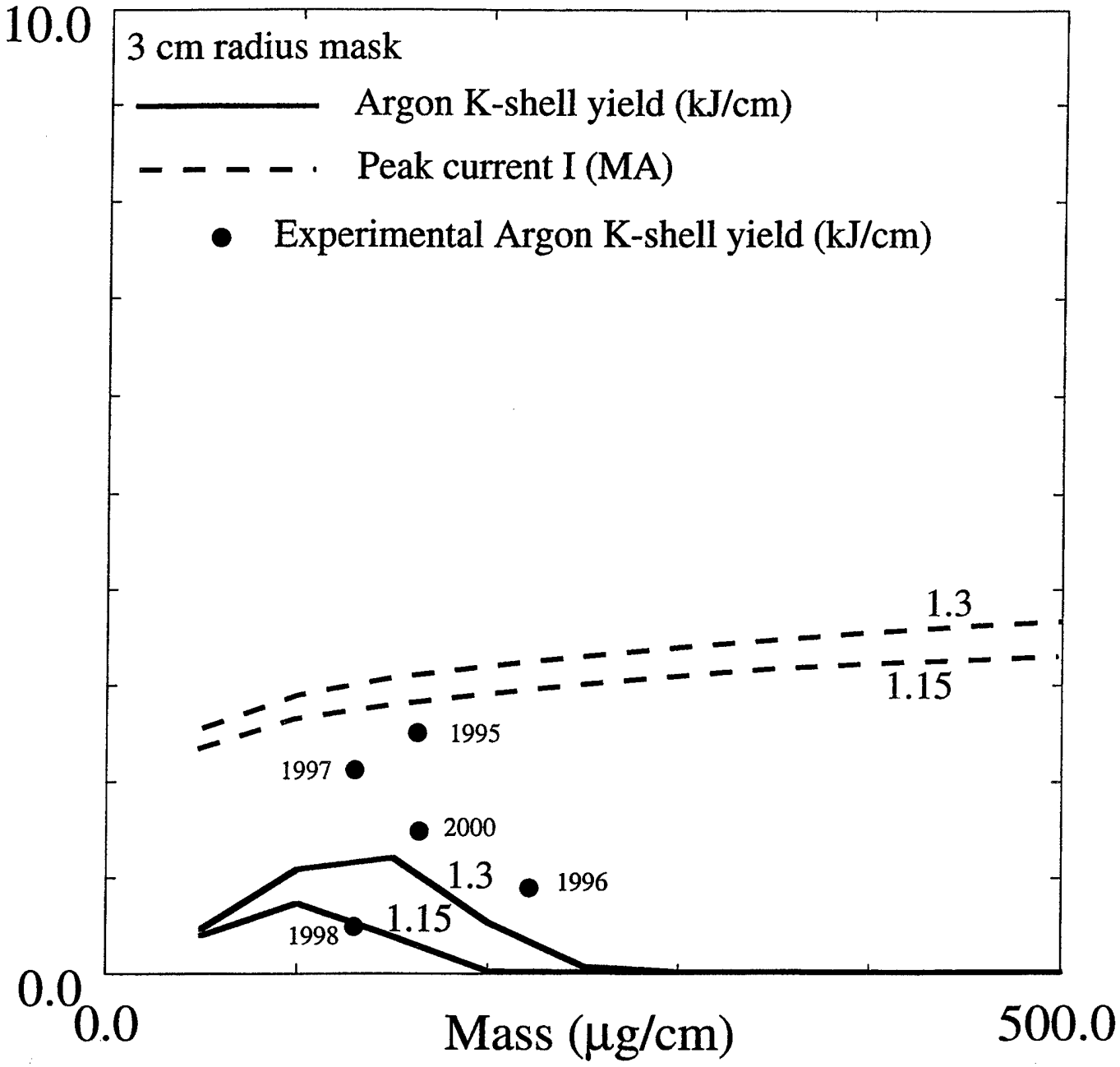

Fig. 12 Snow plow model predictions for peak current and argon K-shell yield as a function of mass load and multipliers of 1.15 and 1.3 on the load current monitor reading of shot 1977. The initial radius and mass distribution are simiar to shots 1995, 1996, 1997, 1998 and 2000.

D. Structured Loads in Direct Drive

In this subsection we investigate the radiative performance of "complex" loads on ACE 4 in direct drive mode. The equivalent circuit representing ACE 4 in direct drive mode is shown on Fig.1. Note the front-end inductance is assumed to be 85 nH when operating in direct drive mode. This high an inductance will have a profound affect on the performance of complex loads on ACE 4. By complex load is meant loads having long implosion times driven directly by the electricity in the absence of any opening switch. Under these conditions stability issues must be thoroughly investigated. In order to identify an operating range of stable loads a number of large diameter structured loads have been investigated and some have remained stable during the run-in and stagnation phases. These results were published in Phys. Rev. Lett. 77, 853 (1996) and are discussed in another section of this report. The loads investigated here included some structured loads and fat shells. The results are based on numerical simulations using the DZAPP and ZPIMP numerical models. ZPIMP is a single zone model containing much of the relevant physics but ignores gradients and has great utility as a scoping code, i.e., identifying the regions of high yield. DZAPP is a fully 1-D radiation hydrodynamics model. It is employed both to verify the ZPIMP calculations and as a benchmark with experimental data. Obviously, structure that develops during the implosion and stagnation phases are ignored in these simulations. However, structure is accounted for off line with a 2-D RMHD model PRISM.

The first series of simulations were performed for load density profiles configured as uniform fills out to a critical radius, R_c, and a linear falloff out to a radius R_0. The length of all the loads is 4 cm unless otherwise noted. The results are summarized on Figure 2 for a variety of total load mass, plasma composition, charging voltage, radius, and K-shell yields. Although some of the loads predict good yields they all suffer from RT stability problems except the last entry on the Table. However, the K-shell yield for those conditions employed is to small to be of interest. Density profiles of this type are not suitable for ACE 4.

The next set of simulations employs an exponential rise and a R^{-3} decay as shown on Figure 3. The three cases investigated were stable. Also note that adding some hydrogen slightly increased the K-shell yield. The outer radius extends outward for a considerable distance but there is little mass out there. This might create an experimental challenge but we have been informed that the mass in the tail can be preionized by a separate source. These results are very encouraging and should be considered for future experiments. Additional simulations will be performed at a lower charging voltage if it is determined that these loads can be generated experimentally.

For an initial density profile composed as a Lorentzian up to R_c and then falls off as a cubic as shown on Figure 4. All these loads are RT stable and produce K-shell yields commensurate with ACE 4's overall performance. The last entry on the Table is for a 2 cm long load and produces a good K-shell yield. Additional simulations can be performed if the loads can be structured properly. Also, because there is little mass in the tail caution must be exercised not to drive shocks during the initiation process.

The final set of simulations treats a fat shell with an inner radius of 1.0 cm and a variable outer radius extending out to 6.0 cm for some of the simulations. The 2-D RMHD simulations suggests that for an outer radius $R_0 > 3.5$ cm the loads are subject to RT instabilities and the 1-D DZAPP results represent an absolute upper bound for the radiative yields and more than likely are reduced by at least a factor of 2 from the values appearing on the Figures. The charging voltage used in these simulations was taken as 640 kV. The loads are all 4.0 cm in length. The gas composition varies from pure neon to pure argon with mixtures by number density between the pure gases. Figure 5 is essentially pure neon and the plots are arranged as follows: the top left plot represents the neon K-shell yield in kJ's, and labeled as such on the plots, as a function of outer radius and total mass. The top right plot represents the argon K-shell yield (which for this case is negligible). The plot in the lower left corner represents the total K-shell yield (neon + argon) while the final plot represents the total yield (neon + argon L- and K- shell). The results presented on Figure 5 for pure neon predict about 20 kJ's K-shell yield for a total initial mass of about 1.0 mg and an outer radius of about 3.0 cm. The predicted yields for $R_0 > 3.5$ cm should

only be considered as estimates due to the development of RT instabilities during the implosion. On the other hand, the total yields are impressive.

For a mixture of neon and argon by number density of 0.75 to 0.25 the results are displayed on Figure 6. The reduction in the neon gave rise to a commensurate reduction in the neon K-shell yield. However, the argon K-shell still remains in the noise. The total yield remains impressive. Figure 7 shows the transition as the mixture becomes 50-50. The neon K-shell yield continues to decrease while the argon K-shell has failed to ignite substantially. The total yield remains impressive and relatively unchanged. In the last 2 Figures 8 and 9 the gas mixture is 25 to 75 and essentially pure argon, respectively. The neon K-shell yield becomes vanishingly low as anticipated but the argon K-shell yield remains bleak. The total yield remains relatively constant. This is not unusual since the decrease in neon L-shell yield is compensated by a corresponding increase in the argon L-shell yield.

In summary ACE 4 in direct drive mode using selected complex loads is a mixed bag. Some of the structured loads are promising K-shell radiators but present new problems in designing nozzles to generate the desired density profiles. For loads of the more familiar standard configurations such as uniform fills or fat shells in direct drive mode with long implosion times the conversion of kinetic energy of implosion to K-shell radiation is very poor resulting in extremely low K-shell yields. Although a limited number of density profiles have been investigated in direct mode either the front-end inductance kills the K-shell yield or the plasma becomes RT unstable reducing the K-shell yield. Unless there are some new load designs that can overcome these difficulties emphasis should shift to tandem puff loads.

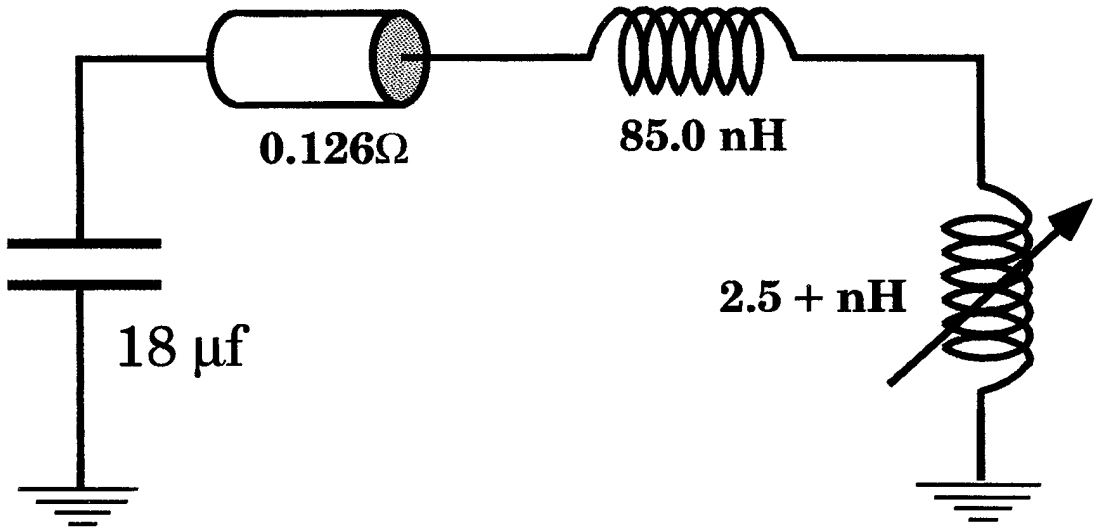

ACE-IV Equivalent Circuit

Fig. 1

Summary of DZAPP Simulations of Plasma Implosions on ACE-IV

- Unless otherwise indicated, plasma length DZ = 4.0 cm
- Machine inductances employed were 85nH and 90nH

(A) Constant Fill with Linear Ramp

Mass (mg)	Composition	Voltage (kV)	R_o (cm)	R_c (cm)	$Y_{K\text{-shell}}$ (kJ)
1.0	100% Ar	640	13.0	8.0	**2.280**
2.0	100% Ar	640	13.0	8.0	**4.860**
3.0	100% Ar	640	13.0	8.0	**3.840**
2.0	100% Ar	720	13.0	8.0	**38.720**
1.0	100% Ar	640	9.0	7.0	**5.360**
2.0	100% Ar	640	9.0	7.0	**5.180**
3.0	100% Ar	640	9.0	7.0	**3.820**
1.0	100% Ar	720	9.0	7.0	**7.840**
2.0	100% Ar	720	9.0	7.0	**14.360**
0.5	100% Ar	720	6.0	2.0	**0.810**

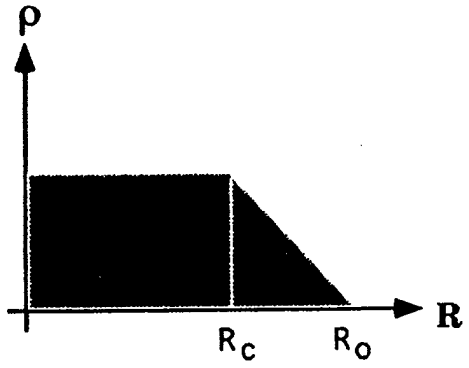

Initial Density Profile:

ρ constant from R=0 to R_c

ρ linear from R= R_c to R_o

Fig. 2

Summary of DZAPP Simulations of Plasma Implosions on ACE-IV

- Unless otherwise indicated, plasma length DZ = 4.0 cm
- Machine inductances employed were 85nH and 90nH

(D) Exponential Falloff $R < R_c$
Cubic Dependence $R > R_c$

Mass (mg)	Composition	Voltage (kV)	R_o (cm)	R_c (cm)	$Y_{K\text{-shell}}$ (kJ)
2.0	100% Ar 0% H	720	15.0	2.0	**14.480**
2.0	90% Ar 10% H	720	15.0	2.0	**15.570**
2.0	80% Ar 20% H	720	15.0	2.0	**15.560**

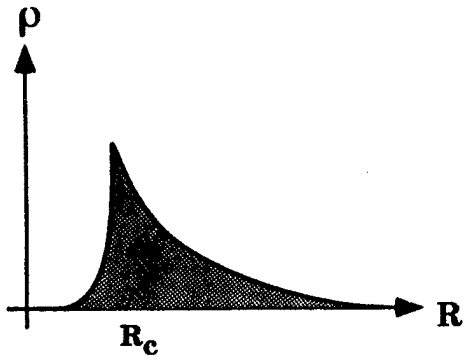

Initial Density Profile:

$$\rho = \rho_o \, e^{-(R_c - R)/\Delta} \quad R < R_c$$

$$\rho = \rho_o \, (R_c/R)^3 \quad R > R_c$$

Fig. 3

Summary of DZAPP Simulations of Plasma Implosions on ACE-IV

- Unless otherwise indicated, plasma length DZ = 4.0 cm
- Machine inductances employed were 85nH and 90nH

(E) Lorentzian Profile for $R < R_c$
Cubic Falloff for $R > R_c$

Mass (mg)	Composition	Voltage (kV)	R_o (cm)	R_c (cm)	$Y_{K\text{-shell}}$ (kJ)
0.5	100% Ar	720	8.0	2.0	2.450
1.0	100% Ar	720	8.0	2.0	----
2.0	100% Ar	720	8.0	2.0	0.260
4.0	100% Ar	720	8.0	2.0	0.0001
0.8	100% Ar	720	5.0	2.0	4.170
1.0	100% Ar	720	5.0	2.0	3.510
1.5	100% Ar	720	5.0	2.0	3.400
1.0	100% Ar (Plasma length DZ=2.0cm)	720	8.0	2.0	13.350

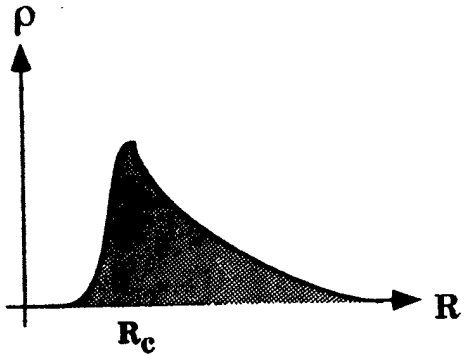

Initial Density Profile:

$$\rho = \frac{\rho_o}{[1 + (R-R_c)^2/\Delta^2]}$$

$$\rho = \rho_o (R_c/R)^3 \quad R>R_c$$

Fig. 4

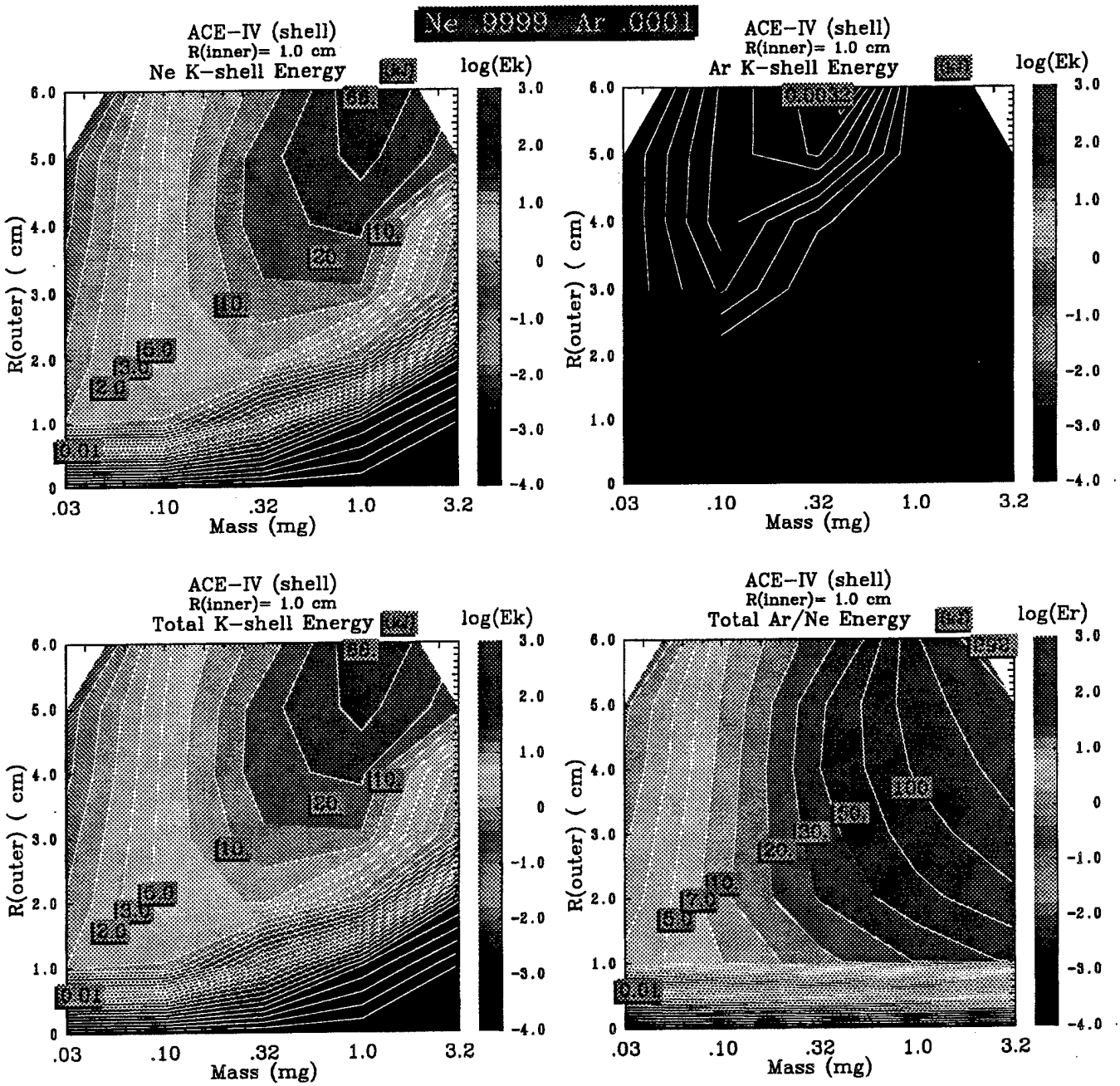
Ne .9999 Ar .0001
ACE-IV (shell)
R(inner)= 1.0 cm
Ne K-shell Energy
log(Ek)
ACE-IV (shell)
R(inner)= 1.0 cm
Ar K-shell Energy
log(Ek)
ACE-IV (shell)
R(inner)= 1.0 cm
Total K-shell Energy
log(Ek)
ACE-IV (shell)
R(inner)= 1.0 cm
Total Ar/Ne Energy
log(Er)
R(outer) (cm)
Mass (mg)
.03
.10
.32
1.0
3.2

Fig. 5

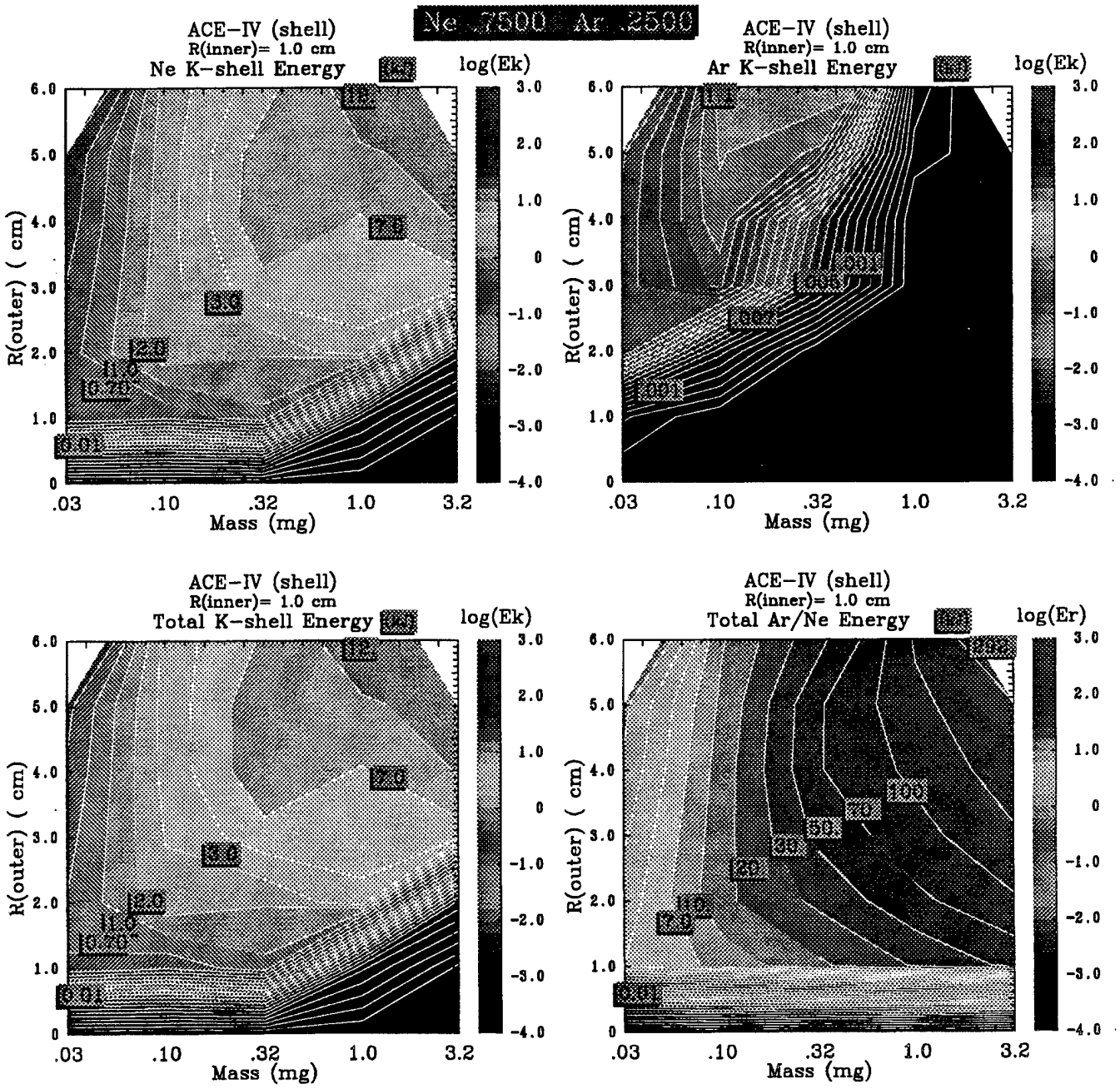
Ne .7500 Ar .2500
ACE–IV (shell)
R(inner)= 1.0 cm
Ne K–shell Energy
log(Ek)
ACE–IV (shell)
R(inner)= 1.0 cm
Ar K–shell Energy
log(Ek)
ACE–IV (shell)
R(inner)= 1.0 cm
Total K–shell Energy
log(Ek)
ACE–IV (shell)
R(inner)= 1.0 cm
Total Ar/Ne Energy
log(Er)
R(outer) (cm)
Mass (mg)
.03
.10
.32
1.0
3.2
0
1.0
2.0
3.0
4.0
5.0
6.0
3.0
2.0
1.0
0
-1.0
-2.0
-3.0
-4.0

Fig. 6

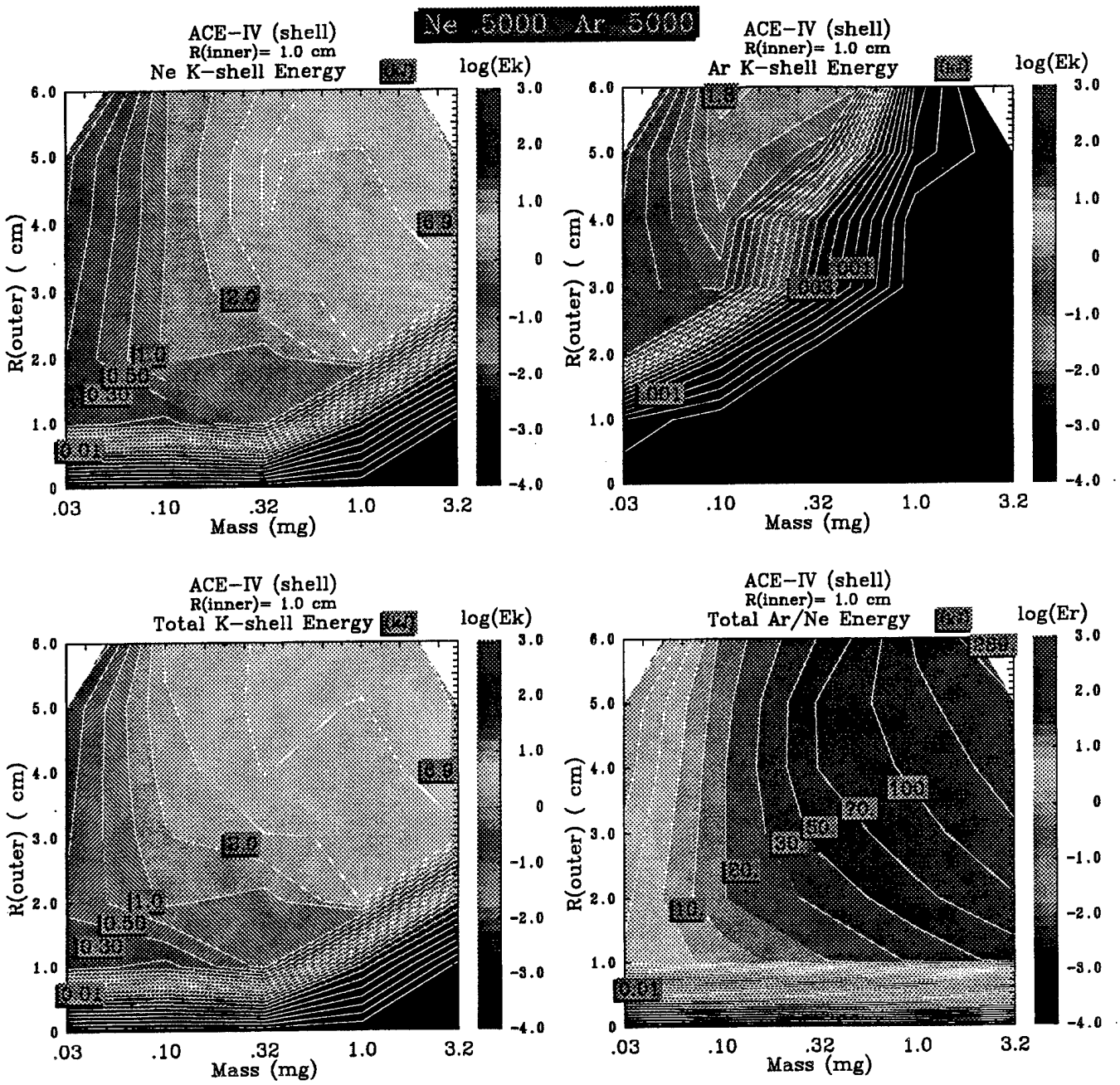
Ne 5000 Ar 5000
ACE-IV (shell)
R(inner)= 1.0 cm
Ne K-shell Energy
log(Ek)
R(outer) (cm)
Mass (mg)
ACE-IV (shell)
R(inner)= 1.0 cm
Ar K-shell Energy
log(Ek)
R(outer) (cm)
Mass (mg)
ACE-IV (shell)
R(inner)= 1.0 cm
Total K-shell Energy
log(Ek)
R(outer) (cm)
Mass (mg)
ACE-IV (shell)
R(inner)= 1.0 cm
Total Ar/Ne Energy
log(Er)
R(outer) (cm)
Mass (mg)

Fig. 7

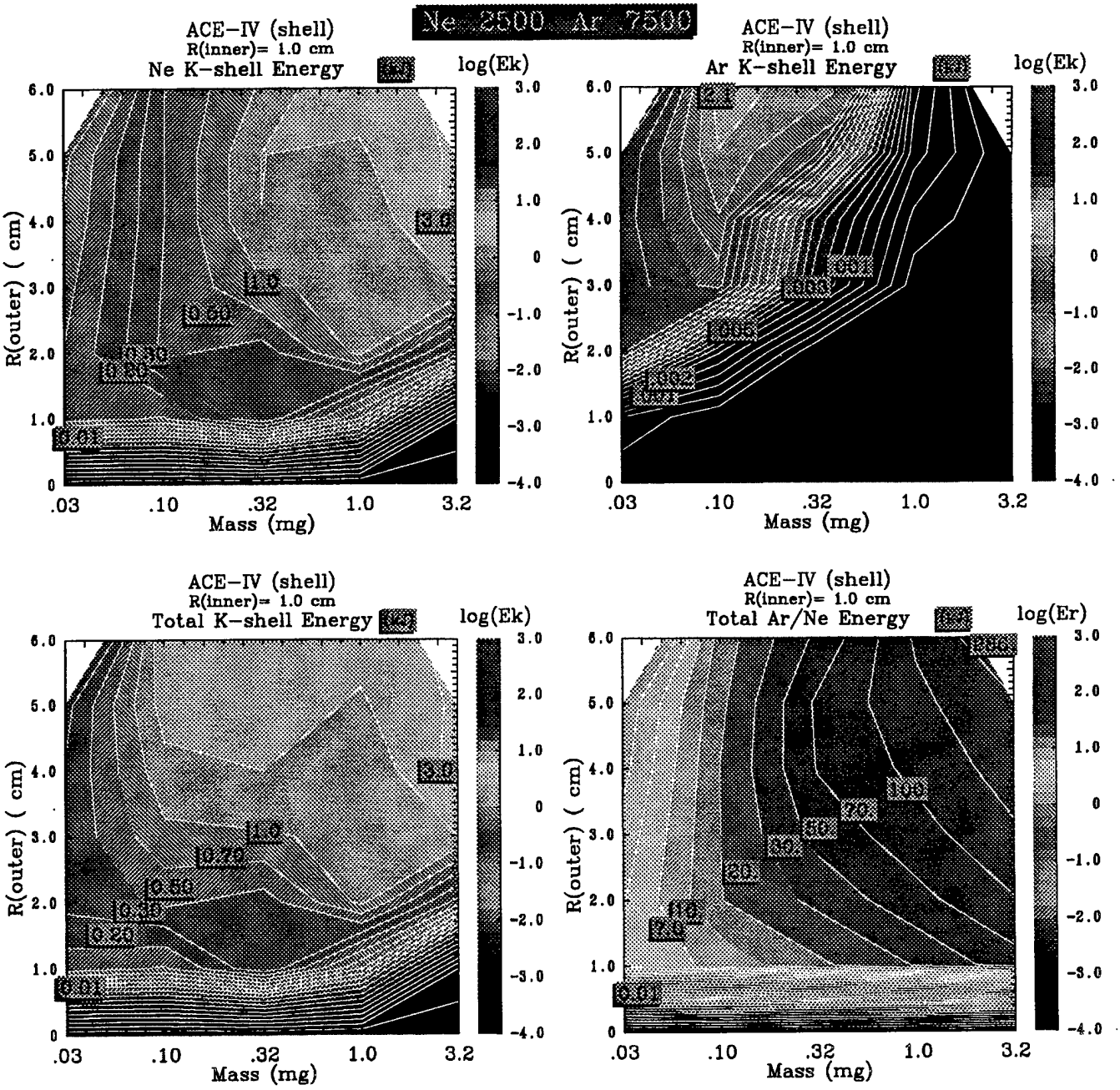
Ne .2500 Ar .7500
ACE–IV (shell)
R(inner)= 1.0 cm
Ne K–shell Energy
log(Ek)
ACE–IV (shell)
R(inner)= 1.0 cm
Ar K–shell Energy
log(Ek)
ACE–IV (shell)
R(inner)= 1.0 cm
Total K–shell Energy
log(Ek)
ACE–IV (shell)
R(inner)= 1.0 cm
Total Ar/Ne Energy
log(Er)
R(outer) (cm)
Mass (mg)
.03
.10
.32
1.0
3.2

Fig. 8

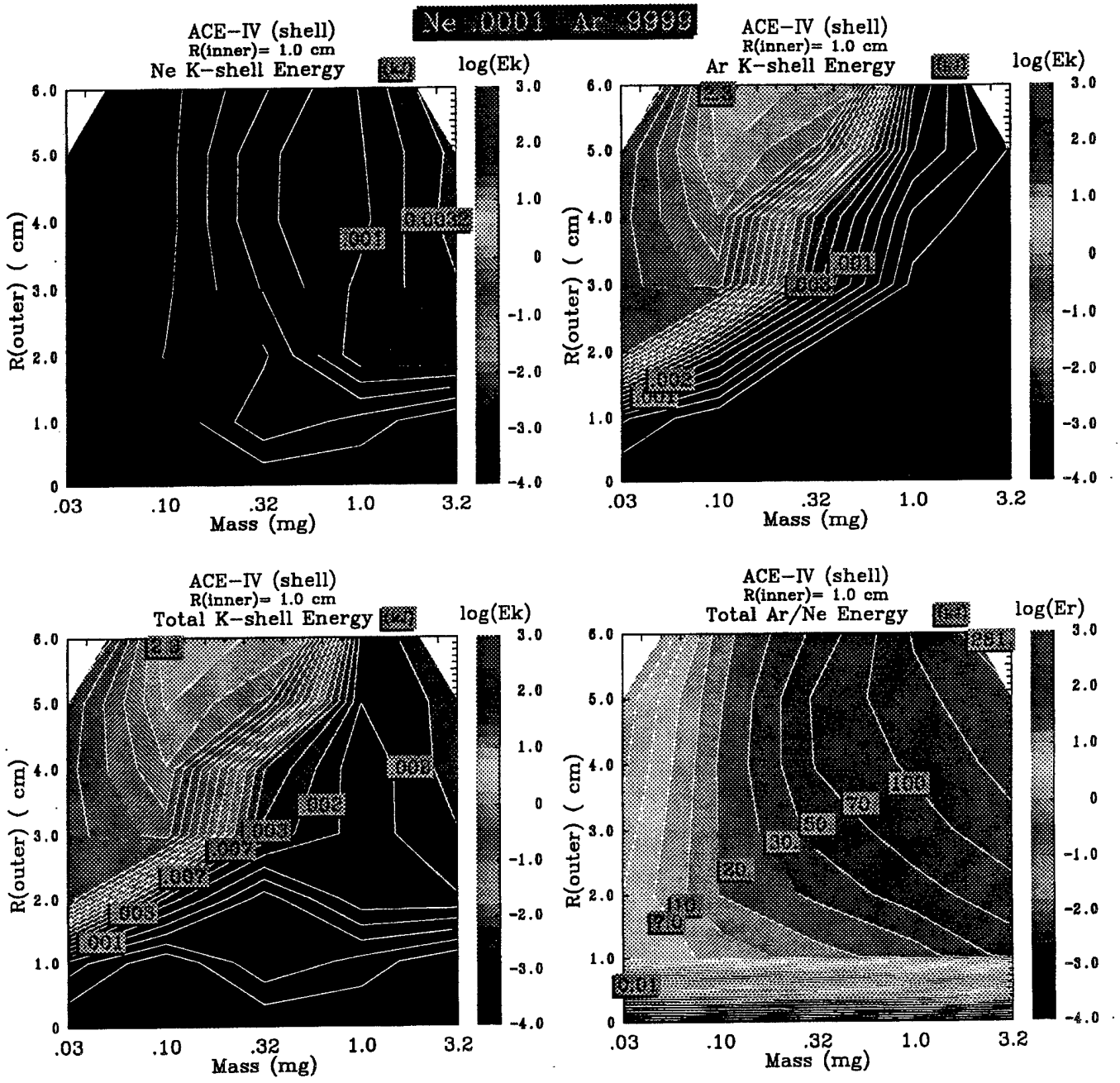
Ne .0001 Ar .9999
ACE-IV (shell)
R(inner)= 1.0 cm
Ne K-shell Energy
log(Ek)
R(outer) (cm)
Mass (mg)
ACE-IV (shell)
R(inner)= 1.0 cm
Ar K-shell Energy
log(Ek)
R(outer) (cm)
Mass (mg)
ACE-IV (shell)
R(inner)= 1.0 cm
Total K-shell Energy
log(Ek)
R(outer) (cm)
Mass (mg)
ACE-IV (shell)
R(inner)= 1.0 cm
Total Ar/Ne Energy
log(Er)
R(outer) (cm)
Mass (mg)

Fig. 9

II. DIAGNOSTIC LINE RATIOS AND K SHELL POWERS EMITTED FROM Ne, Al, Ar AND Ti PINCHES

A. Introduction

The use of spectroscopy to infer plasma conditions in Z-pinch plasmas is well established[1-14]. These inferences are often limited by the accuracy of the models on which they are based, and most early diagnostic methods were limited to optically thin plasmas. Many of the applications of Z pinches involve the use of their emitted x rays; in these cases, the radiation yield and spectrum provide figure-of-merit diagnostics for the plasma. For an early review of Z pinches emphasizing their radiative properties, Ref. 15 may be consulted. After decades of effort and corresponding progress, several fundamental questions about the relationship of the pulsed-power generator and load design to the Z pinch implosion dynamics and on-axis assembly conditions are just beginning to be addressed. For instance, how does the current risetime of the machine affect load performance and how does the initial mass location and distribution impact x-ray production during load assembly?

For meaningful comparisons between theory and experiment to be made, the state of the plasma must be characterizable. The purpose of the present work is to provide an extensive set of K-shell line ratio and power data for four elements frequently employed in present-day Z-pinch generators: neon, aluminum, argon, and titanium. These results, presented in the form of contour plots, demonstrate a one-to-one correspondence between the bulk temperature and density properties of optically thick plasmas and some of the most easily accessible experimental data. In Sec. B, the model and calculations are described, and in Sec. C, the line ratio and power contour plots are presented and the processes which govern the functional variations of these quantities are discussed. Finally, in Sec. D, we summarize a useful method of employing the present data to characterize laboratory z-pinch plasmas and apply it to some of ACE 4's best shots.

B. Description of calculations

The powers and line ratios presented are calculated assuming collisional-radiative-equilibrium (CRE), i.e., a set of rate equations is solved for the steady-state populations of the atomic levels of interest. A recent study [16] employing a 1-D radiation hydrodynamics model of Z pinch implosions has shown that this assumption is valid for the K shell emissions of elements up to and including titanium, but can break down for krypton implosions where lags in ionization times become increasingly important. The processes coupling the levels and determining their populations are: radiative, three-body, and dielectronic recombination, collisional excitation and de-excitation, collisional ionization, spontaneous and induced radiative decay, and photoexcitation.

Detailed radiation transport is necessary to get accurate photoexcitation rates as well as to compute the power outputs of optically thick transitions. As an example of the large line optical depths frequently encountered in Z pinches, consider an aluminum pinch of diameter 2 mm and temperature of 400 eV. At an ion density of 10^{20} cm^{-3}, the H- and He-like stages each account for about 40% of the species present. The optical depths of the Lyman alpha, beta, gamma, and delta resonance lines are, respectively, 340, 54, 19, and 9. For the corresponding He-like lines, the optical depths are twice those given for the H-like stage.

For the four elements considered in this work, Ne, Al, Ar, and Ti, we concentrate on K-shell diagnostics; therefore, the atomic models employed carry only the ground states within the neutral through Be-like ionization stages. For the Li-, He-, and H-like species, individual excited states through principal quantum number n=5 are included. A detailed discussion of the rate equations and the methods for calculating the various atomic rate coefficients is found in Ref. 17. The radiation transport is calculated with a multicell technique based on a matrix of coupling coefficients[18]. Voigt line profiles are used, with the cell-to-cell escape probabilities given in Ref. 19. Ion and electron temperatures are assumed to be equal. This assumption may break down at the lower densities employed in the calculations, and one of the current diagnostic challenges for Z pinches is inferring differences in electron and ion temperatures that generally occur in the core of these plasmas. For all four of the elements, the ion density range for the calculations was chosen to be 10^{19} to 10^{21} cm^{-3}. For this density range, the choice of n=5 as the highest principal quantum number in the

K shell atomic models represents a compromise. According to the formulation of the Inglis-Teller limit given by Griem[20], this choice is approximately correct in the upper (logarithmic) half of our chosen density range, where three-body recombination becomes more important in populating the upper levels. In the lower half of the density range, the existence of levels up to n=7 for Ne, 8 for Al, and 10 for Ar and Ti, is not expected to significantly affect the first two resonance lines whose intensities are principally determined by collisional excitation from the ground state.

The temperature range of interest to K-shell emission varies from element to element. In order to remain in the regime where K-shell emission dominates, higher temperatures must obviously be considered as atomic number increases.

C. Results and discussion

In optically thin plasmas the emission spectrum and line ratios are independent of the size of the plasma, but the power outputs from uniform optically thin cylinders vary as the diameter of the cylinder squared. This behavior is modified as the size of a plasma increases, and it becomes optically thick. The K shell resonance lines become increasingly opaque; however, continuum features usually remain thin. Thus, the effects of plasma opacity is the regime considered here are principally seen in the intensities of the resonance lines. Similarly, while individual line outputs can be significantly reduced by opacity, ratios of lines, both of which are optically thick, will be less affected. Thus, many of the results presented in this section are not strongly dependent on plasma size.

For each of the four elements, results are presented for assumed pinch diameters of 1, 2, and 3 mm, which encompass the pinch sizes most often observed in experiments. The quantities displayed are the ratios of Lyα to the sum of Heα and intercombination $1s^2$-$1s2p^3P_1$, lines, the ratio of Lyβ to Heβ, and the total K shell powers, defined as the sum of resonance lines plus the two continuua corresponding to recombination to the H-like and He-like ground states. Note that for Ar and Ti, the analogous 1-3 intercombination line is strong enough to be included in the β line ratio. These three quantities, for each of three pinch sizes, and four elements, gives a total

of 36 plots, which appear in Figs. 1-12, in ascending order of atomic number and assumed pinch diameter. Figs. 13-15 relax the assumptions of spatially uniform temperature, and of equal ion and electron temperatures to recalculate the case of a 2 mm aluminum pinch. The effects of line opacity are also illustrated by comparison to a calculation which ignores its effects.

One of the clearest characteristics of Figs. 1-12 points the way toward their use in interpreting Z-pinch spectra. The two H-like to He-like line ratios increase with temperature, reflecting the fact that the ratio of the abundances of these two ionic species increases with increasing temperature. Thus these line ratios are predominantly temperature sensitive. Since the 1-3 lines are only about one-sixth as thick as the 1-2 lines, the temperatures obtained from the two ratios can differ in practice. This is especially likely if strong temperature gradients are present in the pinch, because one is, in effect, sampling photons from different sections of the plasma at x-ray energies of considerably different opacity.

Since in each case, temperature is plotted along the vertical axis, and density along the horizontal, a quantity which is sensitive to temperature alone will display contours which are parallel to the horizontal axis. In contrast, purely density sensitive quantities would appear as strictly vertical contours. Contours of the two temperature sensitive line ratios are seen in Figs. 1-12 to be mostly parallel to the horizontal axis. However, deviations from a pure temperature dependence are seen for all four of the elements. This is due to the interplay of two atomic processes which introduce some sensitivity to density. As density increases, the opacities of the optically thick lines also increase. The resulting photopumping leads to an increase of population in the excited states of the two K shell species. When this happens, the mean charge of the plasma increases for a given temperature since the ionization threshold from the excited states is much lower than from the ground state. This is a form of ladder ionization assisted by radiative pumping. Note, for instance, for Ne, that the line ratios for a given temperature initially increase as one proceeds from the lowest ion density of 10^{19} cm^{-3} to higher densities. This directly reflects a higher degree of ionization due to the ladder-pumping effect.

Another process which contributes significantly to the behavior of the line ratios is three-body

recombination. In the regime of the higher densities displayed in Figs. 1-12, this process, whose rate is proportional to the square of the electron density, reduces the level of ionization of the plasma. Thus at high densities, the line ratios generally have the opposite density variation to that seen at lower densities. This can produce a "u" shaped contour which is visible in many of the figures. The line ratio contours are also affected directly by optical depth due to self-absorption of the line radiation. In general, line opacity lessens the increase of radiation as the fractional population of the ground state increases, and similarly limits the rapidity of the decrease in a line's emitted power as the ionization stage from which the line arises begins to burn out. The actual shape of a given line ratio contour reflects the competition and interplay of these effects and processes.

The total K shell power emitted from the resonance lines and the two continuum edges for the four elements and three plasma sizes is plotted in Figs. 1(c)-12(c). All of these contour plots have approximately the same appearance. For the upper two-thirds of the temperature range the isocontours of power are very nearly parallel to the vertical (temperature) axis, indicating an almost pure density dependence. In the lower third of the temperature range, the contours sweep to the lower right toward higher densities. Therefore, in the lower part of the temperature regime at which significant fractions of K shell species exist, K shell power increases with increasing temperature. However, at higher temperatures, further increases in temperature do not result in more x-ray emission, creating a nearly pure density dependence. This phenomenon occurs because the higher temperature merely transfers population from the He-like stage to the hydrogenic species. What is gained in H-like radiation at higher temperatures is lost in He-like. Once a Z pinch plasma is stripped well into the K shell, the most effective way to increase its x-ray output is to increase its density, not its temperature. At much higher temperatures than considered here, the K shell is largely burned out, and the power isocontours sweep toward the upper right when increased temperature results in less power as the bare nucleus increasingly dominates.

As mentioned above, especially at the lower densities considered, or if heating is very rapid, the ion and electron temperatures do not necessarily equilibrate in imploding Z pinches. The ion temperature may remain considerably hotter than that of the electrons for several ns or longer. This

phenomenon is essentially a remnant of the high implosion velocities which impart kinetic energies of tens of keV to the ions prior to on-axis assembly. To gauge the possible effects of high ion temperature on the spectroscopic diagnostics and power output, we have considered the case of a 2 mm diameter aluminum pinch and assumed, as an upper bound, that the ion temperature is 50 times that of the electrons. The results are shown in Figs. 13 (a-c). The principal radiative effect is that the optical depths of the mostly Doppler-broadened lines are all reduced by the square root of the increase in the ion temperature, which in this case is about a factor of 7. Note, however, that the lines will remain optically thick. Recalling the discussion of Sec. B, the alpha line optical depths are reduced to 50-100, and even the delta lines do not become truly thin. Comparison of the line ratio plots of Figs. 13 a and b with the standard case presented in Figs. 5 a and b shows some differences, but no drastic effects. For example, a beta line ratio of 0.5 for an aluminum ion density of 10^{19} cm^{-3}, indicates an electron temperature of 990 eV for the standard equilibrated case, whereas even if the ion temperature exceeded that of the electrons by the factor of 50, the diagnosed temperature would be reduced to just 820 eV. All the line opacities are reduced by the same factor, leaving a lesser effect on the line ratios. These ratios by themselves are not useful in diagnosing differences in ion and electron temperatures. On the positive side, the electron temperature diagnostic remains essentially intact.

As noted above, the effects of line opacity on total K shell power output are weakened by the contribution of the continuum to the radiation. The factor of 7 decrease in line opacity brought about by the assumption of 50 times greater ion temperature does significantly increase the K shell power in the medium density region of the contour plots, as indicated by comparison of Fig. 13 c with Fig. 5 c. Near ion densities of 10^{20} cm^{-3}, the power in the K shell is expected to nearly double for electron temperatures in excess of 550 eV. At lower densities, opacity is less important, whereas at higher densities, three-body recombination enhances the continuum. The fact that opacity affects the emitted powers of the resonance lines much more than the continuum is the basis of a previous demonstration[21] that the line to continuum ratio can be used to diagnose differences in ion and electron temperature.

A more dramatic illustration of the effects of line opacity is seen in the results plotted in Figs. 14 (a-c) which were obtained with the wholly unrealistic assumption that the plasma is optically thin at all photon energies, in all lines and continua. The temperature sensitive H-like to He-like line ratios are reduced at the temperatures and densities covered by these plots, compared to the standard case (Figs. 5 a and b). This reflects the fact that it is more difficult to ionize an optically thin plasma because the lack of photopumping of the excited states reduces the ladder ionization effect discussed above in this Section. Fig. 14 c demonstrates the substantial effect that opacity has on the power output of the K shell. Comparing Figs. 14 c and 5 c reveals that an optically thin aluminum plasma would radiate roughly twice the K shell power at ion densities between 10^{19} and 10^{20} cm^{-3}, and up to 4 times as copiously for a broad range of temperatures at ion densities in excess of 10^{20} cm^{-3}. Figs. 1 c - 12 c also show that the radiated power per unit volume has a much milder variation among very optically thick plasmas of different sizes than the sharp differences which exist between a thin and thick plasma.

Finally, Figs. 15 (a-c) provide a glimpse into a very important area requiring future investigation - the effects of gradients in temperature on diagnostics and power output. In obtaining these plots, the density has been assumed uniform as before, but the temperature was decreased linearly as a function of radius from the center of the cylinder (r=0) to the outer edge, with the outer temperature fixed at 200 eV. The line ratios and power are plotted against the central (r=0) electron temperature. Figs. 15 a and b demonstrate opacity-induced reductions in the two temperature sensitive line ratios compared to the uniform temperature case. Line photons in both K shell ionization stages are absorbed and re-emitted by the cooler outer layer, lowering the line ratios to values characteristic of temperatures well below those of the central core. For instance, at an ion density of 10^{20} cm^{-3}, for a core temperature of 1000 eV, the calculated Lyα to Heα ratio of 1.8 is characteristic of a uniform plasma of 700 eV. Similarly, the Lyβ to Heβ ratio is predicted to be 3.0, which would be emitted by a uniform plasma of 620 eV temperature. Therefore, a hot core can be present in a Z pinch but be difficult to detect directly using the ratios of opaque lines. Indirectly, the gradient in temperature has manifested itself by the inference of different temperatures depending

on the line ratio used.

In Fig. 15 c it is seen (by comparison with Fig. 5 c) that the K shell power reflects the powers produced is different parts of the plasma, i.e., it is reduced by typical factors of 2 to 3 when the core is surrounded by a cooler, less efficiently radiating plasma containing the prescribed linear temperature gradient. Not surprisingly, this temperature decrement can greatly affect both the radiative efficiency and the character of the K shell line spectrum emitted from Z pinches. Full consideration of the scope and range of these effects, as well as the intricate radiation physics underlying their magnitude and behavior, is warranted for future work.

D. Application of the data in general and for ACE 4

Similar contour data has been used to analyze Z pinch plasmas, as discussed in Refs. 7, 9, and 13. What appears to be the most powerful and practical method to proceed has been discussed in detail in Ref. 7. Given the utility of the large amount of multielement data presented here, a summary of this interpretive technique is appropriate.

As discussed above, the line ratio contours are mostly parallel to the horizontal density axis because the ratios mostly depend on plasma temperature. The power contours, by contrast, are mostly vertical since they are usually mostly density sensitive. This suggests that simultaneous measurement of the power per unit length and one or the other of these line ratios will determine a unique plasma temperature and density because of the unique intersection of these horizontal and vertical contours in the (temperature, density) plane.

The procedure consists of, first, a measurement of the characteristic diameter of the pinch using a time-integrated or, preferably, time-resolved x-ray pinhole image. Calibrated spectra are used to get the line ratio(s). The K shell power per unit length can be estimated from the yield, pulsewidth, and measured length of the plasma. Clearly, few if any plasmas are characterized by homogeneity in either temperature or density. The characteristic average values - spatial, temporal, or both - of temperature and density obtained by this suggested analysis are, however, meaningful in the following sense. A certain, presumably sizable, fraction of the plasma is stripped to the K shell.

Most of the K shell x rays are usually due to the 1-2 alpha resonance lines of the He-like and H-like stages. Typically, images of Z pinches filtered in different regions of the x-ray spectrum show that the K shell emission maximizes near the pinch axis. Using the principal sources of radiative power to diagnose the plasma yields characteristic temperatures and densities which are most reflective of that radiation. Since many of the applications of Z pinches depend on their copious x-ray emission[15], it is appropriate to use diagnostics which are based on the emitted powers and ratios of the strongest lines. From the measured size and inferred density of the K shell emission region a K shell radiating mass can be obtained. A fuller discussion of these issues may be found elsewhere[7].

As a useful example of application of this technique, we consider the initial successes (Feb. 96) of the ACE 4 tandem puff experiments with neon and argon. Details of these experiments are covered in Sec. I. Shot 1752 using a neon gas puff produced 30 kJ of K shell x-rays. The initial mass load, according to the NRL Code 6770 interferometric analysis of nozzle flow, was 310 μg/cm. Fig. 16 shows the intersection of the observed K shell power and alpha line ratio in temperature,density space on the relevant contour plots. The inferred electron temperature is 280 eV, the ion density, 5.7 x 10^{18} cm^{-3}. This density coupled with the observed pinch diameter of 13 mm, implies a radiating mass load of 254 μg/cm, which is a very impressive 82% of the cold gas mass puffed in. This compares favorably with the best results achieved on other multi-MA generators.

The best argon result achieved in this tandem puff series was a yield of 6.5 kJ on shot 1763. Fig. 17 illustrates the application of the line ratio/power contour method to this shot. In this case, the radiating mass participation was 26%, less impressive than that derived for the neon shot, but argon requires 9 times the energy per ion to excite to the K shell. When compared to the best result in FY 1995, the density doubled, and mass participation increased by 1.5, leading to the more than sixfold yield improvement of 1 to 6.5 kJ.

Ref. 7 also includes a study in which the single temperatures and densities diagnosed from inhomogeneous plasmas are compared to the actual profiles of those quantities obtained from a radiation hydrodynamics calculation. We refer the reader to that work for a discussion of

conditions of validity of this analysis procedure, as well as issues which can arise in its application and interpretation. Among these are: where does the current flow[22], how does plasma form, how does the energy source divide between implosion kinetic energy and ohmic heating[14], when and how does radiative collapse occur[23–25], can instabilities be minimized or controlled[26], what are the particle velocity distributions[12]? Spectroscopy plays a vital role in the synergism between experiment and theory needed to address and ultimately answer these questions.

E. References

1. P. Burkhalter, J. Davis, J. Rauch, W. Clark, G. Dahlbacka, and R. Schneider, J. Appl. Phys. **50**, 705 (1979).

2. S. Maxon and T. Wainwright, Phys. Fluids **27**, 2535 (1984).

3. M. Gersten *et al.,* Phys. Rev. A **33**, 477 (1986).

4. F. C. Young, S. J. Stephanakis, and V. E. Scherrer, Rev. Sci. Instrum. **57**, 2174 (1986).

5. R. B. Spielman *et al.,* AIP Conf. Proc. **195**, 3 (1989).

6. K. G. Whitney, J. W. Thornhill, J. P. Apruzese, and J. Davis, J. Appl. Phys. **67**, 1725 (1990).

7. M. C. Coulter, K. G. Whitney, and J. W. Thornhill, JQSRT **44**, 443 (1990).

8. C. Deeney *et al.*, Phys. Rev. A **44**, 6762 (1991).

9. C. Deeney *et al.*, J. Appl. Phys. **72**, 1297 (1992)

10. N. Qi, D. A. Hammer, D. H. Kalantar, and K. C. Mittal, Phys. Rev. A **47**, 2253 (1993).

11. C. Deeney *et al.,* J. Appl. Phys. **75**, 2781 (1994).

12. M. E. Foord, Y. Maron, G. Davara, L. Gregorian, and A. Fisher, Phys. Rev. Lett. **72**, 3827 (1994).

13. C. Deeney *et al.,* Phys. Rev. E **51**, 4823 (1995).

14. K. G. Whitney *et al.,* Phys. Plasmas **2**, 2590 (1995).

15. N. R. Pereira and J. Davis, J. Appl. Phys. **64**, R1 (1988).

16. J. W. Thornhill, K. G. Whitney, J. Davis, and J. P. Apruzese, J. Appl. Phys. **80**, 710 (1996).

17. D. Duston and J. Davis, Phys. Rev. A **23**, 2602 (1981).

18. J. P. Apruzese, JQSRT **25**, 419 (1981).

19. J. P. Apruzese, JQSRT **34**, 447 (1985).

20. H. R. Griem, **Plasma Spectroscopy**, McGraw-Hill, New York (1964), p. 125.

21. J. P. Apruzese, J. W. Thornhill, K. G. Whitney, J. Davis, N. Loter, and C. Deeney, Bull. Am. Phys. Soc. **39**, 1557 (1994).

22. D. H. Kalantar and D. A. Hammer, Phys. Rev. Lett. **71**, 3806 (1993).

23. B. E. Meierovich, Sov. J. Plasma Phys. **11**, 831 (1985).

24. A. E. Robson, Phys. Fluids B **1**, 1834 (1989).

25. J. W. Thornhill, J. L. Giuliani, Jr., and J. Davis, J. Appl. Phys. **66**, 4154 (1989).

26. F. L. Cochran, J. Davis, and A. L. Velikovich, Phys. Plasmas **2**, 2765 (1995).

(a)

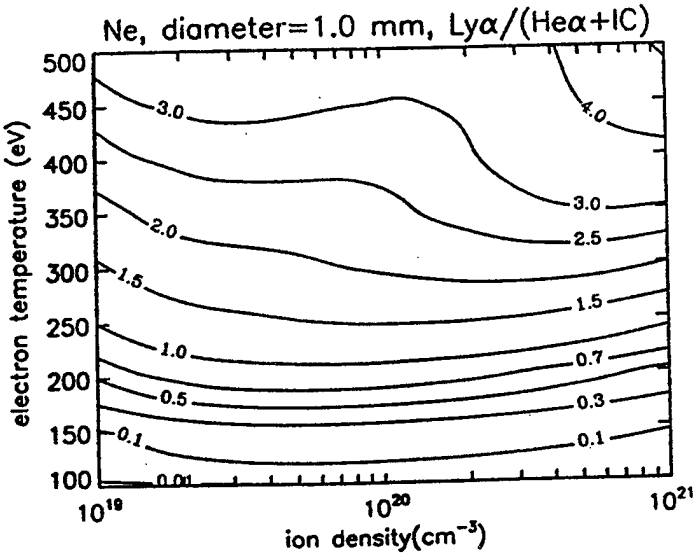

(b)

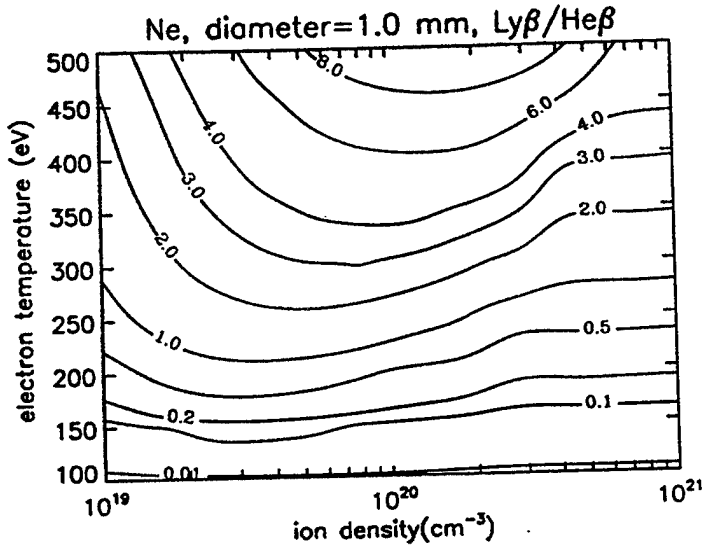

(c)

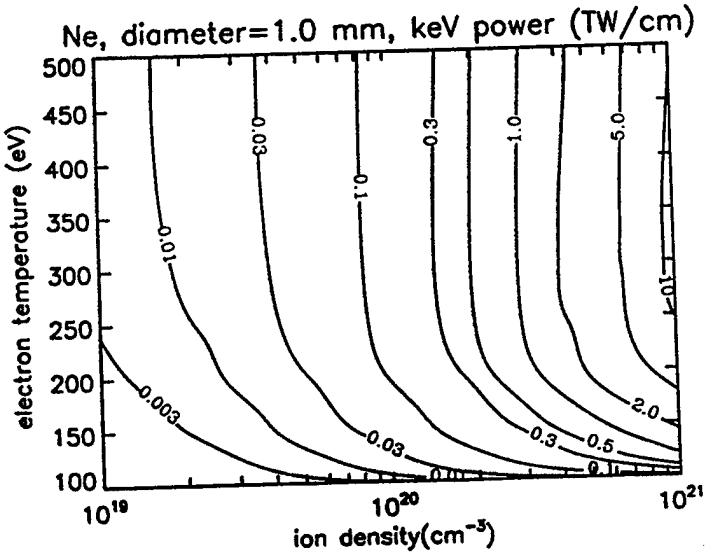

Fig. 1. (a-c) Contours of the indicated line ratios and powers are shown as a function of ion density and electron temperature for a cylindrical neon plasma of diameter 1 mm.

(a)

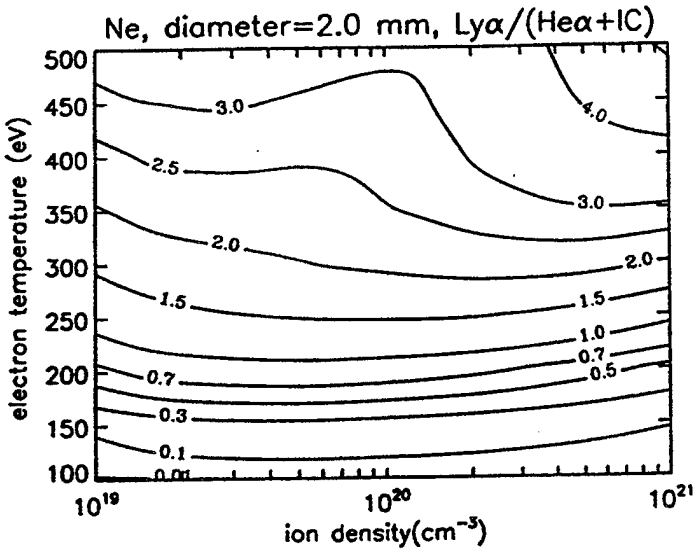

(b)

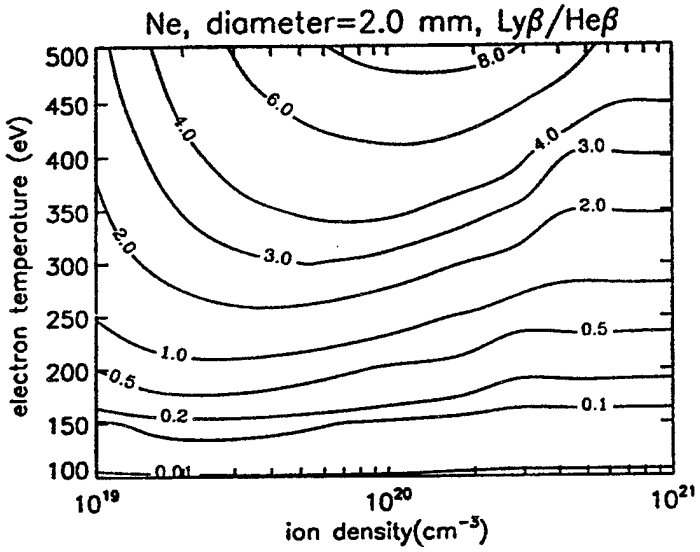

(c)

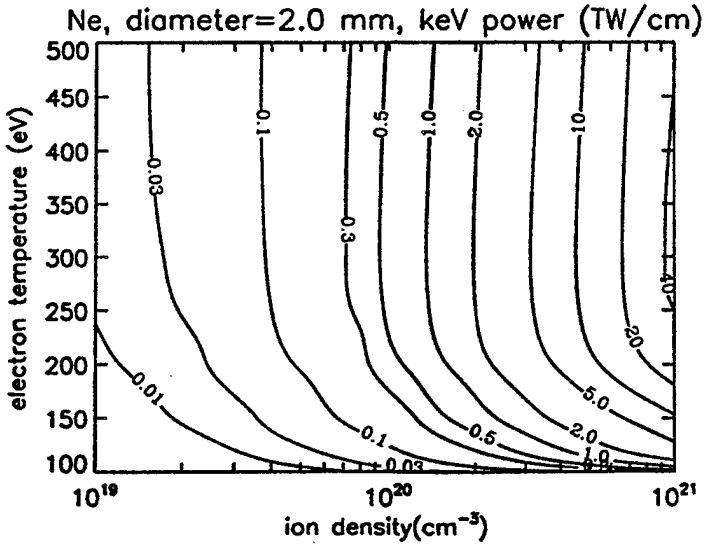

Fig. 2. (a-c) As in Fig. 1, except that the plasma diameter is 2 mm.

(a)

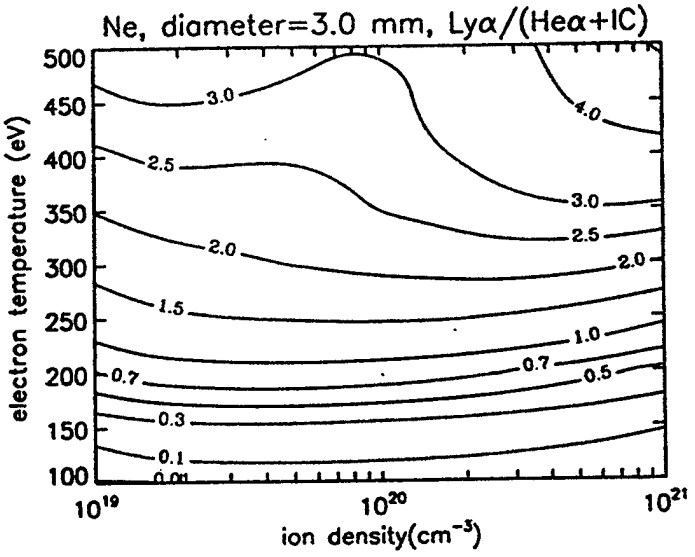

(b)

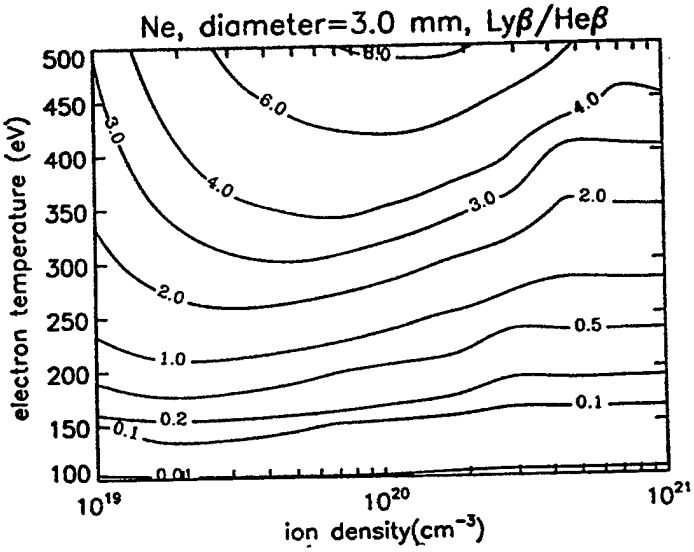

(c)

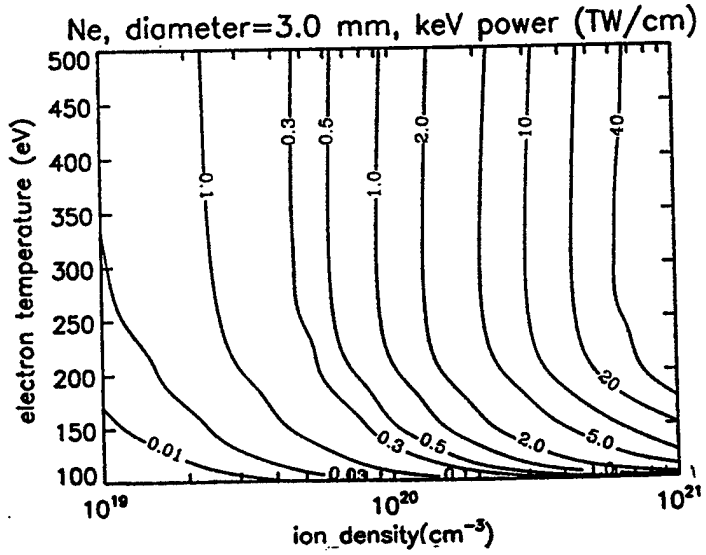

Fig. 3. (a-c) As in Figs. 1 and 2, except that the plasma diameter is 3 mm.

(a)

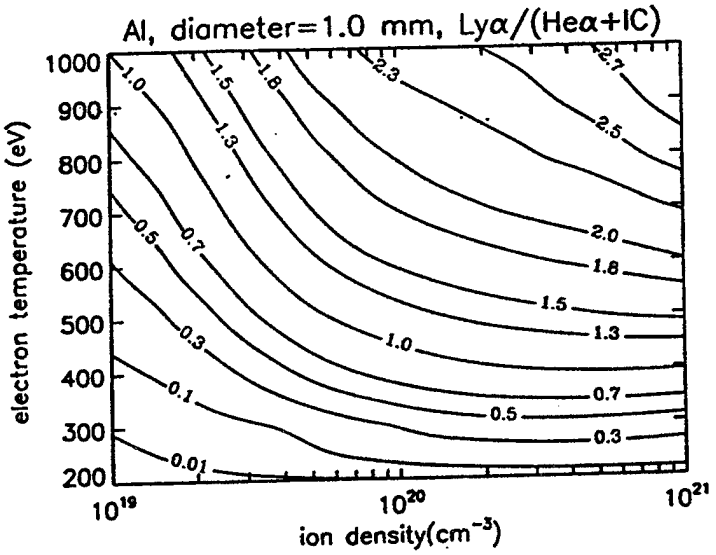

(b)

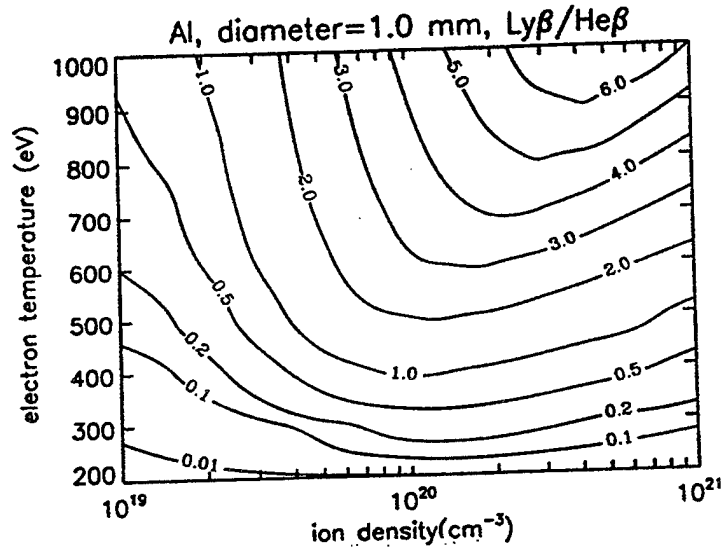

(c)

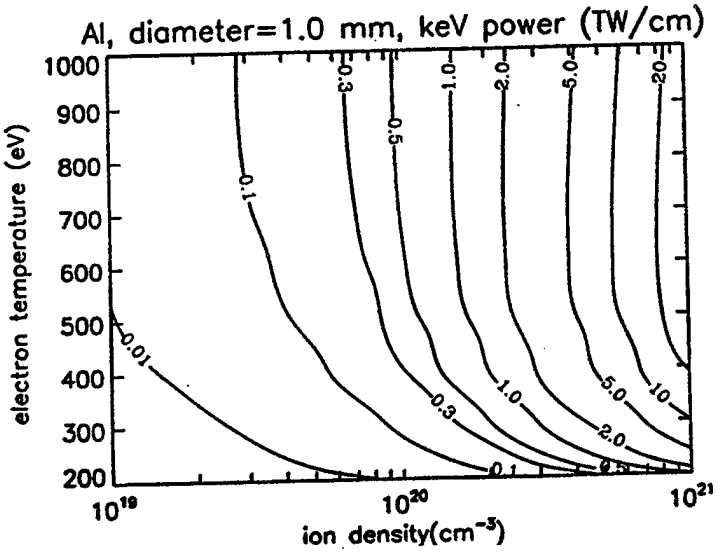

Fig. 4. (a-c) Contours of the indicated line ratios and powers are shown as a function of ion density and electron temperature for a cylindrical aluminum plasma of diameter 1 mm.

(a)

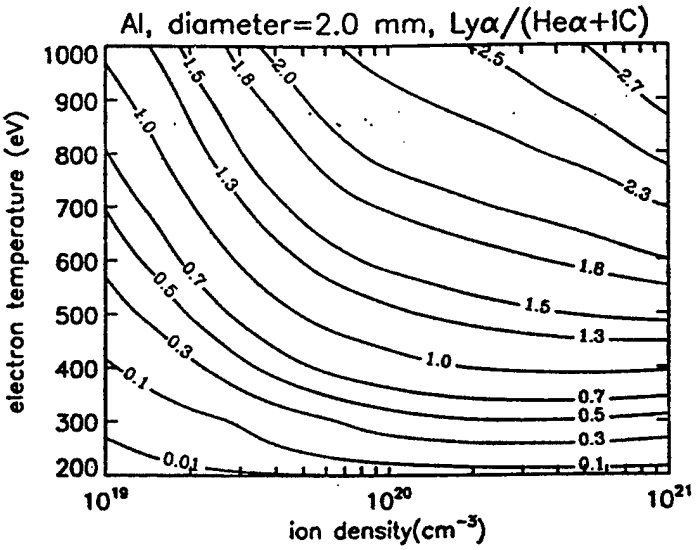

(b)

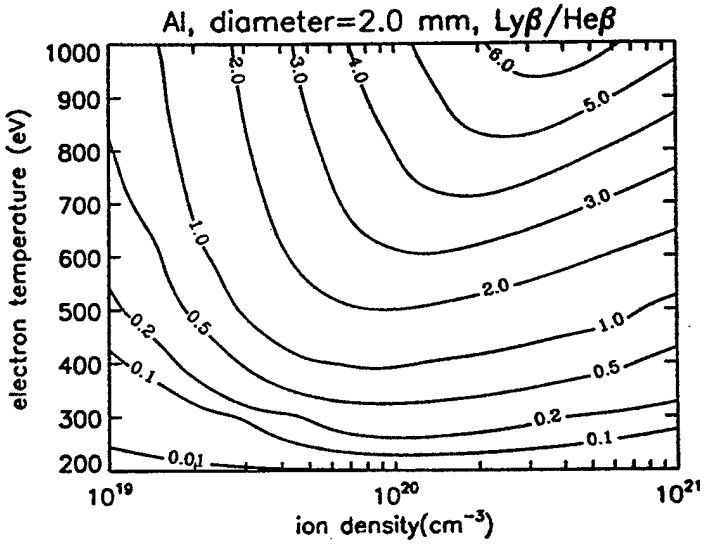

(c)

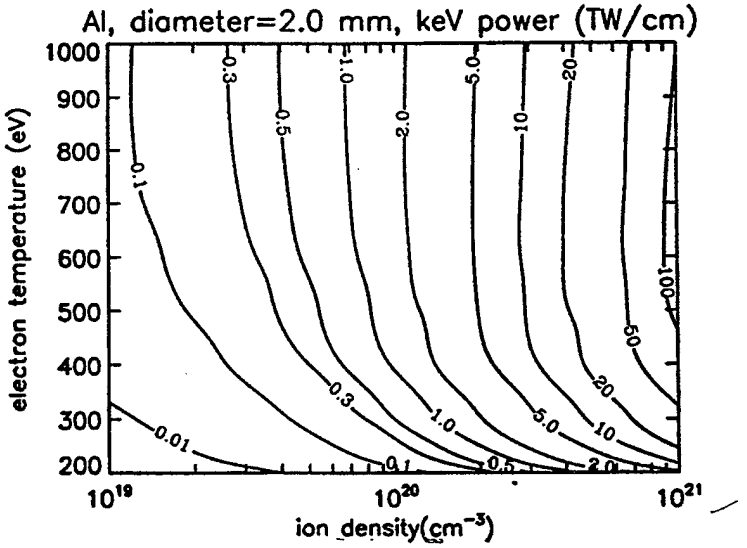

Fig. 5. (a-c) As in Fig. 4, except that the plasma diameter is 2 mm.

(a)

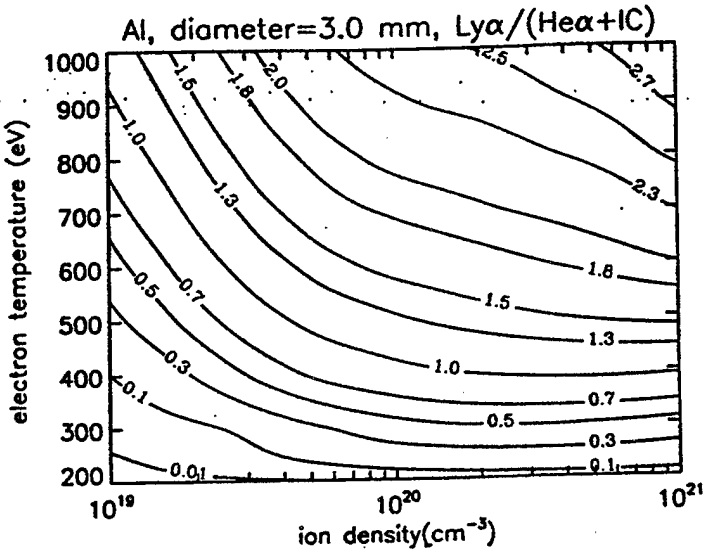

(b)

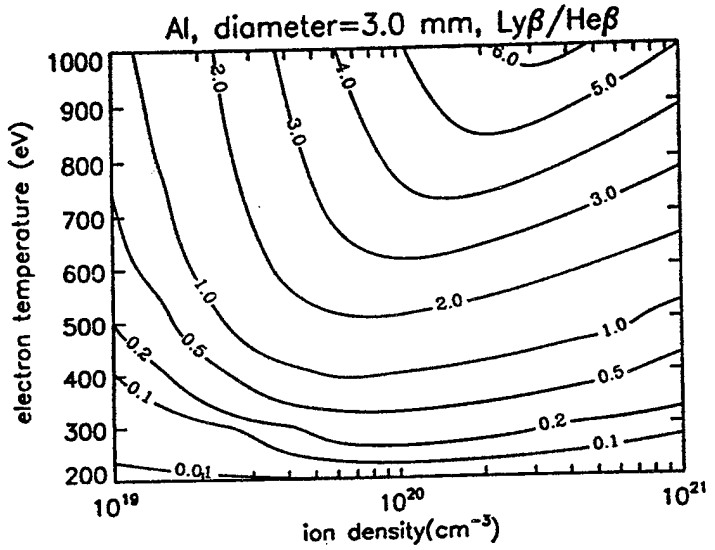

(c)

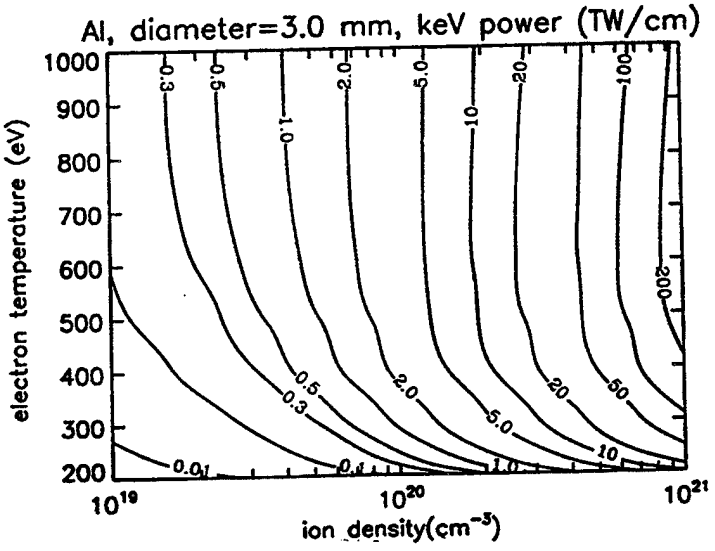

Fig. 6. (a-c) As in Figs. 4 and 5, except that the plasma diameter is 3 mm.

(a)

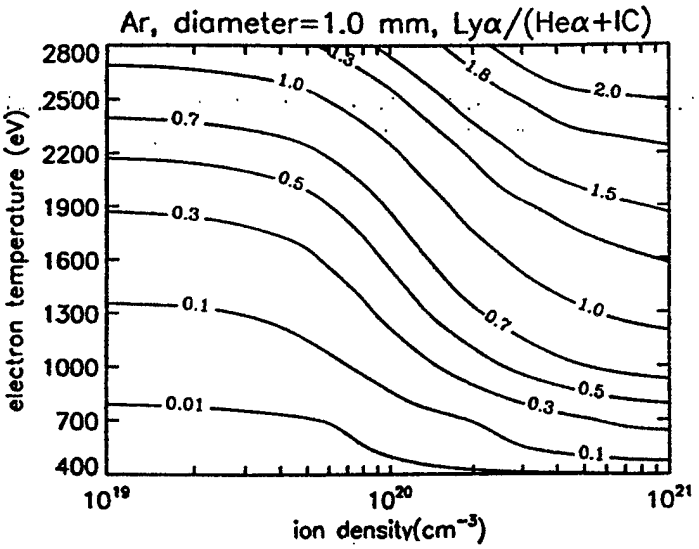

(b)

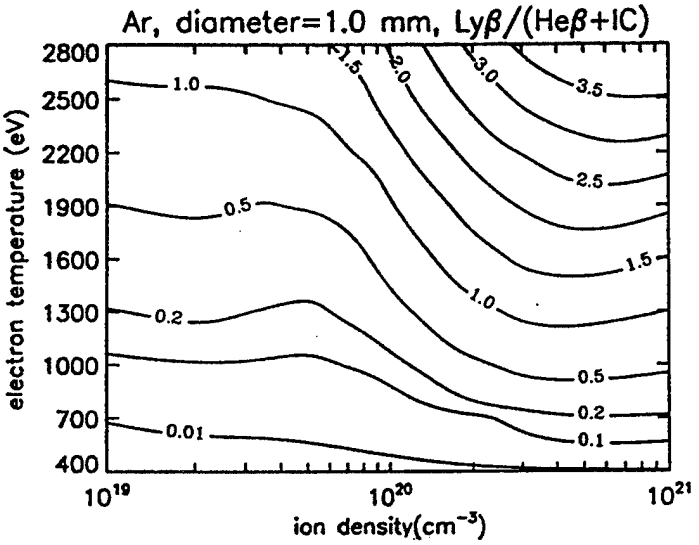

(c)

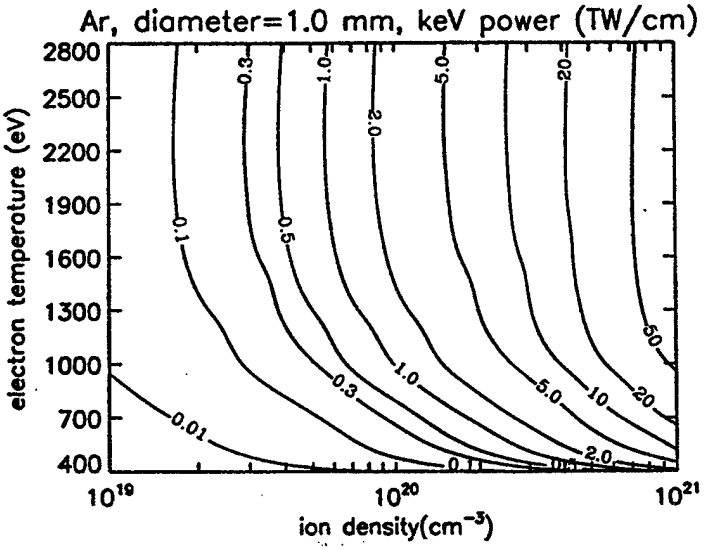

Fig. 7. (a-c) Contours of the indicated line ratios and powers are shown as a function of ion density and electron temperature for a cylindrical argon plasma of diameter 1 mm.

(a)

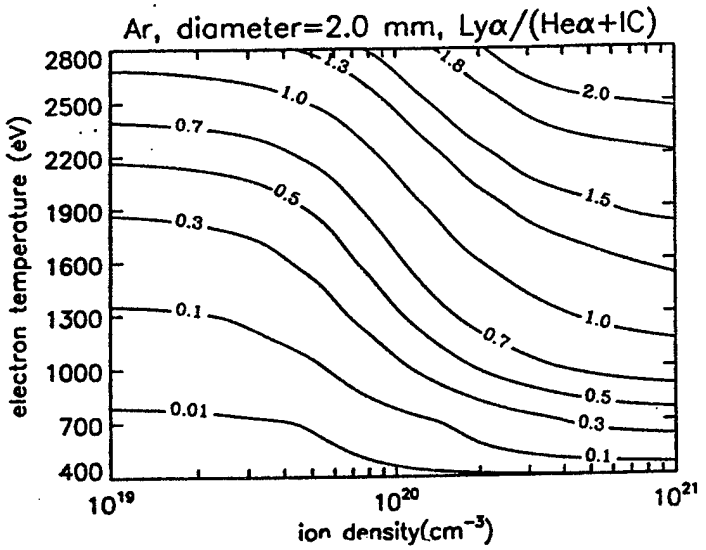

(b)

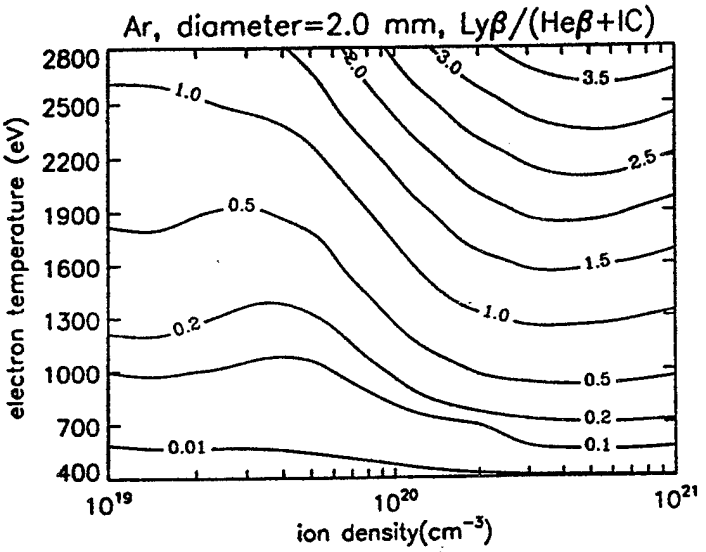

(c)

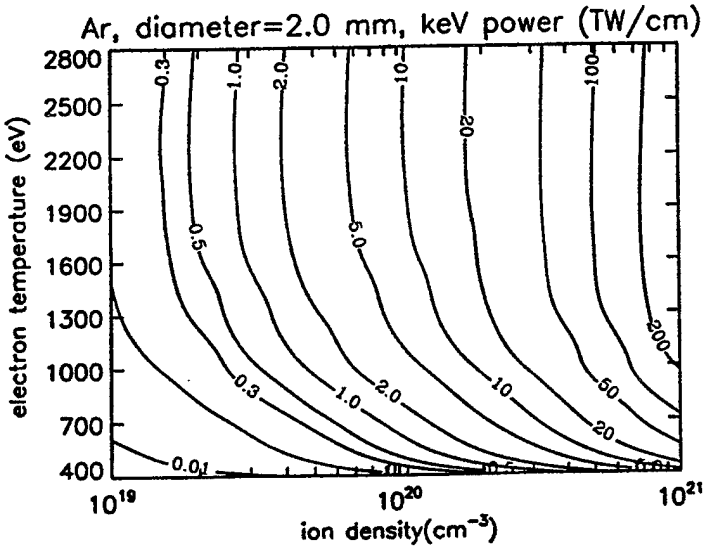

Fig. 8. (a-c) As in Fig. 7, except that the plasma diameter is 2 mm.

(a)

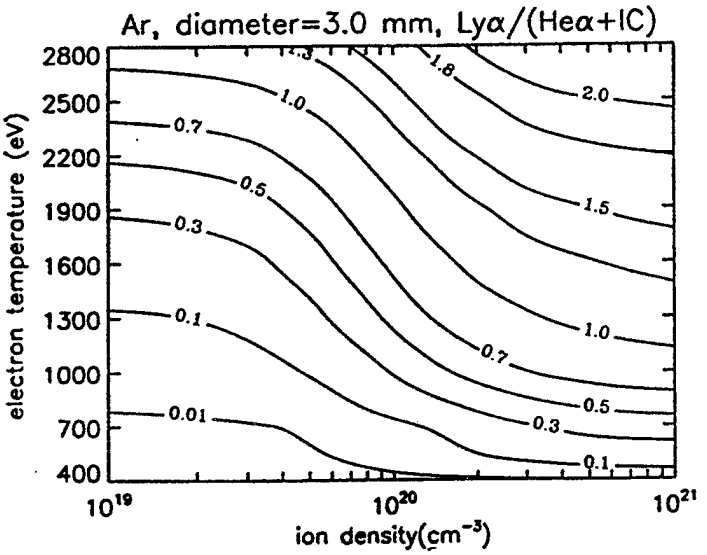

(b)

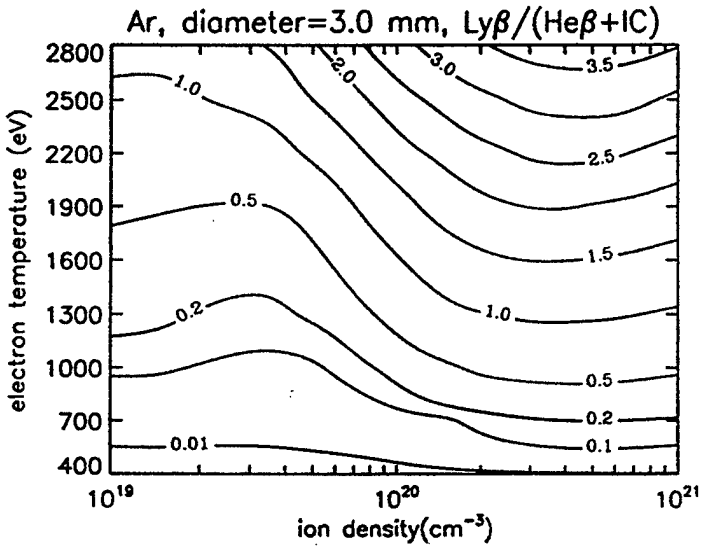

(c)

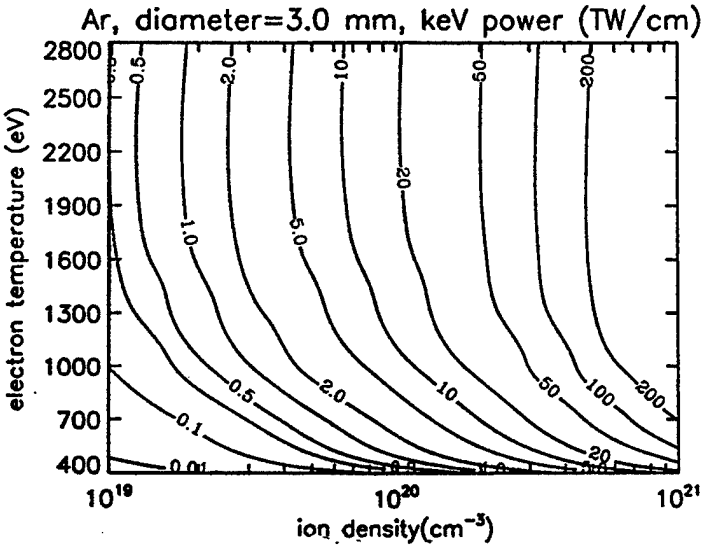

Fig. 9. (a-c) As in Figs. 7 and 8, except that the plasma diameter is 3 mm.

(a)

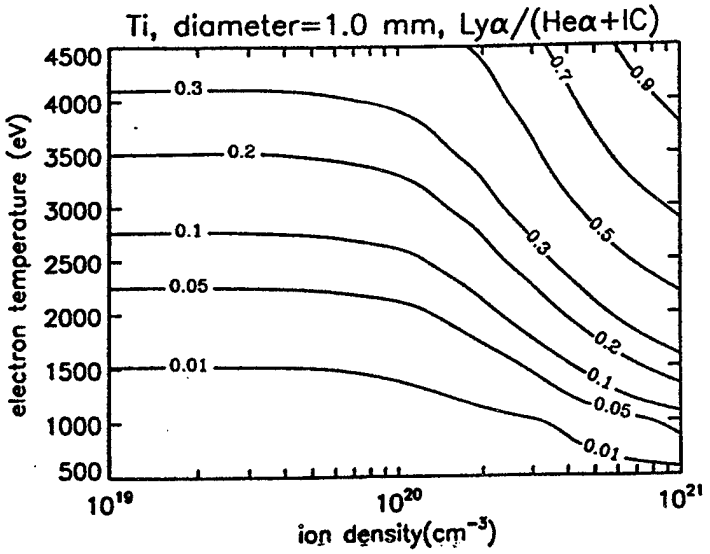

(b)

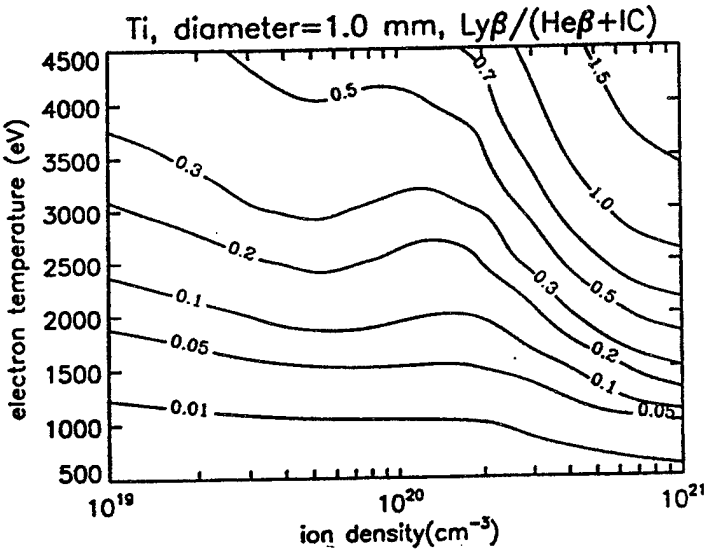

(c)

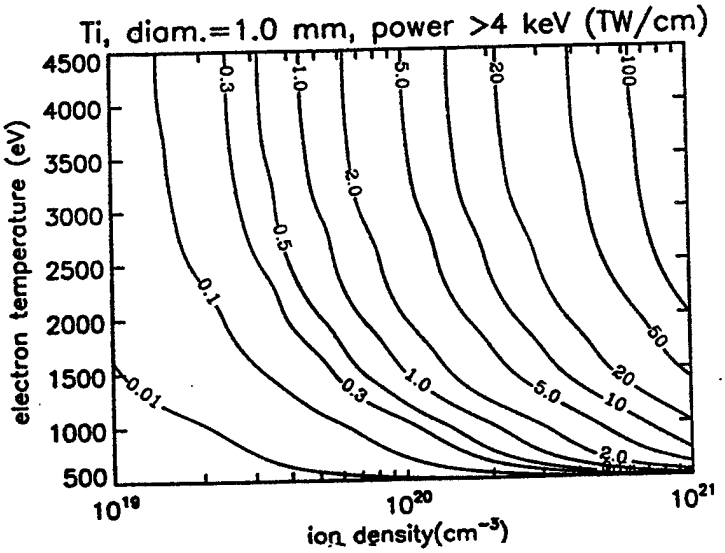

Fig. 10. (a-c) Contours of the indicated line ratios and powers are shown as a function of ion density and electron temperature for a cylindrical titanium plasma of diameter 1 mm.

(a)

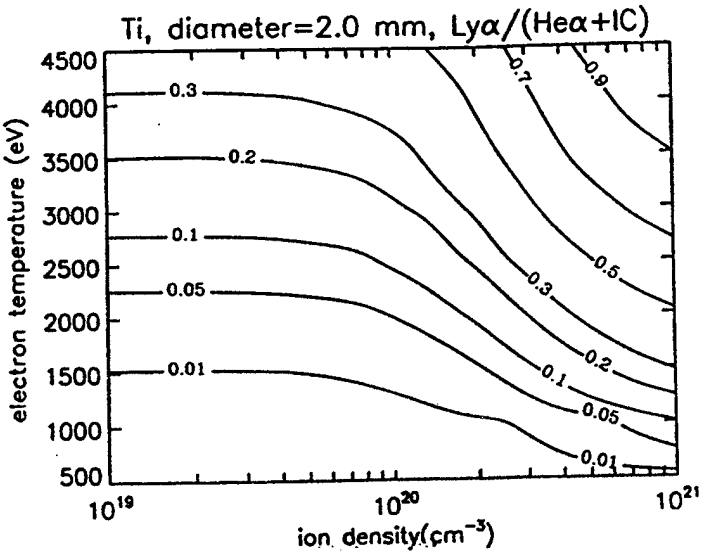

(b)

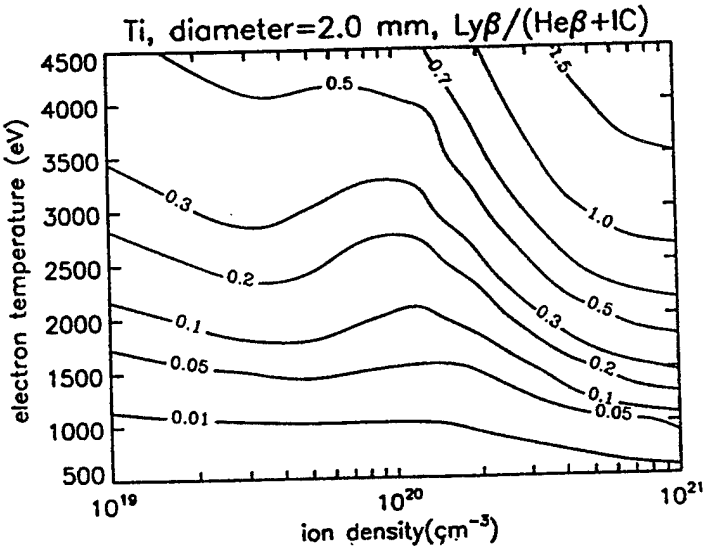

(c)

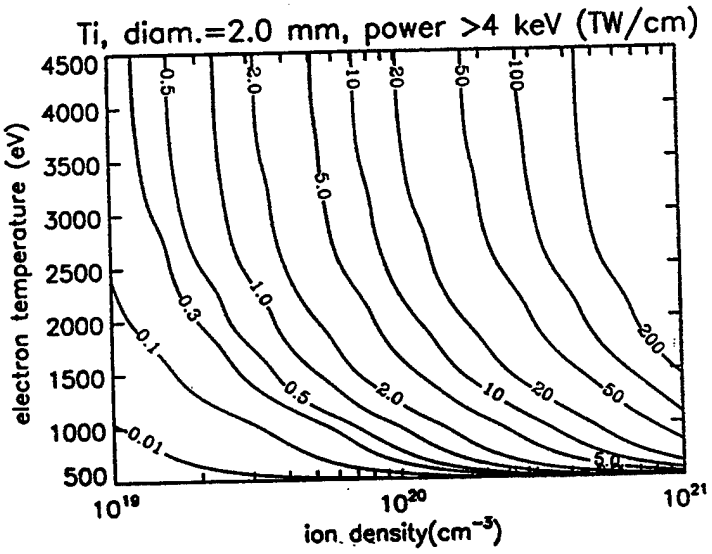

Fig. 11. (a-c) As in Fig. 10, except that the plasma diameter is 2 mm.

(a)

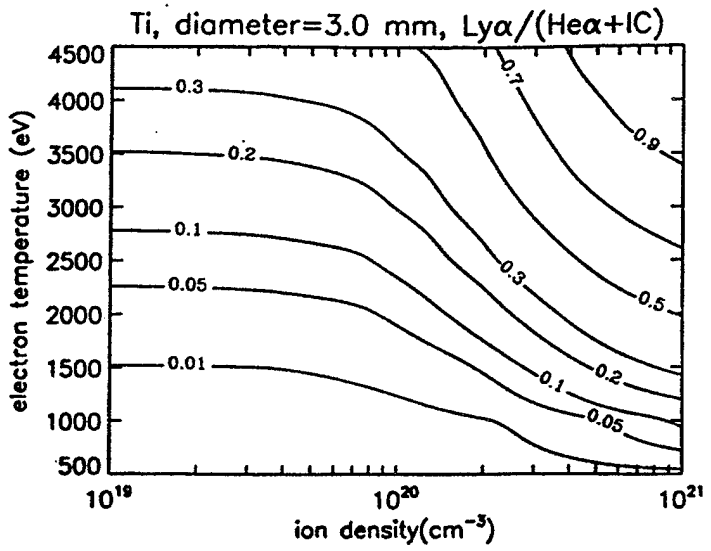

(b)

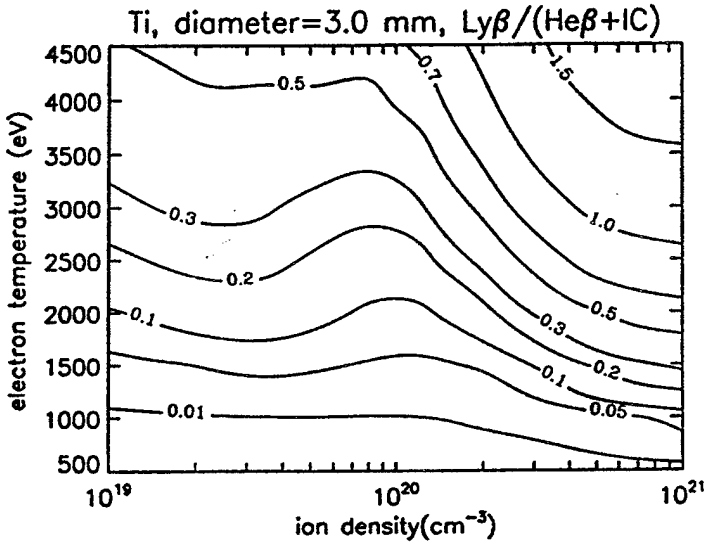

(c)

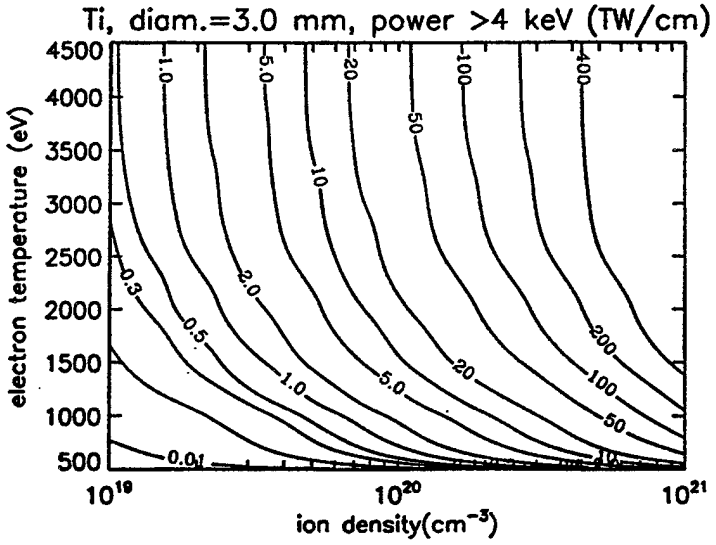

Fig. 12. (a-c) As in Figs. 10 and 11, except that the plasma diameter is 3 mm.

(a)

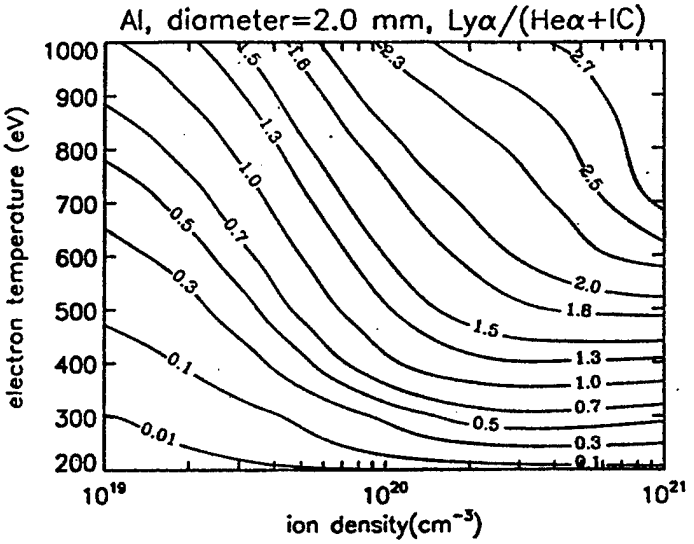

(b)

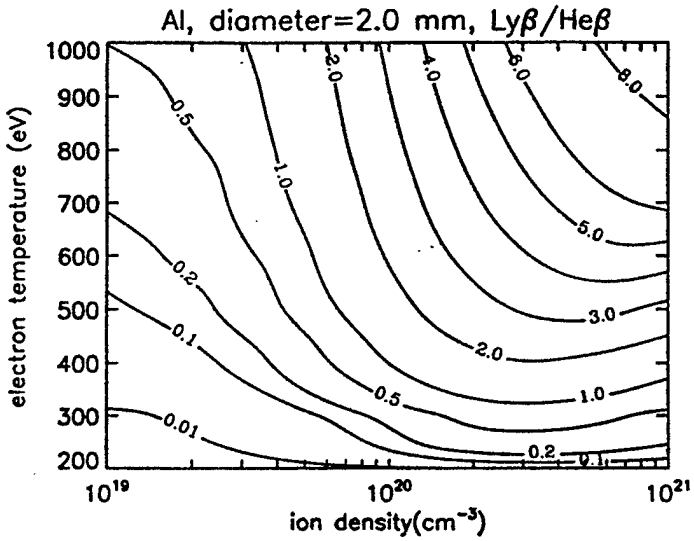

(c)

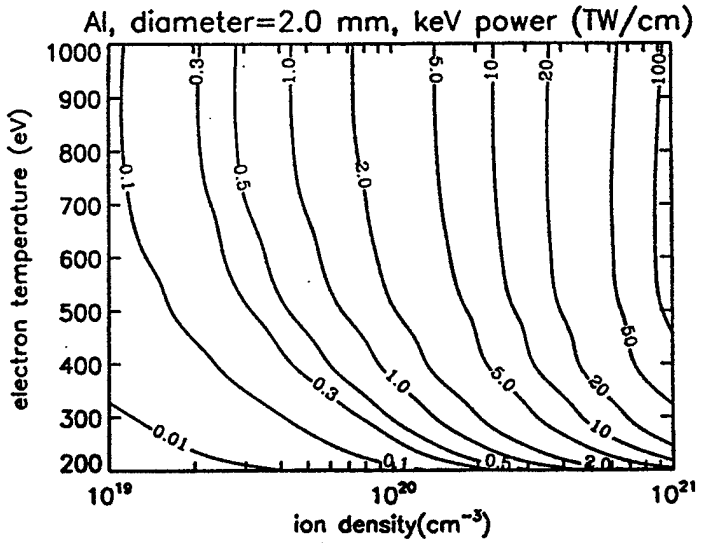

Fig. 13. (a-c) Contours of the indicated line ratios and powers are shown as a function of ion density and electron temperature for a cylindrical aluminum plasma of diameter 2 mm, with the ion temperature assumed to be a factor of 50 greater than the electron temperature.

(a)

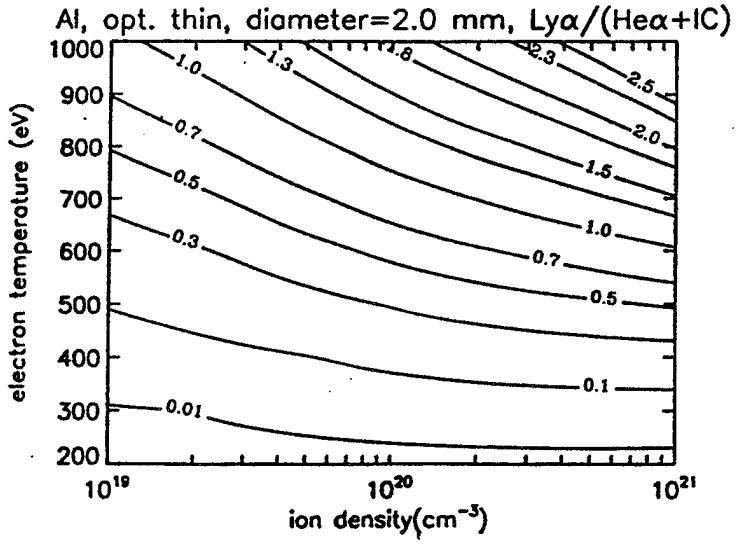

(b)

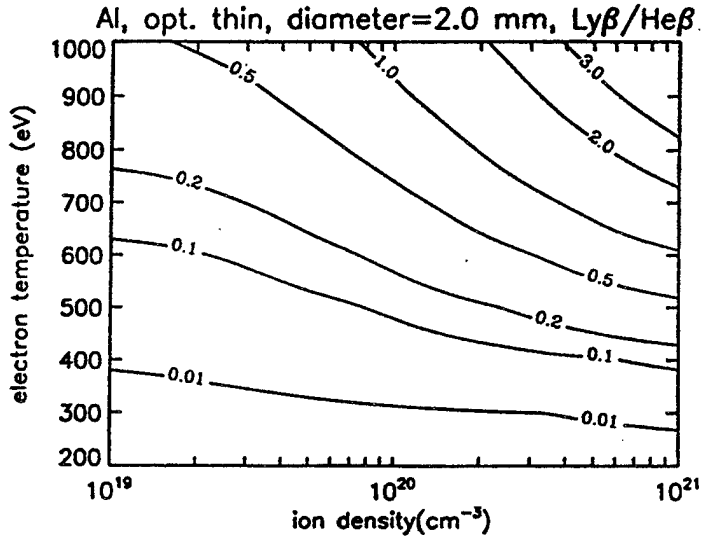

(c)

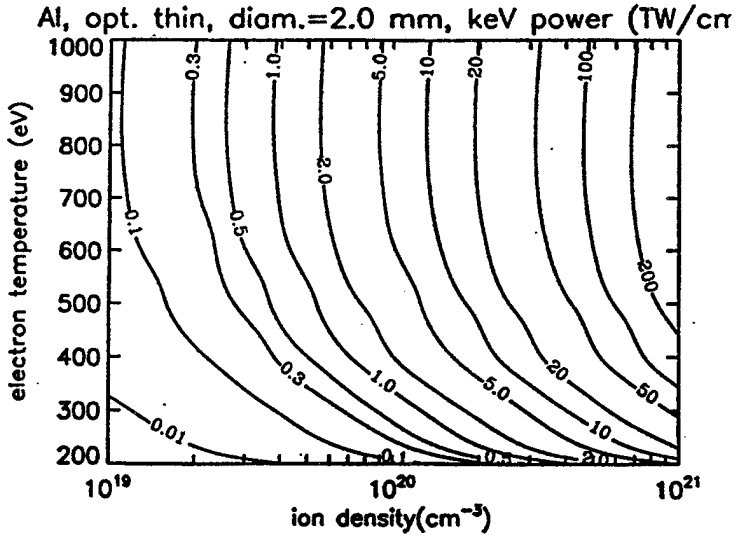

Fig. 14. (a-c) As in Fig. 13, except that the ion and electron temperatures are equal, and the plasma is assumed to be optically thin at all photon energies.

(a)

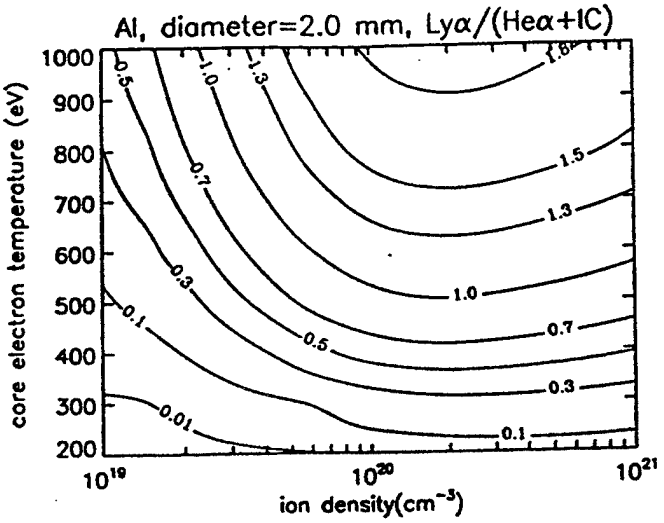

(b)

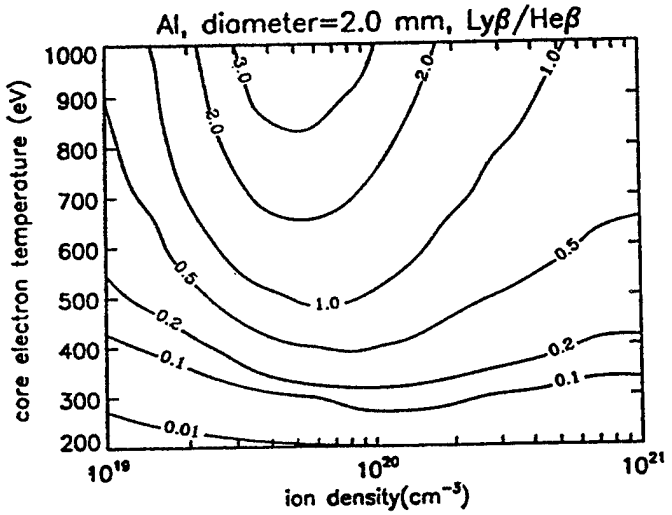

(c)

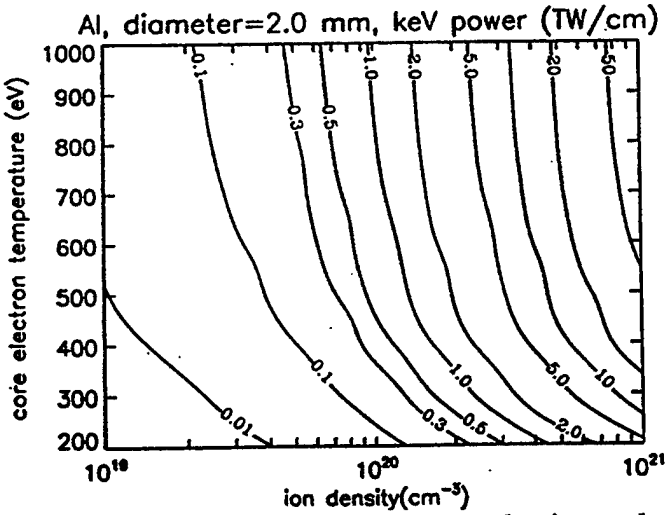

Fig. 15. (a-c) The same contours are displayed for a 2 mm aluminum plasma, but the (equal) electron and ion temperatures are assumed to decline linearly in radius from the core to the outer boundary, whose temperature is fixed at 200 eV. Line ratios and power contours are plotted as a function of the central temperature.

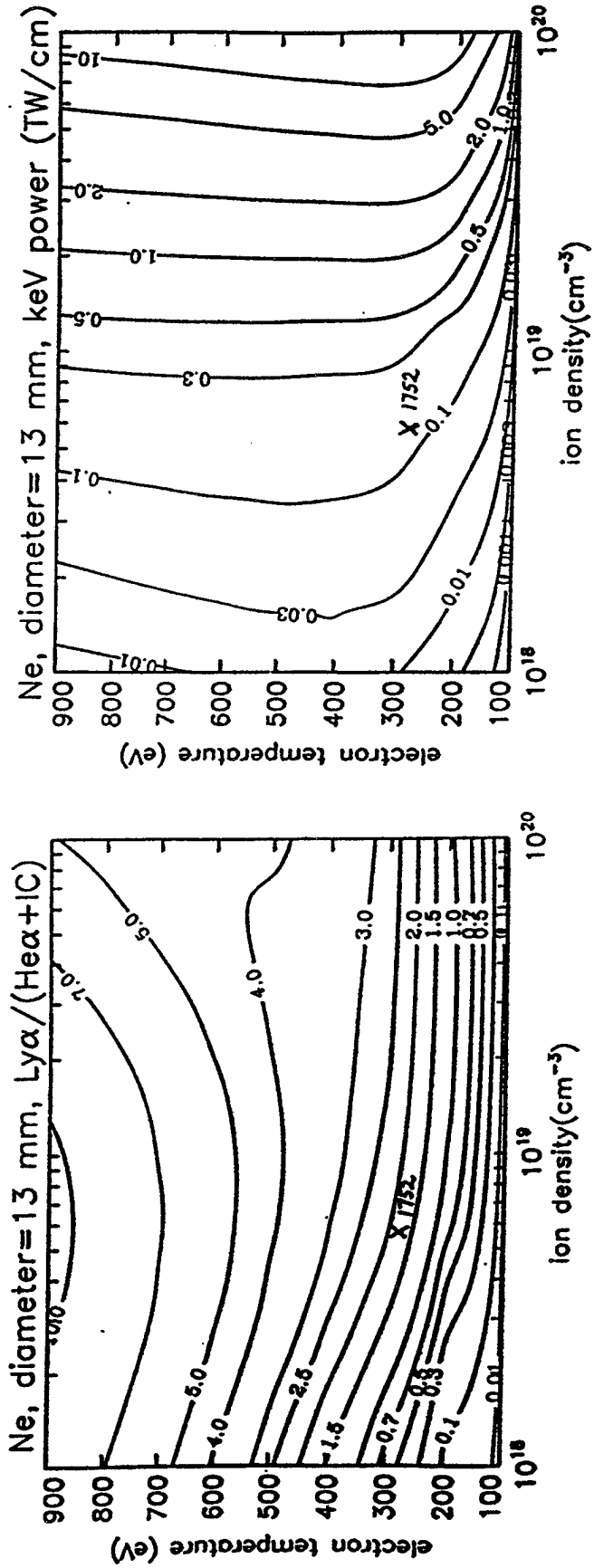

Fig. 16. Intersection of observed alpha line ratio and K shell power at the same point in temperature,density space to derive pinch conditions for ACE 4 tandem puff neon shot 1752.

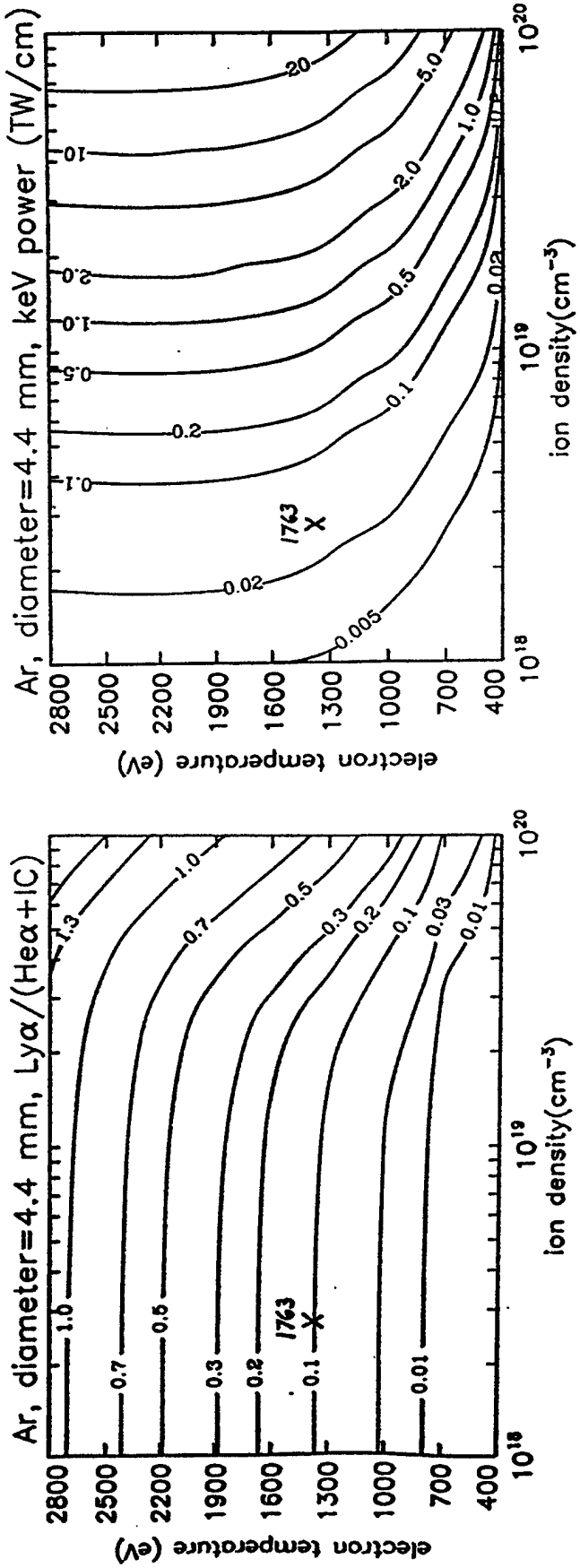

Fig. 17 Intersection of observed alpha line ratio and K shell power at the same point in temperature,density space to derive pinch conditions for ACE 4 tandem puff argon shot 1763.

III. ATOMIC MODEL DEVELOPMENT FOR L-SHELL TITANIUM

An adequate physical description of the dynamics of ionization and x-ray production requires an extensive amount of work in generation of databases. Detailed diagnostic studies, employing these databases for ions in the K-shell that are of interest as PRS (Plasma Radiation Sources) for Z-pinch experiments[1, 2] can then be carried out. These databases have also been used to develop K-shell emission scaling relationships. In order to better understand the plasma dynamics of x-ray scaling, analysis of emission in the L-shell region is important. This analysis not only provides insights into the plasma PRS dynamics outside of the K-shell region, but also helps to better understand how the K-shell emission behavior is influenced by the L-shell emission. The extension of K-shell diagnostic capabilities to L-shell for higher Z elements entails extra efforts because of the complex multiplet structure of L-shell ionization stages. However for any reliable diagnostics or determinations of scaling relationships using x-ray emission from L-shell ions, the populations of these large number of multiplet levels must be properly coupled together and determined accurately.

A procedure to self-consistently determine plasma parameters has been used by this Branch for titanium and other lower Z plasmas in the K-shell[1, 2]. The diagnostics capabilities have been employed to infer electron temperatures, ion densities, and mass fractions from K-shell line ratio and power output data from Z-pinch plasmas. The generalization of this K-shell diagnostic procedure to the L-shell of titanium plasma is under development. In the K-shell case, it is easy to filter out radiation below the K-series lines to measure K-shell powers, since there are no strong emissions from photon energies above the K-shell. For power output measurements of L-shell emission, one must filter out emissions from higher-lying ionization stages. Recently, using an extensive database for fluorine- and neon-like L-shell ionization stages in selenium, it was demonstrated that detailed diagnostic and scaling relationships[3, 4, 5] could be carried out with line ratios replacing L-shell powers.

These developments and diagnostics work now need to be carried out for Li-like and Be-like L-shell ionization stages since there is direct coupling to H-like and He-like ionization stages that one needs to take into account for the ionization calculations. We have thus begun work on the prototype atomic model specifically for Li-like and Be-like ionization stages that is necessary for analyzing and performing diagnostic work on highly resolved x-ray emission from these ionization stages.

Figure 1 shows the energy level diagram of the model containing the multiplet structure for the Li-like and Be-like ionization stages of titanium. The Be-like ionization stage, Ti XIX contains 18 levels including: the $1s^22s^2$ ground level, 2 Δn=0 $1s^22s2p$ and $1s^22p^2$ excited states, the 10 fine-structure levels of the n=3, $2s3s$, $2s3p$ and $2s3d$, configurations, 3 lumped inner-shell n=3 configurations, $2p3s$, $2p3p$, and $2p3d$, one lumped n=4 states and one lumped level of n=5,6, and 7 states. Similarly the Li-like stage, Ti XX contains 9 levels including the ground $1s^22s$ state, the Δn=0 $1s^22p$ excited state, the 5 fine-structure levels $1s^23s$, $1s^23p$, and $1s^23d$ configurations of the n=3 manifold, one lumped n=4 states and one lumped level of the n=5,6, and 7 states. All the excited levels, including the n=3 multiplet levels are coupled to the ground state as well as among themselves.

The atomic data for this calculation was generated using very detailed and accurate atomic codes. All level energies and oscillator strengths and radiative decay rates for transitions from the excited to the ground level as well as among all the excited levels were

calculated using the Relativistic Distorted Wave (DFW) structure code[6]. This involves the calculation of 27 energy levels and 328 oscillator strengths and radiative transition rates. Electron-impact collision strengths and cross-sections for excitation from the ground to all the excited states and the collision coupling among all the excited Li-like and Be-like levels were calculated by using the Relativistic Distorted-Wave (RDW) collisional codes of Refs. [6, 7, 8, 9]. These collisional data are obtained by using three separate codes which produce fully relativistic, state of the art collision strengths at the fine-structure levels.

Dielectronic recombination (DR) data for recombination from Ti XXI to the singly excited states of Ti XX and from Ti XX to the singly excited states of Ti XIX were calculated using the Hartree-Fock with Relativistic (HFR) method of R. D. Cowan[10]. Detailed calculations were carried out for DR branching ratios and rates from the ground state of Ti XXI and ground and Δn=0 states of Ti XX to each specific fine structure levels of Ti XX and Ti XIX respectively. Since the DR process proceeds via electronic capture to autoionizing doubly excited (DBEX) states which eventually stabilize by radiative decay to the recombined states, it is necessary to include a large number of these DBEX states. The DR data generation involve hundreds of energy levels of singly and doubly excited levels as well as autoionization rates and radiative rates from these DBEX states. For low lying DBEX states, DR branching ratios were explicitly calculated, while for higher Rydberg states, a $1/n^3$ falloff extrapolation of these ratios were employed, where n stands for the principal quantum number of the Rydberg electron.

Electron impact ionization from the ground as well as all the excited states of Ti XX and Ti XIX levels can be calculated relativistically from the RDW ionization codes of Refs. [11, 12] which also consists of three separate atomic codes. The radiative recombination rates can also be calculated in future by detailed balancing the photoionization cross sections which can be obtained using a modified version of Cowan's code called, CATS[13] and another code called GIPPER[14]. Collisional-Radiative Equilibrium solutions to a fully coupled single set of rate equations will be generated by post processing these data to obtain the ionization dynamics.

It is apparent that in future high-current driven Z-pinch experiments, for example, involving medium to high Z plasmas, rapid "burn through" in the L-shell is required to generate K-shell ions. This burn-through is inhibited by L-shell radiation losses[15], and when calculating this effect, a detailed level accounting cannot be simplified by an averaging process such as used in the average atom model, which will inhibit all the important and relevant atomic radiation dynamics and render diagnostic work impossible. Thus for any non-LTE diagnostics studies where high densities are achieved and the excited states are collisionally coupled, an atomic model such as ours which include all dominant atomic processes to all the important levels are absolutely essential.

References

[1] M. C. Coulter, K. G. Whitney, and J. W. Thornhill, J. Quan. Spectro. Radiat. Trans. **44**, 443 (1990).

[2] J. P. Apruzese, K. G. Whitney, J. Davis, and P. C. Kepple, J. Quant. Spectrosc. Radiat. Transfer (in press).

[3] A. Dasgupta and K. G. Whitney, Phys. Rev. A **42**, 2640 (1990).

[4] A. Dasgupta and K. G. Whitney, At. Data Nucl. Data Tables **58**, 77 (1994).

[5] A. Dasgupta, K. G. Whitney, H. L. Zhang, and D. H. Sampson, Phys. Rev. E (1996) (in press).

[6] D. H. Sampson, H. L. Zhang, A. K. Mohanty, and R. E. H. Clark, Phys. Rev. A **40**, 604 (1989).

[7] H. L. Zhang, D. H. Sampson and A. K. Mohanty, Phys. Rev. A **40**, 616 (1989).

[8] D. H. Sampson, H. L. Zhang, and C. J. Fontes, At. Data Nucl. Data Tables **48**, 25 (1991).

[9] H. L. Zhang and D. H. Sampson, Phys. Rev. A **47**, 208 (1993).

[10] Atomic structure code of R. D. Cowan following his book it The Theory of Atomic Structure and Spectra (University of California Press, Berkeley, CA, 1981).

[11] H. L. Zhang and D. H. Sampson, Phys. Rev. A **42**, 5378 (1990).

[12] D. H. Sampson and H. L. Zhang, Phys. Rev. A **45**, 1657 (1992).

[13] J. Abdallah, Jr., R. E. H. Clark, and R. D. Cowan, *Theoretical Atomic Physics Code Development I. CATS: Cowan Atomic Structure Code*, Los Alamos National Laboratory manual (December 1988).

[14] R. E. H. Clark and J. Abdallah, Jr., *unpublished.*

[15] J. Davis, J. L. Giuliani, Jr., and M. Mulbrandon, Phys. Plasmas **2**, 1766 (1995).

Titanium L-Shell Energy Level Diagram

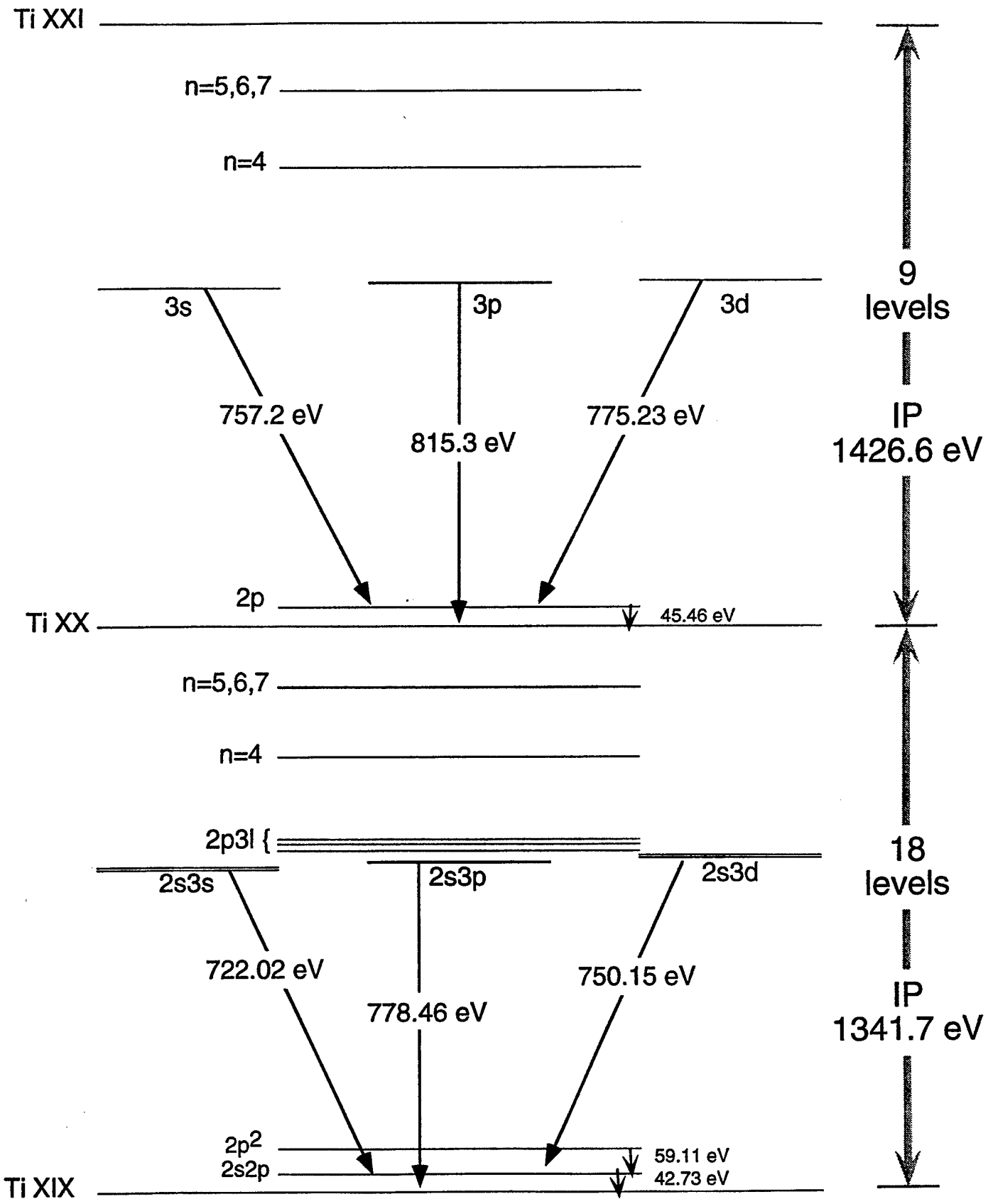

Fig. 1

IV. LONG TIME IMPLOSIONS ON THE DECADE QUAD

The radiative performance of PRS loads on the DECADE QUAD (DQ) was investigated for a number of gas puff loads with implosion times between 200 and 300 ns. The loads are 4 cm in length and are configured as uniform fills with an outer radius that extends out to 6 cm. The numerical simulations were carried out using 1- and 2-D RMHD models with varying degrees of sophistication. 2-D MHD PRISM simulations exhibit surface rippling due to the onset of the Rayleigh-Taylor (RT) instability at $R_0 \sim 3.6$ cm. For values of R_0 in excess of 3.6 cm the RT instability grows exponentially causing the plasma to lose its integrity giving rise to a highly corrugated outer surface exhibiting the classical spike and bubble features so characteristic of a well defined RT instability. Although it has yet to be firmly established that RT unstable plasmas are poor radiators at all wavelengths we will adopt conventional wisdom and assume that unstable plasmas do not radiate as efficiently as stable plasmas in the energy regime of interest here. Therefore, the radiative K-shell results predicted for $R_0 > 3.6$ cm should be considered optimistic.

Numerical simulations were performed for an argon gas puff driven by a DQ transmission line. The equivalent circuit for the DQ is shown on Figure 1. The resistance of 0.25 ohms is under investigation and will be settled once a DQ final design is agreed upon. A typical current profile showing both the peak short circuit current and the load current driving an argon gas puff is shown as a function of time on Figure 2. The peak short circuit current reaches a maximum value of about 7.6 MA while the load current reaches a maximum value slightly in excess of 5.0 MA at about 280 ns. For an argon gas puff load 4.0 cm long and an outer radius of 3.6 cm with a total mass of 1.8 mg the behavior of the load current and the outer radius as a function of time is shown on Figure 3. This implosion has a compression ratio of 10 and an implosion time of 280 ns.

The neon K-shell radiative yield is plotted on Figure 4 as a function of outer radius and total mass; for $R_0 \sim 3$ cm and $M_0 \sim 1.0$ mg the K-shell yield of about 128 kJ is predicted. The total radiative yield as a function of total mass and outer radius is shown on Figure 5. For values of the outer radius between 2 and 3 cm and a total mass between 1 and 3 gm the total yield is very impressive with values in the 240kJ range. The L-shell

accounts for nearly half of the total yield. Although neon is easy to light up from an energetic point of view this total yield is still excellent. Figure 6 shows the K-shell yield for a 50/50 mix by number density of neon and argon. The K-shell yield is about 25 kJ for outer radii between 2 and 3 cm and total masses between 0.1 and 1.0 gm. The argon exists in sufficient quantity that the bulk of the K-shell yield originates from the argon; about 17 kJ from argon and 8 kJ from neon. The total yield is displayed on Figure 7 and is due to both the neon and argon in roughly equal amounts.

For pure argon the results are shown on Figure 8. At about 3 cm radius, which is considered a stable regime, and 0.32 mg the K-shell yield is greater than 30 kJ. This yield is of the same order of magnitude imposed by the DSWA in order that DQ satisfy the Agency requirements. The total yield (Fig. 9) for $R_0 < 3.0$ cm and for masses extending from 0.5 to 3.2 gm is about 250 kJ, a very impressive yield indeed, nearly all from the L-shell of argon. By comparison Double Eagle imploded an aluminum wire array with about 4 MA of current and generated about 150 kJ of L-shell radiation. DQ could be a superb PRS facility by comparison.

In summary, a series of numerical simulations have been performed for long time imploding uniform fill loads composed of neon, neon/argon, and argon over a range of parameters representing stable implosions and produced encouraging yields. However, additional research is required both to optimize the K-shell yields from uniform fills as well as a number of other density structured profiles and shell-like configurations. Also, since a detailed study has not been carried out in conjunction with experiments it would be useful and important to determine the influence of RT instabilities on the K-shell yield. The results of such an investigation would help define the limits on the outer radius and subsequently the implosion time for increasing the K-shell yields.

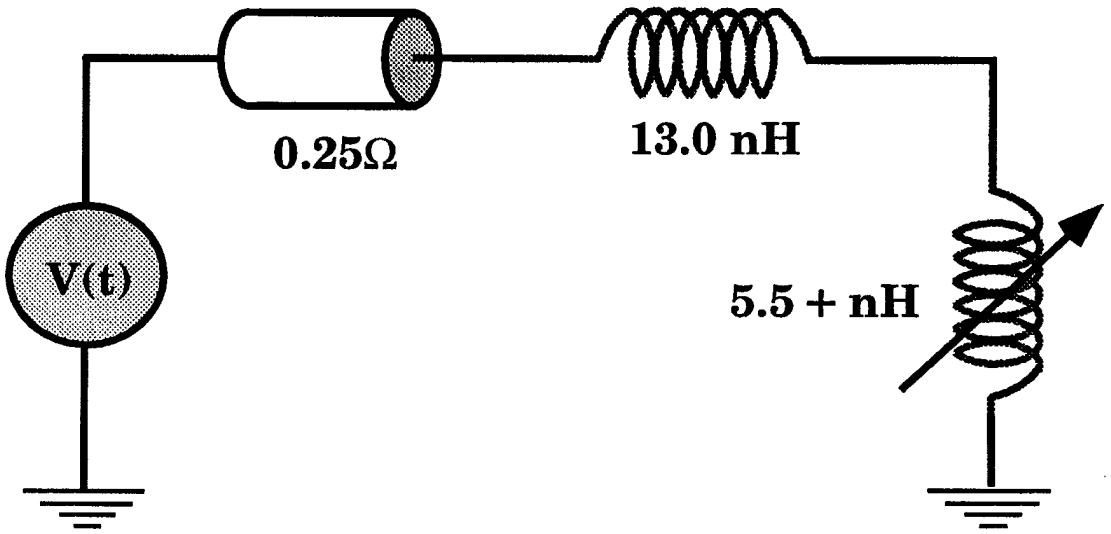

Decade Quad Equivalent Circuit (at the Post Hole Convolute)

Fig. 1

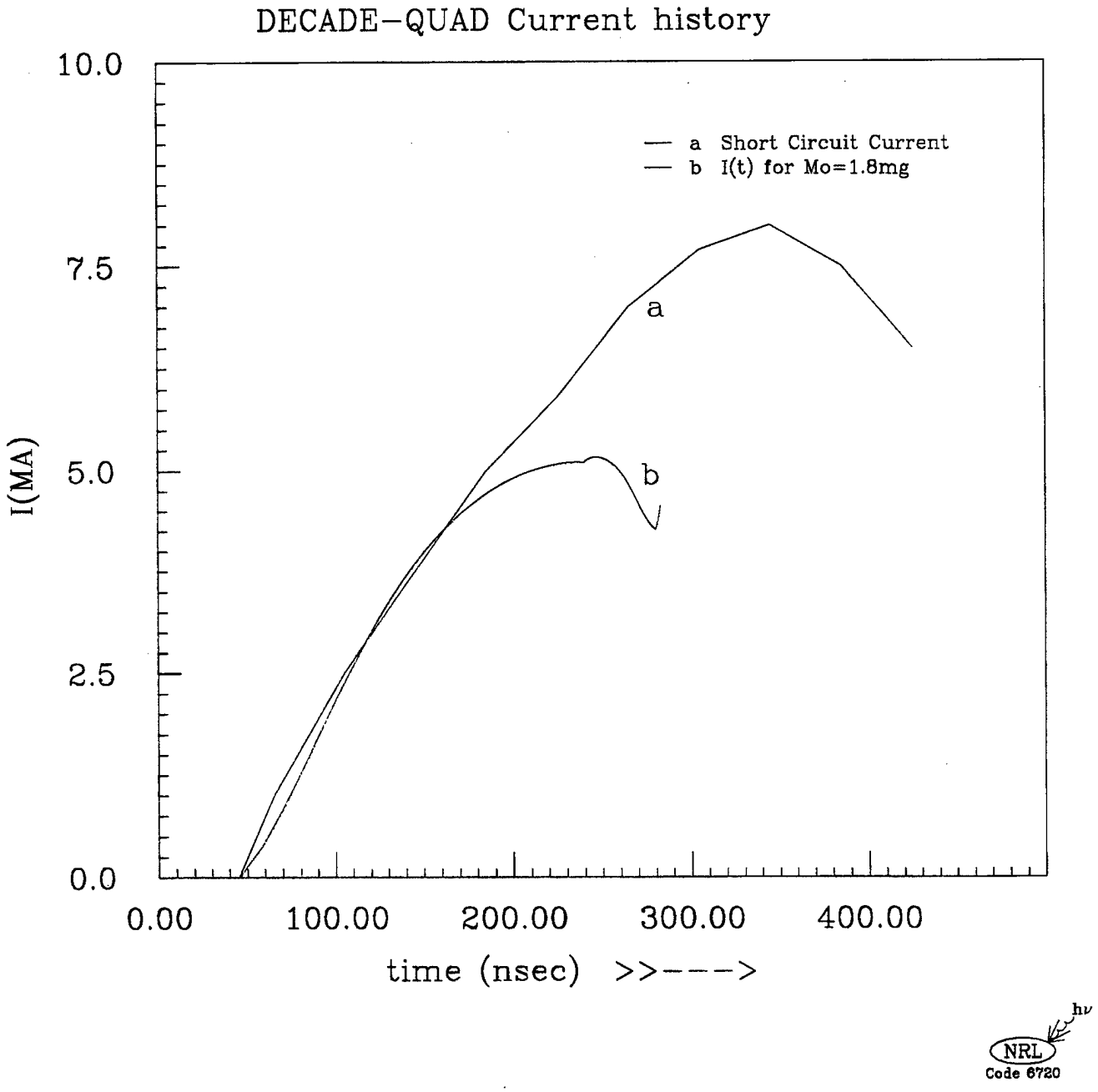
DECADE–QUAD Current history
10.0
7.5
5.0
2.5
0.0
I(MA)
— a Short Circuit Current
— b I(t) for Mo=1.8mg
a
b
0.00
100.00
200.00
300.00
400.00
time (nsec) >>---->
hν
NRL
Code 6720

Fig. 2

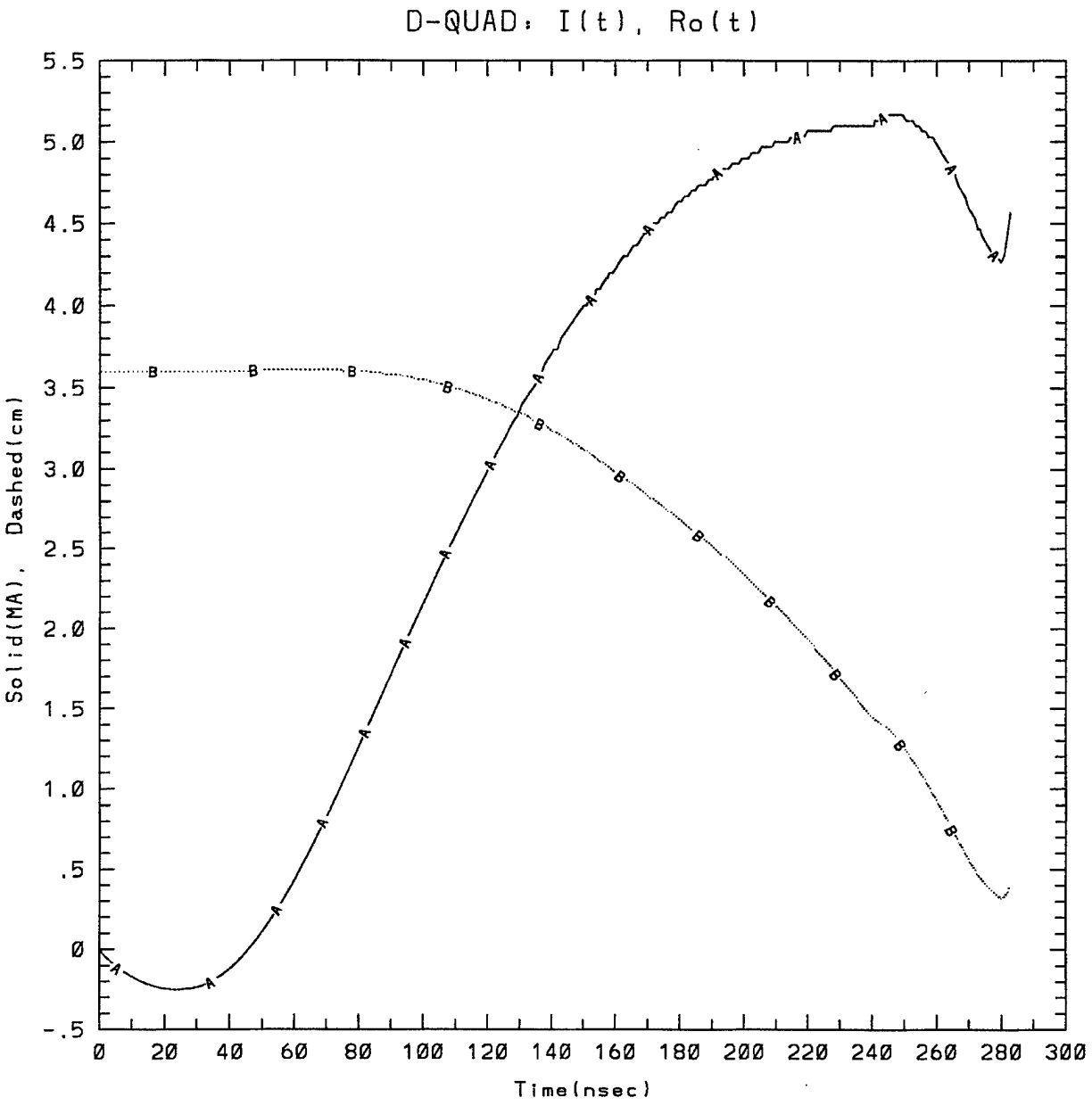
D-QUAD: I(t), Ro(t)
Solid(MA), Dashed(cm)
Time(nsec)
5.5
5.0
4.5
4.0
3.5
3.0
2.5
2.0
1.5
1.0
.5
0
-.5
0
20
40
60
80
100
120
140
160
180
200
220
240
260
280
300

Fig. 3

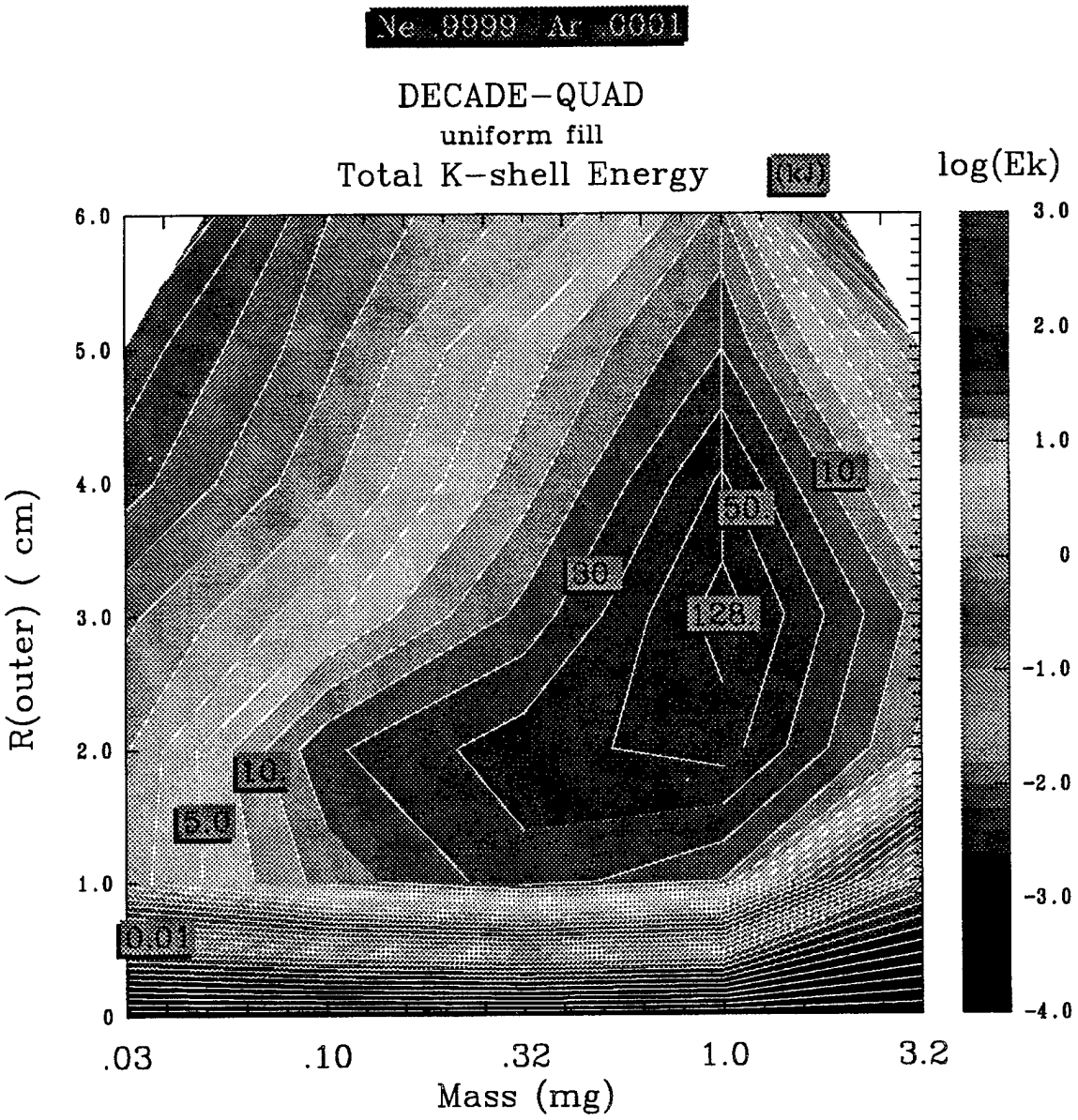
Ne .9999 Ar .0001
DECADE-QUAD
uniform fill
Total K-shell Energy
(kJ)
log(Ek)
3.0
2.0
1.0
0
-1.0
-2.0
-3.0
-4.0
6.0
5.0
4.0
3.0
2.0
1.0
0
R(outer) (cm)
.03
.10
.32
1.0
3.2
Mass (mg)
0.01
5.0
10.
30.
50.
128.
10.

Fig. 4

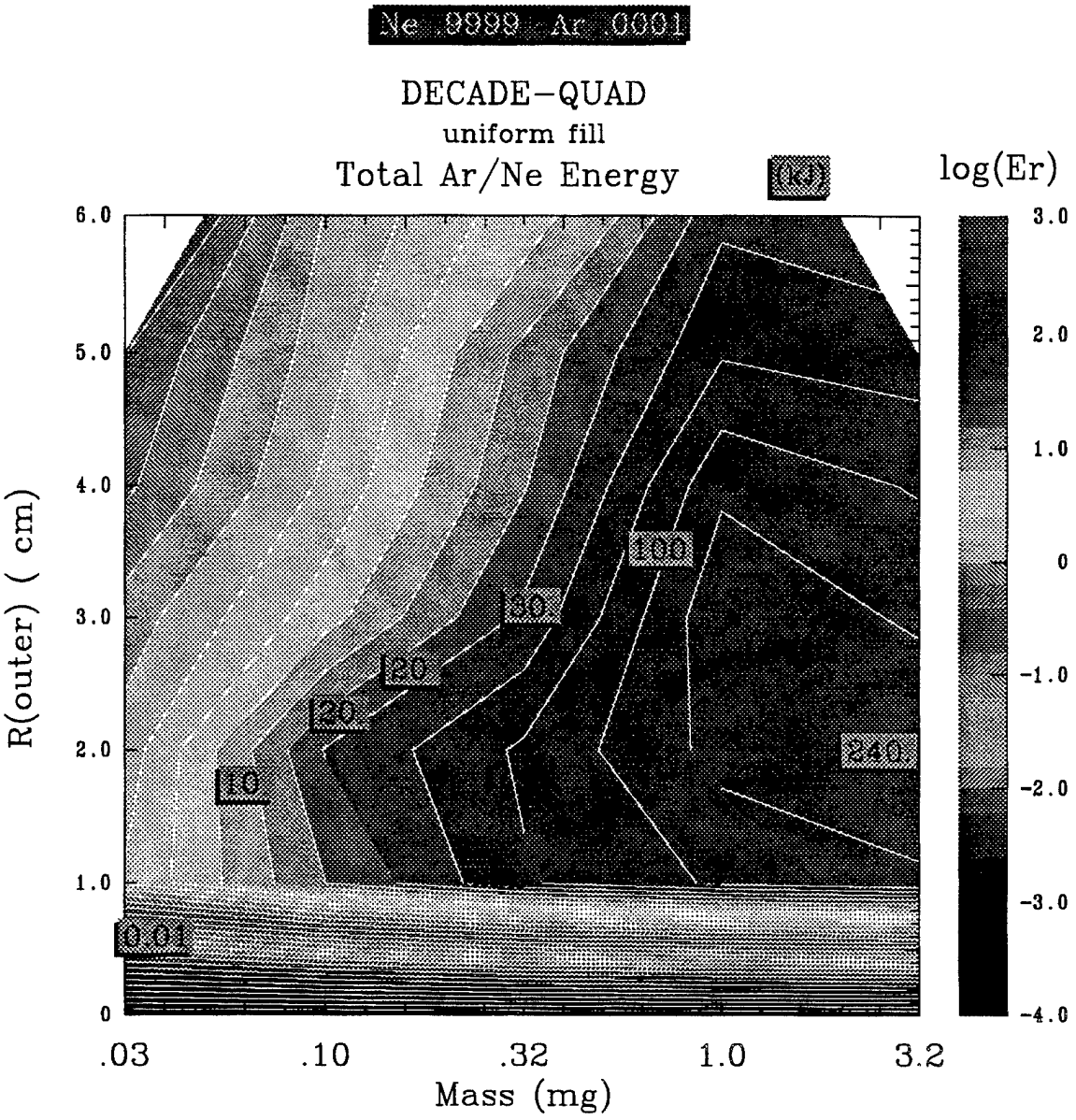
Ne .9999 Ar .0001
DECADE-QUAD
uniform fill
Total Ar/Ne Energy
(kJ)
log(Er)
R(outer) (cm)
Mass (mg)
6.0
5.0
4.0
3.0
2.0
1.0
0
.03
.10
.32
1.0
3.2
3.0
2.0
1.0
0
-1.0
-2.0
-3.0
-4.0
0.01
10
20
20
30
100
240.

Fig. 5

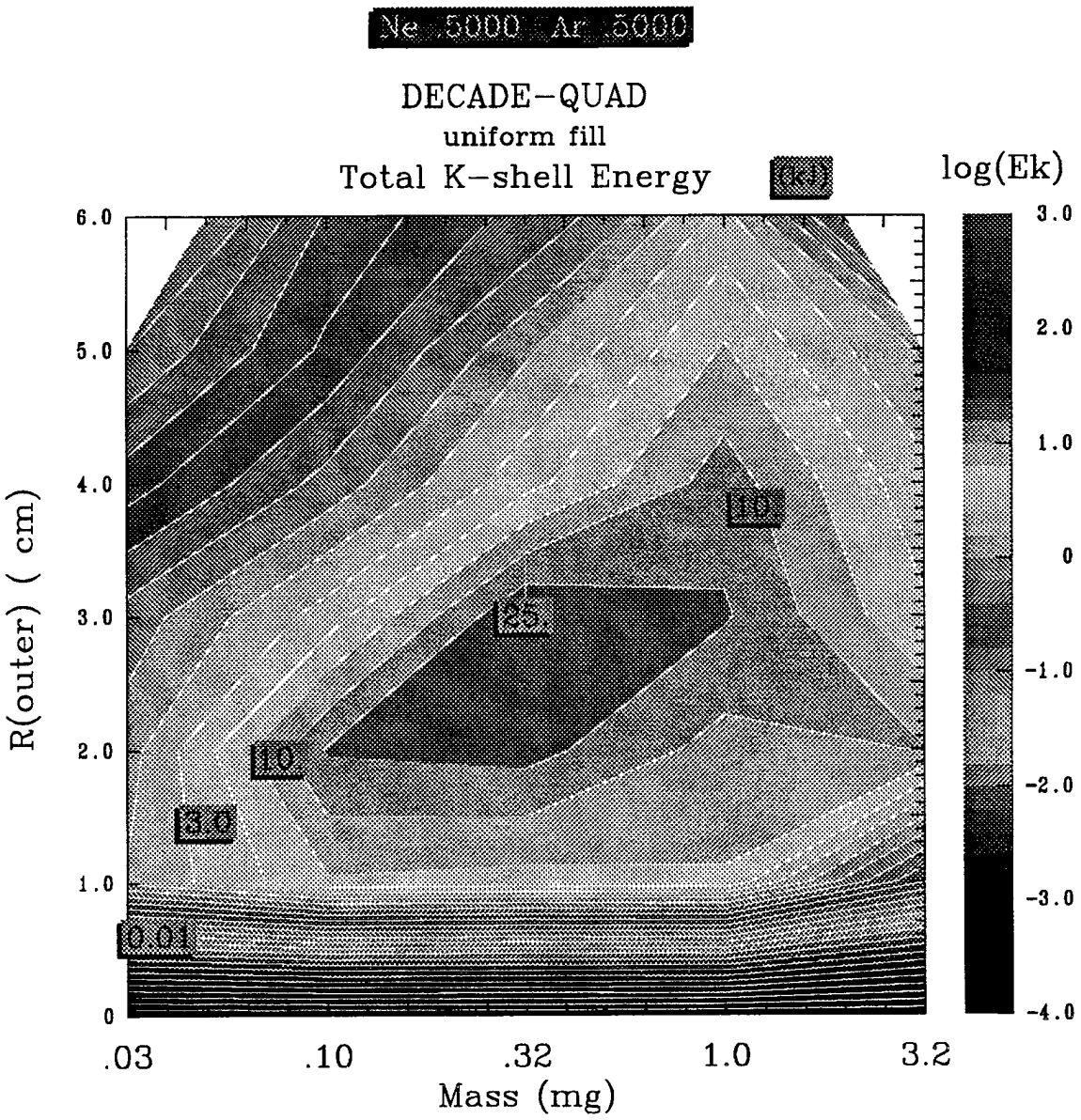
Ne .5000 Ar .5000
DECADE-QUAD
uniform fill
Total K-shell Energy
(k+)
log(Ek)
R(outer) (cm)
6.0
5.0
4.0
3.0
2.0
1.0
0
3.0
2.0
1.0
0
-1.0
-2.0
-3.0
-4.0
.03
.10
.32
1.0
3.2
Mass (mg)
0.01
3.0
10.
25.
10.

Fig. 6

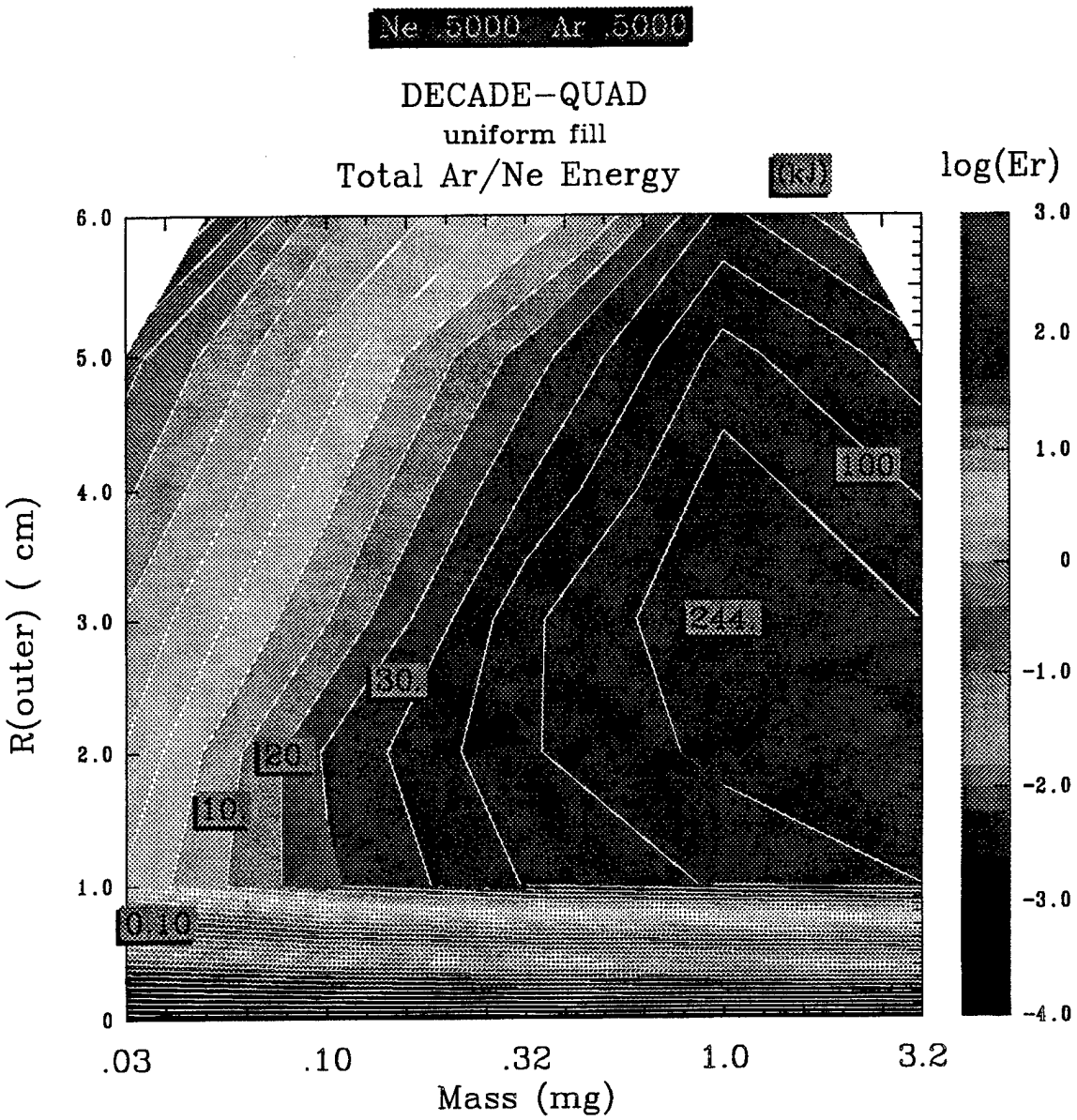
Ne .5000 Ar .5000
DECADE-QUAD
uniform fill
Total Ar/Ne Energy
(kJ)
log(Er)
3.0
2.0
1.0
0
-1.0
-2.0
-3.0
-4.0
6.0
5.0
4.0
3.0
2.0
1.0
0
R(outer) (cm)
100
244
30
20
10
0.10
.03
.10
.32
1.0
3.2
Mass (mg)

Fig. 7

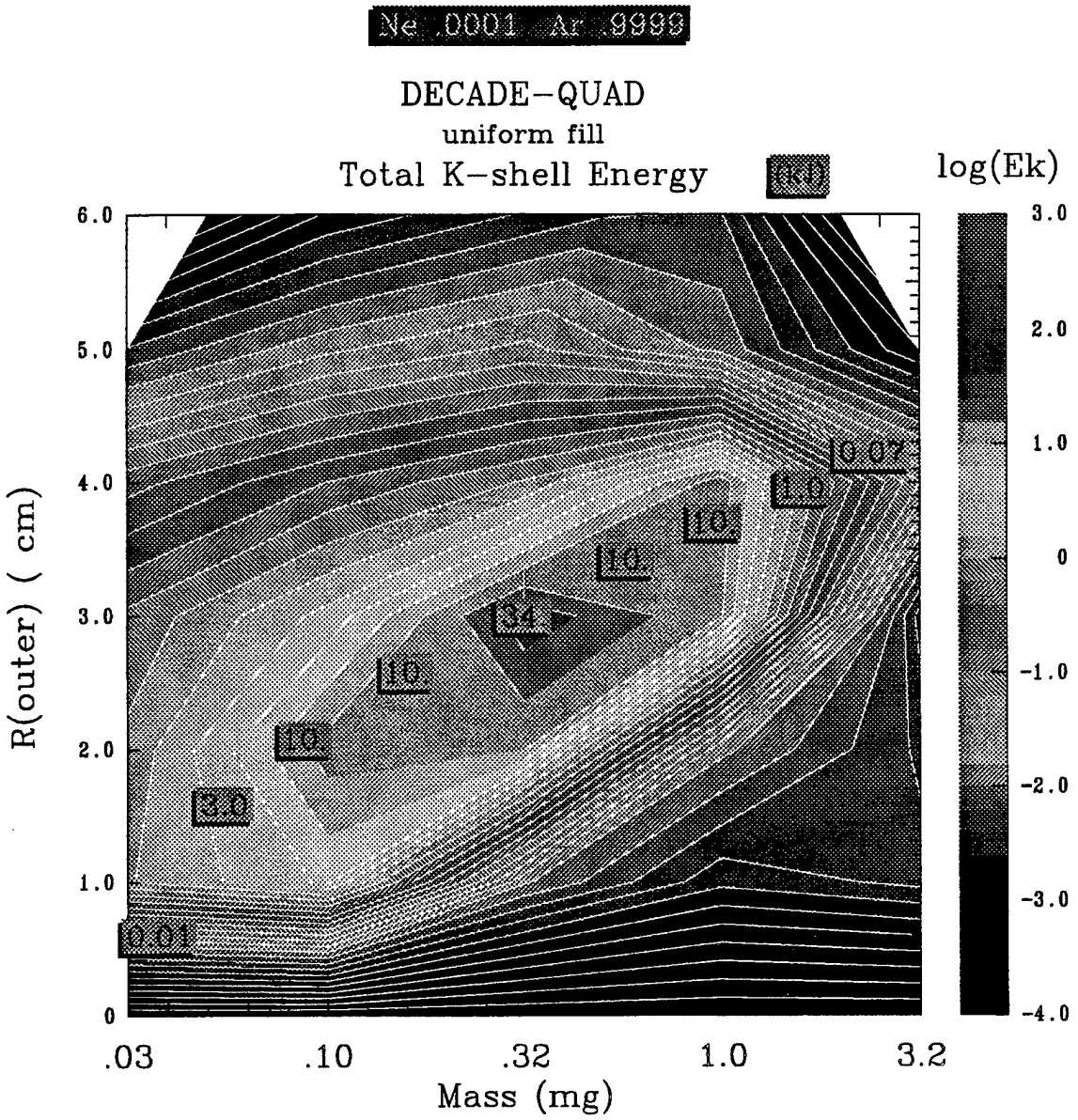
Ne .0001 Ar .9999
DECADE-QUAD
uniform fill
Total K-shell Energy
log(Ek)
R(outer) (cm)
Mass (mg)
6.0
5.0
4.0
3.0
2.0
1.0
0
.03
.10
.32
1.0
3.2
3.0
2.0
1.0
0
-1.0
-2.0
-3.0
-4.0
0.07
1.0
10.
10.
34.
10.
10.
3.0
0.01

Fig. 8

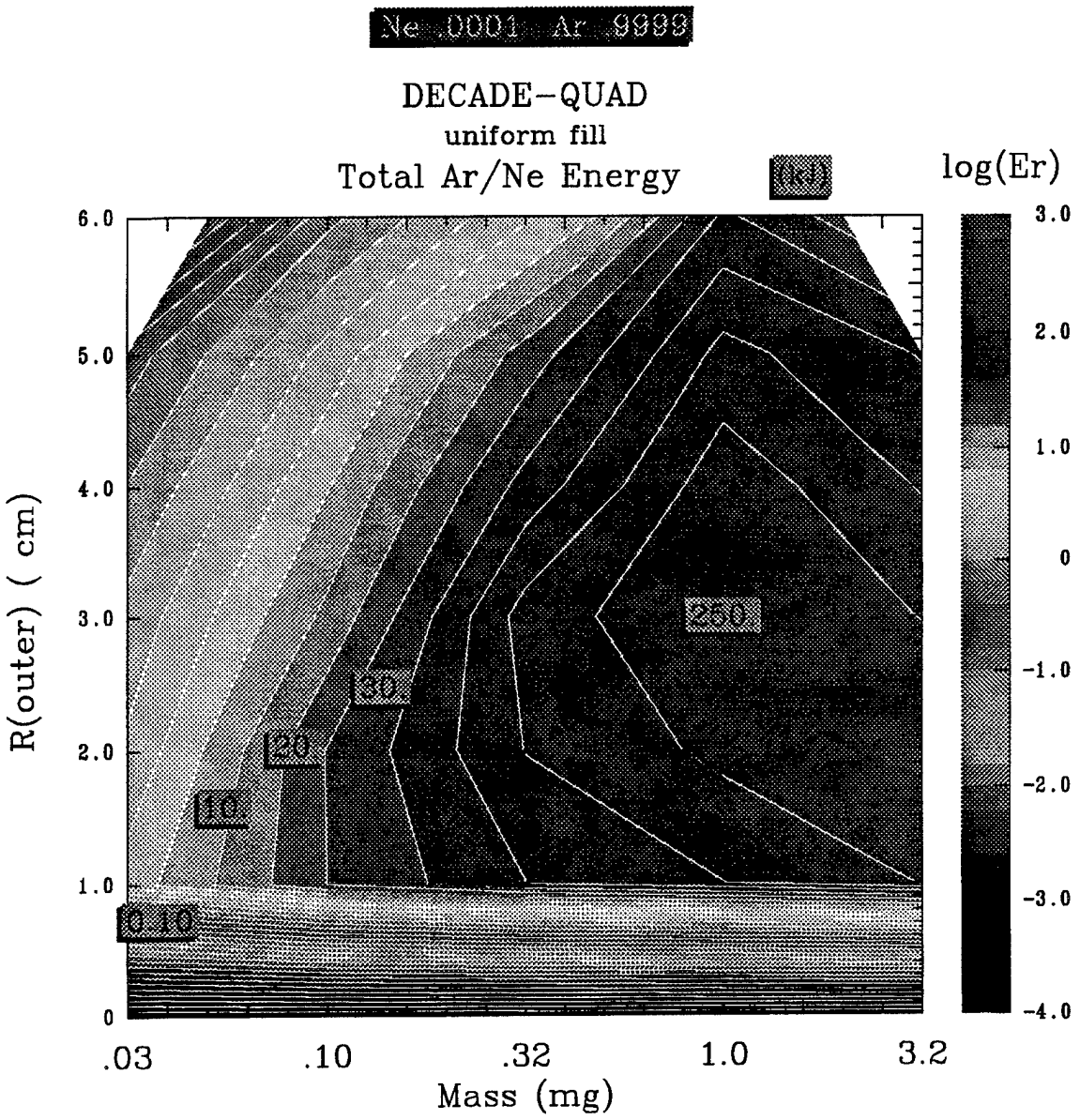
Ne .0001 Ar .9999
DECADE-QUAD
uniform fill
Total Ar/Ne Energy
(kJ)
log(Er)
R(outer) (cm)
6.0
5.0
4.0
3.0
2.0
1.0
0
3.0
2.0
1.0
0
-1.0
-2.0
-3.0
-4.0
250
30
20
10
0.10
.03
.10
.32
1.0
3.2
Mass (mg)

Fig. 9

V. ENERGY COUPLING TO THE PRS ON DECADE QUAD

The primary requirement in any DSWA program for a Decade Plasma Radiation Source (PRS) is an understanding of the machine's performance, the definitive characterization of that performance, and a documentation of strategies for the optimization of that performance. The present study addresses these goals by first constructing a complete model of the pulser and its puff gas load and then suggesting some pathways for improving the pulser's expected K shell x-ray yield.

The full transmission line model of the baseline design for the Decade Quad pulser includes all elements in the device, except for several divertors which aren't relevant until after the PRS has imploded. From the full model a numerical study of energy coupling into a dummy resistive load showed that an output impedance of about 0.325 Ω would minimize the reflected energy. Using the voltage waveform presented at the convolute at that match point, a Thevenin equivalent circuit was constructed for use in driving 1D and 2D radiation hydrodynamic models. The equivalent circuit can also be used to drive an abbreviated "Screamer" transmission line model, as well as other transmission line models used in earlier work.

Care has been taken to arrange model test points at proper locations in order to benchmark the numerical images of Decade with the experimental data derived from several physical voltage and current monitors along the pulse line if the machine is built in the tested baseline configuration, also cited below as the "conservative Schlitt design". With this configuration the best combinations of kinetic energy transfer and adequate mass for radiation are in the domain of 21.875 mgm cm^2 and a 5.0 cm initial radius. Realistically, the successful implosion of such a load is on the edge of feasibility even with some effective Raleigh Taylor mitigation in the design.

A. Baseline Power Flow Characterization

The baseline design point for Decade Quad comprises (i) a Marx bank, (ii) a water line transfer capacitor and switch, (iii) an output water line, (iv) an oil output line , (v) a vacuum insulator stack, (vi) a vacuum pulse forming line and coax to triplate transition, (vii) a triplate MITL and convolute, and (viii) a final disk feed and a load chamber. In this

representation all the elements upstream of the convolute have been assigned the appropriate parallel impedance of four identical elements.

i. Baseline Model Elements

The Decade Quad (DQ) model discussed first, Schlitt's conservative design, is not a

Table A.1 Decade Full Line Elements

Line Component	Delay Time [ns]	Impedance [Ω]	L or C [nH] or [nF]	**Monitor Name** Comments
Marx Capacitance	-	-	4,400	·
Marx Series Res.	-	0.0125	-	**Marx**
Marx Series Ind.	-	-	100	Voltage, Current
Trans Cap Tline	23.0	0.425	9.775	·
Trans Cap Tline	15.0	0.16	2.40	·
Divertor	-	-	-	optional
Trans Cap Tline	15.0	0.16	2.40	·
Trans Cap Shunt	-	7.5	-	·
Trans Cap Tline	6.0	0.20	2.00	·
Trans Cap Tline	75.0	0.078567	5.8925	·
Trans Cap Tline	10.0	0.20	1.20	·
Trans Cap Shunt	-	7.5	-	**Trans Cap**
Trans Cap Tline	5.0	0.20	1.00	Voltage
Divertor	-	-	-	optional
Trans Cap Tline	5.0	0.20	1.00	-
Trans Switch	935	1.0E6→ 0.0025	-	variable, τ_d 3 ns
Output Waterline	0.5	2.75	1.375	·
TTI Branch	250	5.15	1,287.5	Shorted Tline
Output Waterline	1.5	0.30	0.45	·
Output Waterline	61.5	0.125	7.6875	·
Output Waterline	-	-	-	optional
Output Waterline	9.5	0.12504	1.18788	·
Output Waterline	9.5	0.135	1.2825	·
Output Waterline	9.5	0.1375	1.30625	·
Output Waterline	9.5	0.150	1.425	·
Output Waterline	9.5	0.295	2.8025	·
Oil Tline	0.5	2.60	1.300	·
Oil Tline	0.5	1.695	0.8475	·
Oil Tline	0.5	0.925	0.4625	·
Oil Tline	0.5	0.9325	0.46625	·
Oil Tline	0.5	0.94	0.470	·
Oil Tline	0.5	0.95	0.475	**Oil Current**
Oil Tline	0.5	1.085	0.5425	·
Oil Tline	0.5	0.85	0.425	**Tube Voltage**
Oil Tline	0.5	0.875	0.4375	·
Oil Tline	0.5	5.20	2.6	Oil Vacuum Interface

Table A.1 (cont) Decade Full Line Elements

Line Component	Delay Time [ns]	Impedance [Ω]	L or C [nH] or [nF]	**Monitor Name** Comments
Vacuum PFL	0.5	2.925	1.4625	**Output Energy**
Vacuum PFL	2.0	1.525	3.050	·
Coax to Triplate	0.5	1.495	0.7475	·
Coax to Triplate	0.5	1.4625	0.73125	·
Coax to Triplate	0.5	1.4525	0.72625	·
Coax to Triplate	0.5	1.465	0.7325	·
Coax to Triplate	0.5	1.5025	0.75125	·
Coax to Triplate	0.5	1.485	0.7425	·
Triplate	1.5	1.4625	2.19375	·
Triplate	0.5	2.105	1.0525	·
Triplate	0.5	3.525	1.7625	Midplate
Disk	0.25	15.7	3.925	·
Stub	0.25	9.05	2.2625	·
PRS Load	·	·	5.50	**PRS monitors**

definitive one, but it describes a baseline design point utilizing the so-called "legacy" hardware from developments mostly focused to serve the bremsstrahlung source mode and its requisite plasma opening switch (POS). The model is complete, however, in that all relevant elements are described and all the power flow details upstream of the voltage monitors in the output oil line are modeled. In the table above, each element is assigned a lumped inductance or capacitance, while "delay time" usually refers to the signal transit time across an element; "impedance," to the local ratio of line voltage to line current; and τ_d, to the e-folding time of a variable element, usually a resistance. In the case of variable elements the "delay time" is the required offset from the time origin before variation in time begins. The existing test points are named and the waveform arising from them is listed. A transmission line diagram of the model is shown in Fig. V.A.1.

In analyzing the proposed device with respect to its probable PRS performance a well defined sequence of calculation is completed. First the data required to define an equivalent circuit are developed by replacing the model PRS with a purely resistive load. There will always exist an optimum impedance for this dummy load which reflects the least power and energy back upstream. Once that optimum is established the device can be modeled by its (Thevenin) equivalent circuit at any node upstream of the load. Next a matrix of slug PRS

FIG. V.A.1 FULL DECADE || LINE MODEL

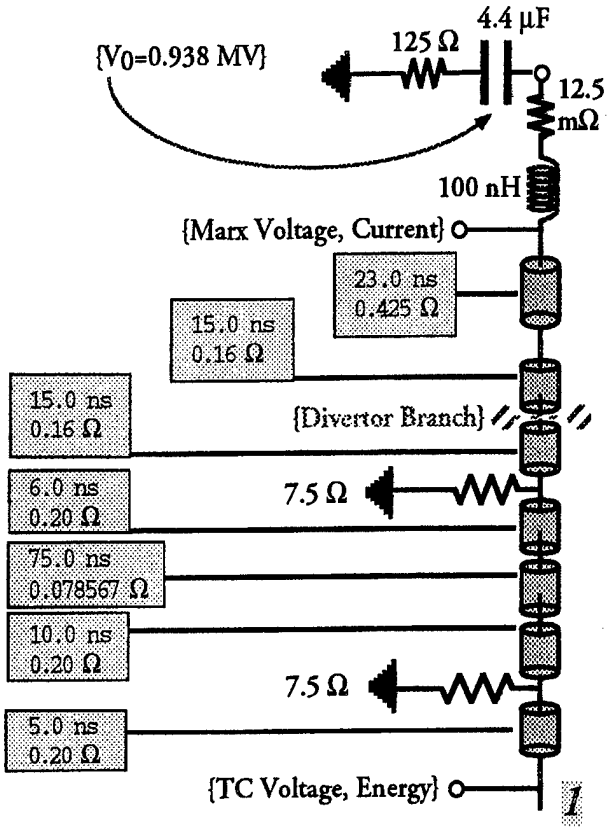

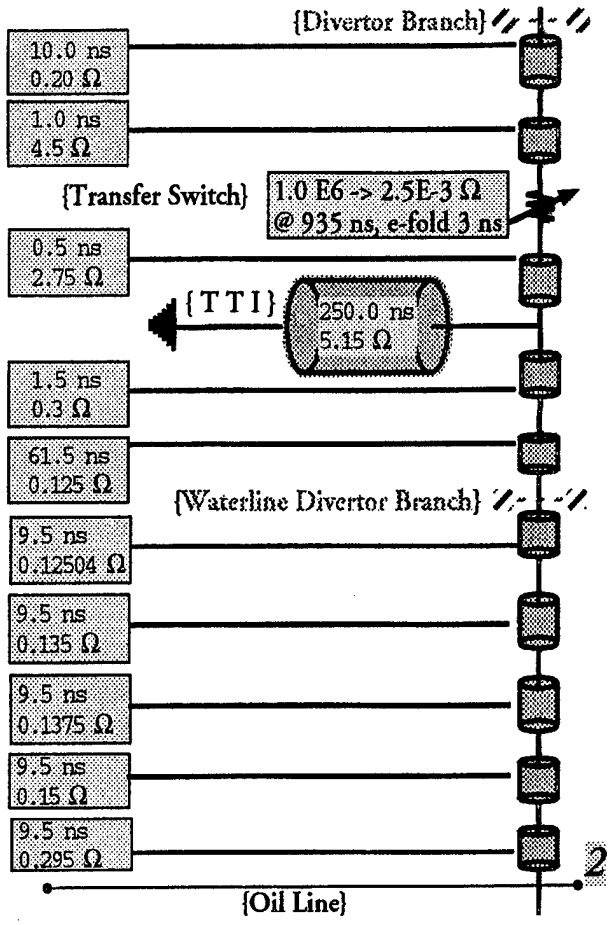

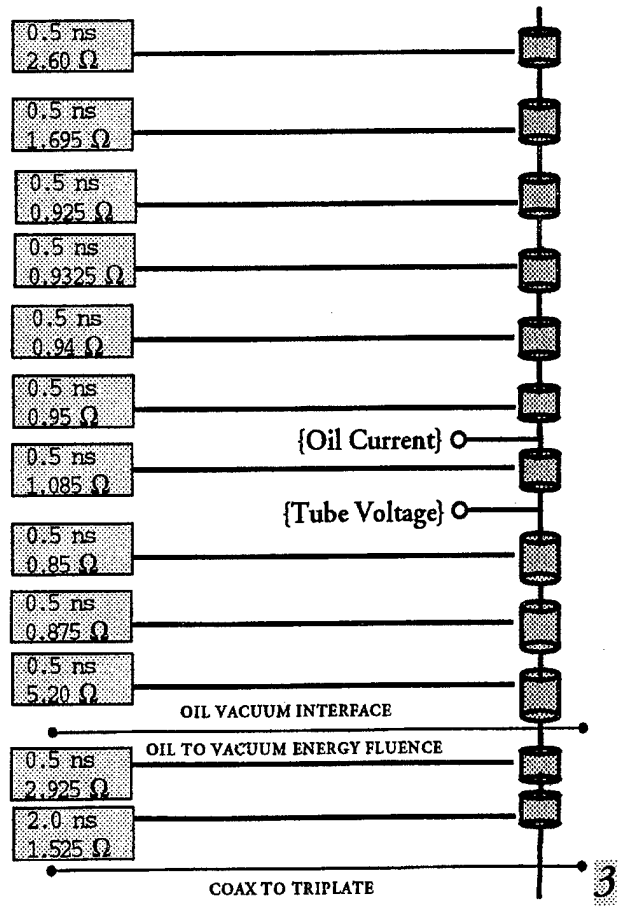

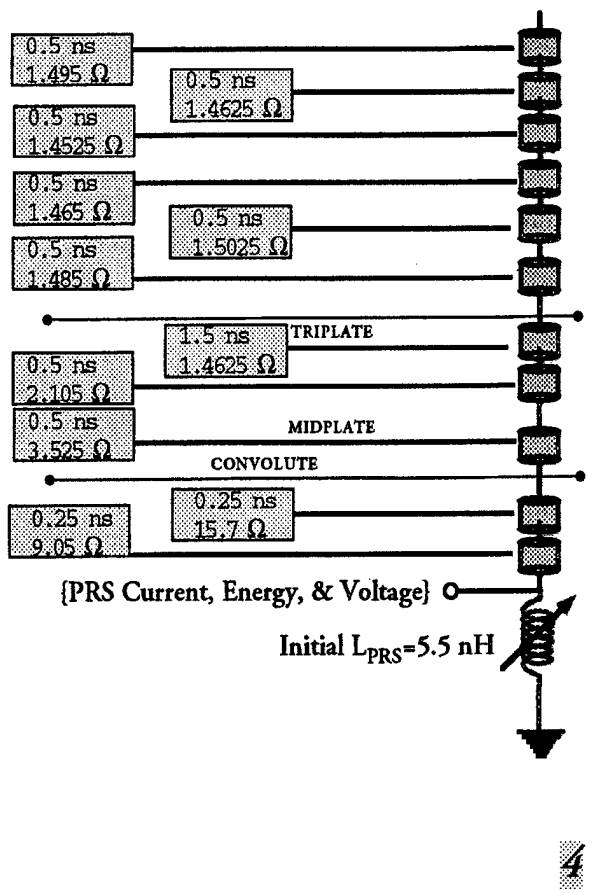

loads at various implosion times and initial radii develops a complete picture of dynamic load coupling to the full device or to its equivalent circuit.

ii. Equivalent Circuit

The resolution of an optimum load impedance for the Decade Quad is straightforward in that one need only vary the resistive load impedance over a given range [0.5$\mu\Omega$ to 5.0MΩ] and examine the energy accumulated in the dummy load at the end of the output pulse [1.5 μs]. Using the baseline listing shown above, a summary of model behavior in such a calculation is shown in Fig. V.A.2. In that figure currents and voltages are on the left ordinate, while accumulated energies are on the right. The Marx current is brought to zero just as the output switches begin to send power to the load. Here at the match point, all current monitors: tube, post hole convolute (phc), and load, track closely to a 3.2 MA peak value. The calculation predicts a peak energy transfer of 613.41 kJ into the 0.325 Ω load — about 60 % of the energy available out of the transfer capacitor. If the load impedance is varied, the relatively broad optimization shown in Fig. V.A.3 is obtained, with about 2/3 of the peak energy available over a full order of magnitude in load impedance. As discussed in more detail below, PRS loads do not generally present impedances of even 0.1 Ω until after the current has begun its so-called inductive notch. The higher optimum impedance for energy transfer has serious implications for the utility of a PRS on the baseline device, although it is certainly not the highest impedance among various DSWA pulsers, c.f. Phoenix at 0.9 Ω.

A similar impedance can be inferred from a comparison of open circuit voltage and short circuit current, as shown in Fig. V.A.4. Separate calculations for a short circuit load and an open circuit load are overlaid during last 500 ns of the pulse. The appropriate choice of an equivalent circuit impedance from the time dependent waveforms is not so compelling and represents a somewhat subjective judgement. An examination of the circuit might also lead to the assumption that the long output water line element [$\approx$70 ns and 0.125 Ω] just downstream of the transit time isolator would operate effectively as a voltage source at the cited impedance. Using this 0.125 Ω driver would be a significant error with respect to energy coupling computations — the equivalent circuit would match to the constructed impedance rather than the true optimum of Fig V.A.3.

FIG. V.A.2 DECADE QUAD
SCHLITT'S CONSERVATIVE @ 325 mΩ Dummy Load

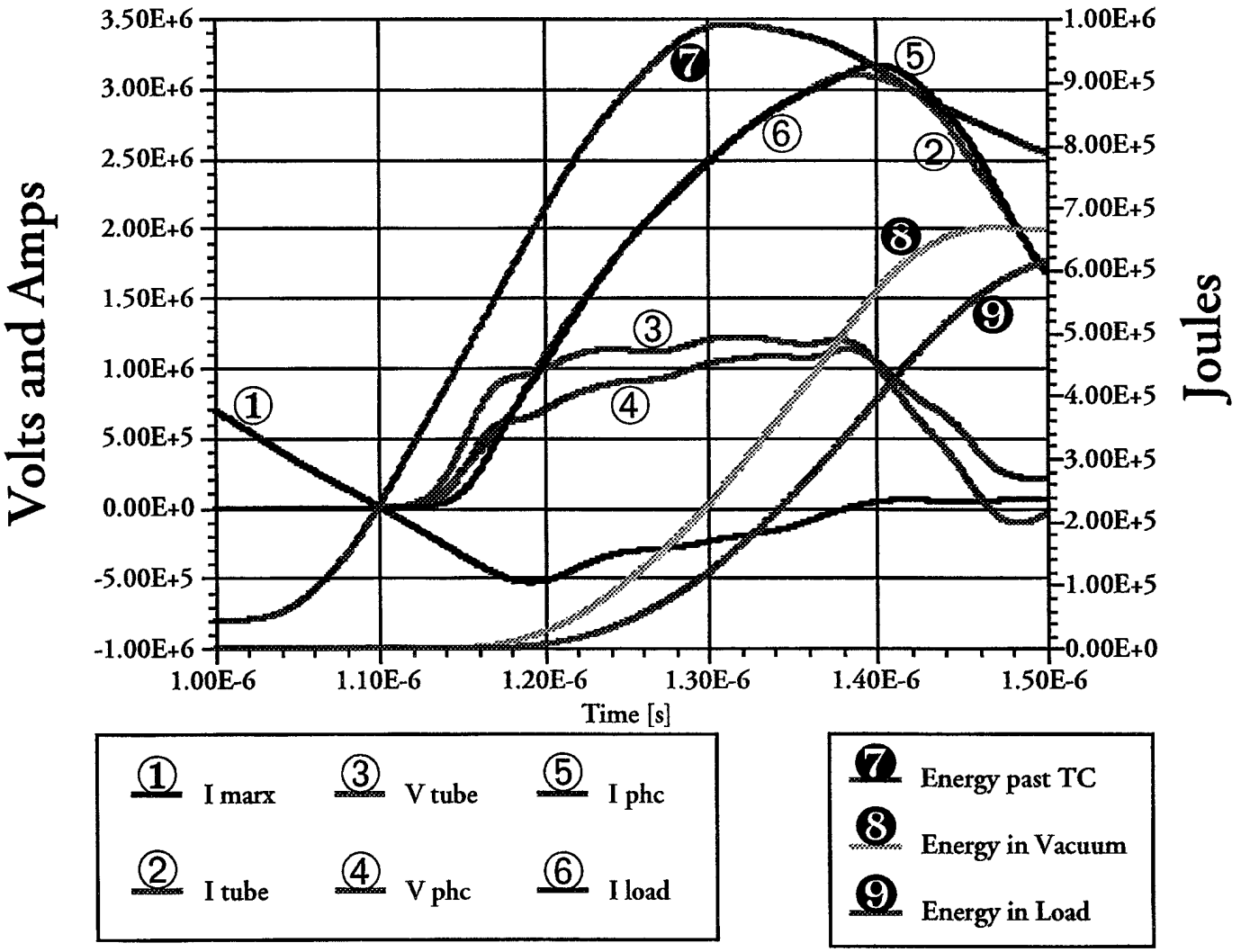

FIG. V.A.3 DECADE QUAD —
SCHLITT'S CONSERVATIVE, MATCHING @ 325 mΩ

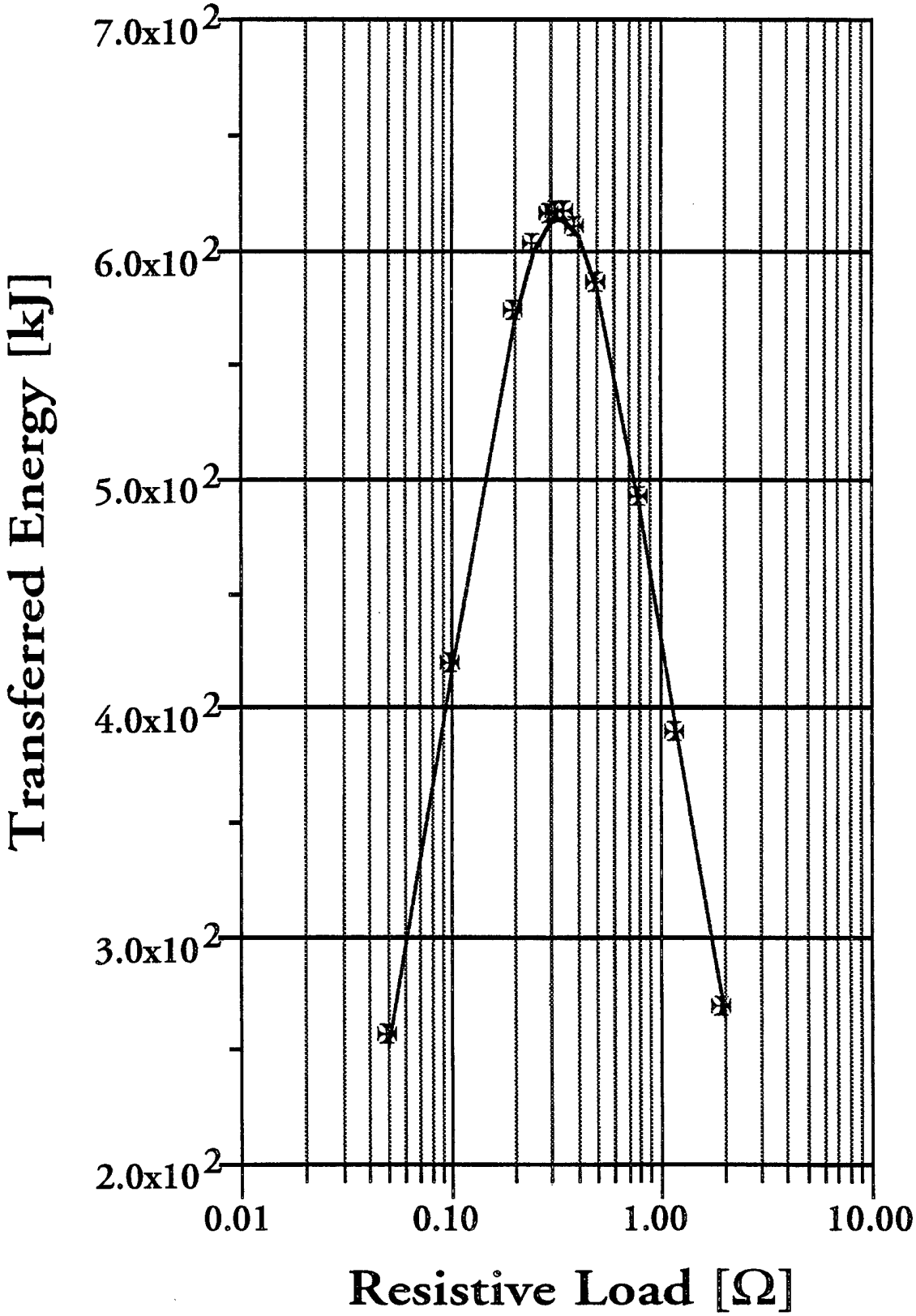

FIG. V.A.4 DECADE QUAD, SCHLITT'S CONSERVATIVE DESIGN — MATCHED LOAD WAVEFORMS

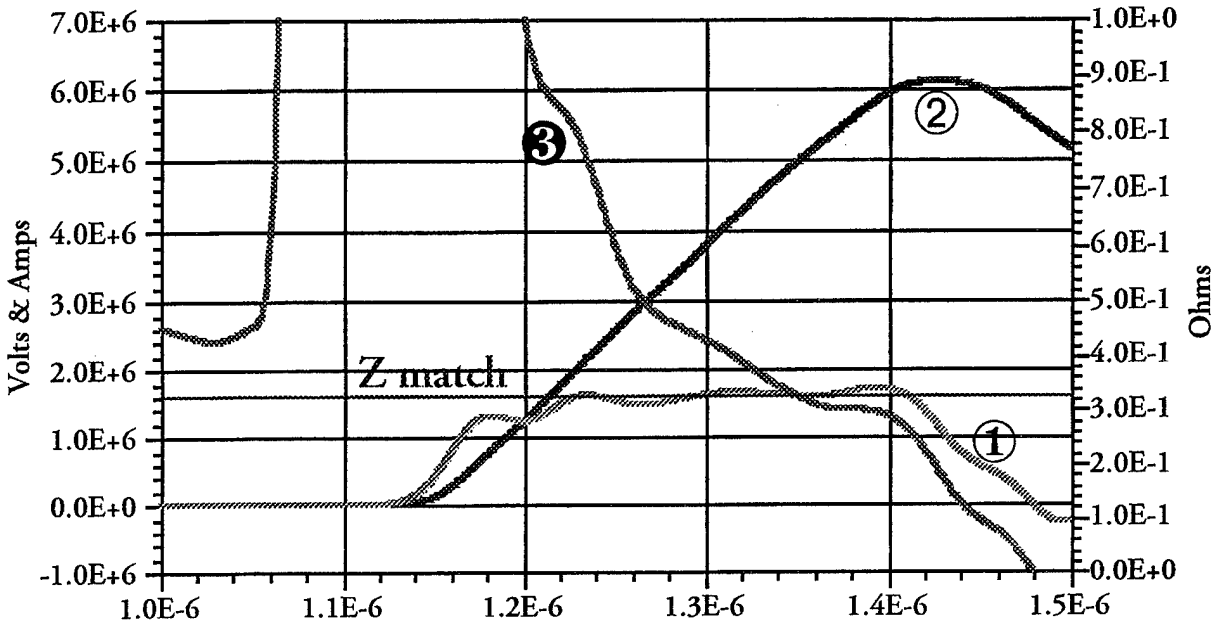

① PHC V_{open}

② PHC I_{short}

③ $Z_{effective}=V_{open} / I_{short}$

For an accurate representation of the baseline Decade Quad, the equivalent circuit shown in Fig. V.A.5a is clearly the best choice. The driver waveform, cf. Fig. V.A.5b, is inferred from the post hole convolute, close to the load, and the equivalent resistance of 0.325 Ω will force an exact match at that impedance to the Screamer model from the convolute on downstream. Within the limitations of such Thevenin equivalents, the simplified circuit will mimic the energy transfer characteristics of the complete model for dynamic loads like the PRS which spend most of their life away from the matching impedance.

iii. PRS Models

In the present context the PRS model available in the Screamer code shall be the basis for comparisons among various mass loadings and power flow events or modifications. This particular PRS model is quite primitive, even for a 0D formulation, but it is equipped with a general scaling rule for PRS output which distills many years of effort into a relatively straightforward calculation. On the basis of accumulated kinetic energy in an imploded slug of material of specified mass and length, the expected yield from any of several commonly used atomic species is computed over the active rundown time. This scaling law is accurate within about a factor of 2 for reasonable 1-D implosions, except for the low η regime where any scaling is questionable.

The slug dynamics is also modified to include the possibility of a twist in the return current rods so as to generate a moderate axial magnetic field component. When such a twist is added, it is the number of turns per unit length, N [m^{-1}], which parameterizes the axial field strength for any inserted level of current. The foil acceleration, motional impedance, and mechanical impedance are changed according to

$$\ddot{R} \propto -\left[1/R + (2\pi N)^2 R\right] I^2$$

$$Z_{motion} \propto -\left[\dot{R}/R + (2\pi N)^2 \dot{R}R\right]$$

$$Z_{mechanical} \propto \left[\dot{R}\ddot{R}/I^2\right]$$

and these modifications are incorporated into the Screamer slug model. The distinction between motional and mechanical impedance is not important for the pure slug model, but in the event of any retarding forces during the rundown or in a snowplow model for a gas puff the two terms contribute as indicated.

FIG. V.A.5A DECADE QUAD, SCHLITT'S CONSERVATIVE DESIGN — EQUIVALENT CIRCUIT AT THE POST HOLE CONVOLUTE

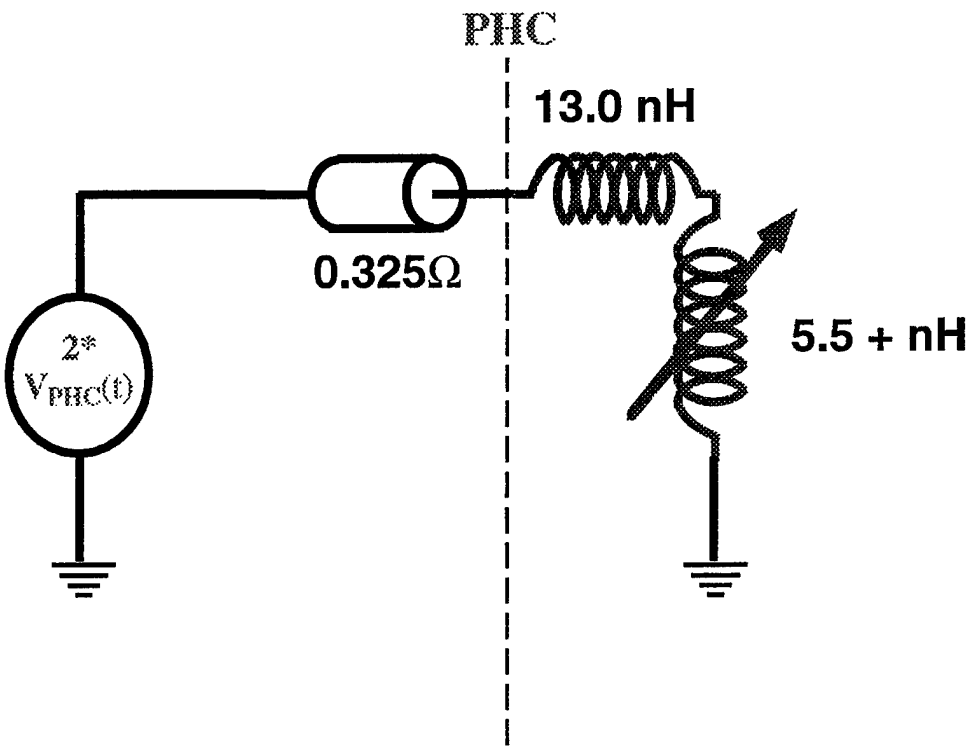

FIG. V.A.5B DECADE QUAD, SCHLITT'S CONSERVATIVE DESIGN — EQUIVALENT CIRCUIT WAVEFORMS

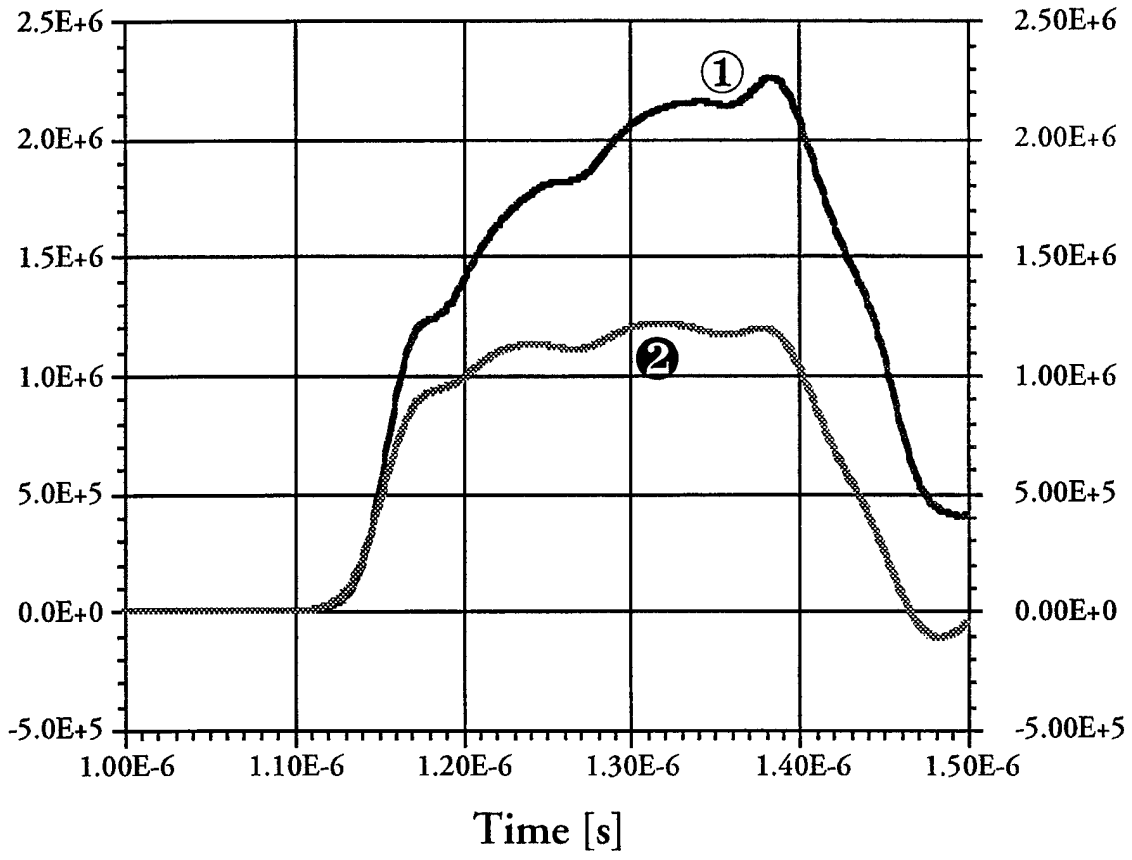

① — V drive = 2*Vphc ❷ — Oil Vmatch

B. Argon Gas Puff Implosion Performance

i. Methodology

Active rundown time is determined by the selection of a minimum radius R_f for the implosion. The common choice to measure kinetic energy delivery at a fixed fraction of the initial radius is modified here. The kinetic energy coupling generally tracks the change in inductance produced in the load, but that inductance change is fixed if the implosion is followed only to a constant fraction of R_o. By having the slug model (implicitly) undergo transition from an annulus to a cylinder at a prescribed lower radius rather than at a prescribed fraction of the initial radius, this final stagnation radius is a fair measure of the change in inductance achieved and can be explicitly tied to experimental observations. The peak load kinetic energy is therefore recorded at this time of assembly, and is then used to compute the expected yield. Therefore, by selecting absolute values of initial and final radius, a coupling study can get a clearer picture of the correlation between inductance change and kinetic energy delivery.

ii. Scaling Law Formulation

The K-shell yield per unit length, kJ / cm, can be written as a function of two parameters. The first

$$\eta \equiv (\frac{v_f}{1.35 \cdot 10^6})^2 \mathcal{Z}^{-2.41}, \qquad (II.1a)$$

is a measure of the excess velocity over that required to gain access to the K-shell of the element of interest, as calibrated to the atomic number $\mathcal{Z}$. For argon this fiducial velocity is $\approx 4.395 \cdot 10^7$ cm/sec. The velocity argument used is that value characteristic of the implosion as the load starts to stagnate. In a slug calculation with a transmission line code like Screamer, the stagnation process is not explicitly computed so we use the final velocity v_f achieved by the slug as it passes under the fixed minimum radius. The second parameter for the scaling law is

$$\beta = min[\ 0.3\ T_{load}\ ,\ 0.3\ T_{load} \frac{M_{load}}{\alpha(\eta, \mathcal{Z})}\ ] \qquad (II.1b)$$

where M_{load} is the total mass loading in [g/cm], and T_{load} is the kinetic energy of the load (in kJ/cm) corresponding to v_f. The function

$$\alpha(\eta, \mathcal{Z}) = 2.58 \cdot 10^{-12} \mathcal{Z}^{5.96} \; exp(\frac{20.6}{\mathcal{Z}^{0.9}}) \; max[\; 1, \frac{\eta^2}{\eta + 12} \;], \qquad (II.1c)$$

measures a mass break point for the so-called transition from efficient to inefficient coupling between kinetic energy and yield.

The final scaling relationship is shown as a surface plot in Fig. V.B.1 over a [M_{load},T_{load}] domain representative of the studies reported here. The yield scaling can be formulated piecewise over four η domains

$$Y_K = \beta \quad (1.5 \leq \eta),$$

$$Y_K = \beta[\; \eta - 0.5 \;] \quad (1.0 \leq \eta < 1.5),$$

$$Y_K = \frac{\beta}{2}[\; 1 - \sqrt{4(1-\eta)} \;] \quad (0.75 \leq \eta < 1.0) \;,$$

$$Y_K = 0 \quad (0 \leq \eta < 0.75) \;. \qquad (II.1d)$$

For a chosen load material ($\mathcal{Z}$) and final radius (R_f), the K-shell yield (Y_K) per unit length (ℓ) can be calculated as a function of the implosion velocity (v_f) and mass loading (M) per unit length. The yield thus depends solely upon the plasma conditions at implosion.

iii. Results

In an initial survey of energy coupling the baseline DQ model was run through about 75 combinations of initial mass, radius and cage twist. In a effort to represent some reasonable choices for the initial radius, three values were selected [7.5, 5.0, 2.5] cm. The most stable, credible loads will be in the lower range of these values, but, should any successful Raleigh Taylor stabilization stategy arise, the large value may become accessible.

The mass loadings for these radii were then selected to hold Mr_0^2 constant and sweep through various implosion times defined by this parameter. The implosion times varied from about 150 ns to 350 ns. A typical implosion calculation for Mr_0^2=25 mg cm^2, ℓ = 3 cm, and r_0 = 5 cm is shown in Fig. V.B.2. Unlike the matched load calculation summarized above, the peak current here rises to the nominal 6.5 MA expected in the foil as it presents

FIG V.B.1 ARGON K SHELL YIELD [KJ/CM]

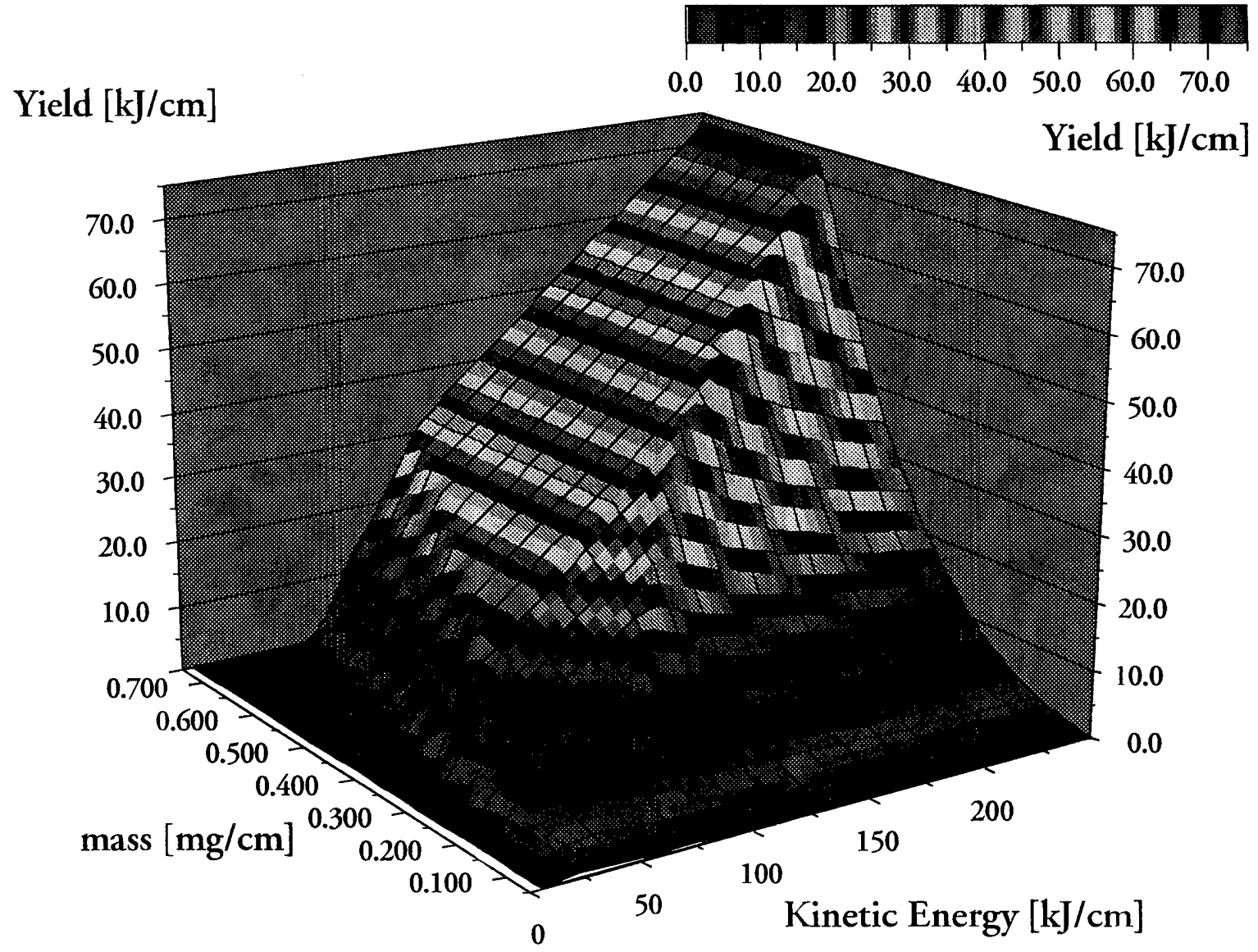

FIG. V.B.2 TYPICAL IMPLOSION WAVEFORMS: Z pinch, 25.0 mg cm^2 from 5.0 cm

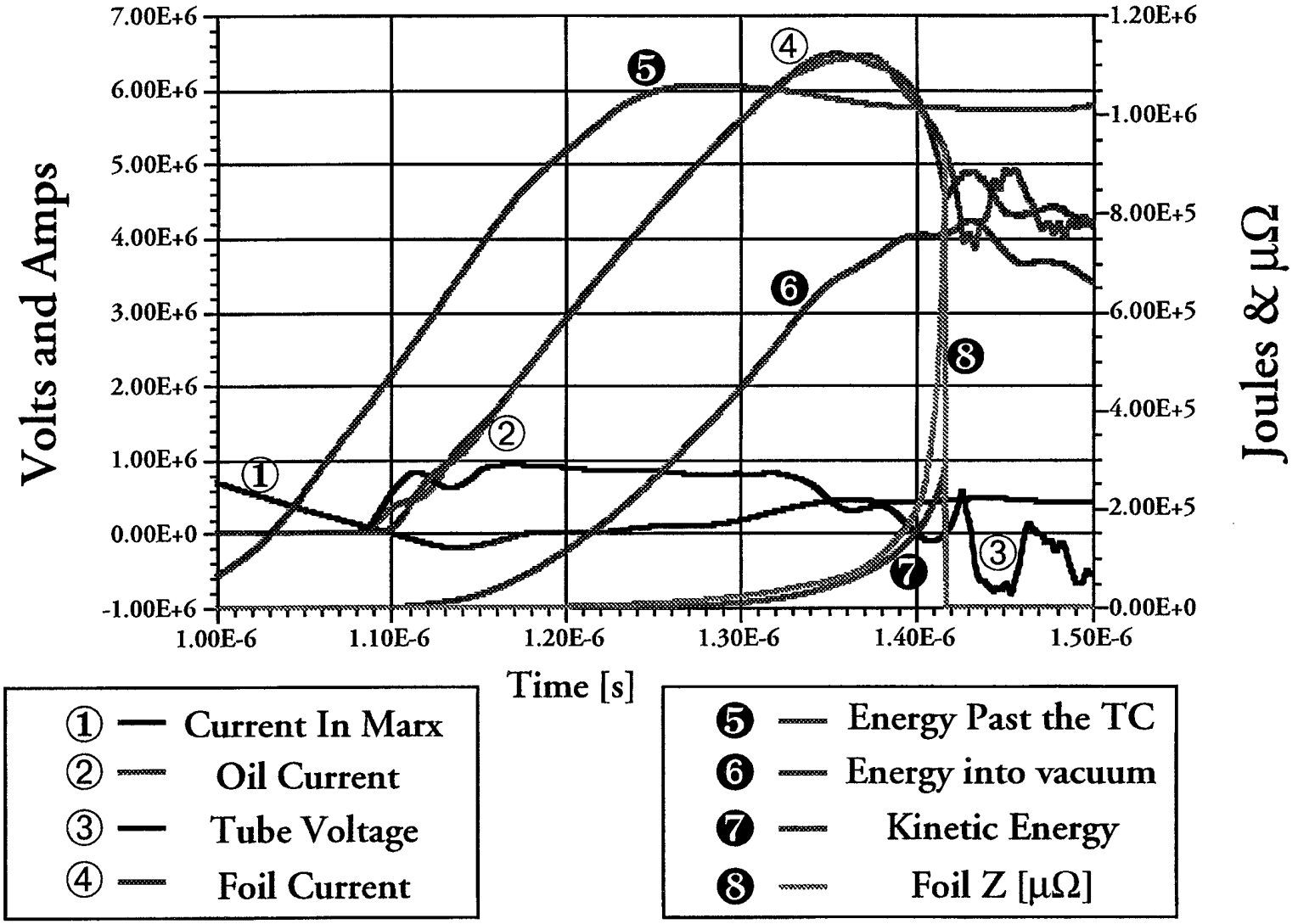

a near short circuit load to the driver until about 80 ns before implosion when the foil current is beginning to roll over into the "inductive notch". As seen in the figure the foil impedance finally rises through 50 mΩ at about the same time — entering the impedance domain where our previous analysis shows the driver will successfully couple energy. As the compression ensues fully 70 % of the final kinetic energy is delivered while the load presents an impedance greater than this value. When the load reaches the minimum radius (2.5 mm here) the available energy is less than half of what could be delivered. Comparing the energy distribution of the implosion case to that of the matched load (c.f. Fig. V.A.2), the energy moved forward of the transfer capacitor is essentially the same in the two cases, but the energy past the insulator into vacuum peaks at about 750 kJ for the PRS case as compared to 660 kJ for the matched load. Reflected power from the mismatched PRS load just sits backed up in the pipeline. These energy differences are well above the resolution limits of the calculation.

The best set of load parameters for kinetic energy transfer was sought over the domains discussed above. Variations in the return current cage twist produced only moderate kinetic energy gains ($\approx$ 10 %) in the long implosion time, large mass cases. These gains were not large enough to compete with the best kinetic energy deliveries obtained with a pure z-pinch. Generally the cage twist strategy is going to be most effective for pulsers that exhibit too short a timescale for good coupling to the kinematics of the PRS and for the Decade Quad this is not a significant factor.

In Fig. V.B.3 the optimum in available kinetic energy is shown over the Mr_0^2 domain for the three standard initial radii, along with the load velocity at minimum radius which is a direct measure of the η value obtained. For Ar the critical velocity for η=1 is $4.395 \cdot 10^5$ [m/s], so that all these cases represent potentially useful emitters. For the larger radii the optimum Mr_0^2 is 21.875 mg cm^2, while it moves back toward 25 mg cm^2 at the lower radii. In available energy there is a significant reward for the ability to implode from a 5.0 cm radius rather than the 2.5 cm radius of characteristic of more conservative load designs. The load design at 5.0 cm radius will probably challenge existing schemes for stabilization. The additional energy available from a radius of 7.5 cm may not be accessible without Raleigh Taylor mitigation.

FIG. V.B.3 OPTIMUM KINETIC ENERGY DELIVERY — SCHLITT'S CONSERVATIVE DESIGN, Pure Z-pinch

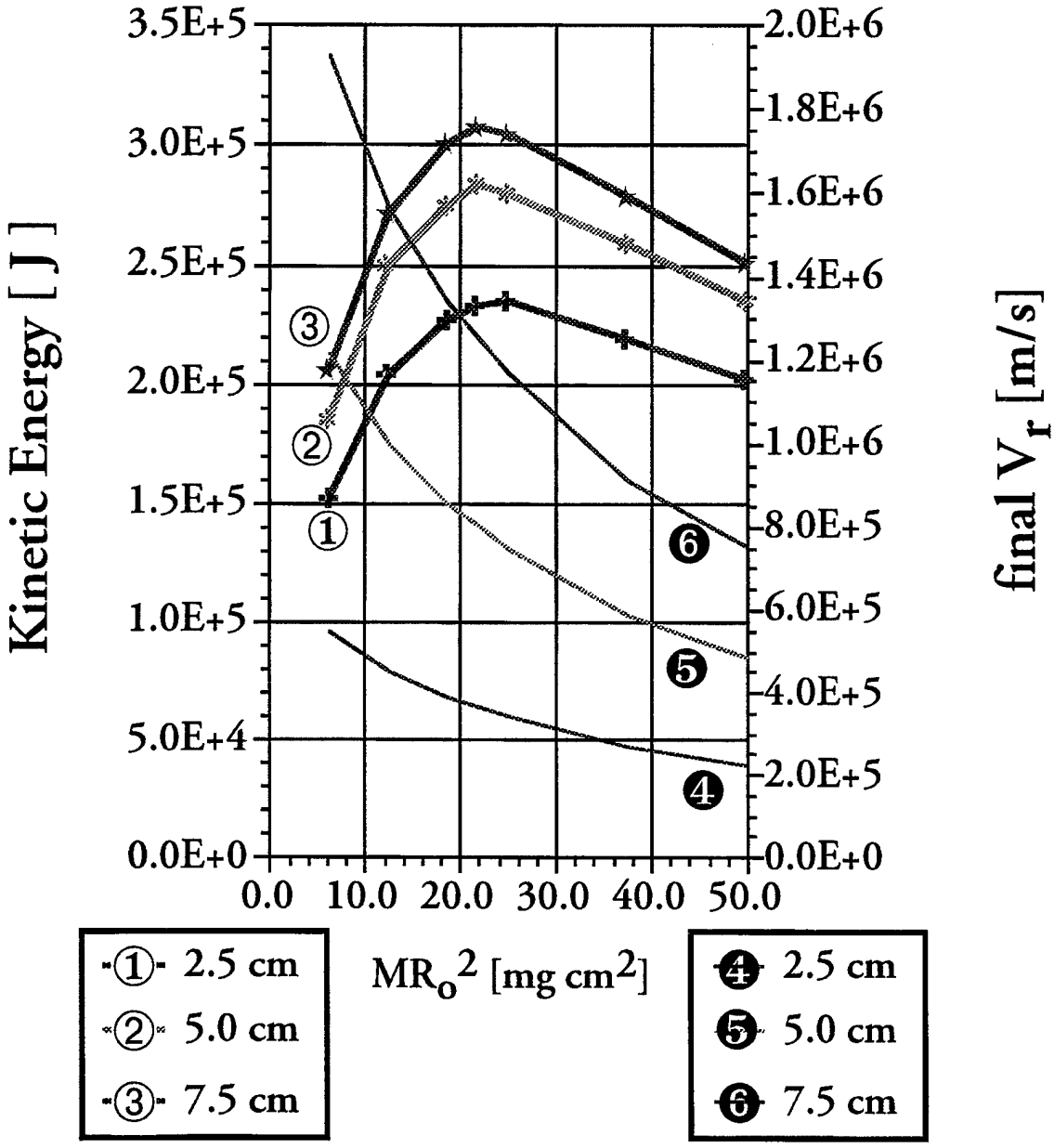

The K-shell yield implications for the performance just shown are illustrated in Fig. V.B.4 on the domain of kinetic energy per cm and mass per cm. The figure shows the position of the two larger radius kinetic energy optima on the global yield surface for Ar arising from the scaling law discussed above. The yield from 2.5 cm is taken from a case well off optimum kinetic energy transfer, the mass must be lowered to get a larger value for η. The result is a premature implosion, but a useful output can still be realized.

C. Conclusions for Argon Gas Puffs on the Decade Quad

The primary upper limit on yield from the conservative Schlitt design is excessive front end impedance. Even without adding the losses from the post hole convolute and MITL feeds, the best expected Ar K-shell yield is perhaps 25 kJ/cm. Evolution to better results is largely determined by how well more kinetic energy can be given to an optimum load mass, including stability effects. This is easy to see from the position of the best coupled large radius loads on the global yield surface, particularly since both these optima represent the *same* implosion time as measured by Mr_0^2. Consider the more practical 5.0 cm load, to move up the yield surface along the best path, i.e. one orthogonal to the constant yield contours, kinetic energy must be added at slightly less mass while maintaining implosion time. The only solution is to add available current, viz. less impedance for the best voltage loading the device can sustain. If reliable load designs from 7.5 cm radius are obtained, then the best path to better yields can involve only adding mass while maintaining velocity. Another option is operating at a radius in between the values of 7.5 cm and 5.0 cm at the *same* level of delivered energy, which would move the optimum mass loading to about 0.2 mg/cm. The winning strategies are more numerous if large radius operation can be obtained, but the common thread among them is access to a lower impedance front end.

In view of the foregoing observations, the Decade Quad reinforces a clear requirement to explore, understand, and remediate the Rayleigh Taylor instability so that longer run down lengths can be used. For the proposed device to operate well in the baseline configuration examined here, initial implosion radii must already be pushed into somewhat uncharted territory. Moreover all approaches to a better position on the yield surface involve even larger initial radii.

FIG. V.B.4 OPTIMUM YIELD IN ARGON — SCHLITT'S CONSERVATIVE DESIGN, Pure Z-pinch

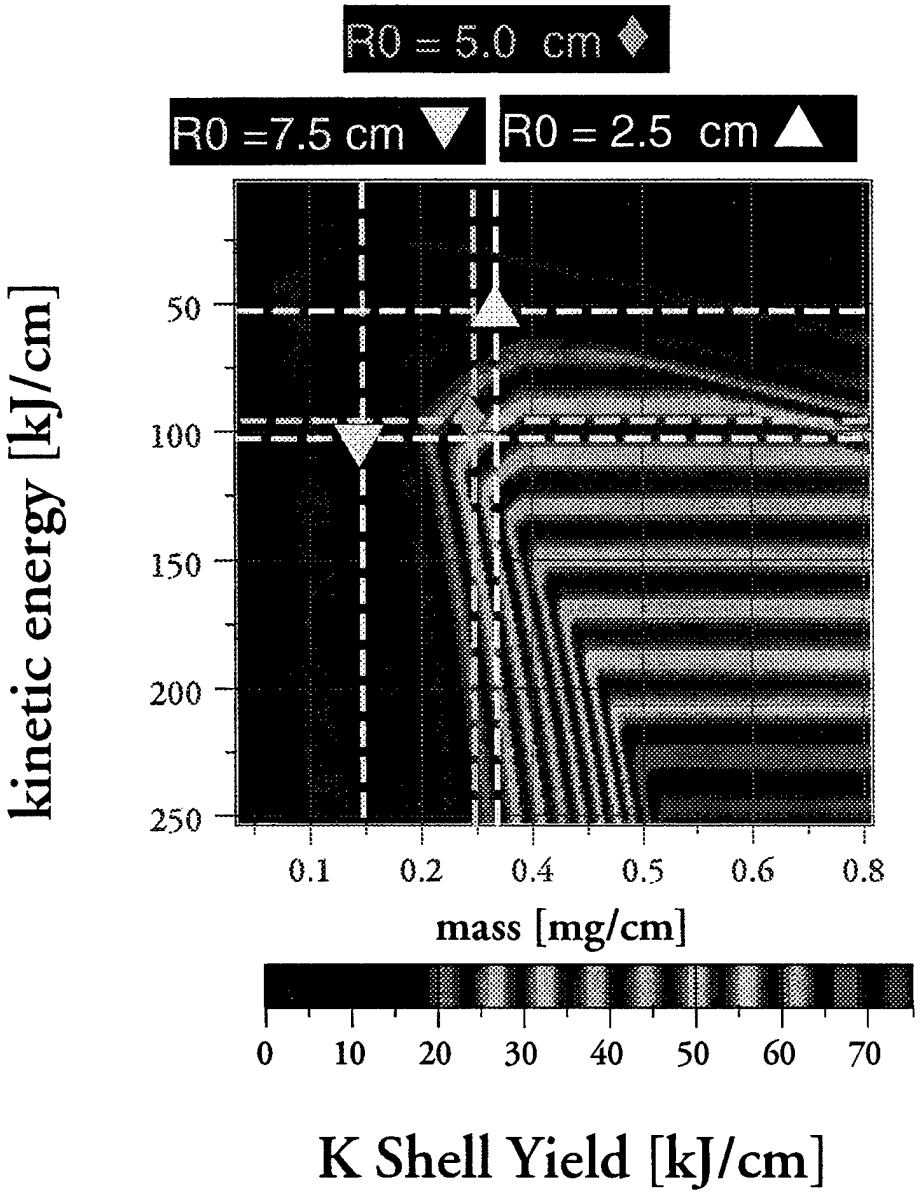

VI. SUPPRESSION OF RAYLEIGH-TAYLOR INSTABILITY BY TAILORING THE DENSITY PROFILE

A. Fundamental Physics of Structured Loads

PRS loads which start out at large radii are known to be Rayleigh-Taylor (R-T) unstable[1]. This presents a problem when trying to design loads for future PRS machines with large currents and long risetimes. Our results from last year (1995) back up this assertion and can be summarized as follows:

(1) Implosions initiated by thin gas puff shells are extremely unstable. The distance over which they travel before being disrupted is severely limited by the large R-T growth rate. Shells are limited to an outside radius of about 2-3 cm. This problem is reduced when uniform fill loads are used and the outside radius can extend out to 5 cm or more. These results were first derived from implosion simulations driven with a constant current wave form. We now consider these results to be optimistic in the case of uniform fills and tailored loads when imploded with a rising current. This is because the rapid rise of the magnetic pressure is too fast to allow the initial mass accretion to slow or invert the acceleration. Suitable modifications to the profiles, however, can reduce this problem. A more detailed discussion on this topic is given below.

(2) In terms of converting kinetic energy, thin shells are the most efficient load designs. These loads are, however, the most susceptible to instability and breakup. Less efficient are uniform fills but these loads are somewhat less constrained by stability considerations. Structured loads are even less efficient kinetic energy converters but are favorable in terms of stability. These results are detailed in Ref. 1.

During this year (1996) we further pursued the topic of stability using loads with tailored density profiles. These loads make it possible to extend the outside radius in order to make better use of long duration pulses. In a tailored load, the magnetic pressure drives a shock wave into a stratified plasma layer with increasing density. The shock wave then slows down and the effective gravity is reduced or, even reversed. The effects of the R-T instability are then minimized or eliminated.

The magnetic energy continues to perform work, accelerating an increasing plasma mass even as the plasma-field interface may feel a deceleration. The mathematical details of this growth inhibition are given in Ref. 2.

Our 2-D radiation-magnetohydrodynamics(RMHD) code, PRISM, was used to study the tailored loads. This code has been discussed in previous reports so it won't be discussed here other than to point out that electrical resistivity, boundary conditions for circuit models, separate energy equations for ions and electrons, and lookup tables for equation-of-state properties and radiative power are included. Argon was used as the load gas in these simulations. In the results discussed below an axial wavelength of 1/3 cm was chosen. Based on our previous work, we have found this to be an appropriate value. In our simulations, we used both a constant current of 5 MA and an applied voltage which results in a current that rises linearly to 5 MA over 200 nsec. The usable portion of the imploding plasma's kinetic energy is its radial kinetic energy, KE_r, whereas its axial kinetic energy, KE_z, (which would be identically zero in a one-dimensional simulation) is an integral measure of perturbation growth. The constant current case is shown in Fig. 1. In can be seen that while the shock wave propagates from 8 to 2 cm, compressing and accelerating the load mass, the acceleration of the interface itself is inverted. Perturbations should then run across the back surface of the load as waves with slowly growing amplitudes. This is the case in our simulations as seen in Fig. 2. The slow growth phase (see Fig. 1) lasts about 190 nsec. Figure 2(a) shows only small-amplitude waves running across the back surface. When the shock wave reaches the inner, high-density part of the load, and the reflected rarefaction wave transmits decreased pressure to the back surface, its acceleration is inverted again, with the result that the classical R-T growth starts to distort the shell at the back surface (see Fig. 2(b)). At this point, the load is compressed into a shell and is subject to the stability criteria established earlier for thin shells. If the shell is sufficiently close to the axis, the central regions of the implosion could remain relatively unaffected by the instability.

In Fig. 3, the kinetic energy curves are shown for the case in which a constant voltage was chosen such that the current would rise linearly to 5 MA over 200 ns, or $V/L = 2.5 \times 10^7$ MA/sec, where L is the inductance. This translates into a linear

rise of the current at early time. The rapid rise of magnetic pressure makes the initial density accumulation provided by the $1/r^3$ initial profile used in the constant current case too slow to invert the acceleration. This can be fixed by imposing a sharper density profile near the outer boundary of the load. Once the density profile has been appropriately tailored for the given current wave form, the results are similar to those shown for the constant current case.

The advantages of tailoring the profile are:

(1) Appreciable magnetic energy is converted to kinetic energy during the slow growth phase. For instance, the center of mass for the load shown in Fig. 1 is located at 3.7 cm, hence the implosion should produce a radiation yield equivalent to that between a shell and solid fill load implosion from about the same radius. Note, however, that a shell placed at 3.7 cm would be completely destroyed by the R-T instability with greatly reduced K-shell output.

(2) A tailored density profile can operate as a switching device, so that it may work with longer current pulses. This shell is assembled while the current is rising and imploded by the peak current when the peak is reached. This cannot be done with a conventional load, which would be either imploded too early or distorted too much by a long current pulse. In addition, it is easier to couple magnetic energy to a load whose initial radius is large. The penalty is that near implosion, the dynamic load inductance may be large.

(3) After the passage of the shock wave, the shell already has some, albeit relatively small, velocity directed to the central axis. This can increase the hydrodynamic efficiency of the acceleration, since the rate of magnetic-to-kinetic energy conversion is proportional to this velocity.

References

1. F. L. Cochran, J. Davis, and A. L. Velikovich, Phys. Plasmas 2, 2765(1995).
2. A. L. Velikovich, F. L. Cochran, and J. Davis, Phys. Rev. Lett. 77, 853(1996).

Figure Captions

1. Radial (KE_r) and axial (KE_z) kinetic energies vs. time for implosion of a load with constant current. The initial density profile is shown in the inset.

2. Density contours corresponding to slow growth phase t=100 ns (a) and rapid growth phase t=250 nsec (b).

3. Radial (KE_r and axial (KE_z) kinetic energies vs time for implosion of a load with constant voltage. The initial density profile is shown in the inset.

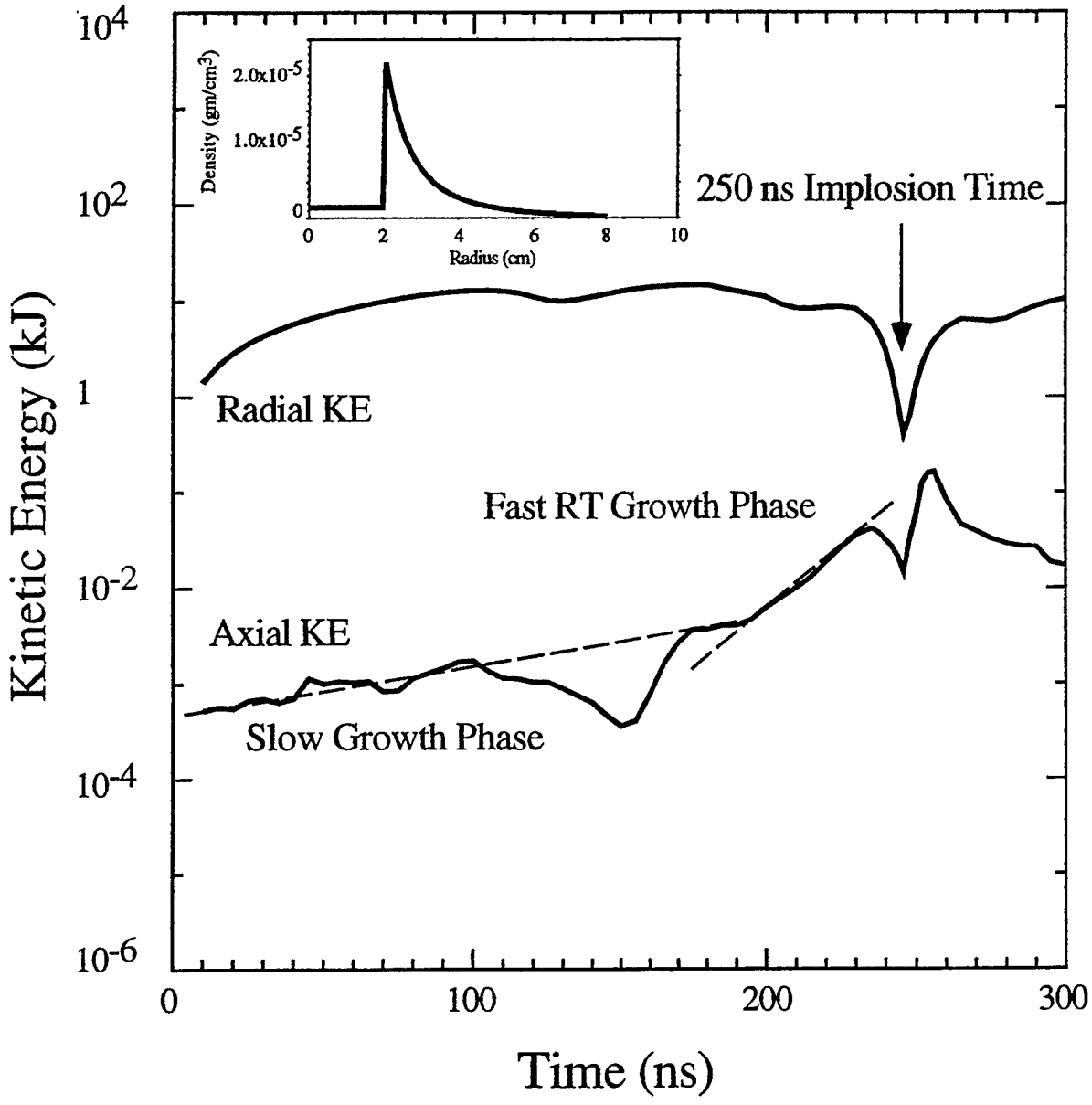
Kinetic Energy (kJ)
10^4
10^2
1
10^{-2}
10^{-4}
10^{-6}
0
100
200
300
Time (ns)
Density (gm/cm^3)
2.0x10^{-5}
1.0x10^{-5}
0
0
2
4
6
8
10
Radius (cm)
250 ns Implosion Time
Radial KE
Fast RT Growth Phase
Axial KE
Slow Growth Phase

Figure 1

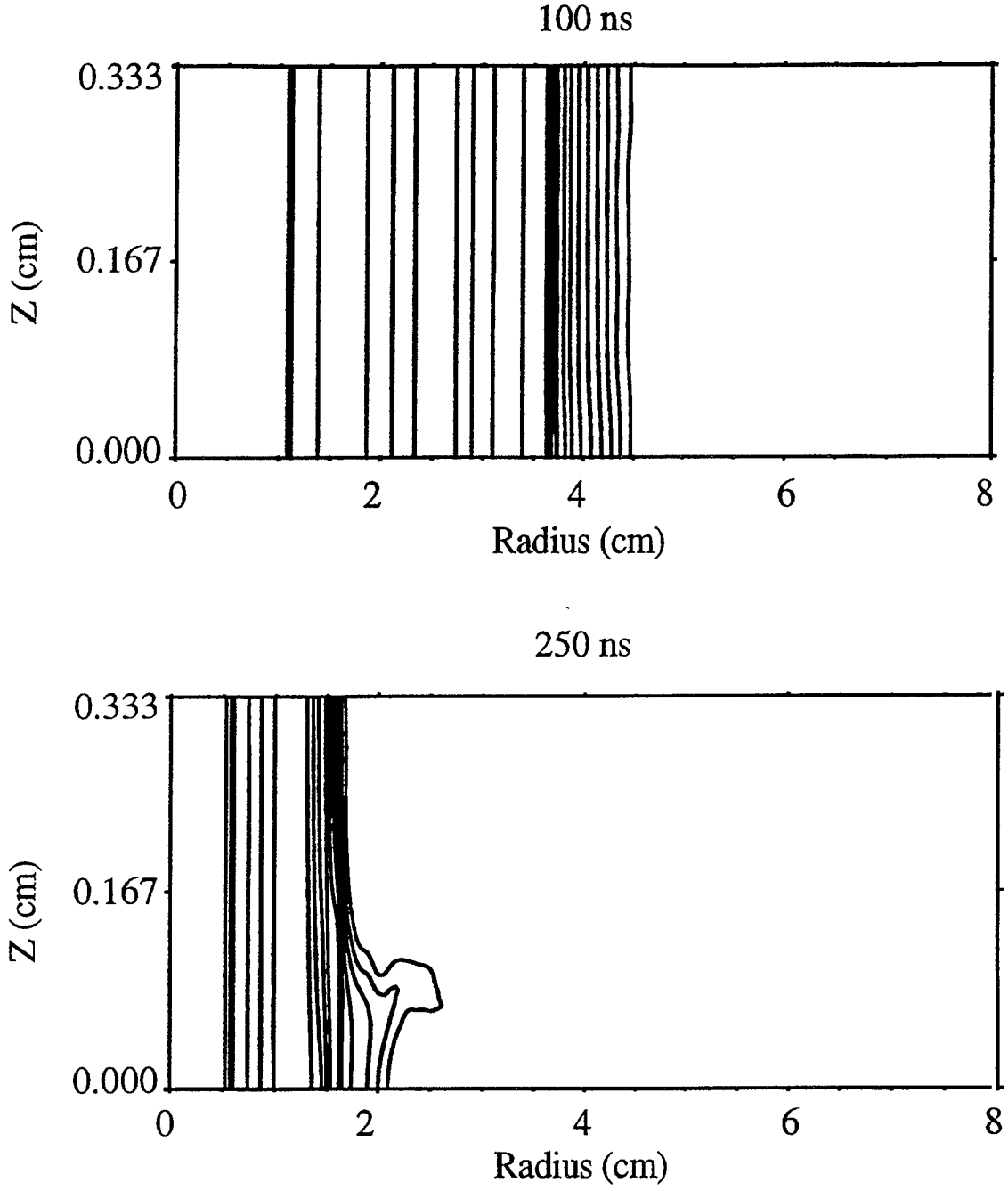
100 ns
0.333
0.167
0.000
Z (cm)
0
2
4
6
8
Radius (cm)
250 ns
0.333
0.167
0.000
Z (cm)
0
2
4
6
8
Radius (cm)

Figure 2

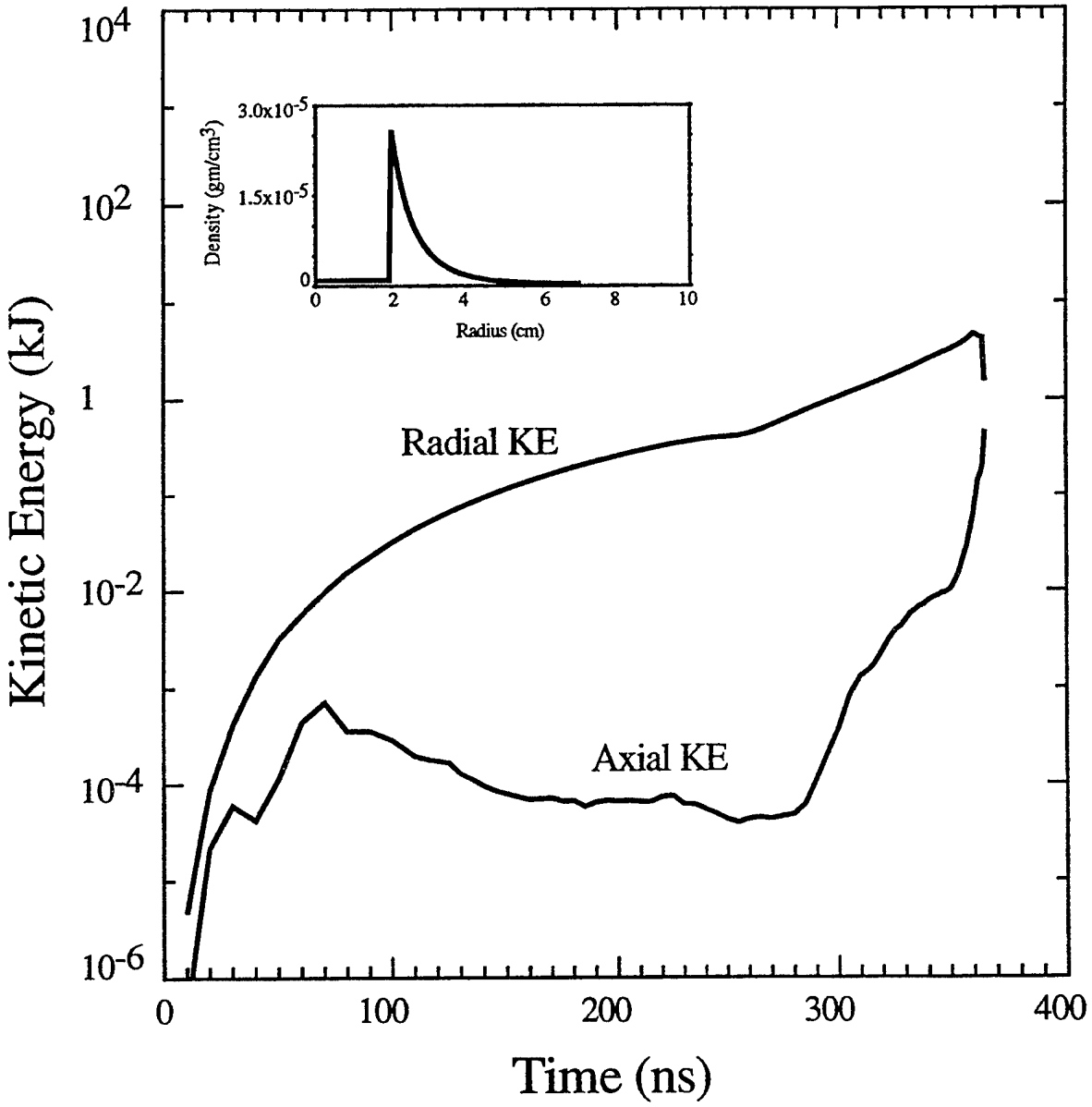
Kinetic Energy (kJ)
10^4
10^2
1
10^{-2}
10^{-4}
10^{-6}
0
100
200
300
400
Time (ns)
Radial KE
Axial KE
Density (gm/cm^3)
3.0x10^{-5}
1.5x10^{-5}
0
0
2
4
6
8
10
Radius (cm)

Figure 3

B. ACE-4 Tandem Puff Load Stability Studies

A major concern for medium and long current risetime implosions is load disruption due to the Rayleigh-Taylor(R-T) instability. This is because these implosions must start from relatively large radii in order to efficiently couple to the electrical energy of the machine. During the past year, we have examined loads with differing radial density profiles in order to assess their stability properties as ACE-4 tandem puff configuration loads. To model ACE-4 tandem puff Argon implosions, we imposed a simple current which rises to 4 MA over 120 nsec and then remains constant during the remainder of the implosion. Simulations were run for loads with density profiles that had radial variations according to $1/r^3$,$1/r^2$,$1/r$, and 1. That is, the density varied inversely according to an exponent, n, where n=0,1,2,3. These approximate various profiles which might be achievable with single or multiple nozzle designs. Each density profile extended from an inner radius of 2 cm out to an outer radius of 9 cm both with and without an extra density variation over the final 2 cm (see the discussion in this report on Rayleigh-Taylor instabilities in Z-pinches with tailored density profiles). All loads were normalized to have an Argon line density of 200 μgm/cm.

Figure 1 shows density profiles for the two extreme cases: $1/r^3$ density variation and hollow fill. For a given total mass, the density is higher near the inner surface and lower at the outside as the radial variation exponent increases. Likewise, the density is lower at the inside as the exponent decreases. The simulations were run with a 10 percent initial perturbation and a wavelength of 0.33 cm.

Figure 2 shows the linear density variation along the axis for the various loads at two times during the implosion. The density variation is measured as the ratio between the maximum line density and the minimum line density for all computational z-slices. At the first time, 120 nsec, this ratio is nearly the same for all cases. This is the time when the current switches from a linear rise case to a flat current. The density variation was also measured 25 nsec before the load stagnated on the central axis. Obviously, this time varies between the load types. At the current transition point, 120 nsec, all of the load types show very little variation across the column. The density variation is different, however, near stagnation.

This value decreases rapidly with increasing exponent so that at n=3 there is very little variation.

The radial and axial kinetic energy for the $1/r^3$ load are shown in Fig. 3. Note that the axial kinetic energy would be zero in a 1-D simulation. Initially, the axial kinetic energy rises as the shell is formed and the current is rising. However, at about 70 nsec the axial kinetic energy peaks and then decreases as the effective gravity is reduced and its vector is turned in the opposite direction. This continues until about 200 nsec when a shell has formed near the original inside surface. After this point, the implosion acts like a shell implosion and is R-T unstable up until stagnation. The penalty for this stable behavior is that the radial kinetic energy increases slowly and flattens just prior to the final shell-like implosion that occurs after 200 nsec. This reduces the amount of energy which is available for conversion to K-shell radiation.

In conclusion, it was found that density tailored loads offer much less density variation at stagnation as compared to a hollow fill or shell load imploded from the same distance. The linear rise phase of the current pulse, while harder to stabilize, does little damage to all types of loads investigated here. Most of the runin occurs during the constant current phase which is more easily stabilized. Larger exponent (i.e., $1/r^3$) profiles give better stability but exponents greater than three were not investigated. There is a practical limit to the density falloff and larger exponent profiles produce density variations which are unrealistic at large radii because of their low density values.

Figure Captions

1. Density profiles for the $\rho \sim 1/r^3$ and hollow fill loads.
2. Line density ratios at 120 nsec and 25 nsec before stagnation for different density profile types.
3. Radial and axial kinetic energy for the $\rho \sim 1/r^3$ load.

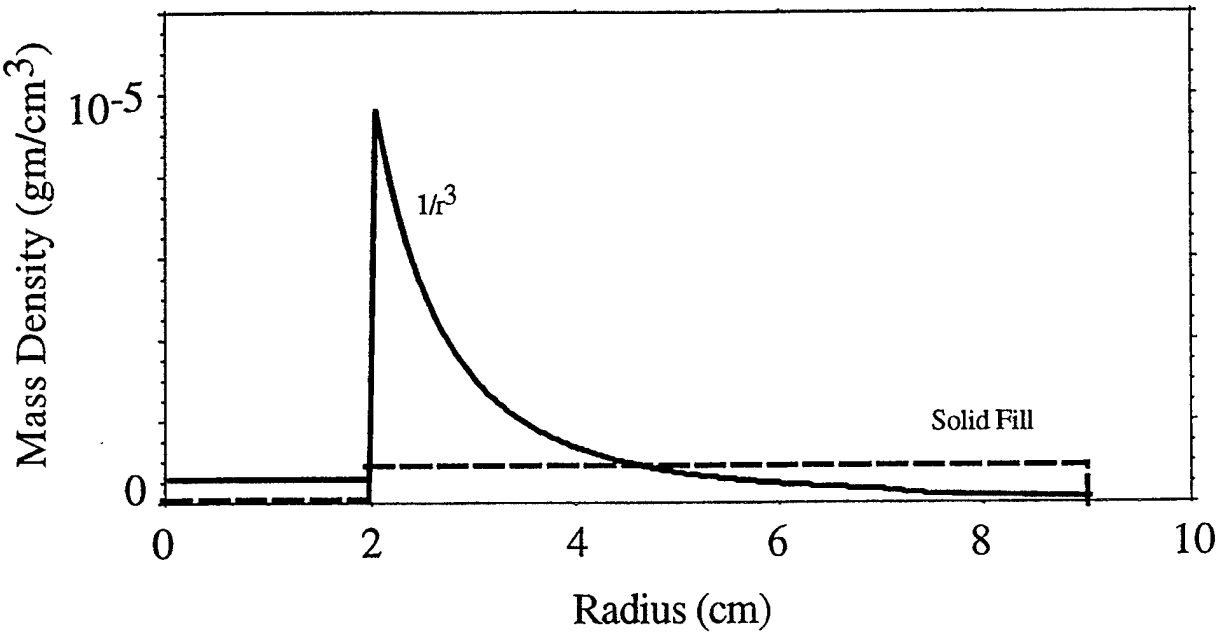

Figure 1

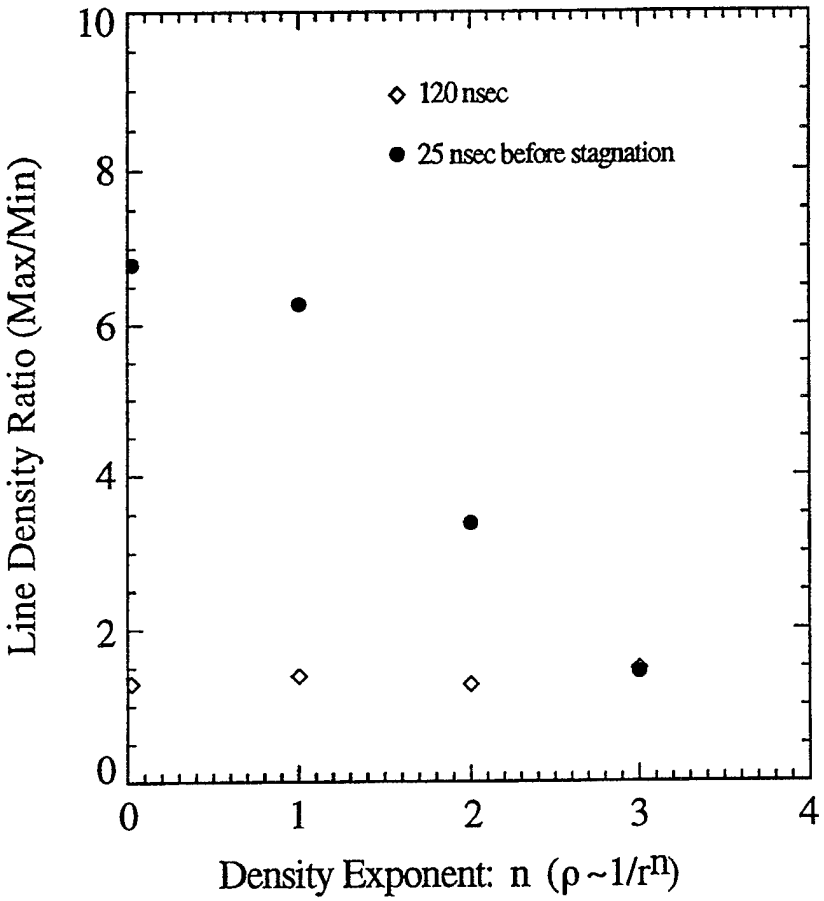
10
8
6
4
2
0
0
1
2
3
4
◇ 120 nsec
● 25 nsec before stagnation
Line Density Ratio (Max/Min)
Density Exponent: n (ρ ~ 1/r^n)

Figure 2

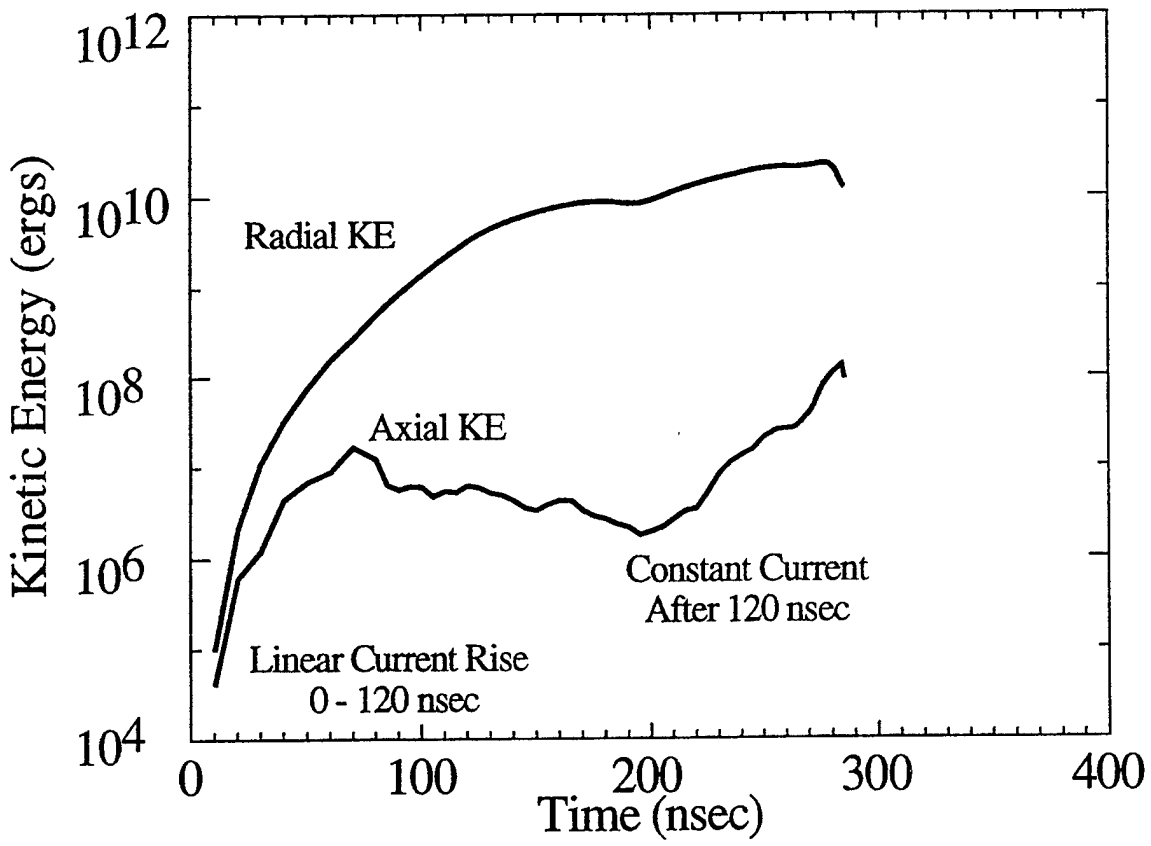
Kinetic Energy (ergs)
10^{12}
10^{10}
10^{8}
10^{6}
10^{4}
Radial KE
Axial KE
Constant Current
After 120 nsec
Linear Current Rise
0 - 120 nsec
0
100
200
300
400
Time (nsec)

Figure 3

VII. ANALYSIS OF TIME-RESOLVED Z-PINCH DATA

A. Introduction

In order to determine how well the dynamics of z-pinch implosions and x-ray generation are understood and how well z-pinch loads are being designed for optimal performance, there must be an interaction between theory and experiment. The right data needs to be taken, and it must then be analyzed from a variety of perspectives as completely and thoroughly as possible. In this section, a new procedure is briefly described with which to carry out this theoretical/experimental interaction and, in the process, to add to the arsenal of methods that can be used to extract valuable information from z-pinch x-ray data in order to improve load design and load performance. The tool being used for this data analysis is Code 6720's one-dimensional (1-D) radiative magnetohydrodynamics code (RMHC). It was applied to the analysis of a 90-wire, aluminum, z-pinch experiment that was conducted on the Saturn accelerator last year at Sandia National Laboratories. In this experiment, the pinch exhibited azimuthally symmetric implosions and two x-ray bursts. These bursts correlated with two radial implosions and are indicative of predicted 1-D RMHC behavior.

The following problems were addressed in the course of the data analysis:

- How should the 90-wire data be analyzed and interpreted? What can be learned from it?
- What temperature and density gradients existed in the plasma during times of strong K-shell emission? Can these gradients be inferred from the data?
- What are the ion temperatures in the assembled plasma?
- How much z-pinch mass participates in the K-shell emission? How does it scale with load design? Can it be increased?

The first two of these problems are the main focus of the discussion that follows.

The results of the 1-D analysis were found to be broadly consistent with an initial, less detailed, x-ray data analysis in which plasma gradients were ignored. However, the ability to reproduce the full set of spectroscopic data in the 1-D analysis was found to be sensitively dependent on the radial gradients that were calculated. *Moreover, an important finding of both the 1-D and non-1-D analyses was that these implosions produced high K-shell powers ($\sim$4.5 TW) and x-ray yields ($\sim$50-55 kJ) with only a small fraction ($\leq$ 20%) of the imploded pinch participating in the x-ray emission. Thus, it is important that more about the gradient structure of z-pinches be learned in order to increase this mass participation and, hence, the x-ray conversion efficiencies beyond those that were achieved in these experiments.*

Calculations of z-pinch dynamics are generally approximate in their treatment of either the geometry, the spatial resolution, or the nonlinear plasma chemistry of the fluid flow. Consequently, detailed comparisons of calculated x-ray data (such as powers, line ratios, and continuum slopes) with these same quantities extracted from experimental measurements have inherent limitations. Some limitations can be reduced by conducting experiments that more closely approximate the geometric assumptions, such as cylindrical or translational symmetry, that are most often made in the calculations. The 90-wire Sandia aluminum array experiment that was analyzed comes very close to meeting this goal. The use of large wire numbers reduces the degree of azimuthal

asymmetry of the imploding plasma and improves the shot-to-shot reproduciblity of the implosion and the degree of cylindrical symmetry that is achieved by the pinch on axis.

On the other hand, overcoming inherent limitations imposed on radiative magnetohydrodynamic code calculations by the inability to adequately spatially resolve the fluid dynamics or to numerically integrate the full ionization and radiation transport dynamics is a more difficult problem to work around. In this case, diagnostic procedures have to be developed that can be used to test the effect that RMHC approximations have on their ability to replicate experimental results. A variety of well-posed, and sucessively more complicated, theoretical calculations, both non-RMHC and RMHC, have been developed to analyze experimental data and to predict this data from first principles, and these developments need to be continued.

An extensive set of time-resolved x-ray measurements was obtained from the 90-wire experiment. The experiment was repeated three times. These three shots had two important characteristics: one, they were highly reproducible by z-pinch standards, and two, the pinhole data they generated was suggestive of approximate, one-dimensional (1-D), cylindrically symmetric, implosion behavior. The data consisted of (1) the measured implosion time, i.e., measured current traces and the K-shell x-ray pulse relative to the current trace, (2) the total x-ray power output pulse, (3) the K-shell power pulse, (4) seven time resolved and fiduciated K-shell pinhole pictures per shot from which the size of the K-shell radiating region as a function of time as well as the implosion time were determined, (5) seven time-resolved and fiduciated K-series spectra per shot from which line ratios as a function of time, especially that of the H-like Lyman-α line emission to the He-like n=2-1 emissions, were determined, and (6) time-resolved electron temperatures that were inferred from the slope of radiative recombination emission as measured by PCDs (photoconducting diodes[1]) or as extracted from the K-series spectra.

A CRE analysis of this data, taken together with an analysis of the free-bound continuum slope, led to an early conclusion that the pinched plasma contained steep temperature gradients,[2] i.e., it contained a small, hot core surrounded by a cooler plasma halo. A similar tentative conclusion was drawn from an analysis of emission data obtained in a mixture experiment in which magnesium was coated onto aluminum wires.[3] Because these gradients have a major influence on the plasma dynamics and on the emission characteristics of the pinch, it is vital that they be accurately diagnosed if possible. The problem is these gradients depend, in general, on the full time history of the implosion dynamics. Consequently, the degree to which the data can presently be reproduced by a 1-D RMHC calculation, and under what assumptions, was investigated. It represents an important step towards developing a diagnostic for both gradients and the dynamics behind their development.

The nonlinearity of z-pinch dynamics makes it generally difficult to obtain complete agreement with all of the data through the adjustment of calculational assumptions. However, in the analysis of the 90-wire experiment, it was found that changes in these assumptions moved one or another of the calculated data toward either closer agreement or greater disagreement with the measured data. Therefore, the process of seeking agreement leads, in principle, to an unambiguous set of physical assumptions offering the best matchup and, therefore, the best diagnostic of the data.

The comparisons that are made between calculated and experimentally measured x-ray data do not yet show perfect agreement between the two datasets. Two cases will be shown, however, that bracket the experimental data and that suggest how improved agreement can be found. The best agreement of all the data comparisons is obtained between the emitted K-shell powers in one

case. The other case, however, points to an explanation of the power behavior that was seen when wire number was varied for fixed array mass and initial radius. The K-shell power, like the total x-ray power (the sum of both sub- and super-kilovolt emissions), is most sensitive to the degree of compressibility of the assembled plasma and to the distribution of energy within the plasma. The comparison of the K-shell powers is generally in better agreement with experimental data than that of the total powers because the calculated total power depends on more of the detailed structure of the atomic model used in the hydro calculation than does the K-shell power (and more detail is, therefore, needed). Line ratios, continuum slopes, and Doppler linewidths, on the other hand, are sensitive to the structure of the temperature and density gradients that are generated in the experiment and that are calculated. Detailed agreement, especially in time, is, therefore, more difficult to obtain between these calculated and measured quantities. It is also dependent on the ionization dynamics of the plasma, and the CRE approximation that is made in the calculations is not generally valid throughout the experimental plasma dynamics.

B. Description of the Experiment

The experiment to be analyzed was conducted with 2-cm long arrays, 1.72 cm in diameter, composed of 90, 13 μm aluminum wires having a total mass of 615 μg. Three shots were taken, labeled 2085, 2094, and 2095. Because of their high degree of reproducibility, we have treated the three separate datasets from these shots as one and have analyzed the data as if it were from one shot. The reproducibility of the K-shell power pulse is illustrated in Figure 1. The power curve from shot 2094 was shifted by -0.8 ns and the power from shot 2095 by -2.3 ns to bring the three main peaks, labeled A, into coincidence. Each of these peaks has approximately a 4-ns FWHM and a peak of 4.3 $\pm$0.4 TW. A second, smaller peak follows the main peak. Figure 1 shows that this secondary peak is the least reproducible part of the power pulse.

Because time-resolved measurements were made, the evolution of the pinch during assembly could be studied. A series of eight pinhole pictures, taken in K-shell x rays, was recorded for shot 2085 for example. They are shown in Figure 2 for a succession of times; peak compression, at 81.5 ns, occurs in the second frame. The pictures show a shell of plasma (frame 1) imploding to the axis, forming a tight pinch (frame 2), re-expanding (frames 3 through 7), and then recompressing (frame 8). This overall picture is consistent with the power curve shown in Figure 1. One can use densitometer traces of the pinhole pictures, averaged over z, to determine the average or mean size of the K-shell emission region as a function of time. Figure 3 contains all of these measured sizes drawn relative to the power pulse from shot 2094. A curve interpolating the position of the pinch, defined by an average over the three shots, is also drawn. The error bars represent timing uncertainties (see the discussion of Figure 1) and the RMS shot-to-shot variations in deriving sizes from the changing, z-dependent, radial shape of the pinch. Radial asymmetries are seen in the pinhole pictures, although they appear to be mild. This observation is consistent with current measurements that were made.

Measurements of the total (unfiltered) power output from the pinch were also made (Figure 4). Like the K-shell power, they exhibit a main peak and a smaller, secondary peak; both correlated with the K-shell peaks. The peak of the total power is approximately six times the size of the K-shell peak. Note that the timing uncertainties are slightly different for the total power than for the K-shell power pulses, i.e., slightly different shifts were needed to bring the total power pulses into coincidence than were needed for the K-shell pulses.

In addition to the pinhole pictures, a set of time-resolved K-series spectra was recorded in each of the three shots. From these spectra, a variety of important information was obtained: ratios of hydrogen-like to helium-like line emission as well as line profiles and linewidths. The data from the three shots, when plotted versus time, present a consistent picture of the 90-wire emission dynamics when compared with both the the power pulses of Figure 1 and the emission region sizes of Figure 3. For example, the Ly-α to He-α (including intercombination line) ratio, for the three shots, together show that hydrogen-like emission reaches its maximum relative to helium-like emission at $\sim$5 ns following peak compression. The ratio subsequently falls, only to reach a second, smaller maximum at the time of the second power peak. The ion temperatures that are inferred from the relative Ly-α and Ly-β linewidths of the three shots, also rise and fall with the power pulse (see Ref. (4)) as do the electron temperatures that are inferred from the continuum slope as measured by PCD detectors (Ref. (2)).

The measurement of the continuum slope from PCD detectors is less precise than a direct measurement from an emission spectrum since it requires the unfolding of a point measurement from a filtered region of the spectrum. However, in order to obtain a continuum slope from a spectrum, one must know the film or microchannel-plate frequency response. Four examples of a slope inference are illustrated in Figure 5. The first three spectra shown in this figure are time-resolved, and recorded for each of the three 90-wire shots at the time (relative to the peak of the x-ray emission) shown in each spectrum. The times are essentially the same for each spectrum, but the continuum slopes that are drawn in each are very different from each other and from the slope inferred from the PCD measurements. The fourth spectrum shown in Figure 5 is the time integrated spectrum recorded on film in shot 2095. Its continuum has a slope corresponding to an electron temperature of 1.9 keV, while the peak electron temperature inferred from the PCD measurements was $\sim$ 1.4 keV.

The spectra in Figure 5 demonstrate some of the experimental uncertainties inherent in any data analysis. However, the effort to analyze the data and to draw quantitative inferences from it aids both the process of obtaining meaningful theoretical interpretations of the data and of assessing the reliability of the data. The main experimental uncertainty in inferring an instantaneous continuum slope (and thus an instantaneous electron temperature) is illustrated in Figure 6. The background level of the microchannel-plate must be located as Figure 6 illustrates, since the slope of the continuum is measured relative to the background and depends on the slope of the background. Note the potential uncertainties involved in locating this background.

Generally speaking, the analysis of the full set of data from the 90-wire shots was successful and produced useful benchmarks for both the 1-D calculations and for making meaningful comparisons between different experiments. The reproducibility and consistency of the shot-to-shot, 90-wire, spectroscopic data promoted its use as a single, substantial, dataset with which to analyze and diagnose the 90-wire experiment, and the success of the endeavor confirmed both the experimental and theoretical consistency. Several analysis methods were employed. The 1-D MHD method was suggested by the smallness of the radial asymmetry present in the pinhole pictures and by the appearance of a bounce and pinch recompression. Both of these observations supported the use of 1-D RMHC simulations to investigate the dynamics of plasma assembly.

C. Data Analysis

Each of the data described above contains features that a reasonably accurate 1-D simulation

of the experiment should approximately reproduce. The K-shell and total powers and the emission region sizes both show evidence of a bounce and a pinch recompression that is typically seen in 1-D MHD implosions. However, the strength and the time delay of the recompression are sensitive functions of the implosion dynamics as evidenced by the shot-to-shot variability of the small peak formed after the pinch bounce. 1-D calculations demonstrate this sensitivity. Other important features of the implosion are that the measured peak in the total power is roughly six times larger than the K-shell peak and that these K-shell emissions emanate from a tight pinch. Finally, hydrogen-like dominates helium-like emission (line and continuum) from the time of peak compression and throughout the bounce and recompression. The maximum of this relative emission is reached $\sim$ 5 ns after the K-shell peak. 1-D calculations demonstrate the sensitivity of these data features to different dynamical assumptions and to the gradients they produce.

To determine the detailed structure of these gradients from a data analysis, one must employ RMHC calculations. While z-pinches implode radially, they, in general, are 3-dimensional flows that produce 3-dimensional gradients. The simulation results to be presented in this section were obtained as the end result of a large series of 1-D RMHC implosion calculations[5] that modeled only the dominant, radial, fluid motion. Because they are 1-D, the calculations must assume symmetrical load accelerations, and hence, they can only phenomenologically model some of the 2-D or 3-D effects that occur during the implosion. In addition, these calculations are driven, at least until assembly, by the Saturn electrical circuit model, which must be accurately known. The calculations are carried out from both a first principles and a phenomenological approach, i.e., 3-D turbulence effects are phenomenologically modeled by using multipliers on the classical transport coefficients (viscosity, heat conduction, and ion-electron heating term). Otherwise, the calculation contains (1) a comprehensive description of the ionization dynamics (2) an accurate, escape probability, description of radiation transport, and (3) the self-consistent coupling of these dynamics to each other and to the fluid dynamics.[5]

The goal of the 1-D analysis was to determine a set of dynamic plasma conditions that approximately reproduced the full set of time-resolved data and gave, therefore, the best representation of the gradient structure of the plasma. The fullness of the dataset allowed this goal to be achieved. A 1-D RMHC analysis of the data proceeds by varying both the plasma initial conditions and a number of dynamical assumptions and approximations[6,7] while calculating the full set of spectroscopic data. Both kinds of variations have the effect of varying the thermalization dynamics of the plasma on axis, and these variations move the calculated data either closer to or further from the experimentally inferred data. The process is continued until the best agreement and interpretation of the experimental data is obtained.

A CRE approximation was used in the calculations to obtain the results that are presented, even though a non-RMHC CRE analysis of the data suggested that non-equilibrium ionization states were generated at late time in the experiment. There are two reasons for using this approximation. One, as in the initial CRE analysis of the spectral data that was given in Ref. (2), these CRE-MHD calculations include the nonlocal effects of line transport, i.e., they contain photo- excitations, deexcitations, and ionizations. However, unlike the previous analysis, these photo-pumpings incorporate the effects of radial gradients in temperature and density. Thus, only one important generalization of the previous non-RMHC analysis is made in this approximation. Two, fully time-dependent-ionization hydrodynamics calculations are more computer intensive than CRE-MHD calculations, and, thus, beyond the scope of this effort.

Since direct comparisons are made between calculated and measured spectral quantities, the 1-D RMHC analysis must ultimately produce a set of plasma gradients that are consistent with, or that provide a good approximation to, the spectral data. Consistency was produced by imposing a number of physical constraints on (1) the initial distribution of plasma that is generated from the exploded wire mass, (2) the calculated late-time current waveform and the resulting energy input to the pinch, (3) the strength of non-radiative, heat energy transport within the pinch and the resulting distribution of plasma energy, (4) the amount of plasma viscosity or compressibility that is generated by the plasma implosion and the resulting rate of kinetic energy thermalization (these added amounts of viscosity are assumed to be generated physically by fluid turbulent motions), and (5) the strength of fluid energy flow into electron thermal energy (this flow is also moderated by the presence of 3-D turbulence).

To summarize, the x-ray data that are most sensitive to temperature and density gradients are

1. the hydrogen-like to helium-like line ratios,
2. the slope of the hydrogen-like free-bound emission,
3. ion-motion broadened linewidths,
4. the ratio of total power to K-shell power, and
5. the ratio of continuum emission to line emission.

In turn, temperature and density gradients depend on the pinch dynamics and are sensitive to

1. the initial distribution of plasma following the explosion of the wires,
2. the amount and distribution of heat flow throughout the plasma, i.e., on the amount of turbulence-enhanced heat conductivity,
3. the amount and distribution of viscosity throughout the plasma, which, again, depends on the amount of plasma turbulence,
4. the amount of radial kinetic energy converted into electron heating, i.e., if the implosion produces a significant amount of turbulence and z-directed motion which is not fully thermalized on axis, then not all of the radial energy generated in a 1-D calculation is convertible into electron thermal energy through the thermalization of kinetic energy into ion thermal energy,
5. the spatial resolution of shock fronts, and
6. radiation loss rates.

The two calculations that will be discussed will focus only on the gradient sensitivity to plasma initial conditions and on the sensitivity of the hydrogen-like to helium-like resonance line ratios to these gradients. The initial conditions for these calculations are shown in Figures (7) and (8). Figure (7) shows the initial distribution of plasma mass, $m(r) \equiv 2 * \pi * \int_0^r dr' r' \rho(r')$, for two cases that correspond to a shell of plasma, centered around 8.6 cm, imploding onto a precursor plasma. As seen, the shell implodes onto significantly more precursor plasma in Case I than in Case II. In both cases, the plasma is contoured so that the precursor plasma is more turbulent than the shell. Thus, the heat conductivity and viscosity are smaller in the shell than in the precursor

core of the plasma. The electron-ion coupling coefficient, however, is reduced by a factor of ten in both cases. The precise contouring of the multiplicative factors for these quantities that was used in the calculations is shown in Figure (8).

The turn-on time and the strength of the K-shell x-ray emission are sensitive to both the distribution of plasma within the inner region and to its turbulence level. Good agreement of the calculated turn-on time with the K-shell power data is achieved in the 1-D calculations only when they are initialized under an assumption that some of the wire mass is blown in toward the axis by the explosion of the wires. This assumption is supported by findings in an experiment in which magnesium was coated onto aluminum wires and observed to radiate on axis a number of nanoseconds prior to the main aluminum radiation pulse and at temperatures that were higher than the aluminum.[3] Direct evidence for precursor plasma formation was also found in a set of recent aluminum experiments that were designed to investigate the early time behavior of exploding wires.[8] Finally, the pinhole pictures taken in this 90-wire experiment also show the presence of precursor plasma.[4]

The size of the pinch and the strength of the temperature and density gradients that are generated on axis are also dependent on the amount of precursor plasma. Figure (9) shows the calculated outer diameter of the pinch as a function of time for Cases I and II. For comparison, it also shows the sizes of the K-shell radiating region that were inferred from a processing of the time-resolved pinhole pictures of the three shots, 2085, 2094, and 2095. Time is meassured in Figure (9) relative to the time of peak compression. At this time, the two plasmas have the calculated temperature and density gradients that are shown in Figure (10). Note, on this figure, that the average measured size of the experimental K-shell region at peak compression is ~ 0.4 mm and that the two cases produce implosions that bound this size. Thus, it is reassuring, in Figure (11), that the two calculations of H-Lyman-α to He-α-plus-He-IC line ratio also effectively bound the measured ratios as a function of time. The late-time drop in the calculated values that occurs in Case I to less than the measured values can be interpreted as an artifact of the CRE calculations, since the data suggests that the plasma does not stay in ionization equilibrium after the plasma begins to rapidly expand.

These Case I and II calculations produce the kinds of pinch implosions and temperature and density gradients at peak compression that appear to bound the x-ray pinhole and spectroscopic data. In this way, they point to the kind of initial condition assumption that is needed in order to obtain a better matchup of this data. However, these calculations must also reproduce the K-shell power data, and, as Figure (12) shows, only Case I does that. The reduction in the amount of precursor plasma that was made in Case II (all other things being essentially the same) has led to a dramatic increase in the peak of the K-shell power pulse and to a reduction in its width. This behavior may explain another feature of the variable-wire-number experiments; namely, the dramatic increase in K-shell power that was observed when the array wire number was increased and intra-wire gap spacing was decreased (Figure (13)). Thus, the behavior seen in Figures (12) and (13) raises two important questions: where does the power curve in Figure (13) turn over, and does the turnover depend on a reduction in the amount of precursor plasma by the use of a large number of wires, on the reduction in the perturbation of the Rayleigh-Taylor instability (as has been suggested by a data analysis at LANL), or on both?

D. Conclusions

The picture that emerged from the 1-D MHD analysis, whose general features were described and illustrated above, depended critically on various pieces of the data. To begin with, the measured and the calculated implosion times and the measured and calculated diode currents are consistent only if all the load mass implodes to the axis. However, a calculation that implodes the full load mass must also show agreement with the time-resolved K-shell pinhole pictures and with the small fraction of the total mass predicted to radiate in the K-shell. These pinhole pictures show that the brightest emissions come from a shell of plasma just before plasma assembly. During and after peak compression, this shell of emission becomes a cylinder that pinches to a diameter of less than 1 mm and rebounds to a diameter of 3 mm before undergoing a secondary collapse to a diameter of 2 mm.

In order to agree with the relative magnitudes of total to K-shell powers seen in the 90-wire experiment, 1-D calculations have to assume that a shell of plasma implodes onto a precursor plasma. In these calculations, the inner plasma with an enhanced viscosity then gets heated to much higher temperatures than the shell, whose viscosity is not enhanced as much. For the most part, the core is ionized in advance of the shell and becomes fully ionized. The gradient in temperature that is created persists throughout stagnation. At the time of maximum compression and emission, the peak in the number of hydrogen-like 2p states occurs just inside the density peak of the shell, and it falls off rapidly in the shell. Thus, a significant fraction of subkilovolt x rays is produced from the cold shell surrounding the hot core.

Physically, to produce this cool shell in a 1-D calculation, it is necessary to assume that the shell is less turbulent than the plasma that is driven towards the axis early. Less turbulence means lower levels of viscosity and heat conduction in the shell than in the core, producing a cooler, denser plasma shell than otherwise.[6] This assumption is consistent with the 2-D analysis described in Ref. (9), which shows that, early in time, the exploded wires merge into an approximate shell (in which less shearing subsequently occurs) of uniformly imploded plasma only when the spacing between wires is small enough (≤ 1.4 mm). The calculations in Ref. (9) also show the production of a small amount of precursor plasma, and experiments (including the 90-wire one[4]) demonstrate its existence.[3,8] Under the assumption that it is produced during the breakdown of the wires, one can also assume that its early inward motion produces shearing and that its collection on axis is more turbulent than that of the main body of plasma.

The Case I optically-thick CRE calculation produced approximately the right amount of K-shell emission and somewhat less total emission than shot 2085. However, the calculated pinch was approximately twice the size of the measured pinch (Figure 10). In part, this is due to the fact that the precursor plasma in these calculations was compressionally heated to kilovolt temperatures. These temperatures impeded further compression when the denser shell imploded onto it. However, Figures (10) and (11) also suggest that a better mass division between the hot core and the cold shell (with more mass in the shell and less in the core) should produce a tighter pinch and better overall agreement with the pinhole and line ratio data. The problem of finding this division needs to be pursued in the future.

To summarize, it would be highly beneficial if gradient (rather than average) conditions could be diagnosed in z-pinch plasmas. Then, it would be possible to better define or to reduce the limitations on the x-ray conversion efficiency that were seen, for example, in the 90-wire experiment (only 20% or less of the array mass participated in K-shell emission). However, in the absence of an understanding of some of the underlying influences on the plasma dynamics, a

wide variety of gradients can be hypothesized. This number can be winnowed if realistic gradients could be approximately calculated using the nonlinear fluid dynamics of the pinch. The analysis of the 90-wire experiment described above is based on the use of time-resolved spectroscopic data to guide in the choice of either the dynamical assumptions, the hydrodynamic zoning, or the ionization dynamic modeling that must be done in z-pinch fluid calculations in order to replicate the data. In this way, an indirect diagnosis of the underlying pinch dynamics can be carried out, and the temperature and density gradients they produce can be inferred. The requirement that all the experimental data be replicated places significant constraints on the assumptions that can be made, leading towards, what appears to be, a promising method for diagnosing z-pinch temperature and density gradients.

In summary, time resolved and fiduciated measurements of diode current and a variety of x-ray outputs are needed in order to achieve meaningful MHD comparisons with and analyses of z-pinch experiments. An analysis of the Saturn data has shown the viability of employing 1-D RMHC calculations in the analysis as a diagnostic for plasma gradients. Moreover, while the 90-wire implosions produced high powers and x-ray yields, they did so with only a small fraction ($\leq 20\%$) of the imploded pinch participating in the x-ray emission. It is important, therefore, that more about the gradient structure of z-pinches be learned in order to increase mass participation and, hence, x-ray conversion efficiencies beyond those achieved in these experiments.

REFERENCES

1. R. B. Spielman, Rev. Sci. Instrum. **66**, 867 (1995).
2. T. W. L. Sanford, T. J. Nash, R. C. Mock, R. B. Spielman, J. F. Seamen, J. S. McGurn, T. L. Gilliland, M. Vargas, K. G. Whitney, J. W. Thornhill, P. E. Pulsifer, and J. P. Apruzese, "Time-dependent Electron Temperature Diagnostics for High-power, Aluminum Z-pinch Plasmas", Rev. Sci. Instrum., (to be published, Jan. 1997).
3. C. Deeney, P. D. LePell, B. H. Failor, J. S. Meachum, S. Wong, J. W. Thornhill, K. G. Whitney, and M. C. Coulter, J. Appl. Phys., **75**, 2781 (1994).
4. T. W. L. Sanford, T. J. Nash, R. C. Mock, R. B. Spielman, K. W. Struve, J. H. Hammer, J. S. De Groot, K. G. Whitney, and J. P. Apruzese, "Dynamics of a High Power Aluminum-wire Z-pinch Implosion", submitted to Phys. of Plasmas.
5. J. W. Thornhill, K. G. Whitney, and J. Davis, J. Quant. Spectrosc. Radiat. Transfer **44**, 251 (1990).
6. J. W. Thornhill, K. G. Whitney, C. Deeney, and P. D. LePell, Phys. Plasmas **1**, 321 (1994).
7. J. W. Thornhill, K. G. Whitney, J. Davis, and J. P. Apruzese, J. Appl. Phys. **80**, July 15, (1996).
8. E. J. Yadlowsky, J. J. Moschella, R. C. Hazelton, T. B. Settersten, G. G. Spanjers, C. Deeney, B. H. Failor, P. D. Lepell, J. Davis, J. P. Apruzese, K. G. Whitney, and J. W. Thornhill, Phys. Plasmas **3**, 1745 (1996).
9. T. W. L. Sanford, G. O. Allshouse, B. M. Marder, T. J. Nash, R. C. Mock, R. B. Spielman, J. F. Seamen, J. S. McGurn, D. Jobe, T. L. Gilliland, M. Vargas, K. W. Struve, W. A. Stygar, M. R. Douglas, M. K. Matzen, J. H. Hammer, J. S. De Groot, J. L. Eddleman, D. L. Peterson, D. Mosher, K. G. Whitney, J. W. Thornhill, P. E. Pulsifer, and J. P. Apruzese, "Improved Azimuthal Symmetry Greatly Increases X-ray Power from Wire-array Z-pinches", Phys. Rev. Lett, to be published.

Figure Captions

Figure 1. K-shell power outputs versus time. The power pulses for the three shots are superposed by shifting shots 2094 and 2095 by the amounts indicated.

Figure 2. Lineouts, averaged over z, as a function of time of the K-shell pinhole pictures taken with the small format camera. These lineouts show a plasma shell imploding to the axis, forming a tight approximately uniform pinch, reexpanding, and then recompressing.

Figure 3. The sizes of the K-shell emission region, inferred from pinhole picture lineouts of the different shots, as a function of time. An interpolating average curve of K-shell emission sizes is drawn relative to the K-shell power curve for shot 2094.

Figure 4. Total power outputs versus time. The power pulses for the three shots are superposed by shifting shots 2094 and 2095 by the amounts indicated.

Figure 5. Three measured time-resolved, aluminum, K-series spectra for the three shots, 2085, 2094, and 2095 at the times (relative to peak compression) shown, and one time-integrated spectrum. Also drawn are exponential fits to the hydrogen-like free-bound continuum slope. The continuum slope for the time-integrated spectrum yields an electron temperature of 1.9 keV.

Figure 6. Measured time-resolved, aluminum, K-series spectrum for shot 2085 at 2.5 ns following peak compression. Two lines are drawn that define approximately the same background level for the line emission but that lead to very different continuum slopes and to very different electron temperature inferences.

Figure 7. The initial, integrated mass density versus radius for the two 1-D CRE-MHD calculations, labeled Case I and Case II. Approximately 75% of the mass lies in a shell surrounding the initial array location for Case I, while $\sim$ 84% of the mass lies in the shell in Case II.

Figure 8. The distribution of multipliers used in the Case I and Case II calculations are shown as a function of radius for the initial positioning of the plasma. Both viscosity and heat conductivity are enhanced toward the plasma interior in the two cases, while the electron-ion coupling rate is reduced uniformly throughout the plasma by a factor of ten in both cases.

Figure 9. Time histories of the calculated outer radii of the two imploding plasmas, which are defined for Cases I and II by the initial plasma distributions of Figure (7).

Figure 10. Calculated temperature and ion density profiles at the time of peak compression for the Case I and Case II calculations. The two calculations bound the size of the 90-wire experimental plasma, which had an average radius of 0.4 mm at peak compression.

Figure 11. Calculated ratio of hydrogen-like to helium-like n=2 to n=1 emissions in aluminum for the two calculations labeled Case I and Case II. These ratios are compared to the measured ratios from the three shots. The K-shell power of shot 2094 is also shown for reference.

Figure 12. The calculated K-shell power output for the two calculations labeled Case I and Case II are compared to the K-shell power of shot 2094.

Figure 13. The total peak powers that were measured in two sets of variable-wire-number, fixed-mass, fixed-radius aluminum wire experiments are plotted as a function of the initial intra-gap spacing of the wires in the array. In one set of experiments, the initial array radius was 8.6 mm, and, in the other set, it was 12 mm. For gap spacings below 1.4 mm, the power increases markedly.

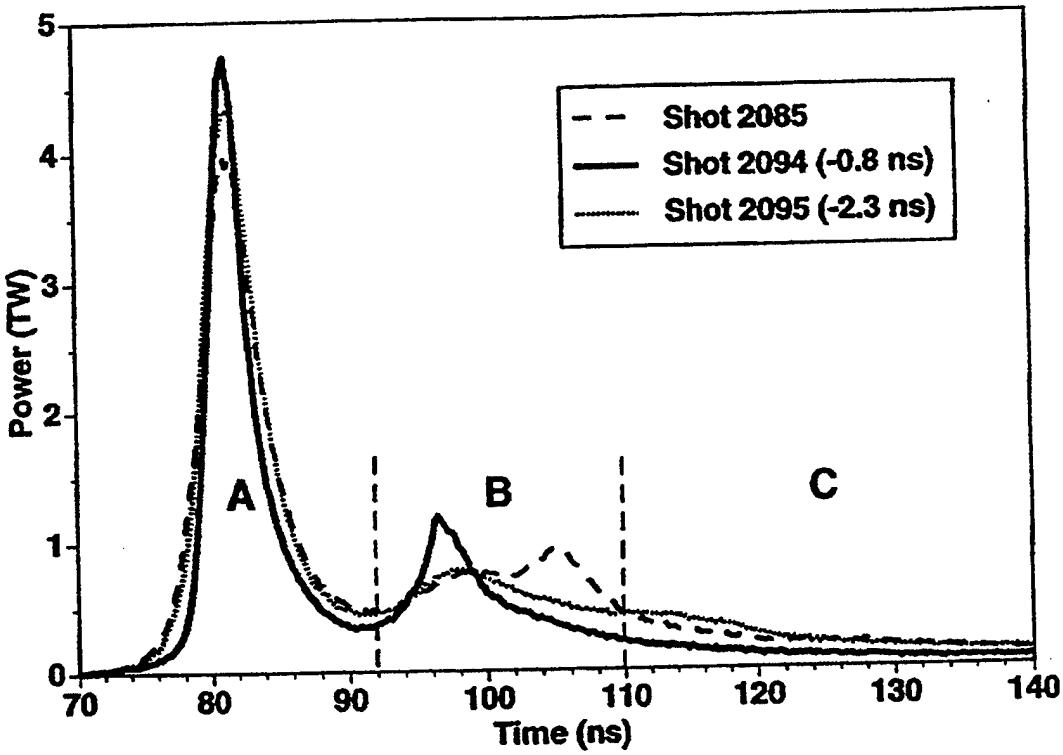
Shot 2085
Shot 2094 (-0.8 ns)
Shot 2095 (-2.3 ns)
A
B
C
Power (TW)
Time (ns)
0
1
2
3
4
5
70
80
90
100
110
120
130
140

Figure 1

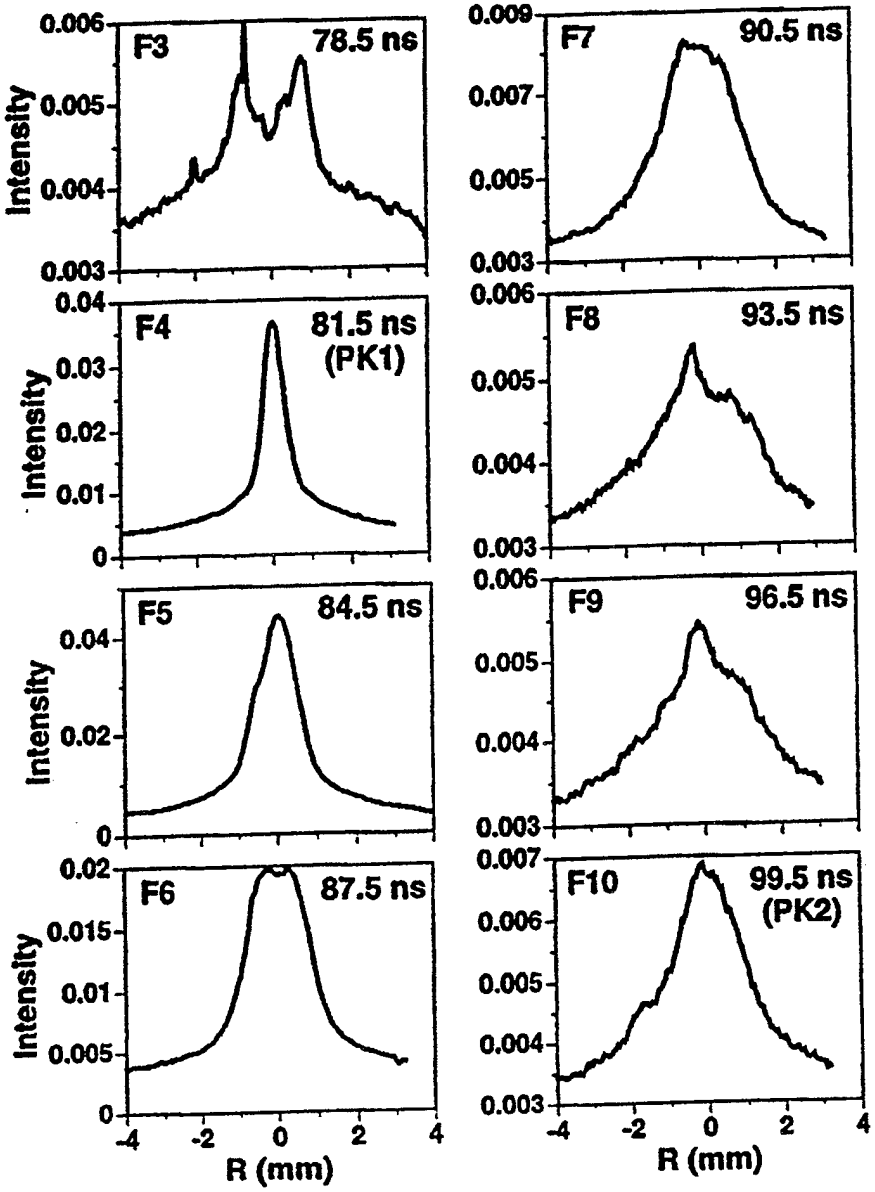
F3
78.5 ns
F4
81.5 ns
(PK1)
F5
84.5 ns
F6
87.5 ns
F7
90.5 ns
F8
93.5 ns
F9
96.5 ns
F10
99.5 ns
(PK2)
Intensity
R (mm)

Figure 2

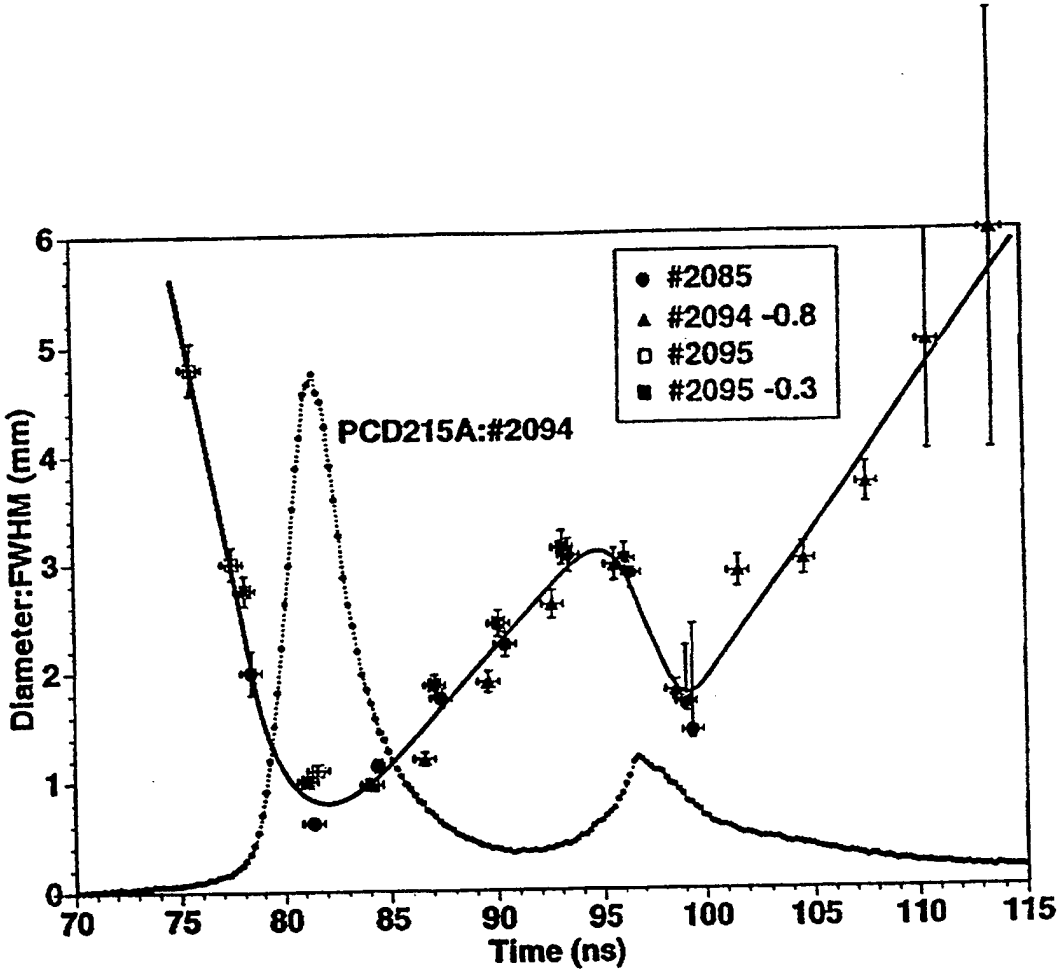
#2085
#2094 -0.8
#2095
#2095 -0.3
PCD215A:#2094
Diameter:FWHM (mm)
Time (ns)
0
1
2
3
4
5
6
70
75
80
85
90
95
100
105
110
115

Figure 3

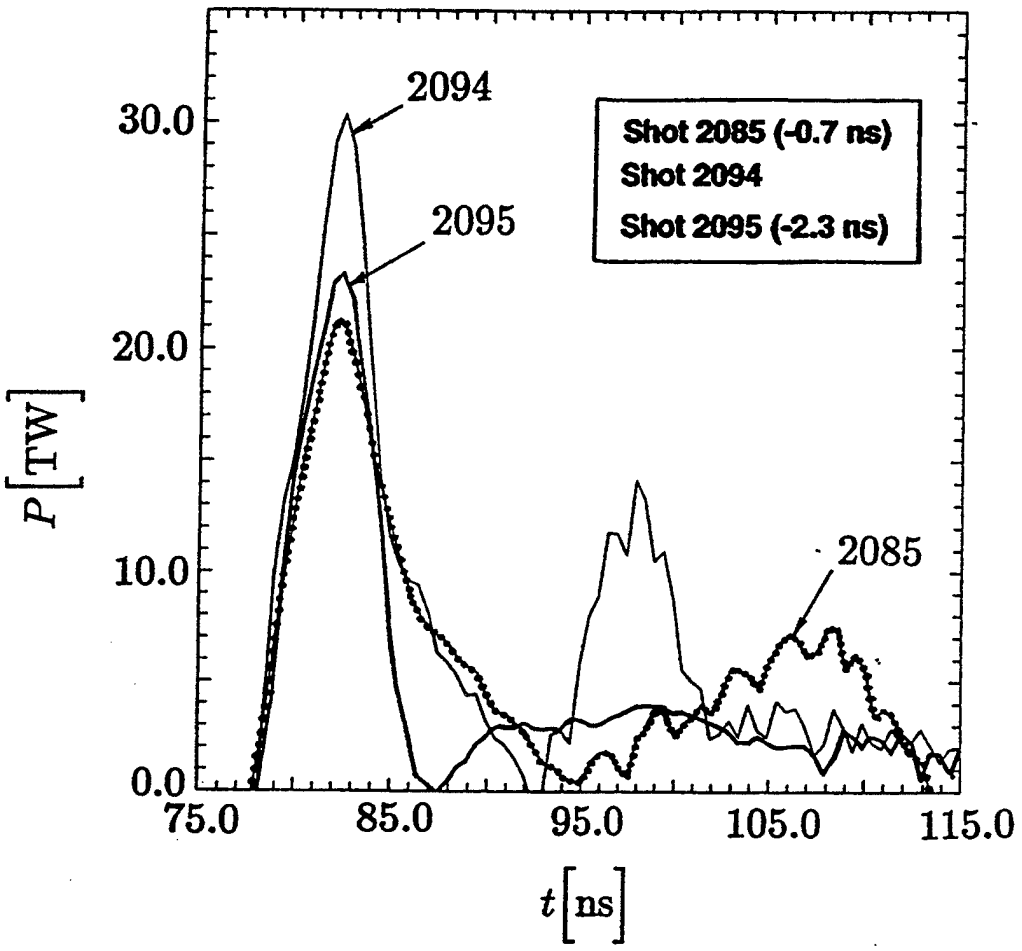
2094
2095
2085
Shot 2085 (-0.7 ns)
Shot 2094
Shot 2095 (-2.3 ns)
30.0
20.0
10.0
0.0
P [TW]
75.0
85.0
95.0
105.0
115.0
t [ns]

Figure 4

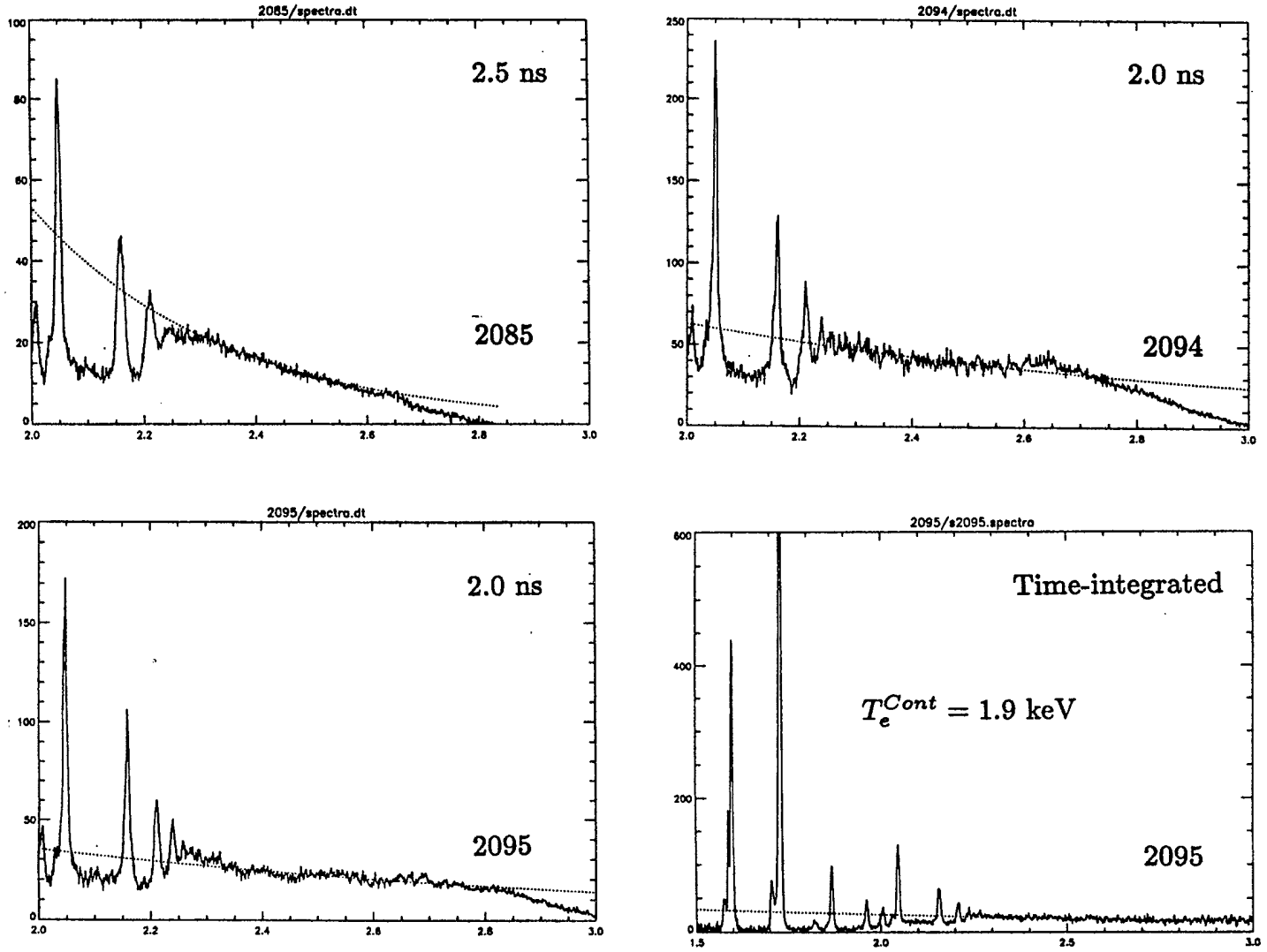
2085/spectra.dt
2.5 ns
2085
2094/spectra.dt
2.0 ns
2094
2095/spectra.dt
2.0 ns
2095
2095/s2095.spectra
Time-integrated
$T_e^{Cont} = 1.9$ keV
2095

Figure 5

Inferring a slope from time-resolved micro-channel-plate data requires knowing where to set the background level.

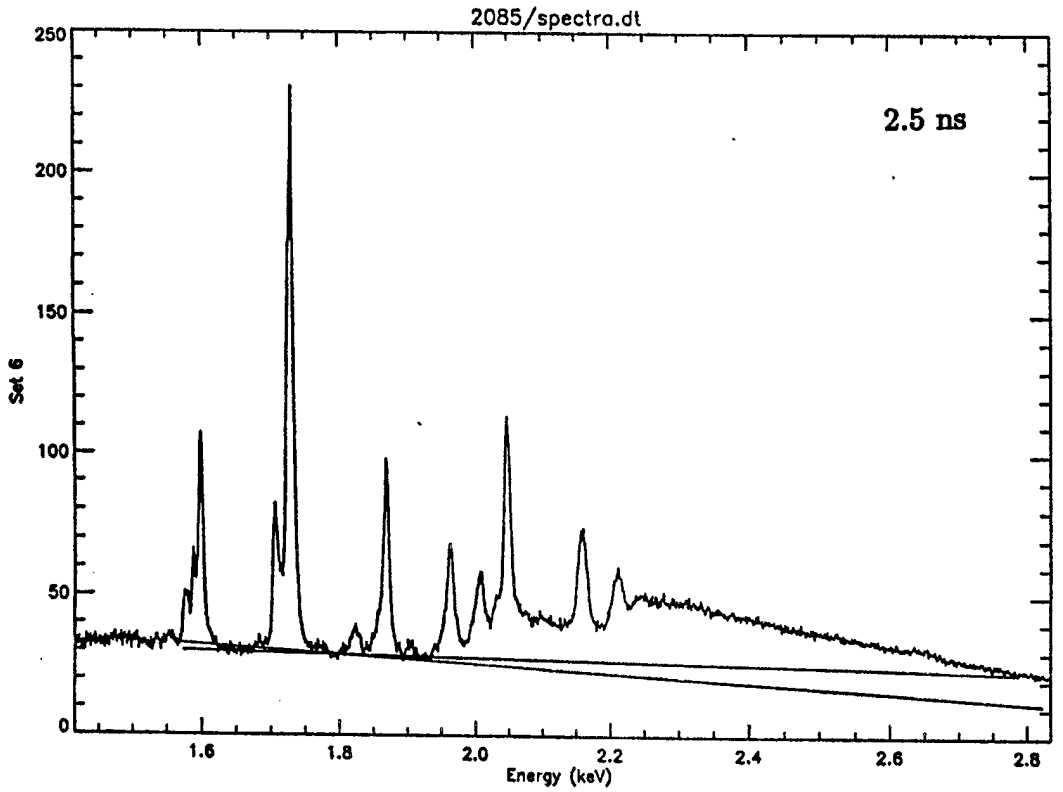

Figure 6

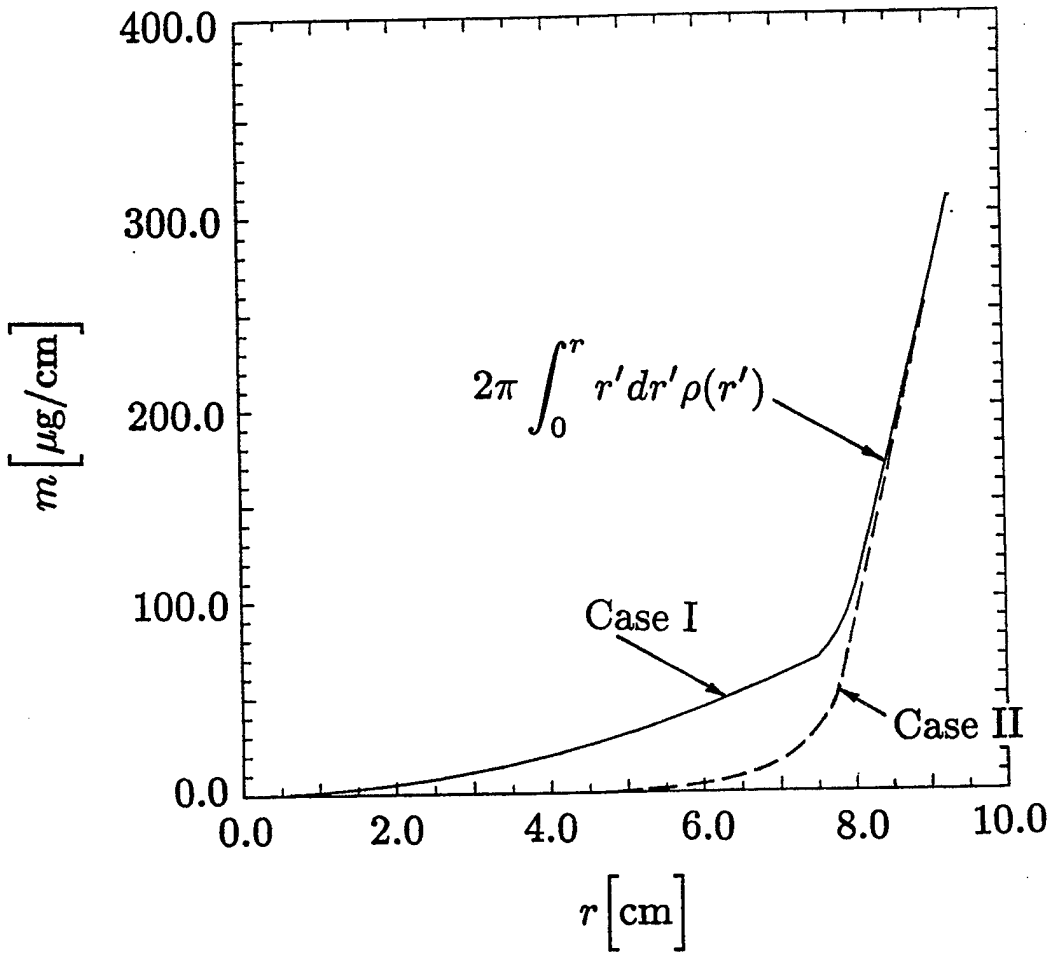
400.0
300.0
200.0
100.0
0.0
0.0
2.0
4.0
6.0
8.0
10.0
$m\left[\mu g/cm\right]$
$r\left[cm\right]$
$2\pi \int_0^r r' dr' \rho(r')$
Case I
Case II

Figure 7

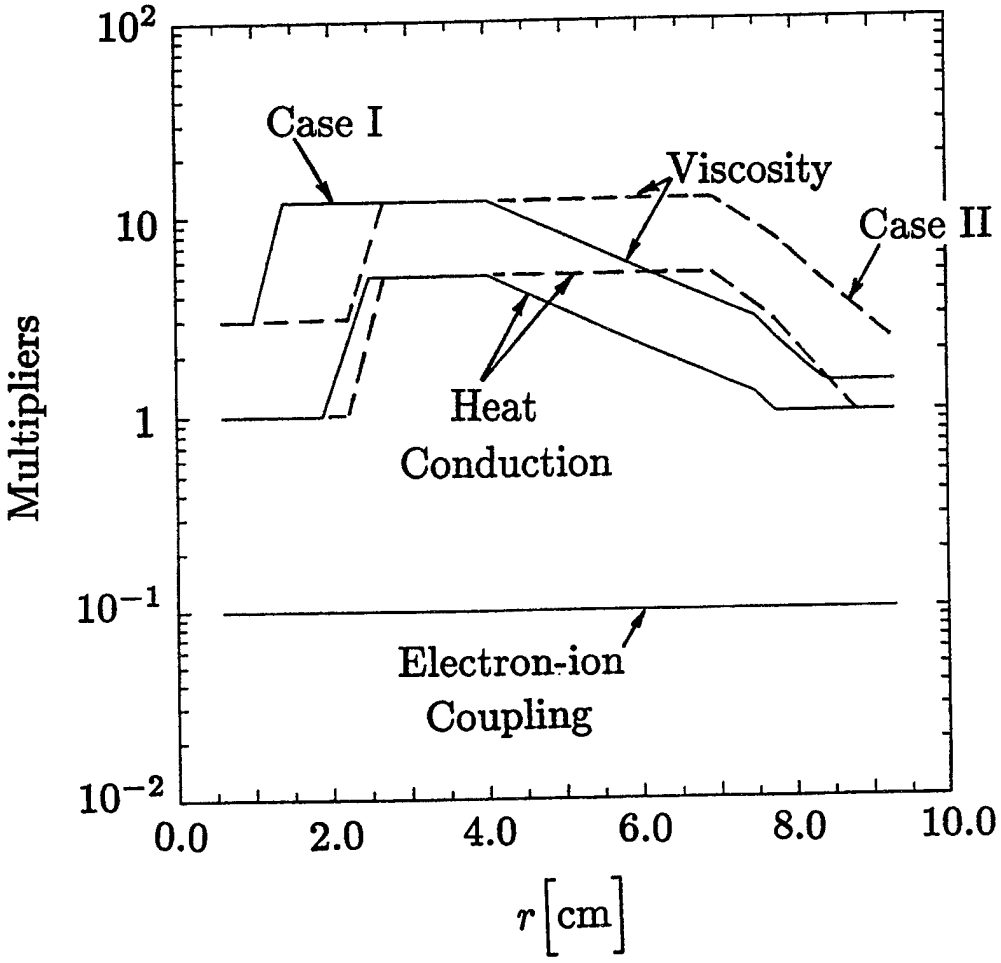
10^2
10
1
10^{-1}
10^{-2}
Multipliers
Case I
Viscosity
Case II
Heat
Conduction
Electron-ion
Coupling
0.0
2.0
4.0
6.0
8.0
10.0
r [cm]

Figure 8

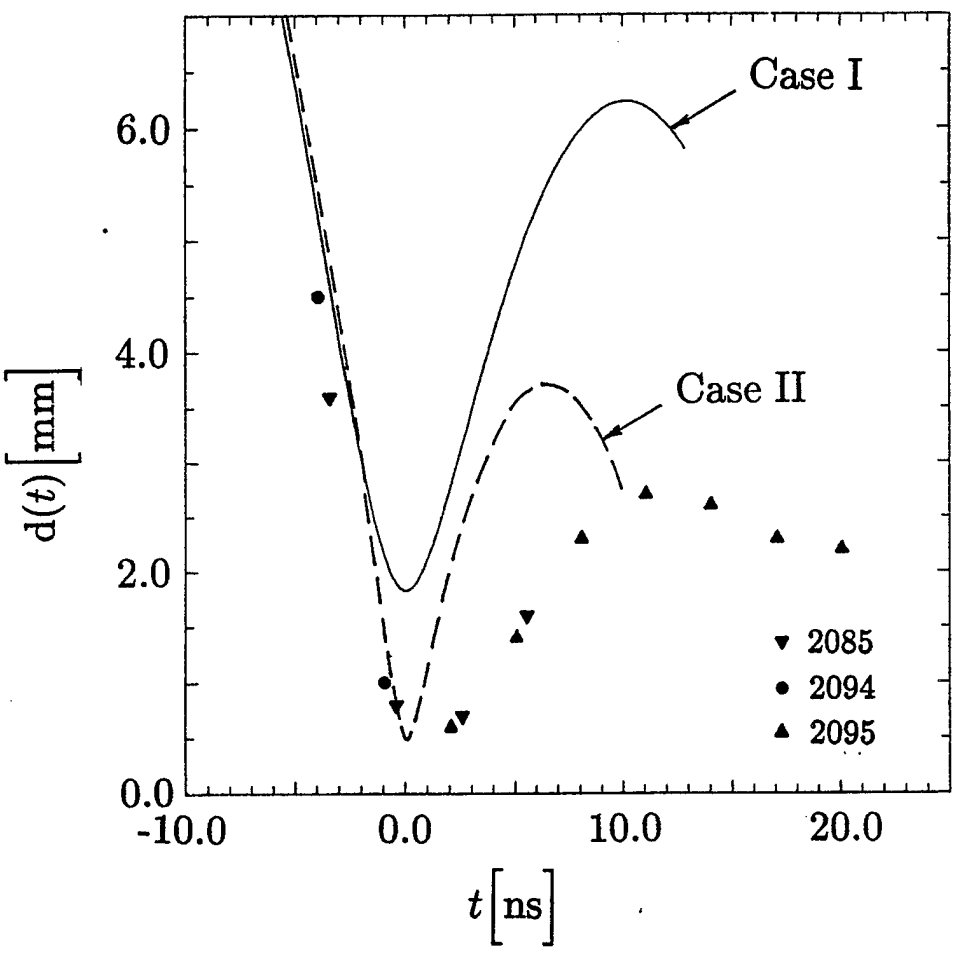

Figure 9

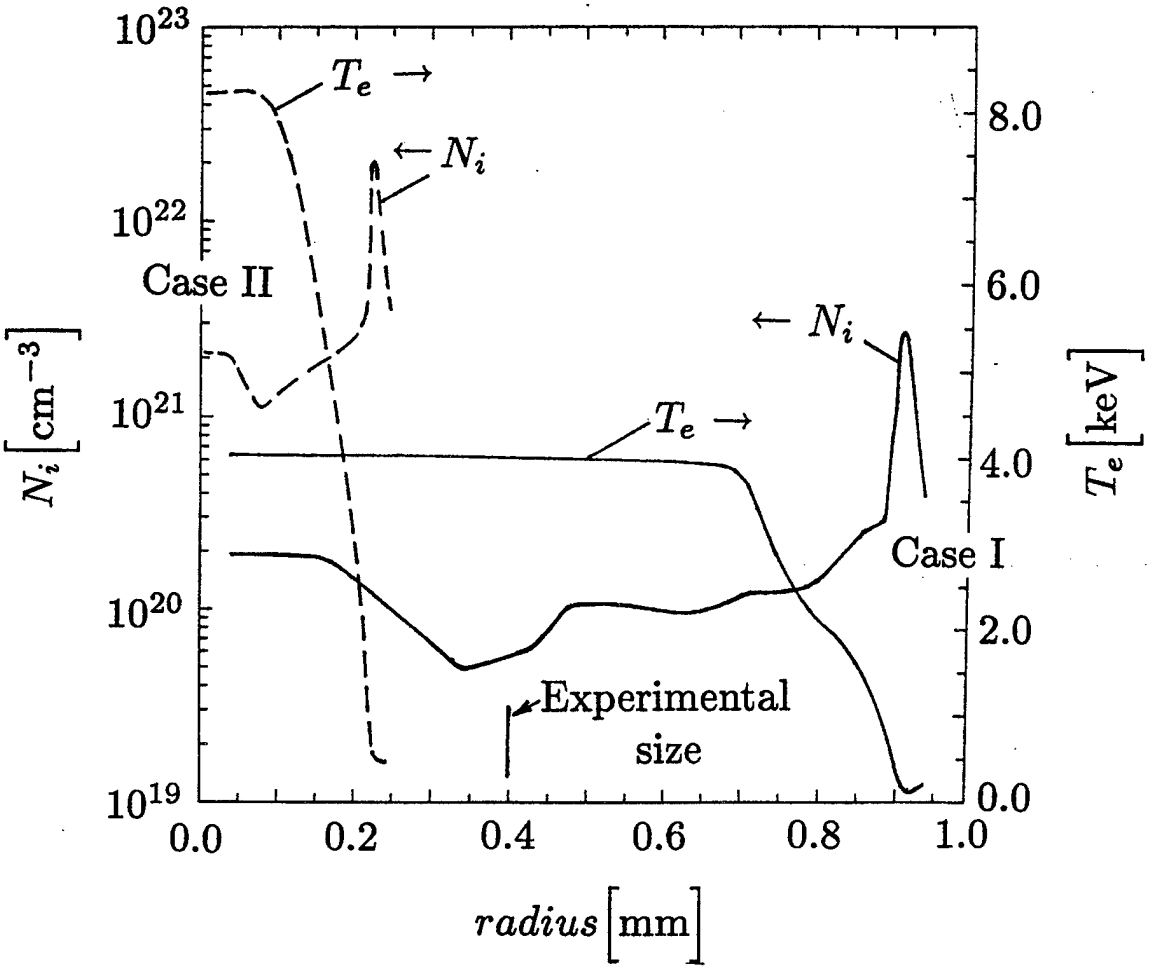
10^{23}
10^{22}
10^{21}
10^{20}
10^{19}
$N_i\left[\mathrm{cm}^{-3}\right]$
$T_e \rightarrow$
$\leftarrow N_i$
Case II
$\leftarrow N_i$
$T_e \rightarrow$
Case I
Experimental
size
8.0
6.0
4.0
2.0
0.0
$T_e\left[\mathrm{keV}\right]$
0.0
0.2
0.4
0.6
0.8
1.0
$radius\left[\mathrm{mm}\right]$

Figure 10

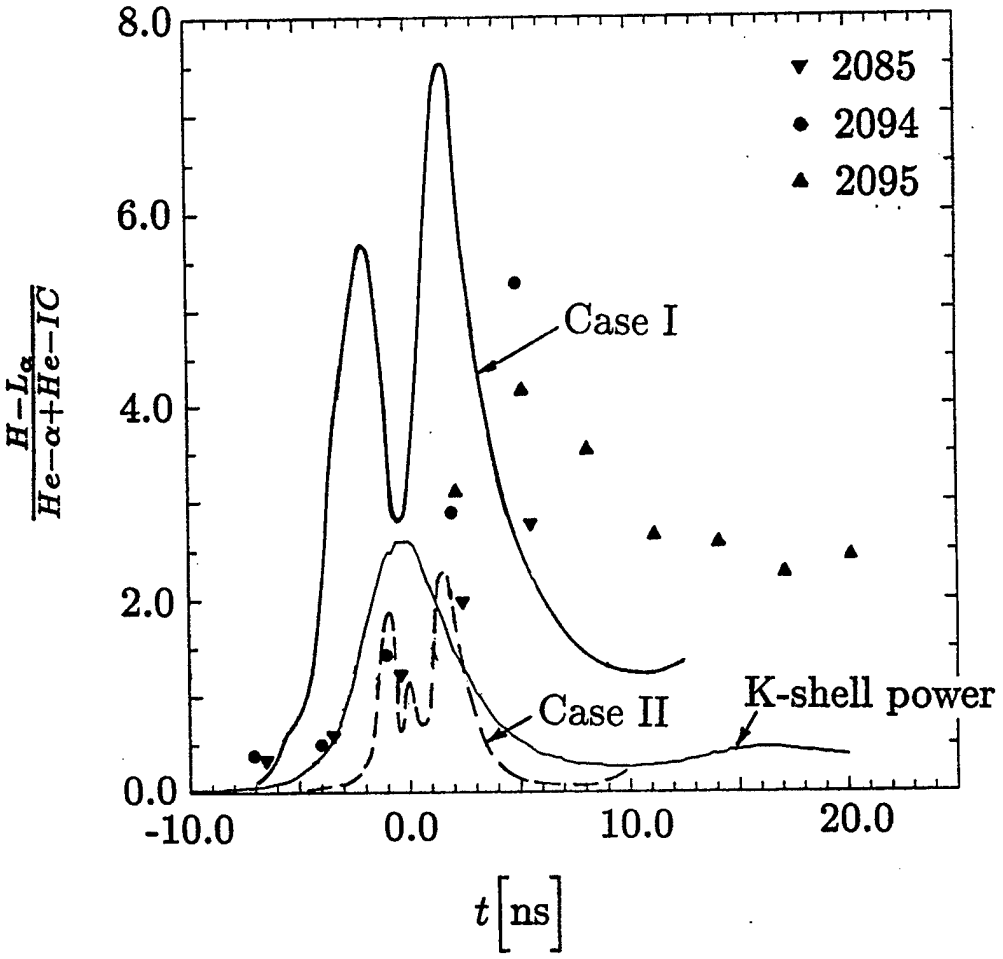
8.0
6.0
4.0
2.0
0.0
-10.0
0.0
10.0
20.0
2085
2094
2095
Case I
Case II
K-shell power
$\frac{H-L_\alpha}{He-\alpha+He-IC}$
$t\left[\mathrm{ns}\right]$

Figure 11

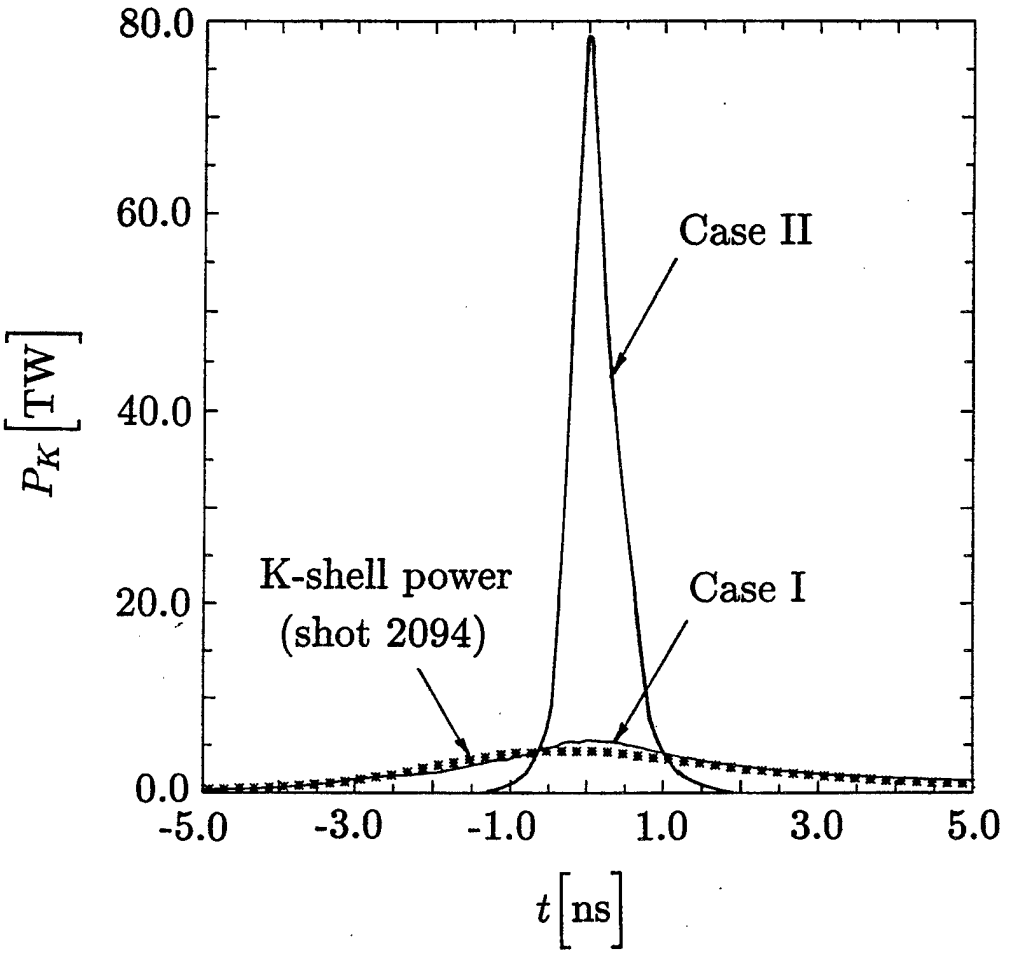
80.0
60.0
40.0
20.0
0.0
P_K [TW]
Case II
K-shell power
(shot 2094)
Case I
-5.0
-3.0
-1.0
1.0
3.0
5.0
t [ns]

Figure 12

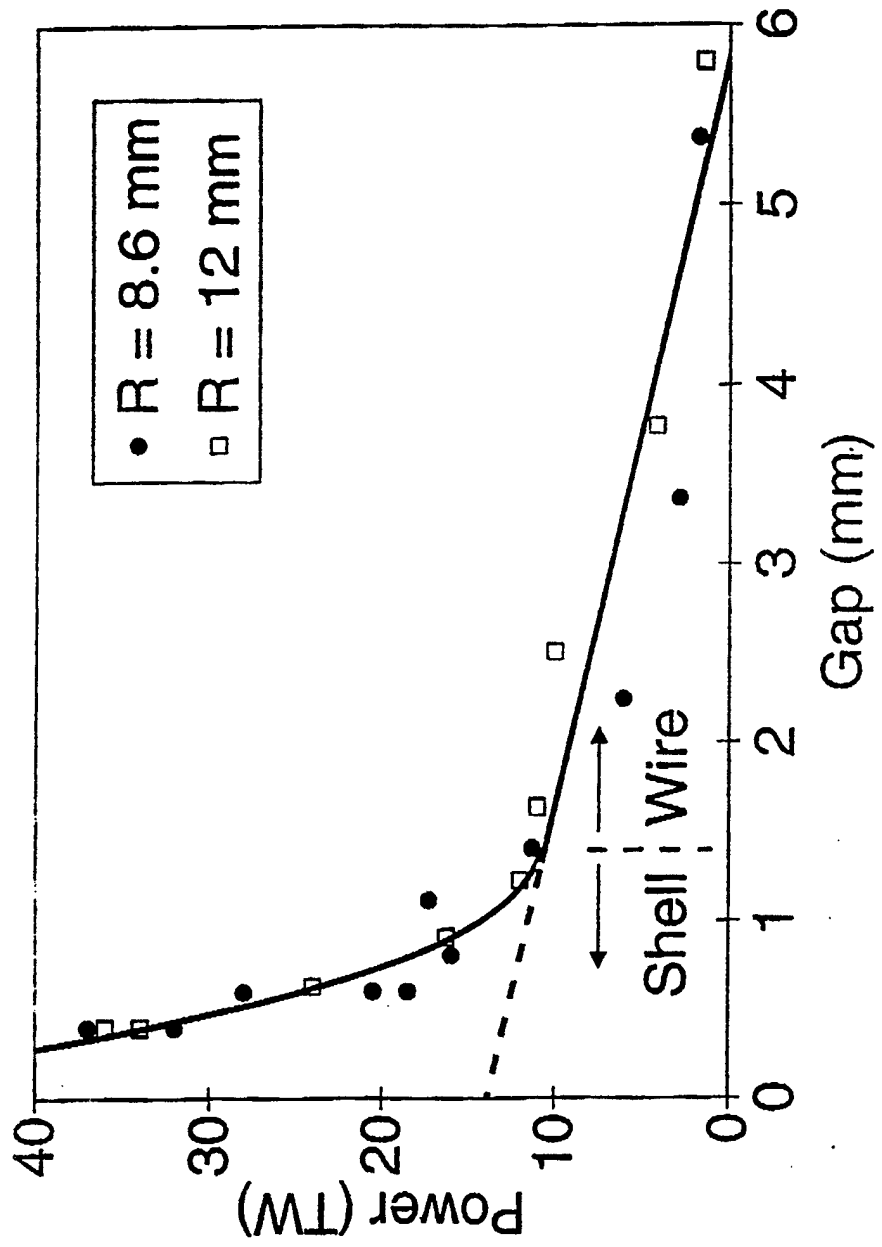

Figure 13

VIII. FAST COMMUTATION OF HIGH CURRENT IN DOUBLE WIRE ARRAY Z PINCH LOADS

In plasma radiation sources (PRS), Z-pinch loads are imploded to generate large amounts of soft x-rays.[1] The performance of PRS is known to be very sensitive to stability of implosions. Better stability means tighter Z-pinch at the stagnation phase, more uniform radiating plasma, and therefore, higher radiative output, and, in particular, greater K-shell yield. Simulations of Z-pinch implosions performed with one-dimensional (1-D) radiative hydrocodes, unless truncated at a certain level of radial compression or otherwise adjusted to achieve quantitative agreement with the experiments, typically predict much higher radiative yield than actually observed. This indicates both the importance of two- and three-dimensional effects in Z-pinch dynamics, and a considerable potential for improving radiative performance of existing pulsed power facilities by making implosions more stable, that is, more 1-D-like, than they conventionally are.

Numerous experiments, starting from the early works with puff-on-puff[2] and double puff[3,4] loads, to recent developments[5-8] have demonstrated the efficiency of structured Z-pinch loads for increasing the uniformity of the stagnated plasma. In particular, experiments on Saturn accelerator at Sandia National Laboratories and related simulation results[5] have demonstrated that increasing the number of wires in an imploded wire array load up to 100 and above makes initially separate wires coalesce early in the implosion, forming a very symmetrical annular plasma shell. New Russian experiments with gas-puff-on-wire-array complex loads on the GIT-4 generator have shown a

remarkable increase in the aluminum K-shell yield and radiative power due to fast switching of the pinch current from the outer gaseous shell to the inner wire array.[6,7]

In this Section, we discuss a load design that might combine the advantages of the two above approaches. Consider a load configured as nested concentric wire arrays, with sufficiently large number of wires in the outer part. Initially, the current is driven through the outer array imploding it. Once the outer array or the annular plasma shell formed from it approaches the inner array, the imploded plasma might penetrate through the gaps between the wires, but the azimuthal magnetic field is trapped due to both the high conductivity of the inner wires and the inductive coupling between the two parts of the array, causing a rapid switching of the total current to the inner part of the array. This is basically the mechanism of current switching in the GIT-4 experiments.[6,7] However, its performance in this particular case is limited because the dynamics of the outer gas puff shell, as shown in numerous experiments, is not fully predictable.[7] A symmetrical outer shell formed from a multi-wire array, as done in Ref. 5, would be much better for this purpose. For the conditions of Saturn experiments,[5, 8] our estimates indicate a possibility of switching a multi-MA current to the inner part of the load within 5-10 ns.

For our simulation, we have developed a versatile dynamic model of an imploded wire array. The wire arrays used as PRS are known to be predominantly inductive loads, and the main feature of our model accordingly is a self-consistent calculation of the current distribution over the wires and the back current posts due to inductive coupling. The results of linear stability analysis[9, 10] and the estimates for the limits on compression ratio associated with azimuthal asymmetries[11] available in the literature have been obtained under the assumption that the current distribution over the wires is either

uniform or otherwise prescribed. Although the earlier results are not directly applicable to the inductive loads, they have been successfully used to test our model in the "prescribed current distribution" regime.

We simulate an array of N wires in a load unit with N_b back current posts. Both the wires and the back current posts are considered straight conductors, parallel to the z axis, carrying currents I_i, $i = 1,...,N$ and $I_{b,k}$, $k = 1,...,N_b$, the total current through the wire array thus being $I = \sum I_i = -\sum I_{b,k}$. The equation of motion for the i-th wire is

$$\mu_i \frac{d^2\mathbf{r}_i}{dt^2} = \frac{\mu_0 I_i}{2\pi} \frac{\partial}{\partial \mathbf{r}_i} \left(\sum_{j=1}^{N}{}' I_j \ln r_{ij} + \sum_{k=1}^{N_b} I_{b,k} \ln r_{ik} \right), \qquad (1)$$

where μ_i and $\mathbf{r}_i$ are line mass and two-dimensional radius-vector of the i-th wire, r_{ij} and r_{ik} denote the distances between the i-th and j-th wires and between the i-th wire and the k-th back current post, respectively; the prime means that the sum does not include $j = i$. When two or more wires collide, they are allowed to pass through each other.

The currents in each of the wires and the back current posts are found from the equations that describe the inductive coupling between them. We introduce $N \times N_b$ rectangular contours elongated along the z axis, which are formed by the wires and the back current posts. The partial current flowing through the i-th wire and closing through the k-th back current post is denoted by I_{ik}, so that the currents in the i-th wire and in the k-th back current post are given by $I_i = \sum_{k=1}^{N_b} I_{ik}$ and $I_k = -\sum_{i=1}^{N} I_{ik}$, respectively. All the contours are connected in parallel to the pulsed power source generating the voltage waveform $V(t)$. Since the imploded wire array is an inductive load,

$$V(t) = d\Phi / dt \ . \qquad (2)$$

The magnetic flux $\Phi(t)$, being therefore the same for each of the above contours, is expressed for the (i,k)-th contour as

$$\Phi(t) = \sum_{j=1}^{N} \sum_{m=1}^{N_b} L_{ik,jm} I_{jm}, \qquad (3)$$

where $L_{ik,jm} = (\mu_0 h / 2\pi) \ln(r_{im} r_{jk} / r_{ij} r_{mk})$ is the mutual inductance between the (i,k)-th and the (j,m)-th contours, and h is the length of wire array. If $i = j$ and/or $m = k$, which means that the two contours share the same wire and/or the same back current post, we have to substitute the wire radius, a_w, instead of r_{ii}, and/or the radius of the back current post, a_b, instead of r_{kk}.

Equations (1) and (2) [or an appropriate circuit equation instead of (2)] constitute a system of $4N+1$ ordinary first-order differential equations for the coordinates and velocities of the wires and the magnetic flux. At each instant of time, the currents in each of the contours are found from the $N \times N_b$ linear equations (3), so that the currents in the wires and the back current posts, the total current and the inductance of the load are determined self-consistently. Since the model includes no dissipations, the sum of magnetic and kinetic energies of the load equals the energy delivered to the load by the external circuit.

As an example, consider an implosion of an array that consists of $N = 16$ identical wires (the total line mass is $\mu = 50$ μg/cm), which initially are uniformly distributed over a circle of radius $R_0 = 10$ mm. The azimuthal asymmetry is caused by the presence of $N_b = 8$ back current posts located at $R_b = 16.7$ mm, and separated by equal

angles. In Fig. 1, we compare the time histories of the average radius $\langle r(t) \rangle = \sum_{i=1}^{N} \mu_i r_i / \mu$ and the configurations of the array at the instant of peak compression (minimum $\langle r(t) \rangle$) calculated under the assumption of constant current $I = 6$ MA, equally distributed over 16 wires and 8 back current posts, and using our model driven by a generic Saturn voltage waveform and circuit,[8] which produces a peak current slightly above 6 MA. Of course, the array is imploded by a constant current much faster than when both the voltage waveform and the time dependence of the load inductance are accounted for. The azimuthal asymmetry of the implosion, which shapes the configuration of the array at peak compression and thus limits the compression ratio, is no less profoundly affected.

A double wire array includes a set of N_1 identical wires uniformly distributed over a circle with $r = R_1$ (the outer part), and another set of N_2 wires located at $r = R_2 < R_1$ (the inner part). Initially, the current is driven primarily through the outer part of the load, whose inductance is lower. When the imploded outer part approaches the inner part and passes inside it, the roles of the two parts are reversed. The set of N_2 wires now has lower inductance, and most of the current is therefore switched to it. Figure 2 presents the results obtained for a double wire array with $N_1 = 32$, $N_2 = 8$, $R_1 = 6$ mm, $R_2 = 2$ mm, the line masses $\mu_1 = 160$ μg/cm and $\mu_2 = 1000$ μg/cm, respectively, in a load unit with $N_b = 8$ back current posts located at $R_b = 1$ cm, the implosion being driven by the same voltage waveform and circuit as above. We see that at $t = 60$ ns most of the current is switched to the inner array, with current rise rate of order of 10^{15} A/s. Here, the main current does not flow through the inner part long enough to implode it. Having bounced

from the axis, the outer part passes through it once again, on the way out, and the main current is switched back to it. Then the process repeats itself.

It must be emphasized, however, that our dynamic model of the implosion shows the worst-case scenario of the current switching. In reality, the outer part of the load approaching the inner part, should be a conducting plasma shell, as in Refs. 6, 7, not a set of separate wires. The azimuthal magnetic field frozen into the plasma has to diffuse through it before the shell is allowed to flow freely into the gap between the inner wires, which is not accounted for in our model. Consequently, an inelastic collision, producing a plasma shell stuck to a wire cage, is likely to occur instead of a free penetration. The current has to be switched to this combined load within a time interval even shorter than that shown in Fig. 2, since the switching takes place in the collision of the two parts of the load, not when the outer part approaches the axis close enough to be shunted by the inner part. Note that with $\mu_1 << \mu_2$, as required for proper timing, both the mass and the symmetry of the combined load are determined by the inner array.

A more realistic scenario of current switching (which, in particular, is more like one realized in Refs. 6, 7) is illustrated by Fig. 3. Without including dissipations in our model, we simulate it plainly by holding the outer part of the load near the axis once it gets there, not letting it bounce (everything else is the same as in Fig. 2). The implosion of the inner part of the load from the initial radius $R_2 = 2$ mm by the 5 MA current switched to it in about 5 ns occurs within 15 ns. Here, high initial symmetry of both parts of the load ensures its uniformity, whereas very large value of the current rise rate contributes to stability of implosion.[12] We can therefore expect the Z-pinch produced in stagnation to be

even tighter than those observed in recent experiments with compact wire arrays,[8] and the radiative performance of the load to increase accordingly.

References

1. N. R. Pereira and J. Davis, J. Appl. Phys. **64** R 1 (1988).
2. T.-F. Chang, A. Fisher, and A. Van Drie, J. Appl. Phys. **69**, 3447 (1991).
3. R. B. Baksht, A. V. Luchinsky, and A. V. Fedyunin, Sov. Phys. - Tech. Phys. **37**, 1118 (1992).
4. R. B. Spielman, T. Nash, and M. Krishnan, Bull. Am. Phys. Soc. **37**, 1578 (1992).
5. T. W. L. Sanford, T. J. Nash, B. M. Marder, R. Humphreys, C. Deeney, R. B. Spielman, J. F. Seaman, R. C. Mock, J. S. McGurn, D. Jobe, T. J. L. Gilliland, M. Vargas, K. Struve, W. A. Stygar, J. H. Hammer, J. L. Eddleman, J. S. DeGroot, D. Mosher, K. G. Whitney, J. P. Apruzese, P. Pulsifer, and Y. Maron, Bull. Am. Phys. Soc. **40**, 1846 (1995).
6. R. B. Baksht, Bull. Am. Phys. Soc. **40**, 1852 (1995).
7. R. B. Baksht, I. M. Datsko, A. A. Kim, A. Yu. Labetsky, S. V. Loginov, V. I. Oreshkin, A. G. Rousskikh, A. V. Fedyunin, and A. V. Shishlov, Plasma Physics Reports **21**, 907 (1995).
8. T. W. L. Sanford, D. Mosher, J. S. DeGroot, J. H. Hammer, B. M. Marder, S. Maxon, T. J. Nash, R. B. Spielman, P. T. Springer, K. Struve, R. S. Thoe, D. R. Welch, W. E. Alley, C. Bruns, J. D. Eddleman, J. Emig, T. L. Gilliland, J. Hernandez, D. Jobe, J. S. McGrun, R. C. Mock, J. F. Seaman, M. Vargas, and G. B. Zimmerman, "X-ray emission from a high-atomic-number z-pinch plasma created from compact wire arrays," Sandia report SAND96-0222, March 1996. Copies may be ordered from the NTIS, Springfield, VA 22161.

9. F. S. Felber and N. Rostoker, Phys. Fluids **24**, 1049 (1981).

10. A. A. Samokhin, Prikl. Mat. Tekh. Fiz., no. 2, 89 (1988).

11. See National Technical Information Service Document No. PB95-144317 (D. Mosher, "Plasma radiation source implosion limits due to azimuthal asymmetries," in *Proc. of the 10th Int. Conf. on High Power Particle Beams*, 20-24 June 1994, San Diego, CA, p. 159). Copies may be ordered from the NTIS, Springfield, VA 22161.

12. J. D. Sethian, A. E. Robson, K. A. Gerber, and A. W. DeSilva, Phys. Rev. Lett. **59**, 892 (1987) (corrig. ibid, p. 1790).

Figure captions

Fig. 1. Configurations of the wire array at peak compression (a) and time histories of the average radius (b). Outer and inner array (a), dotted and solid lines (b) are plotted for the cases of constant current and constant voltage waveform with inductive coupling, respectively.

Fig. 2. (a) Total (solid line) and partial currents in the outer (dotted) and in the inner (dashed line) parts of the double wire array. (b) Time histories of the average radii of the outer (solid line) and the inner (dashed line) parts.

Fig. 3. Same as in Fig. 2 for an inelastic implosion of the outer part.

(a)

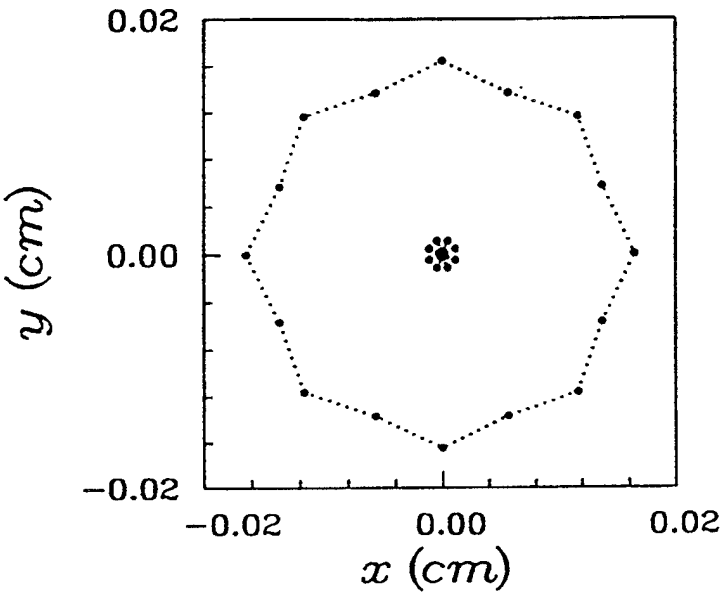
0.02
0.00
−0.02
y (cm)
−0.02
0.00
0.02
x (cm)

(b)

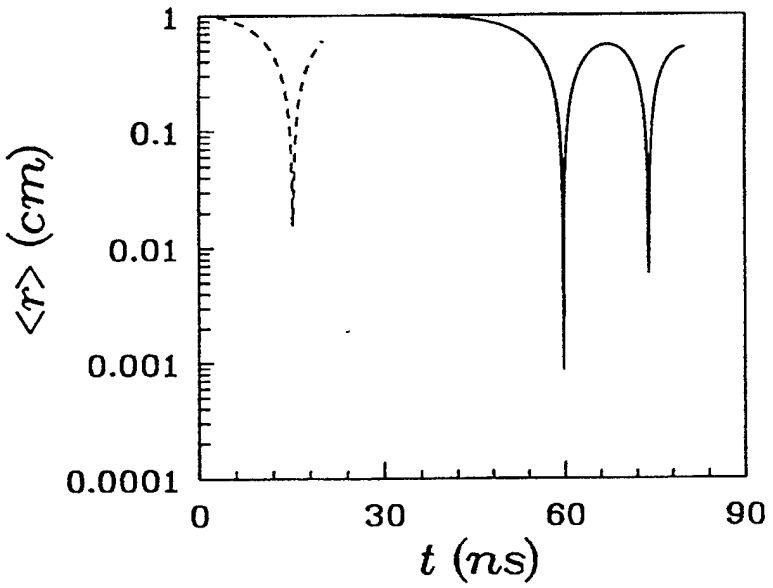
1
0.1
0.01
0.001
0.0001
<r> (cm)
0
30
60
90
t (ns)

Fig. 1

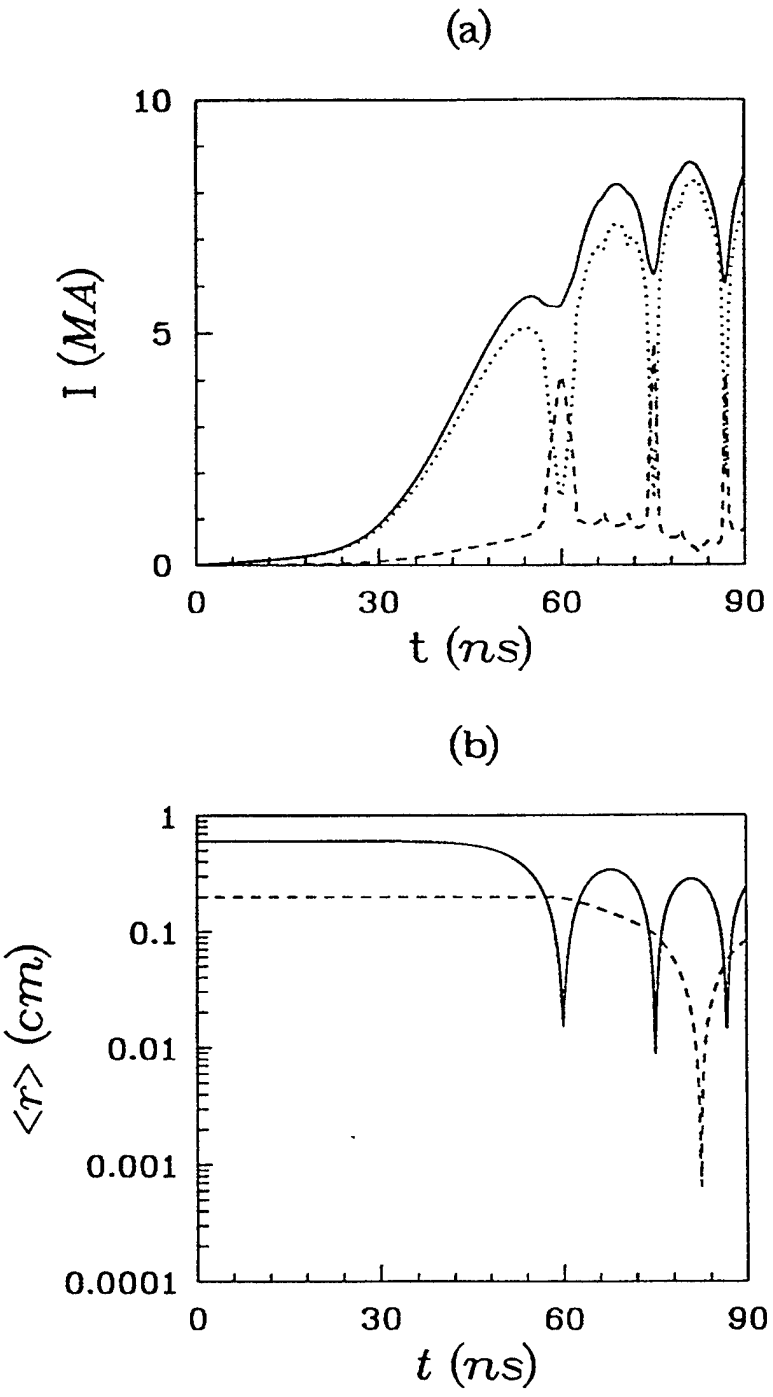

Fig. 2

(a)

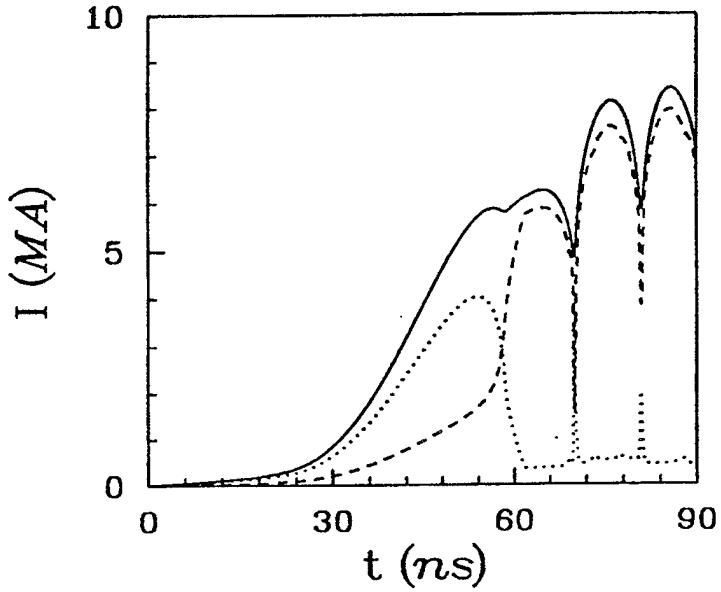

(b)

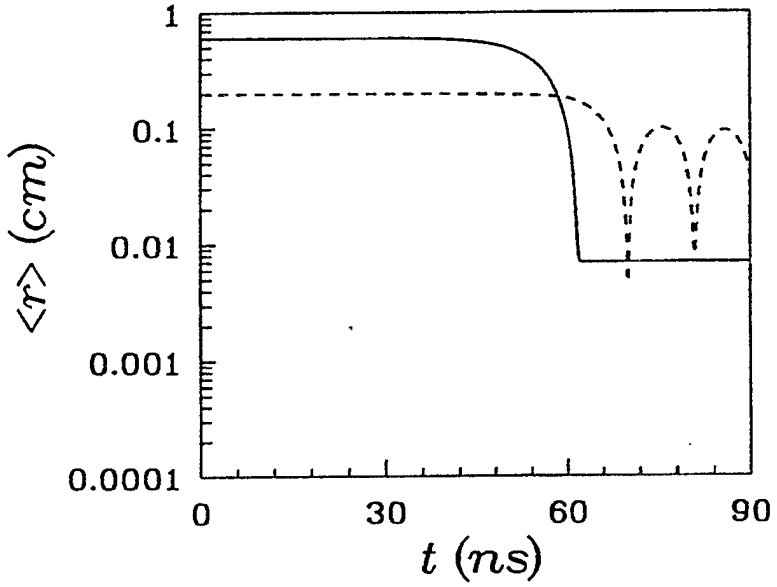

Fig. 3